Summer 2017

Numerical investigation on nonlocal problems with the fractional Laplacian

Siwei Duo

Department: Mathematics and Statistics

Recommended Citation

Duo, Siwei, "Numerical investigation on nonlocal problems with the fractional Laplacian" (2017). *Doctoral Dissertations*. 2742.
https://scholarsmine.mst.edu/doctoral_dissertations/2742

NUMERICAL INVESTIGATION ON NONLOCAL PROBLEMS WITH THE FRACTIONAL LAPLACIAN

by

SIWEI DUO

A DISSERTATION

Presented to the Graduate Faculty of the

MISSOURI UNIVERSITY OF SCIENCE AND TECHNOLOGY

In Partial Fulfillment of the Requirements for the Degree

DOCTOR OF PHILOSOPHY

in

MATHEMATICS

2017

Approved by

Dr. Yanzhi Zhang, Advisor
Dr. Xiaoming He
Dr. Vy Khoi Le
Dr. John R. Singler
Dr. Thomas Vojta

ABSTRACT

Nonlocal models have recently become a powerful tool for studying complex systems with long-range interactions or memory effects, which cannot be described properly by the traditional differential equations. So far, different nonlocal (or fractional differential) models have been proposed, among which models with the fractional Laplacian have been well applied. The fractional Laplacian $(-\Delta)^{\alpha/2}$ represents the infinitesimal generator of a symmetric α-stable Lévy process. It has been used to describe anomalous diffusion, turbulent flows, stochastic dynamics, finance, and many other phenomena. However, the nonlocality of the fractional Laplacian introduces considerable challenges in its mathematical modeling, numerical simulations, and mathematical analysis.

To advance the understanding of the fractional Laplacian, two novel and accurate finite difference methods – the weighted trapezoidal method and the weighted linear interpolation method are developed for discretizing the fractional Laplacian. Numerical analysis is provided for the error estimates, and fast algorithms are developed for their efficient implementation. Compared to the current state-of-the-art methods, these two methods have higher accuracy but less computational complexity. As an application, the solution behaviors of the fractional Schrödinger equation are investigated to understand the nonlocal effects of the fractional Laplacian. First, the eigenvalues and eigenfunctions of the fractional Schrödinger equation in an infinite potential well are studied, and the results provide insights into an open problem in the fractional quantum mechanics. Second, three Fourier spectral methods are developed and compared in solving the fractional nonlinear Schrödinger equation (NLS), among which the SSFS method is more effective in the study of the plane wave dynamics. Sufficient conditions are provided to avoid the numerical instability of the SSFS method. In contrast to the standard NLS, the plane wave dynamics of the fractional NLS are more chaotic due to the long-range interactions.

ACKNOWLEDGMENTS

First and foremost, I would like to express my deepest gratitude to my Ph.D. advisor Dr. Yanzhi Zhang for introducing me to this exciting field of mathematics and for her dedicated help, encouragement, advice and continuous support throughout my Ph.D. It has been my honor to be her first Ph.D. student. Her enthusiasm, integral perspective on research and her mission for providing high-quality work, has made a deep impression on me. I appreciate all her contributions of time, guidance, and funding to make my Ph.D. experience productive and stimulating. I am really glad to be associated with a person like Dr. Yanzhi Zhang in my life.

Besides my advisor, I would like to thank my Ph.D. committee members, Dr. Vy Choi Le, Dr. Xiaoming He, Dr. John Singler and Dr. Thomas Vojta for their helpful comments on my thesis and career advice in general.

I wish to thank my officemates Sabrina Streipert, Gulsah Yeni and Jinyu Du, my roommate Xuejing Liu for their warmly support academically and personally.

Lastly, I would like to thank my family for all their love and encouragement. To my late father Yongshun Duo, who raised me with a love of science, helped me to realize my own potential and always believed in me and encouraged me to follow my dream. To my beloved mother Ruohong Liu, who is supporting me in all my pursuits and showing me that the key to life is enjoyment. My thanks also goes to Guodong Cui for all his love and patient whose faithful support and everlasting encouragement during the final stages of this Ph.D. is deeply appreciated.

TABLE OF CONTENTS

Page

SECTION

APPENDICES

LIST OF ILLUSTRATIONS

Figure Page

LIST OF TABLES

1. INTRODUCTION

In the last couple of decades, nonlocal or fractional differential models have become a powerful tool for modeling phenomena which cannot be described properly by the integer-order partial differential equations. Recent experiments in the study of diffusion processes which take places in various complex systems perform significant deviations from the standard laws of diffusion [21, 67]. Under such settings, the standard Laplacian Δ which processes a mathematical description of the normal diffusion fails to reproduce the observed anomalous diffusion behavior, and the fractional models have to take the place as an alternative modeling approach. So far, different fractional differential models have been proposed, among which models with the fractional Laplacian have been well applied in the field of the anomalous diffusion or dispersion [25, 30], turbulent flows [13, 76], porous media flows, quantum mechanics [33, 63], stochastic dynamics [40], finance [20], and many others.

Contrary to the standard Laplacian, the fractional Laplacian is a nonlocal operator defined on the entire space. Over $\mathbb{R}^d$, the *fractional Laplacian* $(-\Delta)^{\alpha/2}$ is defined via a pseudo-differential operator with symbol $|\xi|^\alpha$ [62, 73]:

$$(-\Delta)^{\alpha/2}u(\mathbf{x}) = \mathcal{F}^{-1}\big[|\xi|^\alpha \mathcal{F}[u]\big], \qquad \text{for } \alpha > 0, \tag{1.1}$$

where $\mathcal{F}$ represents the Fourier transform, and $\mathcal{F}^{-1}$ is the inverse Fourier transform. In a special case with $\alpha = 2$, the definition in (1.1) reduces to the standard Laplace operator $-\Delta$. The definition in (1.1) enables one to utilize the fast Fourier transform to efficiently solve problems involving the fractional Laplacian, however, it is suitable only for problems defined either on the whole space $\mathbb{R}^d$ or on a bounded domain with periodic boundary conditions. In the literature, an equivalent hypersingular integral definition of the fractional

Laplacian $(-\Delta)^{\alpha/2}$ is introduced [28, 62, 73, 80]:

$$(-\Delta)^{\alpha/2}u(\mathbf{x}) \quad = \quad C_{d,\alpha}\ \text{P.V.} \int_{\mathbb{R}^d} \frac{u(\mathbf{x}) - u(\mathbf{y})}{|\mathbf{y}-\mathbf{x}|^{d+\alpha}}\, d\mathbf{y}, \qquad \text{for } \alpha \in (0,2), \tag{1.2}$$

where P.V. stands for the principal value, and $C_{d,\alpha}$ is the normalization constant given by

$$C_{d,\alpha} = \frac{2^{\alpha-1}\alpha\,\Gamma((d+\alpha)/2)}{\sqrt{\pi^d}\,\Gamma(1-\alpha/2)} \tag{1.3}$$

with $\Gamma(\cdot)$ denoting the Gamma function. From the probabilistic point of view, the fractional Laplacian $(-\Delta)^{\alpha/2}$ represents the infinitesimal generator of a symmetric α-stable Lévy process [3, 18]. In contrast to (1.1), the definition in (1.2) can easily incorporate with non-periodic bounded domains. Note that the integral representation in (1.2) is defined for $0 < \alpha < 2$, while the pseudo-differential definition in (1.1) is valid for all $\alpha > 0$. The equivalence of definitions (1.1) and (1.2) for $\alpha \in (0,2)$ are studied in [26, Proposition 3.3] and more discussions can be found in [26, 60, 73, 88] and references therein. Recently, many studies have been carried out on *the Dirichlet fractional Laplacian*, i.e., the fractional Laplacian on a bounded domain with extended homogeneous Dirichlet boundary condition. However, the current understanding of this topic still remains limited, and the main challenges are from the approximation of the hypersingular integral combining with the non-local boundary condition. So far, numerical methods for directly discretizing the Dirichlet fractional Laplacian still remains limited.

The fractional Schrödinger equation was introduced by Laskin [63, 64] as a result of extending the Feynman path integral over Brownian trajectories to Lévy trajectories. It is a fundamental model of factional quantum mechanics that is expected to reveal some novel phenomena that are absent from its standard (non-fractional) counterpart. In [94], a zigzag propagation of light is found in the fractional Schrödinger equation with parabolic potential, which is different from the phenomena that is observed in the standard Schrödinger equation. Moreover, several optical realizations of the fractional Schrödinger equation have been recently proposed in [65, 94, 95], and references therein. Although lots of topics under the context of the standard Schrödinger equation have been well studied, such as the infinite potential well model, the dynamics of the plane waves, due to the nonlocality arises from the fractional Laplacian, the studies of the fractional Schrödinger equation are still very limited.

The Schrödinger equation in an infinite potential well plays an important role in the understanding of the difference between the classical and quantum mechanics. To understand the difference between classical and fractional quantum mechanics, numerous studies have been devoted to finding the eigenvalues and eigenfunctions of the fractional Schrödinger equation in an infinite potential well [8, 27, 47, 48, 50, 59, 63, 66]. However, there is one continuing debate in the literature that whether the fractional linear Schrödinger equation in an infinite potential well has the same eigenfunctions as those of its standard (non-fractional) counterpart [8, 27, 47, 50, 66]. The analytical result still remains open and as conjectured in [66], that the eigenfunctions of the fractional Schrödinger equation cannot be written in terms of elementary functions. The difficulties arise not only in the analysis but also in its computations. So far, no study has been carried out by directly solving the fractional Schrödinger equation with an infinite potential well numerically.

In the study of the standard NLS equation, the plane wave solution is one of the most fundamental solution which plays important role in the study of many other more complex solutions. In the last couple of decades, the modulated plane wave dynamics attracted much attention in the study of NLS equation which has been experimentally confirmed with applications in the modulations of deep water waves [86]. The modulational instability (or the Benjamin–Feir instability) of the plane wave solutions has been well studied which mainly depends on the nonlinearity of the NLS. As shown in [86], the plane waves are always stable if the nonlinearity is defocusing; in contrast, they could have long-wave instability in the focusing case. Due to the conservation properties of the NLS, the unstable perturbations do not grow unboundedly, and thus the recurrence of the plane wave solution is observed in the dynamics of the standard focusing NLS [89]. To numerically study the plane wave dynamics, numerical methods should be able to capture the analytical instability of the plane wave solutions without introducing numerical instability. Recently, many studies have been carried out to understand the instability in solving the plane wave solution by different numerical methods; see [12, 22, 37, 61, 70, 86] and references therein. Similar to the standard NLS, the fractional NLS conserves mass and energy, and admits the plane wave solution. However, the plane wave stability and their dynamics of the fractional NLS have not been studied in detail. In addition, only a few numerical methods are available in the literature for solving the fractional NLS. Both analysis and computations are desired to understand the plane wave stability and dynamics of the fractional NLS.

1.1. OBJECTIVES AND OVERVIEW OF THIS DISSERTATION

The objectives of this dissertation include: (i). The development of accurate and efficient numerical methods for directly discretizing the fractional Laplacian. (ii). The understanding of the solution properties of the fractional Schrödinger equations.

In Part I (Sections 2–7), we develop two novel finite difference methods for directly discretizing the fractional Laplacian and compare them with the exist numerical methods in the literature. Because of the challenges in approximating its hypersingular integral, so far numerical methods for discretizing the fractional Laplacian still remain limited. To avoid integrating the hypersingular integral (1.2) over the entire space, some other nonlocal operators that are closely related to the fractional Laplacian have been proposed in recent years, including the regional fractional Laplacian, the spectral fractional Laplacian, and the peridynamic operator. To understand the connections and differences among these nonlocal operators, in Section 2, we compare the properties of the fractional Laplacian with the other three nonlocal operators from various aspects. We show that on a bounded domain, the spectral fractional Laplacian and regional fractional Laplacian are significantly different from the Dirichlet fractional Laplacian, although they can be used to approximate each other as the power $\alpha \to 2$. The peridynamic operator can provide a consistent approximation to the fractional Laplacian for any $\alpha \in (0, 2)$, but a large horizon size is required to obtain a good approximation, especially when α is small.

It is well known that the central finite difference scheme has the second order of accuracy for discretizing the standard Laplacian if the function is smooth enough. It arises a question that whether we can extend this idea to develop a corresponding second order scheme for the fractional Laplacian. In Sections 3–5, we develop two novel and accurate finite difference methods – the weighted trapezoidal method and the weighted linear interpolation method to directly discretize the fractional Laplacian (1.2). The key idea of both methods is to rewrite the hypersigular integral form of the fractional Laplacian as a weighted integral. By choosing proper weight functions, both of these two methods provide the second order of accuracy for smooth enough functions. We provide error analysis for the local truncation error of both methods in one and two-dimensions. The proof in higher dimensions can follow the same idea as in two-dimensional cases. The main technique used in the analysis of the weighted trapezoidal method is the weighted Montgomery's identity, where its standard counterpart has been widely applied in the error analysis of the standard quadrature rules. The weighted trapezoidal method and the weighted linear interpolation method provide same convergence rates. In one dimension, the difference between their computational costs is insignificant, however, the weighted linear interpolation method has higher computational cost than the weighted trapezoidal method in higher dimensions. In contrast to the one-dimensional case where the single integrals can be evaluated exactly, in higher dimensions, the double/triple integrals can only be evaluated numerically. Due to the basis functions, more double/triple integrals appear in the weighted linear interpolation scheme, which is the main reason that results in higher computational cost in higher dimensions. Because these two methods provide same accuracy, we will use the weighted trapezoidal method as a representation to compare with other numerical methods in the literature.

The current state of the art for directly discretizing the fractional Laplacian is the finite difference method proposed in [49]. To solve the fractional Poisson's equation with homogeneous Dirichlet boundary condition, a finite element method is proposed in [2, 25] recently. In Section 6, we compare our weighted trapezoidal method as a representation with the scheme proposed in [49] for discretizing the fractional Laplacian. We also compare theses two finite difference methods with the finite element method proposed in [2, 25] for solving the fractional Poisson's equation and address the computational issues arising in the implementation of the finite element method. Our comparison results show that the weighted trapezoidal method has higher accuracy than the finite difference method in [49], moreover, its implementation is much simpler than the finite element method for solving the fractional Poisson's equation.

In contrast to the standard Laplacian, the discretization of the fractional Laplacian results in a large dense matrix A due to its nonlocality. A direct computation of the matrix-vector product A**u** has large computational costs, especially in higher dimensions. In Section 7, we introduce a fast algorithm for computing the matrix-vector product A**u** of the discretized fractional Laplacian with a vector-valued function. In fact, the discretized fractional Laplacian is a symmetric Toeplitz matrix whose structure can be exploited through the use of fast algorithms [15, 81, 84], and its computation can be achieved efficiently by using the fast Fourier transform (FFT). In addition, this fast algorithm can be directly extended to higher dimensions.

In Part II (Sections 8 and 9), as the applications of the fractional Laplacian, we study the solution properties of the fractional Schrödinger equation. In Section 8, we numerically study the ground and the first excited states of the fractional Schrödinger equation in an infinite potential well. The study of its eigenvalues and eigenfunctions has attracted massive attention from both physicists and mathematicians. There is a continuing debate in the literature that whether the fractional linear Schrödinger equation in an infinite potential well has the same eigenfunctions as those of its standard (nonfractional) counterpart. By introducing a normalized fractional gradient flow combine with the weighted trapezoidal method, we numerically solve the eigenvalue problem of the fractional Schrödinger equation. Our numerical results suggest that the eigenfunctions of the fractional Schrödinger equation differ from those of the standard Schröodinger equations.

In Section 9, we study the modulational stability of the plane waves and their dynamics of the fractional nonlinear Schrödinger equation (NLS) both analytically and numerically. Firstly, we present the linear stability analysis of the plane wave solution and find that the stability in the fractional NLS is more complicated than that in the standard NLS. In contrast to the standard NLS, the plane waves are no longer always stable in the defocusing fractional NLS, the instability appears for the fractional power $\alpha \in (0, 1]$. Besides the linear stability analysis, numerical simulation is a powerful tool to further understand the plane wave dynamics from its nonlinear stage. Since the plane wave solutions are studied, the periodic boundary condition is naturally associated with the fractional NLS. Thus, we adopt the pseudo-differential definition of the the fractional Laplacian $(-\Delta)^{\alpha/2}$ in (1.1), which enables us to utilize the fast Fourier transform to efficiently solve the problem. We develop three Fourier spectral methods i.e., the split-step Fourier spectral (SSFS) method, the Crank-Nicolson Fourier spectral (CNFS), and the relaxation Fourier spectral (ReFS) method, for solving the fractional NLS. Our results suggest that the SSFS method is more efficient for studying the long-time behaviors of the plane wave solutions of the fractional NLS, since it preserves the dispersion relation. The plane wave dynamics of the fractional NLS are numerically studied by the SSFS method, and it suggests different phenomena from that in standard Schrödinger equation, such as the disappearance of the well-known recurrence of the plane wave solution for $\alpha \neq 2$ and the leakage of the low-frequency instability to high frequency. The fractional power α represents the strength of the long-range interactions, the smaller the the fractional power, the stronger the long-range interactions, and more chaotic the dynamics of the fractional NLS. Since the numerical simulation by SSFS method introduces instabilities that have no analytical counterpart, we provided sufficient conditions for the mesh size and time step to avoid such numerical instabilities.

Finally, the conclusions of this dissertation are made in Section 10.

2. DIRICHLET FRACTIONAL LAPLACIAN AND RELATED OPERATORS

In contrast to the entire space, the fractional Laplacian (1.2) on a bounded domain associated with the Dirichlet boundary condition (the Dirichlet fractional Laplacian) is of great interest, not only from the mathematical point of view, but also in practical applications. Any equation involving the Dirichlet fractional Laplacian has to be enclosed by a nonconventional, nonlocal boundary condition imposed on the complement of the physical domain where the governing equation is defined. Besides the hypersingularity from the fractional Laplacian (1.2), the nonlocal boundary condition also introduces significant challenge, especially in the numerical simulations. To avoid evaluation and analysis over the entire space, one common approach is to "*truncate*" and approximate the integral of the Dirichlet fractional Laplacian. Therefore, some other nonlocal operators that are closely related to the Dirichlet fractional Laplacian have been proposed in recent years, including the regional fractional Laplacian, the spectral fractional Laplacian, and the peridynamic operator. In this section, we study and compare the properties of the Dirichlet fractional Laplacian with the other three related nonlocal operators. Our main purpose to understand the connections and differences among these nonlocal operators. Let $\Omega \subset \mathbb{R}^d$ denote an open bounded domain, and $\Omega^c = \mathbb{R}^d \backslash \Omega$ represents the complement of Ω.

2.1. DIRICHLET FRACTIONAL LAPLACIAN

Recently, many studies have been carried out on *the Dirichlet fractional Laplacian* (also known as the *restricted fractional Laplacian*), i.e., the fractional Laplacian on a bounded domain Ω with extended homogeneous Dirichlet boundary condition ($u(\mathbf{x}) \equiv 0$ for $\mathbf{x} \in \Omega^c$). However, the current understanding of this topic still remains limited, and the main challenge is from the non-locality of the operator. In the following, we will discuss some fundamental properties of the Dirichlet fractional Laplacian.

Probablisticly, the Dirichlet fractional Laplacian $(-\Delta)^{\alpha/2}$ represents the infinitesimal generator of a symmetric α-stable Lévy process that particles are killed upon leaving the domain Ω [18, 79, 88]. One fundamental issue in the study of the Dirichlet fractional Laplacian is its eigenvalues and eigenfunctions. So far, their exact results still remain unknown, and only some estimates and approximations can be found in the literature. It shows in [17] that on a convex domain $\Omega \subset \mathbb{R}^d$, the k-th eigenvalue λ_k (for $k \in \mathbb{N}$) of the Dirichlet fractional Laplacian $(-\Delta)^{\alpha/2}$ are bounded by [17]:

$$\frac{1}{2}\mu_k^{\alpha/2} \le \lambda_k \le \mu_k^{\alpha/2}, \qquad \text{for } \alpha \in (0, 2), \tag{2.1}$$

where μ_k represents the k-th eigenvalue of the Dirichlet standard Laplace operator $-\Delta$ on the same domain Ω. That is, the eigenvalue of the fractional Laplacian is always smaller than that of the standard Laplacian $-\Delta$. If a one-dimensional (i.e., $d = 1$) domain is considered, the estimates in (2.1) can be improved, and sharper bounds can be found for two special cases, such as $k = 1$ and $\alpha \in (0, 2)$ in [3, 35], and $\alpha = 1$ and $k = 1, 2, 3$ in [3]. More discussion on the eigenvalue bounds can be found in [39, 51, 87, 88] and references therein. Furthermore, in a one-dimensional interval $(-1, 1)$, the asymptotic approximation of the eigenvalue λ_k is given by [59]:

$$\lambda_k = \left(\frac{k\pi}{2} - \frac{(2-\alpha)\pi}{8}\right)^{\alpha} + O\left(\frac{2-\alpha}{k\sqrt{\alpha}}\right), \qquad \text{for } k \in \mathbb{N}. \tag{2.2}$$

It further shows that if $\alpha \ge 1$, the eigenvalue λ_k (for $k \in \mathbb{N}$) is simple, and the corresponding eigenfunction satisfies $\varphi_k(-x) = (-1)^{k-1}\varphi(x)$. Compared to the studies on eigenvalues, the understanding of eigenfunctions is even less. It shows in [75] that the eigenfunction φ_k (for $k \in \mathbb{N}$) are Hölder continuous up to the boundary of a smooth bounded domain $\Omega \subset \mathbb{R}^d$. Recent numerical results on eigenvalues and eigenfunctions of the Dirichlet fractional Laplacian can be found in [32, 33].

The fractional Poisson equation is one main building block in the study of fractional PDEs, which takes the following form [2, 25, 31, 35]:

$$(-\Delta)^{\alpha/2}u(\mathbf{x}) = f(\mathbf{x}), \qquad \text{for } \mathbf{x} \in \Omega, \tag{2.3}$$

$$u(\mathbf{x}) = 0, \qquad \text{for } \mathbf{x} \in \Omega^c. \tag{2.4}$$

In (2.4), the extended homogeneous boundary conditions are imposed on Ω^c, distinguishing from the classical Poisson problem where boundary conditions are added on $\partial\Omega$. This difference can be explained from probabilistic interpretation of the standard and fractional Laplacian. The standard Laplace operator represents the infinitesimal generator of a Brownian motion with continuous sample paths; thus for a particle in domain Ω, it must leave the domain via the boundary points on $\partial\Omega$. By contrast, the fractional Laplacian is the infinitesimal generator of a symmetric α-stable Lévy process with discontinuous sample paths; particles may "jump" out of the domain without touching any boundary points on $\partial\Omega$. Hence, the solution on Ω can be determined by the values at $\partial\Omega$ in the context of classical Poisson equations but not in the context of fractional Poisson equations.

2.2. SPECTRAL FRACTIONAL LAPLACIAN

The *spectral fractional Laplacian* (also known as the *fractional power of the Dirichlet Laplacian*, or the *"Navier" fractional Laplacian*) is defined via the spectral decomposition of the standard Laplace operator [1, 69, 75], i.e.,

$$(-\Delta_\Omega)^{\alpha/2}u(\mathbf{x}) = \sum_{k\in\mathbb{N}} c_k\, \mu_k^{\alpha/2}\varphi_k(\mathbf{x}), \qquad \text{for } \alpha > 0, \tag{2.5}$$

where μ_k and φ_k are the k-th eigenvalue and normalized eigenfunction of the standard Dirichlet Laplace operator $-\Delta$ on the domain Ω. From a probabilistic point of view, it represents the infinitesimal generator of a subordinate killed Brownian motion, i.e., the process that first kills Brownian motion in a bounded domain Ω and then subordinates it via a $\alpha/2$-stable subordinator [78, 79]. Here, we include the domain Ω in the notation $(-\Delta_\Omega)^{\alpha/2}$ to reflect this process and to distinguish it from the fractional Laplacian $(-\Delta)^{\alpha/2}$. Specially, if $\alpha = 2$ the definition in (2.5) reduces to the standard Dirichlet Laplace operator $-\Delta$ on the domain Ω.

The spectral fractional Laplacian is a nonlocal operator, and it is often used in the analysis of (partial) differential equations. The eigenvalues and eigenfunctions of the spectral fractional Laplacian are clearly suggested from its definition in (2.5), that is, the k-th eigenvalue of $(-\Delta_\Omega)^{\alpha/2}$ is $\mu_k^{\alpha/2}$, and the corresponding eigenfunction is $\varphi_k(\mathbf{x})$. We remark that the spectral fractional Laplacian and the Dirichlet fractional Laplacian represent generators of different processes, which is also reflected by their eigenvalues and eigenfunctions. The eigenfunctions of the spectral fractional Laplacian are smooth up to the boundary as the boundary allows, while those of the Dirichlet fractional Laplacian are only Hölder continuous up to the boundary [75]. Additionally, it is easy to conclude from (2.1) that the k-th eigenvalue of the Dirichlet fractional Laplacian is always smaller than that of the spectral fractional Laplacian, for $k \in \mathbb{N}$.

2.3. REGIONAL FRACTIONAL LAPLACIAN

The *regional fractional Laplacian* (also known the *censored fractional Laplacian*) is defined as [10, 43, 45, 46]:

$$(-\Delta)_\Omega^{\alpha/2} u(\mathbf{x}) = C_{d,\alpha}\, \text{P.V.} \int_\Omega \frac{u(\mathbf{x}) - u(\mathbf{y})}{|\mathbf{y} - \mathbf{x}|^{d+\alpha}}\, d\mathbf{y}, \qquad \text{for } \alpha \in (0, 2), \tag{2.6}$$

with the constant $C_{d,\alpha}$ defined in (1.3). In contrast to the fractional Laplacian, the regional fractional Laplacian $(-\Delta)_\Omega^{\alpha/2}$ represents the infinitesimal generator of a censored α-stable process that is obtained from a symmetric α-stable Lévy process by restricting its measure to Ω [78]. If the domain $\Omega = \mathbb{R}^d$, the regional fractional Laplacian collapses to the fractional

Laplacian $(-\Delta)^{\alpha/2}$. To distinguish it from the fractional Laplacian $(-\Delta)^{\alpha/2}$, we include the subscript 'Ω' in the operator $(-\Delta)_{\Omega}^{\alpha/2}$ to indicate the restriction of the α-stable Lévy process to the domain Ω.

The regional fractional Laplacian is different from the Dirichlet fractional Laplacian, although they are freely interchanged in some literature. In fact, a symmetric α-stable Lévy process killed upon leaving the domain Ω (represented by the Dirichlet fractional Laplacian) is a subprocess of the censored α-stable process (represented by the regional fractional Laplacian) killing inside the domain Ω, i.e., the trajectories may be killed inside Ω through Feynman-Kac transform [79]. Moreover, we will illustrate their difference using a simple example. Consider a one-dimensional interval $\Omega = (-l, l)$. Let u be a smooth function satisfying $u(x) = 0$ for $x \in \Omega^c$. Then the difference between the regional fractional Laplacian and the Dirichlet fractional Laplacian can be computed as:

$$\begin{aligned}
Q_1 u(x) &= \Big((-\Delta)^{\alpha/2} - (-\Delta)_{\Omega}^{\alpha/2}\Big)u(x) \\
&= C_{1,\alpha}\left(\int_{\mathbb{R}} \frac{u(x)-u(y)}{|x-y|^{1+\alpha}}\,dy - \int_{-l}^{l} \frac{u(x)-u(y)}{|x-y|^{1+\alpha}}\,dy\right) \\
&= C_{1,\alpha}\left(\int_{-\infty}^{-l} \frac{1}{|x-y|^{1+\alpha}}\,dy + \int_{l}^{\infty} \frac{1}{|x-y|^{1+\alpha}}\,dy\right)u(x) \\
&= \frac{C_{1,\alpha}}{\alpha}\left(\frac{1}{(l+x)^{\alpha}} + \frac{1}{(l-x)^{\alpha}}\right)u(x), \qquad \text{for } x \in \Omega. \qquad (2.7)
\end{aligned}$$

We find that in the limit case of $\alpha \to 2$, the difference between the regional fractional Laplacian and the Dirichlet fractional Laplacian vanishes, i.e., $Q_1 \to 0$, due to the constant $C_{1,\alpha} \to 0$. In other words, the regional fractional Laplacian can be used to approximate the Dirichlet fractional Laplacian as $\alpha \to 2$. While in the limit of $\alpha \to 0$, the difference in (2.7) reduces to $Q_1 u \to u$, i.e., the Dirichlet fractional Laplacian can be written as the summation of the regional fractional Laplacian and an identity operator. Otherwise, if $\alpha \gg 0$ and $\alpha \ll 2$, the difference $Q_1 u \sim O(1/(l-|x|)^{\alpha})$, which does not tend to zero for any fixed l, and as $x \to \pm l$, there is $|Q_1 u| \to \infty$.

In contrast to the fractional Laplacian, the current understanding on the regional fractional Laplacian still remains very limited. Recently, the interior regularity of the regional fractional Laplacian is discussed in [46, 68]. It shows that if $u \in C^{p,s}(\Omega)$ for $s \in (\alpha, 1]$ or $u \in C^{p+1,s}(\Omega)$ for $s \in (\alpha - 1, \min(\alpha, 1)]$, then there is $(-\Delta)_\Omega^{\alpha/2} u \in C^p(\Omega)$, where $p \in \mathbb{N}$. So far, no results of the eigenvalues or eigenfunctions on the regional fractional Laplacian can be found in the literature. Here, we expect that our numerical results could provide insights into the understanding of the properties of the regional fractional Laplacian in the future.

2.4. PERIDYNAMIC OPERATOR

The peridynamic models were originally proposed as a reformation of the classical solid mechanics in [77]. In contrast to the classical models, it properly accounts for the near-field nonlocal interactions so as to effectively model elasticity problems with discontinuity and other singularities. The general form of this nonlocal operator has the following form:

$$\mathcal{L}u(\mathbf{x}) = \int_{B(\mathbf{x},\delta)} K(\mathbf{x},\mathbf{y})\big(u(\mathbf{x}) - u(\mathbf{y})\big)\, d\mathbf{y}, \tag{2.8}$$

where $B(\mathbf{x}, \delta)$ denotes a ball with its center at point $\mathbf{x}$ and radius δ, which represents the interaction region of point $\mathbf{x}$. The kernel function $K(\mathbf{x}, \mathbf{y}) = K(|\mathbf{x} - \mathbf{y}|)$ describes the interaction strength between points $\mathbf{x}$ and $\mathbf{y}$. The constant $\delta > 0$ denotes the size of material horizon, and in practical applications it is often chosen to be a small number.

Recently, the operator (2.8) with specially chosen kernel function is used to approximate the fractional Laplacian [25, 44]. We will refer it as the *peridynamic operator* and denote it as

$$(-\Delta)_\delta^{\alpha/2} u(\mathbf{x}) = C_{d,\alpha} \int_{B(\mathbf{x},\delta)} \frac{u(\mathbf{x}) - u(\mathbf{y})}{|\mathbf{x} - \mathbf{y}|^{d+\alpha}}\, d\mathbf{y}, \tag{2.9}$$

i.e., the kernel function in this case is taken as:

$$K_\delta(\mathbf{x},\mathbf{y}) = \begin{cases} \dfrac{C_{d,\alpha}}{|\mathbf{x}-\mathbf{y}|^{d+\alpha}}, & \text{if } \mathbf{y} \in B(\mathbf{x},\delta), \\ 0, & \text{otherwise.} \end{cases}$$

In other words, $K_\delta(\mathbf{x},\mathbf{y})$ in the peridynamic operator represents a hard-threshold of the kernel function $K(\mathbf{x},\mathbf{y}) = C_{d,\alpha}/|\mathbf{x}-\mathbf{y}|^{d+\alpha}$ of the fractional Laplacian, which can be viewed as a truncation of $K(\mathbf{x},\mathbf{y})$ in the fractional Laplacian. In the limit case of $\delta \to \infty$, the peridynamic operator (2.9) coincides with the fractional Laplacian (1.2), and thus it is often used to approximate the fractional Laplacian by choosing a sufficiently large δ [25, 44]. On the other hand, note that the kernel function $K(\mathbf{x},\mathbf{y})$ has an algebraic decay of order $d+\alpha$, which presents a heavy tail that accounts for considerable far field interactions. Hence, the cutoff of the kernel function $K(\mathbf{x},\mathbf{y})$ outside of the horizon $B(\mathbf{x},\delta)$ may have a significant impact on its approximation to the fractional Laplacian as we shall show next.

Similarly, we choose a smooth function u satisfying $u(x) = 0$ for $x \in \Omega^c$ with $\Omega = (-l, l)$ to illustrate the difference between the peridynamic operator and the Dirichlet fractional Laplacian on a bounded domain. Here, we assume that the horizon size δ in (2.9) is large enough, such that $\delta > \max\{l-x, l+x\}$ for any point $x \in (-l, l)$. Then, we can compute their difference as:

$$\begin{aligned} Q_2u(x) &= \Big((-\Delta)^{\alpha/2} - (-\Delta)^{\alpha/2}_\delta\Big)u(x) \\ &= C_{1,\alpha}\Big(\int_{\mathbb{R}} \frac{u(x)-u(y)}{|x-y|^{1+\alpha}}\,dy - \int_{x-\delta}^{x+\delta} \frac{u(x)-u(y)}{|x-y|^{1+\alpha}}\,dy\Big) \\ &= C_{1,\alpha}\left(\int_{-\infty}^{x-\delta} \frac{1}{|x-y|^{1+\alpha}}\,dy + \int_{x+\delta}^{\infty} \frac{1}{|x-y|^{1+\alpha}}\,dy\right)u(x) \\ &= \frac{C_{1,\alpha}}{\alpha}\frac{2}{\delta^\alpha}\,u(x), \qquad \text{for } x \in \Omega. \end{aligned} \tag{2.10}$$

It shows that the difference of these two operators is of order $O(1/\delta^{\alpha})$ when $u(x)$ is uniformly bounded on Ω, hence their difference vanishes as $\delta \to \infty$. On the other hand, the convergence of the peridynamic operator to the fractional Laplacian as $\delta \to \infty$ depends on the power α, and it may degenerate rapidly for small α. Additionally, in the limit case of $\alpha \to 2$, the difference $Q_2 u \to 0$, because the coefficient $C_{d,\alpha} \to 0$.

The peridynamic operator in (2.9) can be viewed as the infinitesimal generator of a symmtric α-stable process by restricting its measure to $B(\mathbf{x}, \delta)$. In contrast to the regional fractional Laplacian operator, the interaction region of point $\mathbf{x}$ in the peridynamic operator is symmetric with respect to itself. Hence, the peridynamic operator is expected to provide a symmetric approximation for a homogeneous elastic material.

In summary, the fractional Laplacian (1.2), spectral fractional Laplacian (2.5), regional fractional Laplacian (2.6), and the peridynamic operator (2.9) are all nonlocal operators in which every point $\mathbf{x}$ interacts with other points $\mathbf{y}$ over certain long distance. For a point $\mathbf{x} \in \Omega$, the fractional Laplacian $(-\Delta)^{\alpha/2}$ accounts for the interactions between $\mathbf{x}$ and $\mathbf{y}$ for all $\mathbf{y} \in \mathbb{R}^d \backslash \{\mathbf{x}\}$. By contrast, the interaction region of $\mathbf{x}$ in the regional fractional Laplacian $(-\Delta)_{\Omega}^{\alpha/2}$ is truncated to $\Omega \backslash \{\mathbf{x}\}$, i.e., the same domain of $\mathbf{x}$, while the interaction region of the peridynamic operator $(-\Delta)_{\delta}^{\alpha/2}$ reduces to $B(\mathbf{x}, \delta) \backslash \{\mathbf{x}\}$. We will further compare them in Section 2.5.

2.5. NUMERICAL COMPARISONS

In this section, we further compare these four nonlocal operators by studying their nonlocal effects, eigenvalues and eigenfunctions, and the solution behavior of the corresponding nonlocal problems. In our simulations, the spectral fractional Laplacian is discretized by using the finite difference method combined with matrix transfer techniques introduced in [30], while the other three operators are discretized by the weighted trapezoidal method developed in Section 3. Our numerical results provide insights not only to further understand these operators but also to improve the analytical results in the literature.

In the following, we will consider the one-dimensional cases. For notational simplicity, we will also use $\mathcal{L}_h$ to represent the fractional Laplacian, $\mathcal{L}_s$ for the spectral fractional Laplacian, $\mathcal{L}_r$ for the regional fractional Laplacian, and $\mathcal{L}_p$ for the peridynamic operator.

2.5.1. Nonlocal Effects of Operators.

We compare the nonlocal effects of these four operators by acting them on functions with compact support on the domain $\Omega = (-1, 1)$.

Example 1. Consider the function

$$u(x) = \begin{cases} \sin\Big(\dfrac{\pi(1+x)}{2}\Big), & \text{if } \ x \in \Omega, \\ 0, & \text{otherwise}, \end{cases} \qquad x \in \mathbb{R}, \tag{2.11}$$

which is continuous on the whole space $\mathbb{R}$. It is easy to obtain that

$$(-\Delta_\Omega)^{\alpha/2}u(x) = \Big(\frac{\pi}{2}\Big)^{\alpha} \sin\Big(\frac{\pi(1+x)}{2}\Big), \qquad \text{for } \ x \in \Omega,$$

that is, the function from the spectral fractional Laplacian can be found exactly, while we will numerically compute the functions from the other three operators.

In Figure 2.1, we compare the function $\mathcal{L}_i u$ for $i = s,\ h,\ r$, or p. The results clearly suggest the difference between these four operators, especially the function $\mathcal{L}_s u$ from the spectral fractional Laplacian is significantly different from those of the other three operators. It shows that for any $\alpha \in (0, 2)$, the function $\mathcal{L}_s u$ is proportional to the function u on $(-1, 1)$. In contrast, the properties of $\mathcal{L}_i u$ (for $i = h, r$, or p) significantly depend on the parameter α. For $\alpha \in (0, 1)$, the function $\mathcal{L}_i u$ exists on the closed domain $\overline{\Omega}$, but they are very different between operators. The smaller the parameter α, the larger the differences. For $\alpha \in [1, 2)$, the function $\mathcal{L}_i u$ does not exist at the boundary points, i.e., $x = \pm 1$. As $\alpha \to 2$, the function $\mathcal{L}_i u$ (for $i = h, r$, or p) converges to $-u_{xx}$ for $x \in (-1, 1)$.

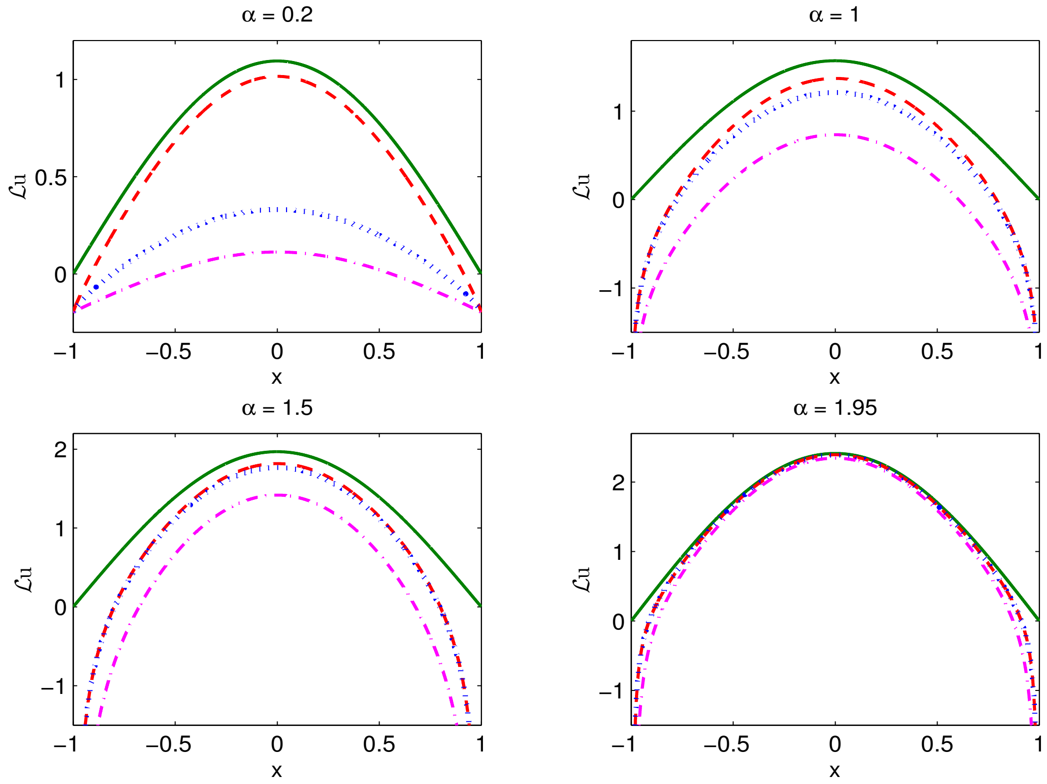

Figure 2.1. Comparison of $\mathcal{L}u$ with u in (2.11). The operator $\mathcal{L}$ represents $\mathcal{L}_s$ (solid line), $\mathcal{L}_h$ (dashed line), $\mathcal{L}_r$ (dashdot line), or $\mathcal{L}_p$ with $\delta = 4$ (dotted line). Note that the plots in y-direction are partially presented for $\alpha = 1$, 1.5 or 1.95.

Additionally, Figure 2.1 shows that both the regional fractional Laplacian and peridynamic operator can be used to approximate the fractional Laplacian, if α is close to 2 (see Figure 2.1 for $\alpha = 1.95$). For small α, the results from the regional fractional Laplacian are inconsistent with that from the fractional Laplacian. However, the peridynamic operator can still provide a good approximation to the fractional Laplacian by enlarging the horizon size δ. Figure 2.2 presents the differences between the functions $\mathcal{L}_pu$ and $\mathcal{L}_hu$ for various α and δ. It shows that for a fixed horizon size δ, the difference between these two operators dramatically decreases as α increases. On the other hand, Figure 2.2 implies that for small α the convergence of the function $\mathcal{L}_pu$ to $\mathcal{L}_hu$ could be very slow. For instance,

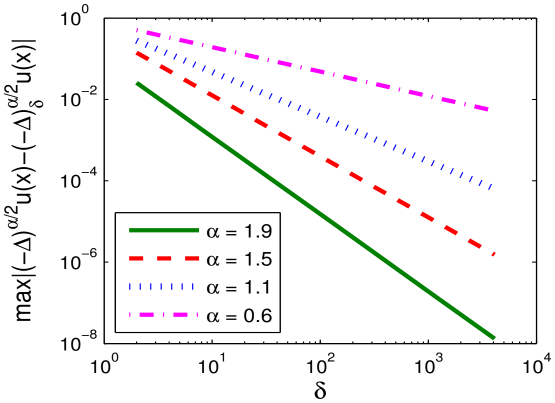

Figure 2.2. Difference $\max|\mathcal{L}_h u - \mathcal{L}_p u|$ versus the horizon size δ for various α, with $u(x)$ defined in (2.11),

for $\alpha = 0.6$, the difference in Figure 2.2 is around 0.005 for a horizon size $\delta = 4000$. In fact, the nonlocal interactions decay slowly for small α, and thus a large horizon size δ is needed for the peridynamic operator to better approximate the fractional Laplacian.

Example 2. Consider the function

$$u(x) = \begin{cases} (1-x^2)^{q+\frac{\alpha}{2}}, & \text{for } x \in \Omega, \\ 0, & \text{otherwise}, \end{cases} \qquad x \in \mathbb{R}, \tag{2.12}$$

for $q \in \mathbb{N}$. For the fractional Laplacian, the analytical solution can be found as:

$$(-\Delta)^{\alpha/2}u(x) = \frac{2^\alpha \Gamma(\frac{\alpha+1}{2})\Gamma(\frac{\alpha}{2}+q+1)}{\sqrt{\pi}\Gamma(q+1)}\, {}_2F_1\left(\frac{\alpha+1}{2}, -q; \frac{1}{2}; x^2\right) \tag{2.13}$$

for $x \in \Omega$, where ${}_2F_1$ denotes the Gauss hypergeometric function. Moreover, we can obtain the exact values of $(-\Delta)_\Omega^{\alpha/2}u$ and $(-\Delta)_\delta^{\alpha/2}u$ by using their relation to the fractional Laplacian in (2.7) and (2.10), respectively. For the spectral fractional Laplacian, we numerically computed $(-\Delta_\Omega)^{\alpha/2}u$ by the finite difference method proposed in [30].

Figure 2.3 displays the function $\mathcal{L}_i u$ for various α, where u is defined in (2.12) with $q = 2$. It shows that the function $\mathcal{L}_i u$ exists on the closed domain $[-1, 1]$ for any $\alpha \in (0, 2)$, but their values are very different, especially for small α. For the spectral fractional Laplacian, the values of $\mathcal{L}_s u$ at the boundary are always zero, which inherits from its definition in (2.5). For the regional fractional Laplacian, the function u in (2.12) with $q = 2$ satisfies the conditions that $u \in C^2([-1, 1])$ and $u'(\pm 1) = 0$, which guarantee the existence of the function $\mathcal{L}_r u$ for any $\alpha \in (0, 2)$ [46]. Since the function $u(\pm 1) = 0$ and the relations in (2.7) and (2.10), the values of $\mathcal{L}_i u$ (for $i = h, r$ and p) are the same at boundary points, but they are nonzero. Figure 2.3 also shows that both the regional fractional Laplacian and the peridynamic operator with relatively small δ could provide a good approximation to the fractional Laplacian, if α is large (see Figure 2.3 for $\alpha = 1.95$).

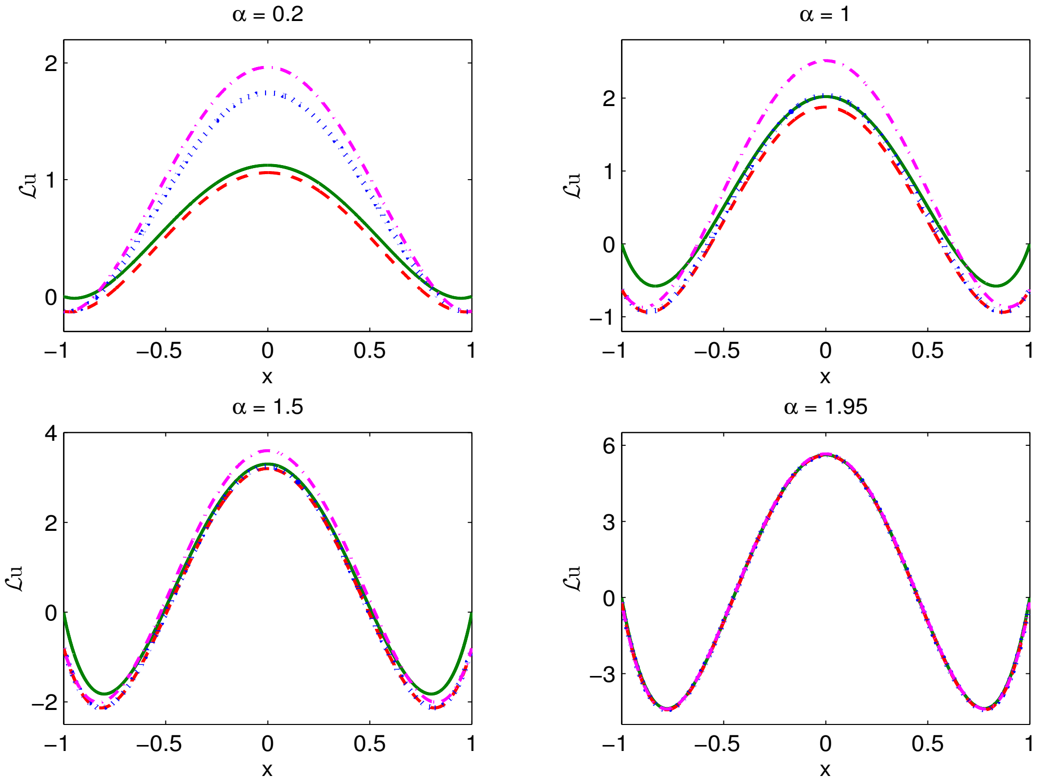

Figure 2.3. Comparison of $\mathcal{L}u$ with u in (2.12) and $q = 2$. The operator $\mathcal{L}$ represents $\mathcal{L}_s$ (solid line), $\mathcal{L}_h$ (dashed line), $\mathcal{L}_r$ (dash-dot line), or $\mathcal{L}_p$ with $\delta = 4$ (dotted line).

While α is small, although the peridynamic operator can be still used to approximate the fractional Laplacian with a large δ, the regional fractional Laplacian is inconsistent with the fractional Laplacian.

Figure 2.3 additionally shows that as $\alpha \to 2$, the differences between the four operators become insignificant (see Figure 2.3 for $\alpha = 1.95$), and the function $\mathcal{L}_i u$ (for $i = h, s, r,$ or p) converges to $-\partial_{xx}u$, that is, the four operators converge to the standard Dirichlet Laplace operator $-\Delta$. In contrast to cases of $\alpha \to 2$, the functions $\mathcal{L}_h u$ from the fractional Laplacian and $\mathcal{L}_s u$ from the spectral fractional Laplacian converge to u, as $\alpha \to 0$, while $\mathcal{L}_r u$ from the regional fractional Laplacian and $\mathcal{L}_p u$ from the peridynamic operator converge to a zero function; see Figure 2.4.

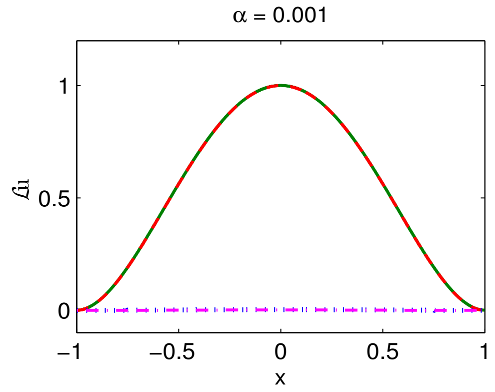

Figure 2.4. Comparison of $\mathcal{L}u$ with u in (2.12) and $q = 2$. The operator $\mathcal{L}$ represents $\mathcal{L}_s$ (solid line), $\mathcal{L}_h$ (dashed line), $\mathcal{L}_r$ (dash-dot line), or $\mathcal{L}_p$ with $\delta = 4$ (dotted line).

Moreover, our numerical results suggested that for $\alpha \in [1, 2)$, if the function $u \in C^{1,\alpha/2}(\overline{\Omega})$ and $u'(\pm 1) = 0$, then the regional fractional Laplacian $\mathcal{L}_r u$ exists; see Figure 2.5. Hence, we conjugate that the regularity results in [46] might be able to improve to $u \in C^{1,\alpha/2}(\overline{\Omega})$ at least for one-dimensional case. More analysis needs to be carried out for further understanding this issue.

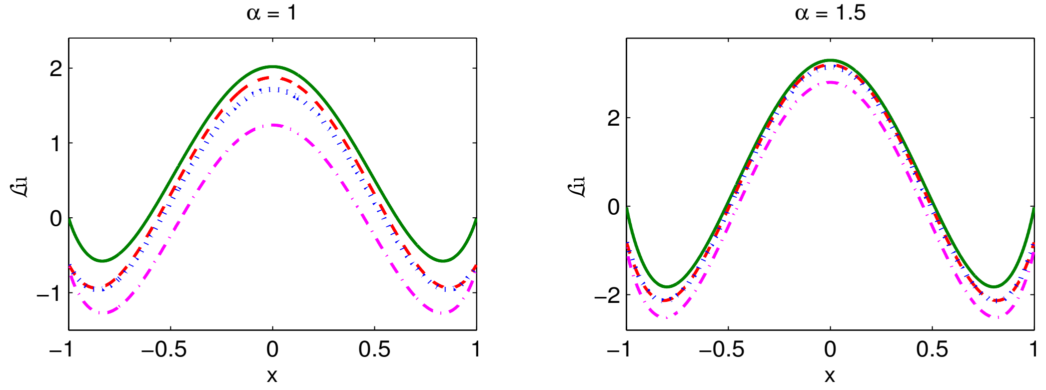

Figure 2.5. Comparison of $\mathcal{L}u$ with u in (2.12) and $q = 1$. The operator $\mathcal{L}$ represents $\mathcal{L}_s$ (solid line), $\mathcal{L}_h$ (dashed line), $\mathcal{L}_r$ (dash-dot line), or $\mathcal{L}_p$ with $\delta = 4$ (dotted line).

2.5.2. Eigenvalues and Eigenfunctions. In this section, we compare the four nonlocal operators by studying their eigenvalues and eigenfunctions on a one-dimensional bounded domain $\Omega = (-l,\, l)$.

Denote λ_k^i and ϕ_k^i as the k-th (for $k \in \mathbb{N}$) eigenvalue and eigenfunction of the nonlocal operator $\mathcal{L}_i$ on Ω with the corresponding homogeneous Dirichlet boundary conditions, where $i = h,\, s,\, r$, or p. It is well known that the eigenvalues and eigenfunctions of the spectral fractional Laplacian $\mathcal{L}_s$ can be found analytically, i.e.,

$$\lambda_k^s = \mu_k^{\alpha/2} = \left(\frac{k\pi}{2l}\right)^{\alpha/2}, \qquad \phi_k^s(x) = \sqrt{\frac{1}{l}}\sin\left(\frac{k\pi}{2}\left(1 + \frac{x}{l}\right)\right), \qquad x \in (-l, l),$$

for $k \in \mathbb{N}$. For the other operators, so far no analytical results can be found in the literature, and thus we will compute their eigenvalues and eigenfunctions numerically.

Table 2.1. Comparison of the eigenvalues for different operators, where the eigenvalues of the standard Dirichlet Laplace operator $-\Delta$ are presented in most right column. For each k, upper row: λ_k^s; middle row: λ_k^h; lower row: λ_k^r.

k \ α	0.2	0.5	0.7	0.9	1	1.2	1.5	1. 8	1.95	1.999	
1	1.0945	1.2533	1.3718	1.5014	1.5708	1.7193	1.9687	2.2543	2.4123	2.4663	2.4674
	0.9575	0.9702	1.0203	1.1032	1.1578	1.2971	1.5976	2.0488	2.3520	2.4650	
	0.0003	0.0038	0.0170	0.0640	0.1135	0.2939	0.8088	1.6602	2.2444	2.4628	
2	1.2573	1.7725	2.2285	2.8018	3.1416	3.9498	5.5683	7.8500	9.3206	9.8583	9.8696
	1.1966	1.6016	1.9733	2.4583	2.7549	3.4870	5.0600	7.5033	9.2082	9.8559	
	0.1878	0.4593	0.6729	0.9799	1.2026	1.8719	3.6509	6.7378	8.9854	9.8512	
3	1.3635	2.1708	2.9598	4.0357	4.7124	6.4252	10.230	16.287	20.550	22.172	22.207
	1.3191	2.0289	2.7294	3.6987	4.3171	5.9121	9.5948	15.800	20.384	22.169	
	0.3085	0.8626	1.3646	2.0823	2.5760	3.9902	7.7500	14.701	20.049	22.161	
4	1.4442	2.5066	3.6201	5.2283	6.2832	9.0744	15.750	27.335	36.012	39.406	29.478
	1.4106	2.3873	3.4131	4.9055	5.8925	8.5350	15.020	26.725	35.794	39.401	
	0.3981	1.2091	2.0140	3.2054	4.0292	6.3902	12.811	25.313	35.349	39.391	
5	1.5101	2.8025	4.2322	6.3912	7.8540	11.861	22.011	40.847	55.645	61.558	61.685
	1.4817	2.6949	4.0371	6.0733	7.4607	11.293	21.191	40.115	55.374	61.552	
	0.4700	1.5149	2.6231	4.3230	5.5171	8.9817	18.670	38.408	54.820	61.540	
8	1.6590	3.5449	5.8809	9.7564	12.566	20.847	44.547	95.187	139.14	157.51	157.91
	1.6400	3.4612	5.7133	9.4550	12.175	20.225	43.509	94.122	138.72	157.50	
	0.6296	2.2799	4.2751	7.6101	10.072	17.552	40.218	91.591	137.85	157.49	
10	1.7347	3.9633	6.8752	11.926	15.708	27.249	62.256	142.24	215.00	246.06	246.74
	1.7189	3.8886	6.7186	11.632	15.317	26.598	61.096	140.96	214.48	246.05	
	0.7095	2.7090	5.2735	9.7490	13.145	23.749	57.377	137.92	213.39	246.02	
20	1.9926	5.6050	11.169	22.255	31.416	62.601	176.09	495.30	830.70	983.56	986.96
	1.9836	5.5525	11.042	21.981	31.025	61.854	174.45	493.09	829.69	983.53	
	0.9779	4.3810	9.5850	19.998	28.657	58.439	169.09	487.74	827.58	983.49	

In Table 2.1, we present the eigenvalues of the fractional Laplacian $\mathcal{L}_h$, spectral fractional Laplacian $\mathcal{L}_s$, and regional fractional Laplacian $\mathcal{L}_r$, on the domain $\Omega = (-1, 1)$. We leave the peridynamic operator $\mathcal{L}_p$ out of our comparison here, since its spectrum depends on the horizon size δ. The eigenvalues of the standard Dirichlet Laplace operator $-\Delta$ are presented in most right column in Table 2.1. For each k, the upper row represents λ_k^s; the middle row represents λ_k^h; the lower row represents λ_k^r.

From Table 2.1 and our extensive numerical studies, we find

$$\lambda_k^r < \lambda_k^h < \lambda_k^s, \qquad \text{for } \alpha \in (0,2) \text{ and } k \in \mathbb{N},$$

that is, the eigenvalues of the regional fractional Laplacian are much smaller than those of the fractional Laplacian and spectral fractional Laplacian. However, as $\alpha \to 2$ the eigenvalue λ_k^i of these three operators converges to $\mu_k = k^2\pi^2/4$ – the kth eigenvalue of the standard Dirichlet Laplace operator $-\Delta$ on $(-1, 1)$.

In [75], it is proved that the first eigenvalue of the fractional Laplacian is strictly smaller than that of the spectral fractional Laplacian, i.e., $\lambda_1^h < \lambda_1^s$, for $\alpha \in (0, 2)$. Our numerical results in Table 2.1 confirm this conclusion and additionally suggest that the eigenvalue λ_k^h is strictly smaller than λ_k^s, for any $k \in \mathbb{N}$. Furthermore, we present the difference between the eigenvalues λ_k^s and λ_k^h for various α and k in Figure 2.6. It shows that the difference between the eigenvalues λ_k^s and λ_k^h depends on both parameters α and k. For a given $k \in \mathbb{N}$, there exists a critical value α_k where the gap between λ_k^s and λ_k^h is maximized. The value of α_k increases as $k \in \mathbb{N}$ increase (see Figure 2.6 left). On the other hand, as $k \in \mathbb{N}$, the relative difference between the eigenvalues λ_k^s and λ_k^h decreases quickly (see Figure 2.6 right).

In Figure 2.7, we compare the first and second eigenfunctions of the fractional Laplacian, the spectral fractional Laplacian, and the regional fractional Laplacian. For any $\alpha \in (0, 2)$, the eigenfunctions for these three operators are all symmetric (for odd

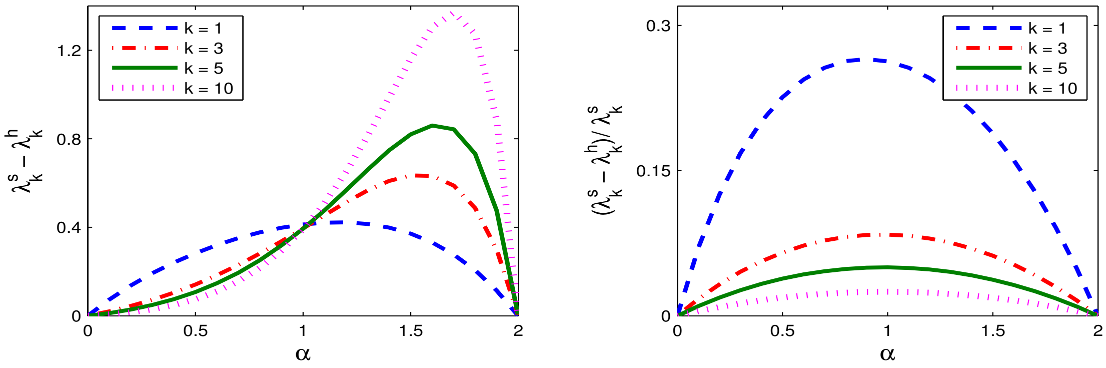

Figure 2.6. The absolute (left panel) and relative (right panel) differences in the eigenvalues of the fractional Laplacian and spectral fractional Laplacian.

k) or antisymmetric (for even k) with respect to the center of the domain Ω. Especially, the eigenfunctions of the spectral fractional Laplacian are independent of the parameter α, which are also the eigenfunctions of the standard Dirichlet Laplace operator $-\Delta$. In contrast, the eigenfunctions of the other two operators significantly depend on α, and as $\alpha \to 2$, they converge to $\sin(k\pi(1+x)/2)$ – the eigenfunctions of the standard Dirichlet Laplace operator $-\Delta$. Our numerical observations in Figure 2.7 justify the regularity results in [75, Theorem 1], that is, the eigenfunctions of the fractional Laplacian is no better than Hölder continuous up to the boundary, while the eigenfunctions of the spectral fractional Laplacian are smooth up to the boundary as the boundary allows.

From our extensive studies, we find that the eigenvalues of the fractional Laplacian $\mathcal{L}_h$, the spectral fractional Laplacian $\mathcal{L}_s$, and the regional fractional Laplacian $\mathcal{L}_r$ reduces as the domain size increases. In particular, if the domain size increases by a ratio of κ, the k-th (for $k \in \mathbb{N}$) eigenvalues decreases by a ratio of κ^α. Additionally, we explore the eigenvalues of the peridynamic operators for different δ. It shows that the eigenvalue increases as δ decreases.

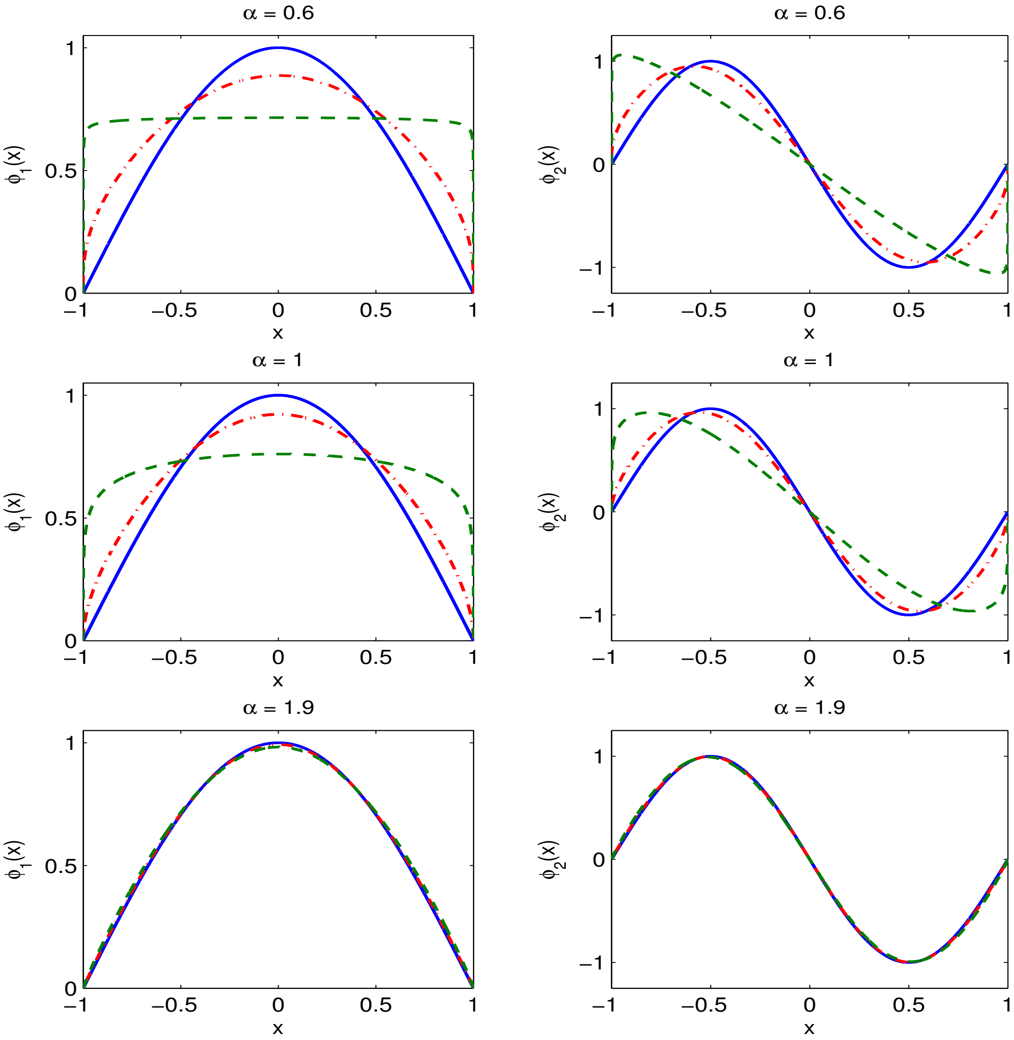

Figure 2.7. The first (left panel) and second (right panel) eigenfunctions of the spectral fractional Laplacian (solid line), fractional Laplacian (dash-dot line), and regional fractional Laplacian (dashed line). Note that the eigenfunctions of the spectral fractional Laplacian are independent of $\alpha > 0$.

In this section, we compare the properties of the Dirichlet fractional Laplacian with some related nonlocal operators, i.e., the spectral fractional Laplacian, the regional fractional Laplacian, and the peridynamic operator. Our study shows that their differences are significant on a bounded domain. Probabilistically, they represent the generators of different stochastic processes. In addition, the eigenvalues and eigenfunctions of these four operators are different, although they all converge to those of the classical Laplace operator as $\alpha \to 2$. In conclusion, our extensive numerical investigations suggest that these three nonlocal operators can only serve as good approximations of the Dirichlet fractional Laplacian under some special situations but the deviations could be large as the fractional power α is relatively small. As $\alpha \to 2$, all the four operators collapse to the classical Dirichlet Laplacian. For relatively small α, to provide a good approximation of the Dirichlet fractional Laplacian, the horizon size δ of the peridynamic operator must be taken sufficiently large; differently, the regional fractional Laplacian generally provides inconsistent results from the fractional Laplacian.

3. THE WEIGHTED TRAPEZOIDAL METHOD IN 1D

The traditional trapezoidal method is widely used in the field of numerical integration, and it has the second order of accuracy if the integrand function is smooth enough. However, the fractional Laplacian defined in (1.2) is a hypersingular integral, and directly applying the traditional trapezoidal method fails to provide the optimal accuracy or to be convergent. It is known that the weighted quadrature rules are advantageous in approximating the hypersingular integrals [23, Chapter 5]. By introducing a weight function, the hypersingular integral is formulated as a weighted integral of a weaker singular function.

In this section, we will develop a novel finite difference method based on the weighted trapezoidal rule to discretize the fractional Laplacian (1.2) in one dimension (1D). The error analysis will be provided for functions with different smoothness conditions. Some numerical examples are presented to justify the analytical results.

3.1. NUMERICAL SCHEME

Consider the fractional Laplacian defined in (1.2). We focus on the discretization of the fractional Laplacian on a one-dimensional bounded domain Ω with *homogeneous* Dirichlet boundary conditions, i.e., $u(x) \equiv 0$ for $x \in \Omega^c$. Our scheme can be also used for nonhomogeneous constant boundary conditions, i.e., $u(x) = g$ with g a constant for $x \in \Omega^c$. In this case, one can define $v = u - g$, and there is $(-\Delta)^{\alpha/2}v = (-\Delta)^{\alpha/2}u$.

Letting $\xi = |x-y|$, we can rewrite the one-dimensional fractional Laplacian in (1.2) as

$$(-\Delta)^{\alpha/2}u(x) = -C_{1,\alpha}\int_0^{\infty} \frac{u(x-\xi) - 2u(x) + u(x+\xi)}{\xi^{1+\alpha}}\, d\xi. \qquad (3.1)$$

Define domain $\Omega = (a, b)$, and choose a constant $L = |\Omega| = b - a$. We further write the integral in (3.1) as:

$$\begin{aligned}(-\Delta)^{\alpha/2}u(x) &= -C_{1,\alpha}\bigg(\int_0^L \frac{u(x-\xi) - 2u(x) + u(x+\xi)}{\xi^{1+\alpha}}\,d\xi \\ &\quad + \int_L^\infty \frac{u(x-\xi) - 2u(x) + u(x+\xi)}{\xi^{1+\alpha}}\,d\xi\bigg). \qquad (3.2)\end{aligned}$$

Note that for any $x \in (a,\ b)$ and $\xi \geq L$, there is $(x \pm \xi) \in \mathbb{R}\backslash(a,\ b)$, and thus the function $u(x \pm \xi) \equiv 0$. Hence, the second integral in (3.2) reduces to

$$\int_L^\infty \frac{u(x-\xi) - 2u(x) + u(x+\xi)}{\xi^{1+\alpha}}\,d\xi = -2u(x)\int_L^\infty \frac{1}{\xi^{1+\alpha}}d\xi = -\frac{2}{\alpha L^\alpha}u(x), \qquad (3.3)$$

that is, it can be computed exactly.

Now, we will approximate the first integral in (3.2) numerically. Choose a positive integer N, and define the mesh size $h = L/N$. Denote grid points $\xi_i = ih$, for $0 \leq i \leq N$; evidently $\xi_N = L$. First, we introduce a splitting parameter $\gamma \in (\alpha, 2]$. The choice of γ is important in determining the accuracy of our method, and we will carry out more discussion later. Then, we can formulate the first integral in (3.2) as:

$$\begin{aligned}\int_0^L \frac{u(x-\xi) - 2u(x) + u(x+\xi)}{\xi^{1+\alpha}}\,d\xi &= \int_0^L \psi_\gamma(x,\xi)\xi^{\gamma-(1+\alpha)}\,d\xi \\ &= \sum_{i=1}^N \int_{\xi_{i-1}}^{\xi_i} \psi_\gamma(x,\xi)\,\xi^{\gamma-(1+\alpha)}\,d\xi, \qquad (3.4)\end{aligned}$$

where for notational simplicity we define the function

$$\psi_\gamma(x,\xi) = \frac{u(x-\xi) - 2u(x) + u(x+\xi)}{\xi^\gamma}. \qquad (3.5)$$

That is, the first integral in (3.2) can be viewed as an weighted integral of ψ_γ, with $\xi^{\gamma-(1+\alpha)}$ representing the weight function. For $2 \le i \le N$, we use the weighted trapezoidal rule to approximate the integrals in (3.4), i.e.,

$$\begin{aligned}\int_{\xi_{i-1}}^{\xi_i} \psi_\gamma(x,\xi)\,\xi^{\gamma-(1+\alpha)}\,d\xi \;&\approx\; \frac{1}{2}\Big(\psi_\gamma(x,\xi_{i-1}) + \psi_\gamma(x,\xi_i)\Big)\int_{\xi_{i-1}}^{\xi_i} \xi^{\gamma-(1+\alpha)}d\xi \\ &=\; \frac{1}{2(\gamma-\alpha)}\Big(\xi_i^{\gamma-\alpha} - \xi_{i-1}^{\gamma-\alpha}\Big)\Big(\psi_\gamma(x,\xi_{i-1}) + \psi_\gamma(x,\xi_i)\Big), \qquad (3.6)\end{aligned}$$

for any $\gamma = (\alpha, 2]$. While for $i = 1$, we will divide our discussion into two cases based on different choice of the splitting parameter, i.e., $\gamma \in (\alpha, 2)$ or $\gamma = 2$.

Case 1. *The splitting parameter* $\gamma \in (\alpha, 2)$. For $i = 1$, we can approximate the integral as

$$\int_{\xi_0}^{\xi_1} \psi_\gamma(x,\xi)\,\xi^{\gamma-(1+\alpha)}d\xi \;\approx\; \frac{1}{2(\gamma-\alpha)}\xi_1^{\gamma-\alpha}\psi_\gamma(x,\xi_1), \qquad (3.7)$$

which can be formally obtained using the weighted trapezoidal rule, i.e.,

$$\int_{\xi_0}^{\xi_1} \psi_\gamma(x,\xi)\,\xi^{\gamma-(1+\alpha)}d\xi \;\approx\; \frac{1}{2}\Big(\lim_{\xi\to 0}\psi_\gamma(x,\xi) + \psi_\gamma(x,\xi_1)\Big)\int_0^h \xi^{\gamma-(1+\alpha)}\,d\xi.$$

Assuming that u is smooth enough, the above limit is zero, i.e.,

$$\lim_{\xi\to 0}\psi_\gamma(x,\xi) \approx \lim_{\xi\to 0}\xi^{2-\gamma}u''(x) = 0.$$

Combining (3.2)–(3.4) and (3.6)–(3.7), we obtain the numerical approximation of the fractional Laplacian $(-\Delta)^{\alpha/2}$ as:

$$\begin{aligned}(-\Delta)_{h,\gamma}^{\alpha/2}u(x) \;=\; &-\frac{C_{1,\alpha}}{2(\gamma-\alpha)}\Big[\xi_1^{\gamma-\alpha}\psi_\gamma(x,\xi_1) + \sum_{i=2}^{N}\Big(\xi_i^{\gamma-\alpha} - \xi_{i-1}^{\gamma-\alpha}\Big)\Big(\psi_\gamma(x,\xi_{i-1}) \\ &+\psi_\gamma(x,\xi_i)\Big)\Big] + \frac{2C_{1,\alpha}}{\alpha L^\alpha}u(x), \qquad \text{for } x \in (a,\, b), \qquad (3.8)\end{aligned}$$

where the function ψ_γ is defined in (3.5).

Define grid points $x_i = a + ih$, for $0 \le i \le N$. Let u_i be the numerical approximation of $u(x_i)$. Using the definition of ψ_γ in (3.5), we further obtain the fully discretized scheme as:

$$(-\Delta)_{h,\gamma}^{\alpha/2} u_i = -C_{1,\alpha}\Big(a_0\, u_i + \Big(\sum_{j=1}^{i-1} a_j u_{i-j} + \sum_{j=1}^{N-1-i} a_j u_{i+j}\Big)\Big), \tag{3.9}$$

for $i = 1, 2, \ldots, N-1$, where

$$a_j = \frac{1}{2(\gamma-\alpha)h^\alpha} \begin{cases} \dfrac{(j+1)^{\gamma-\alpha} - (j-1)^{\gamma-\alpha}}{j^\gamma}, & \text{for} \quad j = 1, \ldots, N-1, \\ \dfrac{N^{\gamma-\alpha} - (N-1)^{\gamma-\alpha}}{N^\gamma}, & \text{for} \quad j = N, \end{cases}$$

$$a_0 = -2\Big(\sum_{j=1}^{N} a_j + \frac{1}{\alpha L^\alpha}\Big).$$

Denote the vector $\mathbf{u} = (u_1, u_2, \cdots, u_{N-1})^T$. Then, the scheme (3.9) can then be expressed in matrix-vector form, i.e., $(-\Delta)_{h,\gamma}^{\alpha/2}\mathbf{u} = \mathrm{A}\mathbf{u}$, where A is the matrix representation of the Dirichlet fractional Laplacian, defined as

$$\mathrm{A} = \begin{pmatrix} a_0 & a_1 & \ldots & a_{N-3} & a_{N-2} \\ a_1 & a_0 & a_1 & \cdots & a_{N-3} \\ \vdots & \ddots & \ddots & \ddots & \vdots \\ a_{N-3} & \ldots & a_1 & a_0 & a_1 \\ a_{N-2} & a_{N-3} & \ldots & a_1 & a_0 \end{pmatrix}_{(N-1)\times(N-1)}, \tag{3.10}$$

where A is a symmetric Toeplitz matrix.

Case 2. *The splitting parameter* $\gamma = 2$. In this case, the integral for $i = 1$ can be approximated by

$$\int_{\xi_0}^{\xi_1} \psi_\gamma(x,\xi)\xi^{\gamma-(1+\alpha)}d\xi = \int_{\xi_0}^{\xi_1} \psi_2(x,\xi)\xi^{1-\alpha}d\xi \approx \frac{1}{2-\alpha}\xi_1^{2-\alpha}\psi_2(x,\xi_1), \tag{3.11}$$

where the function

$$\psi_2(x,\xi) = \frac{u(x+\xi) - 2u(x) + u(x-\xi)}{\xi^2} \tag{3.12}$$

can be viewed as the central difference approximation of $u''(x)$. It is easy to verify that if $\gamma = 1 + \alpha/2$, the approximation (3.7) coincides with (3.11). As we will show in Section 3.2, the scheme resulting from $\gamma = 1 + \alpha/2$ or 2 in fact has an optimal convergence rate.

Combining (3.2)–(3.4), (3.6) with $\gamma = 2$, and (3.11) yields the numerical approximation of the fractional Laplacian $(-\Delta)^{\alpha/2}$ as:

$$\begin{aligned}(-\Delta)_{h,\gamma}^{\alpha/2}u(x) \;&=\; -\frac{C_{1,\alpha}}{2(2-\alpha)}\Big[2\xi_1^{2-\alpha}\psi_2(x,\xi_1) + \sum_{i=2}^{N}\left(\xi_i^{2-\alpha} - \xi_{i-1}^{2-\alpha}\right)\Big(\psi_2(x,\xi_{i-1}) \\ &\qquad +\psi_2(x,\xi_i)\Big)\Big] + \frac{2C_{1,\alpha}}{\alpha L^\alpha}u(x), \qquad \text{for } x \in (a,\, b), \end{aligned} \tag{3.13}$$

Following similar lines for $\gamma \in (\alpha, 2)$, we get the fully discretized scheme at point $x = x_i$ as in (3.9), but different coefficients, i.e.,

$$a_j = \frac{1}{2(2-\alpha)h^\alpha}\begin{cases} 2^{2-\alpha} + 1, & \text{for} \quad j = 1, \\ \dfrac{(j+1)^{2-\alpha} - (j-1)^{2-\alpha}}{j^2}, & \text{for} \quad j = 2, \dots, N-1, \\ \dfrac{N^{2-\alpha} - (N-1)^{2-\alpha}}{N^2}, & \text{for} \quad j = N, \end{cases}$$

$$a_0 = -2\Big(\sum_{j=1}^{N} a_j + \frac{1}{\alpha L^\alpha}\Big).$$

Similarly, we can write the discretized scheme into a matrix-vector form, which we will omit here for brevity.

Remark 3.1.1. *As $\alpha \to 2$, both the schemes with $\gamma = 1 + \alpha/2$ and $\gamma = 2$ exactly reduce to the central difference scheme for the classical Laplace operator $-\Delta$, i.e.,*

$$-\Delta_h u_i = \frac{1}{h^2}\Big[-u_{i-1} + 2u_i - u_{i+1}\Big], \quad \textit{for} \;\; i = 1, 2, \dots, N-1.$$

3.2. ERROR ESTIMATES

In the following, we provide error estimates on the weighted trapezoidal scheme in discretizing the fractional Laplacian. The main technique that used in our proof is the weighted Montgomery's identity. The standard Montgomery's identity has been generalized in different ways with applications to numerical integration, especially the error analysis of different types of quadrature rules. We will extend this idea by using the weighted Montgomery's identity to prove the accuracy of our weighted trapezoidal method.

First, we will review the standard Montgomery identity for n-time differentiable functions and make remarks on how it is applied to prove the accuracy of the trapezoidal method for functions with different smoothness conditions.

Theorem 3.2.1 (Standard Montgomery identity [14]). *Let $f : [a, b] \to \mathbb{R}$ be a mapping such that $f^{(n)}$ exists. Then for any $x \in [a, b]$, we have the identity*

$$\int_a^b f(t)dt = \sum_{j=1}^{n} \frac{(b-x)^j + (-1)^{j-1}(x-a)^j}{j!} f^{(j-1)}(x) \\ +(-1)^n \int_a^b P_n(x,t) f^{(n)}(t)dt, \tag{3.14}$$

where the Peano kernel $P_n(x, t)$ is defined by

$$P_n(x,t) = \begin{cases} \dfrac{(t-a)^n}{n!}, & for \quad t \in [a, x], \\ \dfrac{(t-b)^n}{n!}, & for \quad t \in (x, b]. \end{cases}$$

The standard Montgomery's identity is well applied in the proof of numerical quadrature rules, especially the trapezoidal rules.

For functions $f \in C^1([a, b])$, the standard Montgomery identity in (3.14) reduces to

$$\int_a^b f(t)dt - (b-a)f(x) = -\int_a^b P_1(x,t) f'(t)dt. \tag{3.15}$$

Letting $x = a$ or $x = b$ in (3.15) and then taking the average leads to the following identity

$$\begin{aligned}&\int_a^b f(t)dt - \frac{b-a}{2}\left[f(a)+f(b)\right]\\ &= -\frac{1}{2}\int_a^b \left[(t-a)+(t-b)\right] f'(t)dt,\end{aligned}$$

By triangle inequality, there exists a constant $C > 0$, such that

$$\left|\int_a^b f(t)dt - \frac{b-a}{2}\left[f(a)+f(b)\right]\right| \leq C(b-a)^2 \max_{t\in[a,b]} |f'(t)|,$$

which implies the 1st order accuracy of the composite trapezoidal rule for $f \in C^1([a,b])$.

Following the similar lines, we can apply the Montgomery's identity to obtain the error estimates of the trapezoidal rule for $f \in C^2([a,b])$. For functions $f \in C^2([a,b])$,

$$\left|\int_a^b f(t)dt - \frac{b-a}{2}\left[f(a)+f(b)\right]\right| \leq C(b-a)^3 \max_{t\in[a,b]} |f''(t)|,$$

which implies the 2nd order accuracy of the composite trapezoidal rule for $f \in C^2([a,b])$.

To prove the accuracy of the weighted trapezoidal method, the Montgomery's identity needs to be generalized to a weighted version. We reviewed the weighted Montgomery's identity in the following theorem.

Theorem 3.2.2 (Weighted Montgomery's identity [56])**.** *Let $f : [a,b] \to \mathbb{R}$ be a mapping such that $f^{(n)}$ exists, and $w : [a,b] \to [0,\infty)$ be weight function, then for any $x \in [a,b]$, we have*

$$\int_a^b w(t)f(t)dt = \sum_{j=1}^{n}(-1)^{j-1}Q_{j,w}(x)f^{(j-1)}(x) + (-1)^n \int_a^b P_{n,w}(x,t)f^{(n)}(t)dt, \quad (3.16)$$

where

$$Q_{j,w}(x) = \frac{1}{(j-1)!}\int_a^b (x-s)^{j-1}w(s)ds,$$

and the weighted Peano kernel $P_{n,w}(x,t)$ *is defined by*

$$P_{n,w}(x,t) = \begin{cases} \dfrac{1}{(n-1)!}\displaystyle\int_a^t (t-s)^{n-1} w(s)ds, & \textit{for} \quad t \in [a,x], \\ \dfrac{1}{(n-1)!}\displaystyle\int_b^t (t-s)^{n-1} w(s)ds, & \textit{for} \quad t \in (x,b], \end{cases} \tag{3.17}$$

As special cases of the weighted Montgomery's identity for n-time differentiable functions, we rewrite the weighted Montgomery's identity in more simple expressions for the first and second order differentiable functions in the following corollary. The results will be applied to the error analysis of the weighted trapezoidal method.

Corollary 3.2.1. *Let* $w, f : [a,b] \to \mathbb{R}$ *be integrable functions.*

(i). If f' *exists on* $[a,b]$*, there is*

$$f(x)\int_a^b w(t)dt - \int_a^b w(t)f(t)dt = \int_a^b P_{1,w}(x,t)f'(t)\,dt, \tag{3.18}$$

(ii). If f'' *exists on* $[a,b]$*, there is*

$$\begin{aligned} & f(x)\int_a^b w(t)dt - \int_a^b w(t)f(t)dt \\ &= f'(x)\int_a^b (x-t)w(t)\,dt - \int_a^b P_{2,w}(x,t)f''(t)\,dt, \end{aligned} \tag{3.19}$$

where the weighted Peano kernel $P_{n,w}$ $(n = 1,2)$ *is defined in (3.17).*

As an application of Theorem 3.2.1, letting $x = a$ or $x = b$ in (3.18) (or (3.19)) and then taking the average, we have the following lemma for the weighted trapezoidal rule.

Lemma 3.2.1. *Let* $w, f : [a,b] \to \mathbb{R}$ *be integrable functions.*

(i). If f' *exists on* $[a,b]$*, there is*

$$\begin{aligned} & \int_a^b \Big(f(x) - \frac{f(a)+f(b)}{2}\Big)w(x)dx \\ &= -\frac{1}{2}\int_a^b \Big(\int_b^x w(y)dy + \int_a^x w(y)dy\Big)f'(x)dx. \end{aligned} \tag{3.20}$$

(ii). If f'' exists on $[a, b]$, there is

$$\begin{aligned}
&\int_a^b \Big(f(x) - \frac{f(a)+f(b)}{2}\Big) w(x)dx \\
&= \frac{1}{2}\int_a^b \Big(\int_a^x w(y)(x-y)dy + \int_b^x w(y)(x-y)dy\Big) f''(x)\,dx \\
&-\frac{1}{2}\left(f'(a)\int_a^b w(y)(a-y)dy + f'(b)\int_a^b w(y)(b-y)dy\right). \qquad (3.21)
\end{aligned}$$

Denote the multiindex $\boldsymbol{\kappa} = (\kappa_1, \dots, \kappa_d)$, where each $\kappa_i \geq 0$ for $i = 1, 2, \dots, d$, and $|\boldsymbol{\kappa}| = \kappa_1 + \cdots + \kappa_d$. For $u : \mathbb{R}^d \to \mathbb{R}$, define the $\boldsymbol{\kappa}$-th partial derivative

$$\partial_{\kappa_1,\dots,\kappa_d} u := \frac{\partial^m}{\partial x_1^{\kappa_1} \partial x_2^{\kappa_2} \cdots \partial x_d^{\kappa_d}}, \quad \text{where} \quad |\boldsymbol{\kappa}| = m.$$

On an open bounded set $\Omega \subset \mathbb{R}^d$ and for $\nu \in (0, 1]$, denote the Hölder space $C^{0,\nu}(\Omega)$ for function $u : \Omega \to \mathbb{R}$ with exponent ν, i.e.,

$$C^{0,\nu}(\Omega) = \Big\{ u \in C^0(\Omega) \,\Big|\, \sup_{\substack{\mathbf{x},\mathbf{y}\in\Omega \\ \mathbf{x}\neq\mathbf{y}}} \frac{|u(\mathbf{x}) - u(\mathbf{y})|}{|\mathbf{x}-\mathbf{y}|^\nu} < \infty \Big\}.$$

For an integer $n \geq 0$ and $\mathbb{N} = \{0, 1, \dots\}$, we denote

$$C^{n,\nu}(\Omega) = \Big\{ u \in C^n(\Omega) \,|\, \partial^{\boldsymbol{\kappa}} u \in C^{0,\nu}(\Omega), \text{ for } \boldsymbol{\kappa} \in \mathbb{N}^d \text{ and } |\boldsymbol{\kappa}| \leq n \Big\}.$$

For notational convenience, we will write $\psi_\gamma(\xi) = \psi_\gamma(x, \xi)$ in the rest of this section. Next, we will present the properties of ψ_γ in the following lemma:

Lemma 3.2.2. *Let $\alpha \in (0, 2)$ and $0 < \xi < \infty$.*

(i). If $u \in C^{1,\alpha/2}(\mathbb{R})$, the derivative $\psi'_\gamma(\xi)$ ($\gamma \in (\alpha, 2]$) exists. Furthermore, there is

$$|\psi_\gamma^{(m)}(\xi)| \leq C\xi^{\alpha/2+1-(m+\gamma)}, \qquad m = 0,\ 1, \qquad (3.22)$$

where C is a positive constant.

(ii). If $u \in C^{3,\alpha/2}(\mathbb{R})$, the derivative $\psi_2^{(m)}(\xi)$ exists, for $m = 1, 2$. Furthermore, there is

$$|\psi_2^{(m)}(\xi)| \leq C\xi^{\alpha/2+1-m}, \qquad m = 1,\ 2, \tag{3.23}$$

where C is a positive constant.

Proof. By Taylor's Theorem, there exist $\eta_1 \in [x-\xi, x]$ and $\eta_2 \in [x, x+\xi]$, such that

$$\begin{aligned}\psi_\gamma(\xi) &= \xi^{-\gamma}\left[u(x-\xi) - 2u(x) + u(x+\xi)\right]\\ &= \xi^{1-\gamma}\left[u'(\eta_2) - u'(\eta_1)\right]\end{aligned}$$

Then, since $u \in C^{1,\alpha/2}(\mathbb{R})$, there exists a positive constant C, such that

$$|\psi_\gamma(\xi)| \leq C\xi^{\alpha/2+1-\gamma}.$$

By Taylor's Theorem, there exist $\zeta_1 \in [x-\xi, x]$ and $\zeta_2 \in [x, x+\xi]$, such that

$$\begin{aligned}\psi_2'(\xi) &= -\gamma\xi^{-\gamma-1}\left[u(x-\xi) - 2u(x) + u(x+\xi)\right] + \xi^{-\gamma}\left[-u'(x-\xi) + u'(x+\xi)\right]\\ &= -\gamma\xi^{-\gamma}\left[u'(\zeta_2) - u'(\zeta_1)\right] + \xi^{-\gamma}\left[u'(x+\xi) - u'(x-\xi)\right].\end{aligned}$$

Then, since $u \in C^{1,\alpha/2}(\mathbb{R})$, there exists a positive constant C, such that

$$|\psi_\gamma'(\xi)| \leq C\xi^{\alpha/2-\gamma}.$$

The proof of part (ii) can follow the same lines as the proof of part (i), for brevity, we will omit the detail here. □

Remark 3.2.1. *Lemma 3.2.2 provides the bound estimates of* $\psi_\gamma^{(m)}(\xi)$ *for* $u \in C^{1,\alpha/2}(\mathbb{R})$ *and* $\psi_2^{(m)}(\xi)$ *for* $u \in C^{3,\alpha/2}(\mathbb{R})$*. Different to (i), part (ii) in Lemma 3.2.2 does not hold for* $\gamma \neq 2$*. Increasing the smoothness of the function from* $C^{1,\alpha/2}(\mathbb{R})$ *to* $C^{3,\alpha/2}(\mathbb{R})$ *will lead to an increment of order* $O(\xi^\gamma)$ *only for* $\gamma = 2$*.*

Define the norm

$$\|u\|_{\infty,\,\Omega} = \max_{x\in\Omega} |u(x)|.$$

To short the lengthy notation in the proof of Theorem 3.2.3 and 3.2.4, we define the following function:

$$K_{(a,b)}^{(m)}(x) = \int_a^x w(y)(x-y)^m \, dy + \int_b^x w(y)(x-y)^m \, dy, \tag{3.24}$$

for $x \in [a, b]$ and $m = 0, 1$.

Then, we have the following error estimates on our finite difference scheme for the fractional Laplacian:

Theorem 3.2.3. *Suppose that* $u \in C^{1,\alpha/2}(\mathbb{R})$ *has finite support on an open set* $\Omega \in \mathbb{R}$*, and* $(-\Delta)_{h,\gamma}^{\alpha/2}$ *in (3.9) is a finite difference approximation of the fractional Laplacian* $(-\Delta)^{\alpha/2}$*. Then, for any* $\gamma \in (\alpha, 2]$*, there is*

$$\|(-\Delta)^{\alpha/2}u(x) - (-\Delta)_{h,\gamma}^{\alpha/2}u(x)\|_{\infty,\,\Omega} \le Ch^{1-\alpha/2}, \qquad \textit{for } \ \alpha \in (0,2) \tag{3.25}$$

with C *a positive constant depending on* α *and* γ*.*

Proof. Define the error function

$$e_{\alpha,\gamma}^h(x) \;\; = \;\; (-\Delta)^{\alpha/2}u(x) - (-\Delta)_{h,\gamma}^{\alpha/2}u(x).$$

Case 1. For $\gamma \in (\alpha, 2)$, we obtain from (3.6) and (3.7) that,

$$\begin{aligned} e^h_{\alpha,\gamma}(x) &= -C_{1,\alpha}\Big[\int_{\xi_0}^{\xi_1} \psi_\gamma(\xi)\, \xi^{\gamma-(1+\alpha)} d\xi - \frac{1}{2}\psi_\gamma(\xi_1)\int_{\xi_0}^{\xi_1} \xi^{\gamma-(1+\alpha)} d\xi \\ &\quad + \sum_{i=2}^{N}\Big(\int_{\xi_{i-1}}^{\xi_i} \psi_\gamma(\xi)\, \xi^{\gamma-(1+\alpha)} d\xi - \frac{1}{2}\big(\psi_\gamma(\xi_{i-1}) + \psi_\gamma(\xi_i)\big)\int_{\xi_{i-1}}^{\xi_i} \xi^{\gamma-(1+\alpha)} d\xi\Big)\Big] \\ &= -C_{1,\alpha}(I + II). \end{aligned} \tag{3.26}$$

Noticing that $\xi_0 = 0$ and $\xi_1 = h$, we can write the term I as:

$$\begin{aligned} |I| &= \Big|\int_{\xi_0}^{\xi_1} \big(\psi_\gamma(\xi) - \frac{1}{2}\psi_\gamma(\xi_1)\big)\xi^{\gamma-(1+\alpha)} d\xi\Big| \\ &\le \int_0^h |\psi_\gamma(\xi)|\xi^{\gamma-(1+\alpha)} d\xi + \frac{1}{2}|\psi_\gamma(h)|\int_0^h \xi^{\gamma-(1+\alpha)} d\xi. \end{aligned} \tag{3.27}$$

Using Lemma 3.2.2 (i) with $m = 0$, we obtain

$$|I| \le \int_0^h \xi^{\alpha/2-\gamma+1} \cdot \xi^{\gamma-(1+\alpha)} d\xi + Ch^{\alpha/2-\gamma+1} \cdot h^{\gamma-\alpha} \le Ch^{1-\alpha/2}. \tag{3.28}$$

Now, we move to the estimate of term II. Using Lemma 3.2.1 (i) by taking $w(\xi) = \xi^{\gamma-(1+\alpha)}$ and recall the definition (3.24), we obtain

$$\begin{aligned} |II| &= \Big|\sum_{i=2}^{N}\int_{\xi_{i-1}}^{\xi_i} \Big(\psi_\gamma(\xi) - \frac{\psi_\gamma(\xi_{i-1}) + \psi_\gamma(\xi_i)}{2}\Big)\, \xi^{\gamma-(1+\alpha)}\, d\xi\Big| \\ &= \frac{1}{2}\Big|\sum_{i=2}^{N}\int_{\xi_{i-1}}^{\xi_i} K^{(0)}_{(\xi_{i-1},\xi_i)}(\xi)\psi'_\gamma(\xi)\, d\xi\Big| \le Ch\Big|\sum_{i=2}^{N}\int_{\xi_{i-1}}^{\xi_i} \xi^{\gamma-(1+\alpha)}|\psi'_\gamma(\xi)|\, d\xi\Big|. \end{aligned}$$

By Lemma 3.2.2 (i) with $m = 1$, we obtain

$$|II| \le Ch\Big|\sum_{i=2}^{N}\int_{\xi_{i-1}}^{\xi_i} \xi^{\gamma-(1+\alpha)} \cdot \xi^{\alpha/2-\gamma}\, d\xi\Big| \le Ch^{1-\alpha/2}. \tag{3.29}$$

Combining (3.26), (3.28) and (3.29) yields

$$|e^h_{\alpha,\gamma}| \le |\,I\,| + |\,II\,| \le Ch^{1-\alpha/2},$$

for any $x \in \Omega$, which leads to (3.25) immediately.

Case2: For $\gamma = 2$, the error function is slightly different from (3.26), which is

$$\begin{aligned} e^h_{\alpha,\gamma}(x) &= -C_{1,\alpha}\Big[\int_{\xi_0}^{\xi_1}\big(\psi_2(\xi) - \psi_2(\xi_1)\big)\xi^{1-\alpha}d\xi \\ &\qquad + \sum_{i=2}^{N}\int_{\xi_{i-1}}^{\xi_i}\Big(\psi_2(\xi) - \frac{\psi_2(\xi_{i-1}) + \psi_2(\xi_i)}{2}\Big)\xi^{1-\alpha}d\xi\Big] \\ &= -C_{1,\alpha}(\widetilde{I} + \widetilde{II}). \end{aligned} \tag{3.30}$$

The estimation of term $\widetilde{II}$ follows exactly the same line as in proving (3.29) by simply taking $\gamma = 2$. For term $\widetilde{I}$, by the triangle inequality, we have

$$\begin{aligned} |\,\widetilde{I}\,| &= \Big|\int_{\xi_0}^{\xi_1}\big(\psi_2(\xi) - \psi_2(\xi_1)\big)\xi^{1-\alpha}d\xi\Big| \\ &\le \int_0^h |\psi_2(\xi)|\xi^{1-\alpha}d\xi + |\psi_2(h)|\int_0^h \xi^{1-\alpha}d\xi. \end{aligned} \tag{3.31}$$

Using Lemma 3.2.2 (i) with $m = 0$, we obtain

$$|\,\widetilde{I}\,| \le \int_0^h \xi^{\alpha/2-1}\cdot\xi^{1-\alpha}d\xi + Ch^{\alpha/2-1}\cdot h^{2-\alpha} \le Ch^{1-\alpha/2}. \tag{3.32}$$

Therefore, we proved that for $\gamma = 2$, $|e^h_{\alpha,\gamma}| \le Ch^{1-\alpha/2}$. □

Remark 3.2.2. *Theorem 3.2.3 shows that for* $u \in C^{1,\alpha/2}(\mathbb{R})$*, the accuracy of our method is* $O(h^{1-\alpha/2})$ *for small mesh size h, i.e., its convergence for low regularity function is slow, especially as* $\alpha \to 2$*. This result is consistent with the central difference scheme for the classical Laplace operator, which is not convergent if* $u \in C^{1,1}(\mathbb{R})$ *or even* $C^2(\mathbb{R})$*.*

Next, we will show that for a smooth enough function u, the accuracy of our method can be improved to $O(h^2)$ uniformly for any $\alpha \in (0, 2)$.

Theorem 3.2.4. *Suppose that $u \in C^{3,\alpha/2}(\mathbb{R})$ has finite support on an open set $\Omega \in \mathbb{R}$, and $(-\Delta)^{\alpha/2}_{h,\gamma}$ defined in (3.9) is a finite difference approximation of the fractional Laplacian $(-\Delta)^{\alpha/2}$. If the parameter is chosen as $\gamma = 2$ or $1 + \alpha/2$, there is*

$$\|(-\Delta)^{\alpha/2}u(x) - (-\Delta)^{\alpha/2}_{h,\gamma}u(x)\|_{\infty,\Omega} \le Ch^2, \qquad \textit{for} \;\; \alpha \in (0,2) \tag{3.33}$$

with C a positive constant depending on α.

Proof. For brevity, we start with the local truncation errors in (3.30) for $\gamma = 2$ and (3.26) for $\gamma = 1 + \alpha/2$.

First, we focus on the case of $\gamma = 2$ by considering the local truncation error in (3.30). For term $\widetilde{I}$, by Taylor theorem, we obtain

$$\begin{aligned} |\widetilde{I}| &= \left|\int_0^h (\psi_2(\xi) - \psi_2(\xi_1))\,\xi^{1-\alpha}d\xi\right| \\ &\le \int_0^h |\psi_2(\xi) - \psi_2(\xi_1)|\xi^{1-\alpha}d\xi \\ &\le Ch \max_{\eta\in[0,h]} |\psi_2'(\eta)| \int_0^h \xi^{1-\alpha}d\xi \le Ch^{3-\alpha/2}. \end{aligned} \tag{3.34}$$

For term $\widetilde{II}$, by Lemma 3.2.1 (ii) for the second order differentiable function ψ_2, we get

$$\begin{aligned}
\widetilde{II} &= \sum_{i=2}^{N} \int_{\xi_{i-1}}^{\xi_i} \Big(\psi_2(\xi) - \frac{\psi_2(\xi_{i-1}) + \psi_2(\xi_i)}{2}\Big) \xi^{1-\alpha} d\xi \\
&= \frac{1}{2}\Big[\sum_{i=2}^{N} \int_{\xi_{i-1}}^{\xi_i} \Big(K^{(1)}_{(\xi_{i-1},\xi_i)}(\xi)\psi_2''(\xi)\, d\xi \\
&\qquad - \Big(\psi_2'(\xi_i) K^{(1)}_{(\xi_{i-1},\xi_i)}(\xi_i) - \psi_2'(\xi_{i-1}) K^{(1)}_{(\xi_{i-1},\xi_i)}(\xi_{i-1})\Big)\Big)\Big] \\
&= \frac{1}{2} \sum_{i=2}^{N} \int_{\xi_{k-1}}^{\xi_k} K^{(1)}_{(\xi_{i-1},\xi_i)}(\xi)\psi_2''(\xi)\, d\xi \\
&\quad - \frac{1}{2} \sum_{i=2}^{N-1} \psi_2'(\xi_i) \Big(K^{(1)}_{(\xi_{i-1},\xi_i)}(\xi_i) - K^{(1)}_{(\xi_i,\xi_{i+1})}(\xi_i) \Big) \\
&\quad - \frac{\psi_2'(\xi_N)}{2} K^{(1)}_{(\xi_{N-1},\xi_N)}(\xi_N) + \frac{\psi_2'(\xi_1)}{2} K^{(1)}_{(\xi_1,\xi_2)}(\xi_1) \\
&= \widetilde{II}_1 + \widetilde{II}_2 + \widetilde{II}_3 + \widetilde{II}_4. \qquad (3.35)
\end{aligned}$$

Next, we focus on estimating terms $\widetilde{II}_i$ for $i = 1, 2, 3$ and 4.

Applying definition of $K^{(1)}_{(\xi_{i-1},\xi_i)}(\xi)$ in (3.24), we can easily get

$$\begin{aligned}
\Big| K^{(1)}_{(\xi_{i-1},\xi_i)}(\xi) \Big| &= \Big| \int_{\xi_{i-1}}^{\xi} (\xi - y)\, y^{1-\alpha}\, dy + \int_{\xi_i}^{\xi} (\xi - y)\, y^{1-\alpha}\, dy \Big| \\
&\leq Ch(\xi_i^{2-\alpha} - \xi_{i-1}^{2-\alpha}),
\end{aligned}$$

then we can estimate term $\widetilde{II}_1$ as,

$$\begin{aligned}
|\, \widetilde{II}_1 \,| &\leq Ch^2 \sum_{i=2}^{N} (\xi_i^{2-\alpha} - \xi_{i-1}^{2-\alpha}) \max_{\xi \in [\xi_{i-1},\, \xi_i]} |\psi_2''(\xi)| \\
&\leq Ch^2 \sum_{i=2}^{N} (\xi_i^{2-\alpha} - \xi_{i-1}^{2-\alpha}) \max_{\xi \in [\xi_{i-1},\, \xi_i]} \xi^{\alpha/2-1} \\
&\leq Ch^2 \sum_{i=2}^{N} \Big(\xi_i^{1-\alpha/2} - \xi_{i-1}^{1-\alpha/2}\Big) \frac{\xi_i^{1-\alpha/2} + \xi_{i-1}^{1-\alpha/2}}{\xi_{i-1}^{1-\alpha/2}}, \qquad (3.36)
\end{aligned}$$

where the second inequality is obtained from Lemma 3.2.2 (ii) with $m = 2$. We further obtain

$$|\,\widetilde{II}_1\,| \leq Ch^2 \sum_{i=2}^{N} \left(\xi_i^{1-\alpha/2} - \xi_{i-1}^{1-\alpha/2}\right)(1 + 2^{1-\alpha/2}) \leq Ch^2 L^{1-\alpha/2} \leq Ch^2. \tag{3.37}$$

To estimate term $\widetilde{II}_2$, let's first find the bound of $\left|K^{(1)}_{(\xi_{i-1},\xi_i)}(\xi_i) - K^{(1)}_{(\xi_i,\xi_{i+1})}(\xi_i)\right|$. By Definition (3.24), we have

$$K^{(1)}_{(\xi_{i-1},\xi_i)}(\xi_i) = \int_{\xi_{i-1}}^{\xi_i} (\xi_i - y)\, y^{1-\alpha}\, dy \quad \text{and} \quad K^{(1)}_{(\xi_i,\xi_{i+1})}(\xi_i) = \int_{\xi_{i+1}}^{\xi_i} (\xi_i - y)\, y^{1-\alpha}\, dy,$$

Here we construct an auxiliary function

$$G_i(z) := \int_{z}^{\xi_i} (\xi_i - y)\, y^{1-\alpha}\, dy \quad \text{for} \quad z \in [\xi_{i-1}, \xi_{i+1}] \quad ,$$

the functions $K^{(1)}_{(\xi_{i-1},\xi_i)}(\xi_i)$ and $K^{(1)}_{(\xi_i,\xi_{i+1})}(\xi_i)$ can be represented by $G_i(z)$ as

$$K^{(1)}_{(\xi_{i-1},\xi_i)}(\xi_i) = G_i(\xi_{i-1}) \quad \text{and} \quad K^{(1)}_{(\xi_i,\xi_{i+1})}(\xi_i) = G_i(\xi_{i+1}).$$

Taking derivatives of $G_i(z)$, we get

$$G_i'(z) = (z - \xi_i)z^{1-\alpha}, \quad G_i'''(z) = (2-\alpha)(1-\alpha)z^{-\alpha} + \alpha(1-\alpha)\xi_i z^{-\alpha-1},$$

and it is clear that

$$G_i'(\xi_i) = 0, \quad \text{and} \quad \max_{\eta \in [\xi_{i-1},\xi_{i+1}]} |G_i'''(\eta)| \leq C\xi_i^{-\alpha}.$$

Then, by applying Taylor theorem, we can easily get

$$\begin{aligned}
\left|K^{(1)}_{(\xi_i,\xi_{i+1})}(\xi_i) - K^{(1)}_{(\xi_{i-1},\xi_i)}(\xi_i)\right| &= |G_i(\xi_{i+1}) - G_i(\xi_{i-1})| \\
&\le Ch^3 \max_{\eta\in[\xi_{i-1},\xi_{i+1}]} |G_i'''(\eta)| \\
&\le Ch^3 \xi_i^{-\alpha} \qquad (3.38)
\end{aligned}$$

for $i = 2, 3, \ldots, N$. Therefore, term $\widetilde{II}_2$ is bounded by

$$|\,\widetilde{II}_2\,| = \frac{1}{2}\left|\sum_{i=2}^{N-1} \psi_2'(\xi_i)\left(K^{(1)}_{(\xi_i,\xi_{i+1})}(\xi_i) - K^{(1)}_{(\xi_{i-1},\xi_i)}(\xi_i)\right)\right| \le Ch^3 \sum_{i=2}^{N-1} \xi_i^{-\alpha}|\psi_2'(\xi_i)|. \qquad (3.39)$$

Applying Lemma 3.2.2 (i) with $m = 1$, we get

$$|\,\widetilde{II}_2\,| \le Ch^3 \sum_{i=2}^{N} \xi_i^{-\alpha/2} \le Ch^2 \int_0^L \xi^{-\alpha/2} d\xi \le Ch^2. \qquad (3.40)$$

For term $\widetilde{II}_3$, by Lemma 3.2.2 (i) with $m = 1$, we get

$$|\,\widetilde{II}_3\,| = \frac{1}{2}\left|\psi_2'(\xi_N) K^{(1)}_{(\xi_{N-1},\xi_N)}(\xi_N)\right| \le \frac{1}{2} h^2 \xi_N^{\alpha/2} \max\{\xi_{N-1}^{1-\alpha},\ \xi_N^{1-\alpha}\} \le Ch^2.$$

For term $\widetilde{II}_4$, by applying Lemma 3.2.2 (ii), we obtain

$$|\,\widetilde{II}_4\,| = \frac{1}{2}\left|\psi_2'(\xi_1) K^{(1)}_{(\xi_1,\xi_2)}(\xi_1)\right| \le Ch^{3-\alpha}|\psi_2'(\xi_1)| \le Ch^{3-\alpha/2}.$$

Then, the estimate of $|\,\widetilde{II}\,|$ can be obtained by combining (3.35) with (3.37)–(3.41), i.e.,

$$|\,\widetilde{II}\,| \le |\,\widetilde{II}_1\,| + |\,\widetilde{II}_2\,| + |\,\widetilde{II}_3\,| + |\,\widetilde{II}_4\,| \le Ch^2. \qquad (3.41)$$

Finally, combining (3.30), (3.34) and (3.41), we get

$$|e^h_{\alpha,\gamma}(x)| \le |\,\widetilde{I}\,| + |\,\widetilde{II}\,| \le Ch^2,$$

for any $x \in \Omega$ and $\alpha \in (0,2)$, where $\gamma = 2$.

Next, we focus on the case of $\gamma = 1 + \alpha/2$ by considering the local truncation error in (3.26). For term I, we first rewrite it as

$$\begin{aligned} I &= \int_{\xi_0}^{\xi_1} \Big(\psi_{1+\alpha/2}(\xi) - \frac{1}{2}\psi_{1+\alpha/2}(\xi_1)\Big)\xi^{-\alpha/2} d\xi \\ &= \int_{\xi_0}^{\xi_1} \Big(\psi_2(\xi)\,\xi^{1-\alpha/2} - \frac{1}{2}\psi_2(\xi_1)\,\xi_1^{1-\alpha/2}\Big)\xi^{-\alpha/2} d\xi \\ &= \int_0^h \left(\psi_2(\xi) - \psi_2(\xi_1)\right)\xi^{1-\alpha} d\xi. \end{aligned} \tag{3.42}$$

It is clear to see from (3.30) that $I = \widetilde{I}$, so the estimation of $\widetilde{I}$ follows exactly the same line as the estimation of term I in (3.34).

Now, we focus on the estimation of term II. Different to the estimation of term $\widetilde{II}$ for $\gamma = 2$, which can be done directly by using Lemma 3.2.2 (ii), since γ is taken to be $1 + \alpha/2$, no similar results hold in this case, to prove the second order accuracy, we should firstly rewrite term II by separating it into three terms including one is exactly the term $\widetilde{II}$. This separation step is not removable, which plays the important role to prove the second order accuracy for $\gamma = 1 + \alpha/2$. We rewrite term II as follows,

$$\begin{aligned} II &= \frac{1}{4}\sum_{i=2}^{N}\int_{\xi_{i-1}}^{\xi_i} \left(\psi_2(\xi_{i-1}) + \psi_2(\xi_i)\right)\left(2\xi^{1-\alpha/2} - \xi_{i-1}^{1-\alpha/2} - \xi_i^{1-\alpha/2}\right)\xi^{-\alpha/2} d\xi \\ &\quad + \frac{1}{4}\sum_{i=2}^{N}\int_{\xi_{i-1}}^{\xi_i} \left(\xi_i^{1-\alpha/2} - \xi_{k-1}^{1-\alpha/2}\right)\left(\psi_2(\xi_{i-1}) - \psi_2(\xi_i)\right)\xi^{-\alpha/2} d\xi \\ &\quad + \sum_{i=2}^{N}\int_{\xi_{i-1}}^{\xi_i} \Big(\psi_2(\xi) - \frac{\psi_2(\xi_{i-1}) + \psi_2(\xi_i)}{2}\Big)\xi^{1-\alpha} d\xi \\ &= II_1 + II_2 + \widetilde{II} \end{aligned} \tag{3.43}$$

For term II_1, a direct calculation shows that it vanishes, i.e.,

$$II_1 = \frac{1}{4}\sum_{i=2}^{N}\left[\psi_2(\xi_{i-1}) + \psi_2(\xi_i)\right]\int_{\xi_{i-1}}^{\xi_i} \left(2\xi^{1-\alpha/2} - \xi_{i-1}^{1-\alpha/2} - \xi_i^{1-\alpha/2}\right)\xi^{-\alpha/2} d\xi = 0. \tag{3.44}$$

For term II_2, we obtain

$$\begin{aligned}
|\,II_2\,| &= \frac{1}{4}\Big|\sum_{i=2}^{N}\int_{\xi_{i-1}}^{\xi_i}(\xi_i^{1-\alpha/2}-\xi_{k-1}^{1-\alpha/2})\,(\psi_2(\xi_{i-1})-\psi_2(\xi_i))\xi^{-\alpha/2}d\xi\Big| \\
&\le C\sum_{i=2}^{N}|\xi_i^{1-\alpha/2}-\xi_{i-1}^{1-\alpha/2}||\psi_2(\xi_{i-1})-\psi_2(\xi_i)||\xi_i^{1-\alpha/2}-\xi_{i-1}^{1-\alpha/2}| \\
&\le Ch^3\sum_{i=2}^{N}\Big(\max_{\xi\in[\xi_{i-1},\,\xi_i]}|\xi^{-\alpha/2}|\Big)^2\Big(\max_{\zeta\in[\xi_{i-1},\xi_i]}|\psi_2'(\zeta)|\Big), \qquad (3.45)
\end{aligned}$$

by Taylor's theorem. Then by applying Lemma 3.2.2 (ii) with $m = 1$ to (3.45), we obtain

$$\begin{aligned}
|\,II_2\,| &\le Ch^3\sum_{i=2}^{N}\Big(\max_{\xi\in[\xi_{i-1},\,\xi_i]}\xi^{-\alpha/2}\Big)^2\max_{\zeta\in[\xi_{i-1},\,\xi_i]}\zeta^{\alpha/2} \\
&\le Ch^2\int_0^L\xi^{-\alpha/2}\le Ch^2.
\end{aligned}$$

Combine (3.43), (3.44), (3.46) and the estimation of term $\widetilde{II}$ in (3.41) we get

$$|\,II\,|\le|\,II_1\,|+|\,II_2\,|+|\,\widetilde{II}\,|\le Ch^2. \qquad (3.46)$$

Finally, combine (3.42), (3.34) and (3.46), we proved

$$|e^h_{\alpha,\gamma}(x)|\le|\,I\,|+|\,II\,|\le Ch^2,$$

for any $x\in\Omega$ and $\alpha\in(0,2)$, where $\gamma = 1+\alpha/2$. □

Theorem 3.2.4 shows that for $u \in C^{3,\alpha/2}(\mathbb{R})$, if the splitting parameter is chosen as $\gamma = 2$ or $1+\alpha/2$, our numerical method has the accuracy of $O(h^2)$ uniformly for any $\alpha\in(0,2)$.

Remark 3.2.3. *The results of Theorem 3.2.4 are consistent with the behavior of the central difference method for the standard Laplacian. Indeed, for* $u \in C^{3,1}(\mathbb{R})$*, by Taylor theorem and mean value theorem, there exist* $x^- \in [x-h, x]$ *and* $x^+ \in [x, x+h]$*, such that*

$$|e^h| = \left|\frac{u(x+h) - 2u(x) + u(x-h)}{h^2} - u''(x)\right| = \frac{1}{6}h|u'''(x^+) - u'''(x^-)| \leq Ch^2.$$

3.3. NUMERICAL EXPERIMENTS

In this section, we numerically study the accuracy of the weighted trapezoidal method in discretizing the fractional Laplacian $(-\Delta)^{\alpha/2}$. Consider a function u of the form:

$$u(x) = \begin{cases} (1-x^2)^{s+\frac{\alpha}{2}}, & \text{for } x \in \Omega = (-1, 1), \\ 0, & \text{otherwise}, \end{cases} \qquad x \in \mathbb{R}, \tag{3.47}$$

for $s \in \mathbb{N}$, as in (2.12). It is easy to verify that $u \in C^{s,\alpha/2}(\mathbb{R})$, and it has compact support on $(-1, 1)$. The fractional Laplacian of $u(x)$ can be found exactly in (2.13) [35, 36]. We will study the accuracy of the weighted Trapezoidal method for different s, implying different smoothness of u.

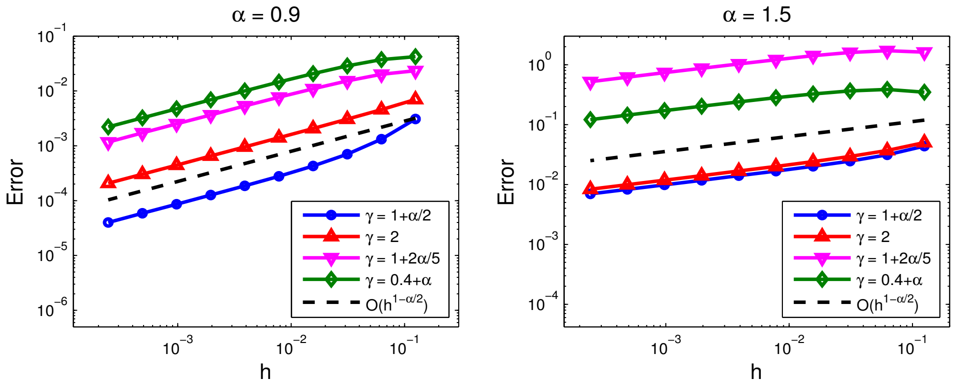

Figure 3.1. Numerical errors $\|(-\Delta)^{\alpha/2}u - (-\Delta)^{\alpha/2}_{h,\gamma}u\|_{\infty,\Omega}$ for different choices of γ, where u is defined in (3.47) with $s = 1$.

Figure 3.1 presents the numerical errors by taking different γ. Although the convergence rate in this case is independent of the splitting parameter $\gamma \in (\alpha, 2]$, our numerical studies (see Figure 3.1) show that the numerical error is considerably lower when choosing $\gamma = 1 + \alpha/2$ or $\gamma = 2$.

Table 3.1. Numerical errors and convergence rates for $u \in C^{1,\alpha/2}(\mathbb{R})$.

h α	1/32	1/64	1/128	1/256	1/512	1/1024	1/2048
0.2	4.846E-4	2.629E-4	1.417E-4	7.615E-5	4.086E-5	2.191E-5	1.174E-5
	c.r.	0.8822	0.8917	0.8961	0.8981	0.8991	0.8996
0.6	1.025E-3	6.497E-4	4.046E-4	2.502E-4	1.543E-4	9.505E-5	5.852E-5
	c.r.	0.6582	0.6834	0.6934	0.6974	0.6990	0.6996
1	2.291E-3	1.544E-3	1.071E-3	7.516E-4	5.297E-4	3.740E-4	2.643E-4
	c.r.	0.5691	0.5278	0.5113	0.5047	0.5020	0.5009
1.5	2.460E-2	2.015E-2	1.675E-2	1.401E-2	1.176E-2	9.874E-3	8.298E-3
	c.r.	0.2885	0.2664	0.2573	0.2534	0.2516	0.2508
1.9	2.891E-2	2.632E-2	2.487E-2	2.381E-2	2.291E-2	2.209E-2	2.132E-2
	c.r.	0.1352	0.0817	0.0628	0.0556	0.0526	0.0513

Tables 3.1 and 3.2 present numerical errors $\|(-\Delta)^{\alpha/2}u - (-\Delta)^{\alpha/2}_{h,\gamma}u\|_{l_\infty(\Omega)}$ and convergence rates of our method for various α, where u is defined in (3.47) with $s = 1$ and $s = 3$, respectively. The symbol 'c.r.' represents convergence rate. We find that for the same mesh size h, the larger the parameter α, the bigger the numerical errors. For $s = 1$, Table 3.1 shows that the convergence rates of our method is $O(h^{1-\alpha/2})$ for any $\alpha \in (0, 2)$, which confirms our analytical results in Theorem 3.2.3. While for $s = 3$, our method has accuracy of $O(h^2)$ for any $\alpha \in (0, 2)$; see Table 3.2. This observation is consistent with our conclusion in Theorem 3.2.4.

Remark 3.3.1. *For $u \in C^{2,\alpha/2}(\mathbb{R})$, we study the convergence rates of our finite difference method numerically; see Figure 3.2. It shows that for $\alpha \le 0.7$ the convergence rate in l_∞-norm is $O(h^2)$. For $\alpha > 0.7$, the convergence rate decreases toward 1, which is better than the case for $u \in C^{1,\alpha/2}(\mathbb{R})$. In fact, this behavior is consistent with that of the classical*

Table 3.2. Numerical errors and convergence rates for $u \in C^{3,\alpha/2}(\mathbb{R})$.

h α	1/32	1/64	1/128	1/256	1/512	1/1024	1/2048
0.2	5.676E-5	1.418E-5	3.544E-6	8.861E-7	2.215E-7	5.538E-8	1.384E-8
	c.r.	2.0009	2.0003	2.0001	2.0000	2.0000	2.0001
0.6	2.230E-4	5.550E-5	1.385E-5	3.461E-6	8.651E-7	2.162E-7	5.406E-8
	c.r.	2.0062	2.0024	2.0009	2.0003	2.0001	2.0000
1	5.643E-4	1.379E-4	3.414E-5	8.490E-6	2.117E-6	5.290E-7	1.321E-7
	c.r.	2.0324	2.0147	2.0074	2.0037	2.0007	2.0011
1.5	2.742E-3	8.050E-4	2.104E-4	5.251E-5	1.286E-5	3.129E-6	7.606E-7
	c.r.	1.7683	1.9356	2.0027	2.0297	2.0391	2.0405
1.9	1.450E-2	4.273E-3	1.140E-3	2.910E-4	7.275E-5	1.801E-5	4.436E-6
	c.r.	1.7631	1.9062	1.9699	1.9999	2.0143	2.0212

central difference approximation to the standard Laplace operator. For $u \in C^{2,1}(\mathbb{R})$*, by mean value theorem, there exist* $x^- \in [x-h, x]$ *and* $x^+ \in [x, x+h]$*, such that*

$$|e^h| = |\psi_2(x,h) - u''(x)| = \left|\frac{1}{2}\left(u''(x^-) - u''(x)\right) + \frac{1}{2}\left(u''(x^+) - u''(x)\right)\right| \le Ch.$$

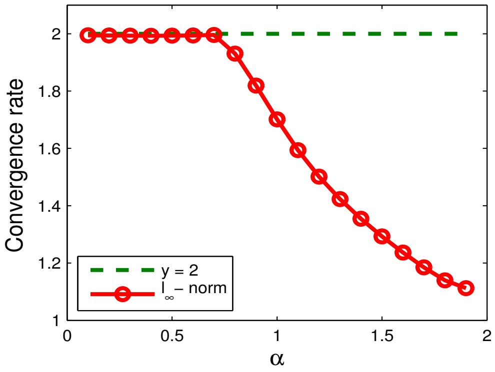

Figure 3.2. Convergence rate versus α for $u \in C^{2,\alpha/2}(\mathbb{R})$ defined in (3.47) with $s = 2$.

In this section, we propose a novel finite difference method based on the weighted trapezoidal rule to discretize the fractional Laplacian in one dimension. The novelty of our method is that a splitting parameter $\gamma \in (\alpha, 2]$ is introduced so that the fractional Laplacian is rewritten as the weighted integral of function $\psi_\gamma(x, \xi)$ with the weight function $\xi^{\gamma-(1+\alpha)}$. Notably, the choice of the splitting parameter γ influences the accuracy of the method. For function $u \in C^{1,\alpha/2}(\mathbb{R})$, our method has an accuracy of $O(h^{1-\alpha/2})$ with h a small mesh size, for any splitting parameter $\gamma \in (\alpha, 2]$, which was also verified by our numerical simulations. For function $u \in C^{3,\alpha/2}(\mathbb{R})$, our method with $\gamma = 1 + \alpha/2$ or 2 has an accuracy of $O(h^2)$, independent of the power $\alpha \in (0, 2)$. In fact, the optimal splitting parameter of our method is $\gamma = 1+\alpha/2$ or 2 in one dimension, while choosing other $\gamma \in (\alpha, 2)$ (but $\gamma \neq 1+\alpha/2$) leads to larger numerical errors. In addition, with $\gamma = 1 + \alpha/2$ or 2, the weighted trapezoidal method closely resembling the central difference scheme for the classical Laplacian, as $\alpha \to 2$.

4. THE WEIGHTED TRAPEZOIDAL METHOD IN HIGHER DIMENSIONS

In this section, we generalize the weighted trapezoidal method for one dimensional fractional Laplacian to higher dimensions. We first introduce our method in two dimension (2D) and then extend it to higher dimensions. In one-dimensional case, the scheme with either $\gamma = 2$ or $1 + \alpha/2$ can provide the second order accuracy for smooth enough functions, however there is only one optimal choice of γ, i.e., $\gamma = 2$, in d-dimension ($d \geq 2$) to get the second order accuracy. The error analysis and numerical examples are provided in detail for 2D case, while the generalization to higher dimension is outlined.

4.1. TWO-DIMENSIONAL CASE

4.1.1. Numerical Scheme.

Consider the 2D fractional Laplacian:

$$(-\Delta)^{\alpha/2}u(\mathbf{x}) = C_{2,\alpha}\mathrm{P}.V.\int_{\mathbb{R}^2} \frac{u(\mathbf{x}) - u(\mathbf{x}')}{|\mathbf{x} - \mathbf{x}'|^{2+\alpha}}\, d\mathbf{x}', \tag{4.1}$$

where $\mathbf{x} = (x, y)$ and $\mathbf{x}' = (x', y')$, and their distance $|\mathbf{x} - \mathbf{x}'| := \sqrt{(x - x')^2 + (y - y')^2}$. We focus on the discretization of the fractional Laplacian on a bounded domain $\Omega = (a_x, b_x) \times (a_y, b_y)$ with homogeneous Dirichlet boundary conditions, i.e., $u(\mathbf{x}) \equiv 0$ for $\mathbf{x} \in \Omega^c$. By changing of variables, i.e., letting $\xi = |x - x'|, \eta = |y - y'|$ and defining vector $\boldsymbol{\xi}= (\xi, \eta)$, the 2D fractional Laplacian in (4.1) can be further written as

$$(-\Delta)^{\alpha/2}u(\mathbf{x}) = C_{2,\alpha} \int_0^\infty \int_0^\infty \psi_\gamma(\mathbf{x}, \boldsymbol{\xi}) \cdot |\boldsymbol{\xi}|^{\gamma-(2+\alpha)}\, d\boldsymbol{\xi}, \tag{4.2}$$

i.e., a weighted integral of $\psi_\gamma(\mathbf{x}, \boldsymbol{\xi})$ with weight function being $|\boldsymbol{\xi}|^{\gamma-(2+\alpha)}$, where for $\gamma \in (\alpha.2]$,

$$\psi_\gamma(\mathbf{x}, \boldsymbol{\xi}) := \Big(\sum_{m,n=0}^{1} u\left(x + (-1)^m \xi, y + (-1)^n \eta\right) - 4u(\mathbf{x})\Big) \cdot |\boldsymbol{\xi}|^{-\gamma}. \tag{4.3}$$

Noticing the fact that the function u is compactly supported on Ω, choose a constant $L = \max\{b_x - a_x, b_y - a_y\}$, we further rewrite the integral in (4.2) as,

$$\begin{aligned}(-\Delta)^{\alpha/2}u(\mathbf{x}) \;\; = \;\; & -C_{2,\alpha}\Big(\int_{(0,L)^2} \psi_\gamma(\mathbf{x}, \boldsymbol{\xi}) \cdot |\boldsymbol{\xi}|^{\gamma-(2+\alpha)}\, d\boldsymbol{\xi} \\ & + \int_{\mathbb{R}^2\backslash(0,L)^2} \psi_\gamma(\mathbf{x}, \boldsymbol{\xi}) \cdot |\boldsymbol{\xi}|^{\gamma-(2+\alpha)}\, d\boldsymbol{\xi}\Big).\end{aligned} \tag{4.4}$$

The second integral in (4.4) can be found exactly. Precisely, for any $\mathbf{x} \in \Omega$, if $(\xi, \eta) \in \mathbb{R}^2\backslash(0, L)^2$, there is $(x \pm \xi, y \pm \eta) \in \mathbb{R}^2\backslash\Omega$, and thus $u(x \pm \xi, y \pm \eta) = 0$. Hence, we obtain

$$\int_{\mathbb{R}^2\backslash(0,L)^2} \psi_\gamma(\mathbf{x}, \boldsymbol{\xi}) \cdot |\boldsymbol{\xi}|^{\gamma-(2+\alpha)}\, d\boldsymbol{\xi} = -4u(\mathbf{x}) \int_{\mathbb{R}^2\backslash(0,L)^2} |\boldsymbol{\xi}|^{-2-\alpha}\, d\boldsymbol{\xi} = -4w_L u(\mathbf{x}), \tag{4.5}$$

where the coefficient w_L is defined by

$$w_L = \int_{\mathbb{R}^2\backslash(0,L)^2} |\boldsymbol{\xi}|^{-2-\alpha}\, d\boldsymbol{\xi}.$$

The main part of the numerical approximation is from the first integral in (4.4). We adopt the uniform mesh by choosing a positive integer N, and define the mesh size $h = L/N$. Denote grid points $\xi_i = \eta_i = ih$, for $0 \le i \le N$, evidently $\xi_N = \eta_N = L$. For brevity, we introduce the notation $\boldsymbol{\xi}_{i,j} := (\xi_i, \eta_j)$ and $|\boldsymbol{\xi}_{i,j}| := \sqrt{\xi_i^2 + \eta_j^2}$ $(i, j = 0, 1, \ldots, N)$,

As the preparation, we define the element

$$I_{ij} := [(i-1)h, ih] \times [(j-1)h, jh], \quad \text{for} \quad 1 \le i, j \le N.$$

For each $\boldsymbol{\xi}_{i,j}$, define the associated element as

$$\widetilde{I_{ij}} = [(i-1)h, (i+1)h] \times [(j-1)h, (j+1)h] \cap [0, L] \times [0, L], \quad \text{for} \quad 0 \le i, j \le N.$$

Then, we formulate the first integral in (4.4) as

$$\int_{(0,L)^2} \psi_\gamma(\mathbf{x}, \boldsymbol{\xi}) \cdot |\boldsymbol{\xi}|^{\gamma-(2+\alpha)} \, d\boldsymbol{\xi} = \sum_{i,j=1}^{N} \int_{I_{ij}} \psi_\gamma(\mathbf{x}, \boldsymbol{\xi}) \cdot |\boldsymbol{\xi}|^{\gamma-(2+\alpha)} \, d\boldsymbol{\xi}. \tag{4.6}$$

If $i \ne 1$ and $j \ne 1$, the integral on I_{ij} can be approximated by the 2D weighted trapezoidal rule as:

$$\begin{aligned} \int_{I_{ij}} \psi_\gamma(\mathbf{x}, \boldsymbol{\xi}) \cdot |\boldsymbol{\xi}|^{\gamma-(2+\alpha)} \, d\boldsymbol{\xi} \approx \frac{1}{4} \Big(&\psi_\gamma(\mathbf{x}, \boldsymbol{\xi}_{i-1,j-1}) + \psi_\gamma(\mathbf{x}, \boldsymbol{\xi}_{i-1,j}) \\ &+ \psi_\gamma(\mathbf{x}, \boldsymbol{\xi}_{i,j-1}) + \psi_\gamma(\mathbf{x}, \boldsymbol{\xi}_{i,j}) \Big) \int_{I_{ij}} |\boldsymbol{\xi}|^{\gamma-(2+\alpha)} \, d\boldsymbol{\xi}. \end{aligned} \tag{4.7}$$

If $i = j = 1$, there is $I_{11} = (0, h) \times (0, h)$, and directly applying the weighted trapezoidal rule leads to

$$\begin{aligned} \int_{I_{11}} \psi_\gamma(\mathbf{x}, \boldsymbol{\xi}) \cdot |\boldsymbol{\xi}|^{\gamma-(2+\alpha)} \, d\boldsymbol{\xi} \approx \frac{1}{4} \Big(&\lim_{\boldsymbol{\xi} \to \mathbf{0}} \psi_\gamma(\mathbf{x}, \boldsymbol{\xi}) + \psi_\gamma(\mathbf{x}, \boldsymbol{\xi}_{1,0}) \\ &+ \psi_\gamma(\mathbf{x}, \boldsymbol{\xi}_{0,1}) + \psi_\gamma(\mathbf{x}, \boldsymbol{\xi}_{1,1}) \Big) \int_{I_{11}} |\boldsymbol{\xi}|^{\gamma-(2+\alpha)} \, d\boldsymbol{\xi}, \end{aligned} \tag{4.8}$$

where we assume the limit exists.

To find the limit, we separate our discussion into two cases:

Case 1: For $\gamma \in (\alpha, 2)$, assuming that u is smooth enough, then the limit goes to zero, i.e.,

$$\lim_{\boldsymbol{\xi} \to \mathbf{0}} \psi_\gamma(\mathbf{x}, \boldsymbol{\xi}) = \lim_{\boldsymbol{\xi} \to \mathbf{0}} \psi_2(\mathbf{x}, \boldsymbol{\xi}) \cdot |\boldsymbol{\xi}|^{2-\gamma} = 0, \tag{4.9}$$

and thus the integral on I_{11} is approximated by

$$\begin{aligned}&\int_{I_{11}} \psi_\gamma(\mathbf{x},\boldsymbol{\xi})\cdot|\boldsymbol{\xi}|^{\gamma-(2+\alpha)}\,d\boldsymbol{\xi}\\ \approx\ &\frac{1}{4}\left(\psi_\gamma(\mathbf{x},\boldsymbol{\xi}_{1,0})+\psi_\gamma(\mathbf{x},\boldsymbol{\xi}_{0,1})+\psi_\gamma(\mathbf{x},\boldsymbol{\xi}_{1,1})\right)\int_{I_{11}}|\boldsymbol{\xi}|^{\gamma-(2+\alpha)}\,d\boldsymbol{\xi}.\end{aligned}\tag{4.10}$$

Case 2: For $\gamma = 2$, we approximate the limit as

$$\lim_{\boldsymbol{\xi}\to\mathbf{0}}\psi_2(\mathbf{x},\boldsymbol{\xi})=\psi_2(\mathbf{x},\boldsymbol{\xi}_{1,0})+\psi_2(\mathbf{x},\boldsymbol{\xi}_{0,1})-\psi_2(\mathbf{x},\boldsymbol{\xi}_{1,1}).$$

Following it, the integral on I_{11} is approximated by

$$\int_{I_{11}}\psi_2(\mathbf{x},\boldsymbol{\xi})\cdot|\boldsymbol{\xi}|^{-\alpha}\,d\boldsymbol{\xi}\approx\frac{1}{2}\left(\psi_2(\mathbf{x},\boldsymbol{\xi}_{1,0})+\psi_2(\mathbf{x},\boldsymbol{\xi}_{0,1})\right)\int_{I_{11}}|\boldsymbol{\xi}|^{-\alpha}\,d\boldsymbol{\xi}.\tag{4.11}$$

Combining (4.6), (4.7) and (4.10) or (4.11), we get, for $\gamma\in(1-\alpha,2)$,

$$\begin{aligned}&\sum_{i,j=1}^{N}\int_{I_{ij}}\psi_\gamma(\mathbf{x},\boldsymbol{\xi})\cdot|\boldsymbol{\xi}|^{\gamma-(2+\alpha)}\,d\boldsymbol{\xi}\\ \approx\ &\frac{1}{4}(\psi_\gamma(\mathbf{x},\boldsymbol{\xi}_{1,0})+\psi_\gamma(\mathbf{x},\boldsymbol{\xi}_{0,1})+\psi_\gamma(\mathbf{x},\boldsymbol{\xi}_{1,1}))\int_{I_{11}}|\boldsymbol{\xi}|^{\gamma-(2+\alpha)}\,d\boldsymbol{\xi}\\ &+\frac{1}{4}\sum_{\substack{i,j=1\\(i,j)\neq(1,1)}}^{N}\left(\psi_\gamma(\mathbf{x},\boldsymbol{\xi}_{i-1,j-1})+\psi_\gamma(\mathbf{x},\boldsymbol{\xi}_{i-1,j})+\psi_\gamma(\mathbf{x},\boldsymbol{\xi}_{i,j-1})+\psi_\gamma(\mathbf{x},\boldsymbol{\xi}_{i,j})\right)\int_{I_{ij}}|\boldsymbol{\xi}|^{\gamma-(2+\alpha)}\,d\boldsymbol{\xi}\\ =\ &\frac{1}{4}\sum_{\substack{i,j=0\\(i,j)\neq(0,0)}}^{N}\psi_\gamma(\mathbf{x},\boldsymbol{\xi}_{i,j})\int_{\widetilde{I}_{ij}}|\boldsymbol{\xi}|^{\gamma-(2+\alpha)}\,d\boldsymbol{\xi};\end{aligned}\tag{4.12}$$

for $\gamma = 2$,

$$
\begin{aligned}
&\sum_{i,j=1}^{N} \int_{I_{ij}} \psi_2(\mathbf{x}, \boldsymbol{\xi}) \cdot |\boldsymbol{\xi}|^{-\alpha} \, d\boldsymbol{\xi} \\
&\approx \frac{1}{2} \left(\psi_2(\mathbf{x}, \boldsymbol{\xi}_{1,0}) + \psi_2(\mathbf{x}, \boldsymbol{\xi}_{0,1}) \right) \int_{I_{11}} |\boldsymbol{\xi}|^{-\alpha} \, d\boldsymbol{\xi} \\
&+ \frac{1}{4} \sum_{\substack{i,j=1 \\ (i,j)\neq(1,1)}}^{N} \Big(\psi_2(\mathbf{x}, \boldsymbol{\xi}_{i-1,j-1}) + \psi_2(\mathbf{x}, \boldsymbol{\xi}_{i-1,j}) + \psi_2(\mathbf{x}, \boldsymbol{\xi}_{i,j-1}) + \psi_2(\mathbf{x}, \boldsymbol{\xi}_{i,j}) \Big) \int_{I_{ij}} |\boldsymbol{\xi}|^{-\alpha} \, d\boldsymbol{\xi} \\
&= \frac{1}{4} \sum_{\substack{i,j=0 \\ (i,j)\neq(1,0),(0,1),(1,1)}}^{N} \psi_2(\mathbf{x}, \boldsymbol{\xi}_{i,j}) \int_{\widetilde{I}_{ij}} |\boldsymbol{\xi}|^{-\alpha} \, d\boldsymbol{\xi} + \frac{1}{4} \psi_2(\mathbf{x}, \boldsymbol{\xi}_{1,1}) \int_{\widetilde{I}_{11} \setminus I_{11}} |\boldsymbol{\xi}|^{-\alpha} \, d\boldsymbol{\xi} \\
&+ \frac{1}{4} \Big(\psi_2(\mathbf{x}, \boldsymbol{\xi}_{1,0}) + \psi_2(\mathbf{x}, \boldsymbol{\xi}_{0,1}) \Big) \left(\int_{I_{12}} |\boldsymbol{\xi}|^{-\alpha} \, d\boldsymbol{\xi} + 2 \int_{I_{11}} |\boldsymbol{\xi}|^{-\alpha} \, d\boldsymbol{\xi} \right).
\end{aligned}
\tag{4.13}
$$

In fact, the left-hand side of (4.12) and (4.13) can be viewed as summing over the squares I_{ij}, while the right-hand side can be viewed as summing over the grid points $\boldsymbol{\xi}_{ij}$ in $(0, L]^2$.

Choosing a positive integer N_x (or N_y) which satisfies $a_x + N_x h$ (or $a_y + N_y h$) is the smallest number such that $a_x + N_x h \geq b_x$ (or $a_y + N_y h \geq b_y$). Define the grid points $x_i = a_x + ih$ for $0 \leq i \leq N_x$ and $y_j = a_y + jh$ for $0 \leq j \leq N_y$. Let $u_{i,j}$ be the numerical approximation of $u(x_i, y_i)$. Combining (4.4)–(4.7) with (4.12) or (4.13), the fully discretization of the 2D fractional Laplacian is given by

$$
\begin{aligned}
(-\Delta)_{h,\gamma}^{\alpha/2} u_{i,j} = -C_{2,\alpha} \Bigg(& a_{0,0}\, u_{i,j} + \sum_{m=1}^{i-1} a_{m,0} u_{i-m,j} + \sum_{m=1}^{N_x-1-i} a_{m,0} u_{i+m,j} \\
& + \sum_{n=1}^{j-1} a_{0,n} u_{i,j-n} + \sum_{n=1}^{N_y-1-j} a_{0,n} u_{i,j+n} \\
& + \sum_{m=1}^{i-1} \Big(\sum_{n=1}^{j-1} a_{m,n} u_{i-m,j-n} + \sum_{n=1}^{N_y-1-j} a_{m,n} u_{i-m,j+n} \Big) \\
& + \sum_{m=1}^{N_x-1-i} \Big(\sum_{n=1}^{j-1} a_{m,n} u_{i+m,j-n} + \sum_{n=1}^{N_y-1-j} a_{m,n} u_{i+m,j+n} \Big) \Bigg),
\end{aligned}
$$

The coefficient $a_{m,n}$ depends on the choice of the splitting parameters.

- If $\gamma \in (\alpha, 2)$,

$$a_{m,n} = \frac{1}{4|\boldsymbol{\xi}_{m,n}|^{\gamma}} \begin{cases} 2\int_{\widetilde{I}_{0n}} |\boldsymbol{\xi}|^{\gamma-(2+\alpha)}\, d\boldsymbol{\xi}, & \text{if} \quad m = 0,\ n = 1, \ldots, N, \\ 2\int_{\widetilde{I}_{m0}} |\boldsymbol{\xi}|^{\gamma-(2+\alpha)}\, d\boldsymbol{\xi}, & \text{if} \quad m = 1, \ldots, N,\ n = 0, \\ \int_{\widetilde{I}_{mn}} |\boldsymbol{\xi}|^{\gamma-(2+\alpha)}\, d\boldsymbol{\xi}, & \text{if} \quad m, n = 1, \ldots, N, \end{cases} \tag{4.14}$$

$$a_{0,0} = -2\left(\sum_{m=1}^{N} a_{m,0} + \sum_{n=1}^{N} a_{0,n}\right) - 4\sum_{m=1}^{N}\sum_{n=1}^{N} a_{m,n} - 4w_L.$$

- If $\gamma = 2$, the calculation of $a_{m,n}$ is the same as in (4.14), except

$$a_{m,n} = \frac{1}{4|\boldsymbol{\xi}_{m,n}|^{2}} \begin{cases} 4\int_{I_{11}} |\boldsymbol{\xi}|^{-\alpha}\, d\boldsymbol{\xi} + 2\int_{I_{12}} |\boldsymbol{\xi}|^{-\alpha}\, d\boldsymbol{\xi}, & \text{if} \quad m = 0,\ n = 1, \\ 4\int_{I_{11}} |\boldsymbol{\xi}|^{-\alpha}\, d\boldsymbol{\xi} + 2\int_{I_{21}} |\boldsymbol{\xi}|^{-\alpha}\, d\boldsymbol{\xi}, & \text{if} \quad m = 1,\ n = 0, \\ \int_{\widetilde{I}_{11}\setminus I_{11}} |\boldsymbol{\xi}|^{-\alpha}\, d\boldsymbol{\xi}, & \text{if} \quad m = 1,\ n = 1. \end{cases}$$

Denote the 2D vector

$$\mathbf{u}_{x,y} = (\mathbf{u}_{x,1}^T, \mathbf{u}_{x,2}^T, \ldots, \mathbf{u}_{x,N_y-1}^T)^T.$$

where $\mathbf{u}_{x,j} = (u_{1,j}, u_{2,j}, \ldots, u_{N_x-1,j})^T$ for $j = 1, 2, \ldots, N_y - 1$. The matrix representation of the 2D fractional Laplacian $(-\Delta)_{h,\gamma}^{\alpha/2} u(x, y)$ is $A^{(2)}\mathbf{u}_{x,y}$, that

$$\mathrm{A}^{(2)} = \begin{pmatrix} A_{x,0} & A_{x,1} & \ldots & A_{x,N_y-3} & A_{x,N_y-2} \\ A_{x,1} & A_{x,0} & A_{x,1} & \cdots & A_{x,N_y-3} \\ \vdots & \ddots & \ddots & \ddots & \vdots \\ A_{x,N_y-3} & \ldots & A_{x,1} & A_{x,0} & A_{x,1} \\ A_{x,N_y-2} & A_{x1,N_y-3} & \ldots & A_{x,1} & A_{x,0} \end{pmatrix}_{(N_x-1)(N_y-1)\times(N_x-1)(N_y-1)},$$

where

$$\mathrm{A}_{x,j} = \begin{pmatrix} a_{0,j} & a_{1,j} & \dots & a_{N_x-3,j} & a_{N_x-2,j} \\ a_{1,j} & a_{0,j} & a_{1,j} & \cdots & a_{N_x-3,j} \\ \vdots & \ddots & \ddots & \ddots & \vdots \\ a_{N_x-3,j} & \dots & a_{1,j} & a_{0,j} & a_{1,j} \\ a_{N_x-2,j} & a_{N_x-3,j} & \dots & a_{1,j} & a_{0,j} \end{pmatrix}_{(N_x-1)\times(N_x-1)},$$

for $j = 0, 1, \dots, N_y - 2$. Notice that $A^{(2)}$ is a block-Toeplitz–Toeplitz-block (BTTB) matrix, i.e., an (N_y-1)-by-(N_y-1) block-Toeplitz matrix with each block $A_{x,j}$ $(j = 0, 1, \dots, N_y-2)$ be an $(N_x - 1)$-by-$(N_x - 1)$ Toeplitz matrix [71].

4.1.2. Error Estimates. In this section, we provide error estimates of the weighted trapezoidal method in 2D. By using the weighted Montgomery's identity for the 1st and 2nd order differentiable functions of two variables, we will provide error analysis for functions with different smoothness conditions.

For notational convenience, we will omit $\mathbf{x}$, and simply use $\psi_\gamma(\boldsymbol{\xi}) := \psi_\gamma(\mathbf{x}, \boldsymbol{\xi})$ in the following. First, we will present the properties of ψ_γ in the following lemmas:

Lemma 4.1.1. *Let $\alpha \in (0, 2)$, $0 \le \xi, \eta < \infty$ and $(\xi, \eta) \neq (0, 0)$.*

(i). If $u \in C^{3,\alpha/2}(\mathbb{R}^2)$, the derivative $\partial_{m,n}\psi_2(\xi, \eta)$ exists, for $m, n = 0, 1, 2$. Furthermore, there is

$$|\partial_{m,n}\psi_2(\xi, \eta) + \partial_{n,m}\psi_2(\eta, \xi)| \le C|\boldsymbol{\xi}|^{\alpha/2+1-(m+n)},$$

for $m, n = 0, 1, 2$ but $m + n > 0$. If one of ξ, η equals zero, we further have

$$|\partial_{1,0}\psi_2(\xi, 0)| \le C\xi^{\alpha/2} \quad \text{and} \quad |\partial_{0,1}\psi_2(0, \eta)| \le C\eta^{\alpha/2}.$$

(ii). If $u \in C^{1,\alpha/2}(\mathbb{R}^2)$, the derivative $\partial_{m,n}\psi_\gamma(\xi,\eta)$ exists, for $m,n = 0,1$. Furthermore, there is

$$\left|\partial_{m,n}\psi_\gamma(\xi,\eta)\right| \le C|\xi|^{\alpha/2+1-\gamma-(m+n)}.$$

Proof. The proof is directly followed by Taylor theorem. □

First, we define the generalized Peano kernel, which will be used in the statement of Theorem 4.1.1.

Definition 4.1.1. *Define functions for all the non-negative integers $k, s = 0, 1, \dots,$*

$$P^{(k,s)}_{(a,b)(c,d)}(x,y) = \int_c^d \int_a^b w(\xi,\eta)\,\frac{(\xi-x)^k}{k!}\,\frac{(\eta-y)^s}{s!}\,d\xi\,d\eta. \tag{4.15}$$

Definition 4.1.2. *Define function space for function $f : [a,b]\times[c,d] \to \mathbb{R}$ and all non-negative integers $m,n = 0,1,\dots,$*

$$C^{m,n}([a,b]\times[c,d]) := \Big\{f : \partial_{p,q}f(s,t) \text{ is continuous for } 0 \le p \le m,\ 0 \le q \le n\Big\}.$$

Next, we reformulate the weighted Montgomery's identity in [52] specially by considering the cases for functions in $C^{1,1}([a,b]\times[c,d])$ and $C^{2,2}([a,b]\times[c,d])$. More general cases for functions in $C^{m,n}([a,b]\times[c,d])$ $(m,n = 0,1,\dots)$ can be found from Theorem 2.2 in [52].

Theorem 4.1.1. *([52, Theorem 2.2]) Let $w, f : [a,b]\times[c,d] \to \mathbb{R}$ be integrable functions.*

(i). If $f \in C^{1,1}([a,b]\times[c,d])$*, we have*

$$\begin{aligned}
&f(x,y)\int_a^b\int_c^d w(s,t)dt\,ds-\int_a^b\int_c^d w(s,t)f(s,t)dt\,ds\\
&=\int_a^b \widehat{P}^{(0,0)}(x,s,y)\partial_{1,0}f(s,y)\,ds+\int_c^d \widetilde{P}^{(0,0)}(x,y,t)\partial_{0,1}f(x,t)\,dt\\
&\quad-\int_a^b\int_c^d \overline{P}^{(0,0)}(x,s,y,t)\partial_{1,1}f(s,t)\,dt\,ds. \qquad (4.16)
\end{aligned}$$

(ii). If $f \in C^{2,2}([a,b]\times[c,d])$*, we have*

$$\begin{aligned}
&f(x,y)\int_a^b\int_b^d w(s,t)dt\,ds-\int_a^b\int_c^d w(s,t)f(s,t)dt\,ds\\
&=-\sum_{\substack{i=0\\(i,j)\neq(0,0)}}^{1}\sum_{j=0}^{1}\partial_{i,j}f(x,y)\,P^{(i,j)}_{(a,b)(c,d)}(x,y)\\
&\quad+\sum_{j=0}^{1}\int_a^b \widehat{P}^{(1,j)}(x,s,y)\partial_{2,j}f(s,y)\,ds+\sum_{i=0}^{1}\int_c^d \widetilde{P}^{(i,1)}(x,y,t)\partial_{i,2}f(x,t)\,dt\\
&\quad-\int_a^b\int_c^d \overline{P}^{(1,1)}(x,s,y,t)\partial_{2,2}f(s,t)\,dt\,ds, \qquad (4.17)
\end{aligned}$$

where $\widehat{P}^{(m,j)}(x,s,y)$*,* $\widetilde{P}^{(i,m)}(x,s,y)$ *and* $\overline{P}^{(m,m)}(x,s,y,t)$ *(*$m=0,1$*) are defined by*

$$\widehat{P}^{(m,j)}(x,s,y) := \begin{cases} P^{(m,j)}_{(a,s)(c,d)}(s,y), & a\le s\le x,\\ P^{(m,j)}_{(b,s)(c,d)}(s,y), & x< s\le b,\end{cases}$$

$$\widetilde{P}^{(i,m)}(x,y,t) := \begin{cases} P^{(m,1)}_{(a,b)(c,t)}(x,t), & c\le t\le y,\\ P^{(m,1)}_{(a,b)(d,t)}(x,t), & y< t\le d,\end{cases}$$

$$\overline{P}^{(m,m)}(x,s,y,t) := \begin{cases} P^{(m,m)}_{(a,s)(c,t)}(s,t), & a \le s \le x,\ c \le t \le y \\ P^{(m,m)}_{(b,s)(c,t)}(s,t), & x < s \le b,\ c \le t \le y \\ P^{(m,m)}_{(a,s)(d,t)}(s,t), & a \le s \le x,\ y \le t \le d \\ P^{(m,m)}_{(b,s)(d,t)}(s,t), & x < s \le b,\ y \le t \le d. \end{cases}$$

The following results are direct applications of Theorem 4.1.1, and will play important role in the error analysis of the 2D weighted trapezoidal method. First, we define a new function to short the lengthy notation in 2D. Some of its properties are also presented and will be used in the error analysis of the weighted trapezoidal method.

Definition 4.1.3. *Define functions for all the non-negative integers* $k, s = 0, 1, \ldots,$

$$\begin{aligned} &K^{(k,s)}_{(a,b)(c,d)}(x,y) \\ &= \int_c^y \Big(\int_a^x w(\xi,\eta) \frac{(a-\xi)^k}{k!} d\xi + \int_b^x w(\xi,\eta) \frac{(b-\xi)^k}{k!} d\xi \Big) \frac{(c-\eta)^s}{s!} d\eta \\ &+ \int_d^y \Big(\int_a^x w(\xi,\eta) \frac{(a-\xi)^k}{k!} d\xi + \int_b^x w(\xi,\eta) \frac{(b-\xi)^k}{k!} d\xi \Big) \frac{(d-\eta)^s}{s!} d\eta. \end{aligned} \tag{4.18}$$

By the Definitions 4.1.1 and 4.1.3, we can rewrite function $K^{(k,s)}_{(a,b)(c,d)}(x,y)$ in the form of the generalized Peano kernels, i.e.,

$$\begin{aligned} K^{(k,s)}_{(a,b)(c,d)}(x,y) = (-1)^{k+s} \Big(& P^{(k,s)}_{(a,x)(c,y)}(a,c) + P^{(k,s)}_{(a,x)(d,y)}(a,d) \\ & + P^{(k,s)}_{(b,x)(c,y)}(b,c) + P^{(k,s)}_{(b,x)(d,y)}(b,d) \Big). \end{aligned}$$

By definition 4.1.3, we have the following properties for function $K^{(k,s)}_{(a,b)(c,d)}(x,y)$. These properties will be used frequently in the proof of Theorems 4.1.2 and 4.1.3.

Property 4.1.1. *Assume* $a < b$, $c < d$, *and* k, s *are non-negative integers.*

(i). If $w(\xi,\eta) = w(\eta,\xi)$, *then we have the following commutative property:*

$$K^{(k,s)}_{(a,b)(c,d)}(x,y) = K^{(s,k)}_{(c,d)(a,b)}(y,x).$$

(ii). For any $h > 0$, if $a, c \geq h$ and $(a, c) \neq (h, h)$, specially by taking $w(\xi, \eta) = |\boldsymbol{\xi}|^{-\alpha}$ gives

$$\begin{aligned} &\left|\left(K^{(k,s)}_{(a-h,a)(c-h,c)} - K^{(k,s)}_{(a,a+h)(c-h,c)} - K^{(k,s)}_{(a-h,a)(c,c+h)} + K^{(k,s)}_{(a,a+h)(c,c+h)}\right)(a, c)\right| \\ &\leq Ch^{3+(k+s)}\left(\sqrt{(a-h)^2 + (c-h)^2}\right)^{-\alpha-1}. \end{aligned} \tag{4.19}$$

Proof. The proof of (i) follows directly by Definition 4.1.3.

To prove part (ii), we can follow the same line as the 1D case, we first construct an auxiliary function

$$G^{(k,s)}_{(a,c)}(x, y) = \int_y^c \int_x^a w(\xi, \eta)\,\frac{(a-\xi)^k}{k!}\,\frac{(c-\eta)^s}{s!}\,d\xi\,d\eta. \tag{4.20}$$

By Definition 4.1.3, we can rewrite the left-hand side of (4.19) as

$$\begin{aligned} &K^{(k,s)}_{(a-h,a)(c-h,c)}(a, c) - K^{(k,s)}_{(a,a+h)(c-h,c)}(a, c) \\ &-K^{(k,s)}_{(a-h,a)(c,c+h)}(a, c) + K^{(k,s)}_{(a,a+h)(c,c+h)}(a, c) \\ =\ &G^{(k,s)}_{(a,c)}(a-h, c-h) - G^{(k,s)}_{(a,c)}(a+h, c-h) \\ &-G^{(k,s)}_{(a,c)}(a-h, c+h) + G^{(k,s)}_{(a,c)}(a+h, c+h). \end{aligned}$$

Applying Taylor theorem at (a, c), we have

$$\begin{aligned} &\Big|G^{(k,s)}_{(a,c)}(a-h, c-h) - G^{(k,s)}_{(a,c)}(a+h, c-h) \\ &-G^{(k,s)}_{(a,c)}(a-h, c+h) + G^{(k,s)}_{(a,c)}(a+h, c+h)\Big| \\ &\leq Ch^{3+(k+s)}\left(\sqrt{(a-h)^2 + (c-h)^2}\right)^{-\alpha-1}, \end{aligned}$$

which directly leads the result. □

Lemma 4.1.2. *Let $w, f : [a, b] \times [c, d] \to \mathbb{R}$ be integrable functions.*

(i). If $f \in C^{1,1}([a,b]\times[c,d])$*, there is*

$$\begin{aligned}
&\int_c^d \int_a^b \left(4f(\xi,\eta) - [f(a,c)+f(a,d)+f(b,c)+f(b,d)]\right) w(\xi,\eta)\, d\xi\, d\eta \\
&= -\int_c^d \int_a^b K^{(0,0)}_{(a,b)(c,d)}(\xi,\eta)\, \partial_{1,1} f(\xi,\eta)\, d\xi\, d\eta \\
&+ \int_a^b \left(K^{(0,0)}_{(a,b)(c,d)}(\xi,d)\, \partial_{1,0} f(\xi,d) - K^{(0,0)}_{(a,b)(c,d)}(\xi,c)\, \partial_{1,0} f(\xi,c)\right) d\xi \\
&+ \int_c^d \left(K^{(0,0)}_{(a,b)(c,d)}(b,\eta)\, \partial_{0,1} f(b,\eta) - K^{(0,0)}_{(a,b)(c,d)}(a,\eta)\, \partial_{0,1} f(a,\eta)\right) d\eta.
\end{aligned}$$

(ii). If $f \in C^{2,2}([a,b]\times[c,d])$*, there is*

$$\begin{aligned}
&\int_c^d \int_a^b \left(4f(\xi,\eta) - [f(a,c)+f(a,d)+f(b,c)+f(b,d)]\right) w(\xi,\eta)\, d\xi\, d\eta \\
&= -\int_c^d \int_a^b K^{(1,1)}_{(a,b)(c,d)}(\xi,\eta) \partial_{2,2} f(\xi,\eta)\, d\xi\, d\eta \\
&+ \sum_{j=0}^{1} (-1)^{j+1} \int_a^b \left(K^{(1,j)}_{(a,b)(c,d)}(\xi,d) \partial_{2,j} f(\xi,d) - K^{(1,j)}_{(a,b)(c,d)}(\xi,c) \partial_{2,j} f(\xi,c)\right) d\xi \\
&+ \sum_{i=0}^{1} (-1)^{i+1} \int_c^d \left(K^{(i,1)}_{(a,b)(c,d)}(b,\eta) \partial_{i,2} f(b,\eta) - K^{(i,1)}_{(a,b)(c,d)}(a,\eta) \partial_{i,2} f(a,\eta)\right) d\eta \\
&- \sum_{\substack{j=0 \\ (i,j)\neq(0,0)}}^{1} \sum_{i=0}^{1} (-1)^{i+j} \left(K^{(i,j)}_{(a,b)(c,d)}(b,d) \partial_{i,j} f(b,d) - K^{(i,j)}_{(a,b)(c,d)}(b,c) \partial_{i,j} f(b,c)\right. \\
&\qquad\qquad \left. - K^{(i,j)}_{(a,b)(c,d)}(a,d) \partial_{i,j} f(a,d) + K^{(i,j)}_{(a,b)(c,d)}(a,c) \partial_{i,j} f(a,c)\right).
\end{aligned}$$

Proof. Applying Theorem 4.1.1 by plugging $(x,y) = (a,c), (a,d), (b,c), (b,d)$ into (4.16) or (4.17), and then summing together will directly lead the results. □

Since the following results will be used very often throughout the proof of Theorems 4.1.2 and 4.1.3, to avoid interrupting the proof of the main theorem, we present them as two Lemmas.

Lemma 4.1.3. *There is a positive constant* $C > 0$*, such that*

$$\int_{\varepsilon}^{L}\int_{\varepsilon}^{L} |\boldsymbol{\xi}|^{-\beta}\, d\xi\, d\eta \le C\varepsilon^{-\beta+2} \quad (\beta > 2) \quad \textit{and} \quad \int_{\varepsilon}^{L}\int_{0}^{\varepsilon} |\boldsymbol{\xi}|^{-\beta}\, d\xi\, d\eta \le C\varepsilon^{-\beta+2} \quad (\beta > 1),$$

where ε *is a positive number which satisfies* $\varepsilon \ll L$*.*

Proof. By using the fact that $|\boldsymbol{\xi}|^{-\beta} < \xi^{-\beta}$ and $|\boldsymbol{\xi}|^{-\beta} < \eta^{-\beta}$, we have

$$\int_{\varepsilon}^{L}\int_{\varepsilon}^{L} |\boldsymbol{\xi}|^{-\beta}\, d\xi\, d\eta \le \int_{\varepsilon}^{L} \xi^{-\beta/2}\, d\xi \cdot \int_{h}^{L} \eta^{-\beta/2}\, d\eta \le C\varepsilon^{-\beta+2}.$$

For the second inequality, we have

$$\int_{\varepsilon}^{L}\int_{0}^{\varepsilon} |\boldsymbol{\xi}|^{-\beta}\, d\xi\, d\eta \le C\varepsilon \int_{\varepsilon}^{L} \eta^{-\beta}\, d\eta \le C\varepsilon^{-\beta+2}.$$

□

Lemma 4.1.4 (2D Chebyshev integral inequality)**.** *Let* f *and* g *be positive functions on* $\Omega = [a, b] \times [c, d]$ *with the same monotonicity, i.e. for any given points* $(s_1, s_2), (t_1, t_2) \in \Omega$*, they satisfy* $[f(s_1, s_2) - f(t_1, t_2)] \cdot [g(s_1, s_2) - g(t_1, t_2)] \ge 0$*, then we have the following inequality*

$$\begin{aligned} &\int_{c}^{d}\int_{a}^{b} f(s_1, s_2)\, ds_1\, ds_2 \cdot \int_{c}^{d}\int_{a}^{b} g(s_1, s_2)\, ds_1\, ds_2 \\ \le\ & (b-a)(d-c)\int_{c}^{d}\int_{a}^{b} f \cdot g\, ds_1\, ds_2. \end{aligned}$$

Proof. Since the functions f and g have the same monotonicity on Ω, we have

$$\begin{aligned}
0 \quad &\leq \int_c^d \int_a^b \int_c^d \int_a^b [f(s_1,s_2) - f(t_1,t_2)] \cdot [g(s_1,s_2) - g(t_1,t_2)]\, dt_1\, dt_2\, ds_1\, ds_2 \\
&= \int_c^d \int_a^b \int_c^d \int_a^b \big[f(s_1,s_2)g(s_1,s_2) - f(s_1,s_2)g(t_1,t_2) \\
&\qquad\qquad + f(t_1,t_2)g(s_1,s_2) - f(t_1,t_2)g(t_1,t_2)\big]\, dt_1\, dt_2\, ds_1\, ds_2 \\
&= 2\big[(b-a)(d-c) \int_c^d \int_a^b f(s_1,s_2)g(s_1,s_2)\, ds_1\, ds_2 \\
&\quad - \int_c^d \int_a^b f(s_1,s_2)\, ds_1\, ds_2 \cdot \int_c^d \int_a^b g(s_1,s_2)\, ds_1\, ds_2\big].
\end{aligned}$$

Thus, we proved the lemma. □

Note that, the inequality for double integrals in Lemma 4.1.4 is a generalization of the Chebyshev integral inequality [41] for single integrals.

Then, we have the following error estimates on the weighted trapezoidal rule:

Theorem 4.1.2. *Suppose that $u \in C^{1,\alpha/2}(\mathbb{R}^2)$ has finite support on the domain Ω. Let $(-\Delta)^{\alpha/2}_{h,\gamma}$ be the finite difference approximation of the fractional Laplacian. For all $\gamma \in (\alpha, 2]$, there is*

$$\|(-\Delta)^{\alpha/2}u(\mathbf{x}) - (-\Delta)^{\alpha/2}_{h,\gamma}u(\mathbf{x})\|_{L_\infty(\Omega)} \leq Ch^{1-\alpha/2}, \qquad \text{for } \alpha \in (0,2) \tag{4.21}$$

with C a positive constant depending on α and γ.

Proof. Define the error function

$$e^h_{\alpha,\gamma}(\mathbf{x}) = (-\Delta)^{\alpha/2}u(\mathbf{x}) - (-\Delta)^{\alpha/2}_{h,\gamma}u(\mathbf{x}).$$

For $\gamma \in (\alpha, 2)$, from (4.4), (4.6) and (4.12), we obtain

$$\begin{aligned}
& e^h_{\alpha,\gamma}(\mathbf{x}) \\
&= -C_{2,\alpha}\Big\{ \int_0^h \int_0^h \left(\psi_\gamma(\xi,\eta) - \frac{1}{4}\Big[\psi_\gamma(h,0) + \psi_\gamma(0,h) + \psi_\gamma(h,h)\Big]\right) |\boldsymbol{\xi}|^{\gamma-(2+\alpha)}\, d\xi\, d\eta \\
&\qquad + \frac{1}{4} \sum_{\substack{j=1 \\ (i,j)\neq(1,1)}}^{N} \sum_{i=1}^{N} \int_{\eta_{j-1}}^{\eta_j} \int_{\xi_{i-1}}^{\xi_i} \left(4\psi_\gamma(\xi,\eta) - \sum_{s=j-1}^{j} \sum_{k=i-1}^{i} \psi_\gamma(\xi_k, \eta_s)\right) |\boldsymbol{\xi}|^{\gamma-(2+\alpha)}\, d\xi\, d\eta \Big\} \\
&= -C_{2,\alpha}(I + II). \qquad (4.22)
\end{aligned}$$

For term I, by triangle inequality and Lemma 4.1.1 (ii) for $m = n = 0$, it's easy to show that

$$\begin{aligned}
I \ \le\ & \int_0^h \int_0^h \Big|\psi_\gamma(\xi,\eta)\Big| \cdot |\boldsymbol{\xi}|^{\gamma-(2+\alpha)}\, d\xi\, d\eta \\
& + \frac{1}{4}\Big|\psi_\gamma(h,0) + \psi_\gamma(0,h) + \psi_\gamma(h,h)\Big| \int_0^h \int_0^h |\boldsymbol{\xi}|^{\gamma-(2+\alpha)}\, d\xi\, d\eta \\
\le\ & C\left(\int_0^h \int_0^h |\boldsymbol{\xi}|^{-\alpha/2-1}\, d\xi\, d\eta + h^{\alpha/2-\gamma+1} \cdot h^{\gamma-\alpha}\right) \le Ch^{1-\alpha/2}.
\end{aligned}$$

For term II, by taking $w(\boldsymbol{\xi}) = |\boldsymbol{\xi}|^{\gamma-(2+\alpha)}$ in Lemma 4.1.2 (i), we obtain

$$II = \frac{1}{4}(II_1 + II_2),$$

where

$$\begin{aligned}
II_1 &= -\sum_{\substack{j=1 \\ (i,j)\neq(1,1)}}^{N} \sum_{i=1}^{N} \int_{\eta_{j-1}}^{\eta_j} \int_{\xi_{i-1}}^{\xi_i} K^{(0,0)}_{I_i I_j}(\xi,\eta) \cdot \partial_{1,1}\psi_\gamma(\xi,\eta)\, d\xi\, d\eta, \\
II_2 &= \sum_{\substack{j=1 \\ (i,j)\neq(1,1)}}^{N} \sum_{i=1}^{N} \Big\{ \int_{\xi_{i-1}}^{\xi_i} \Big(K^{(0,0)}_{I_i I_j}(\xi,\eta_j)\partial_{1,0}\psi_\gamma(\xi,\eta_j) - K^{(0,0)}_{I_i I_j}(\xi,\eta_{j-1})\partial_{1,0}\psi_\gamma(\xi,\eta_{j-1})\Big)\, d\xi \\
&\qquad + \int_{\eta_{j-1}}^{\eta_j} \Big(K^{(0,0)}_{I_i I_j}(\xi_i,\eta)\partial_{0,1}\psi_\gamma(\xi_i,\eta) - K^{(0,0)}_{I_i I_j}(\xi_{i-1},\eta)\partial_{0,1}\psi_\gamma(\xi_{i-1},\eta)\Big)\, d\eta \Big\}.
\end{aligned}$$

In the above equation, we introduce the following notation to short the lengthy notation:

$$K_{I_iI_j}^{(m,m)}(\xi,\eta) := K_{(\xi_{i-1},\xi_i)(\xi_{j-1},\xi_j)}^{(m,m)}(\xi,\eta) \quad \text{for} \quad m = 0, 1. \tag{4.23}$$

For term II_1, by the definition of $K_{I_iI_j}^{(0,0)}(\xi,\eta)$ in (4.1.3) and Lemma 4.1.1 (ii), we have

$$|II_1| \leq C \sum_{j=1}^{N} \sum_{\substack{i=1 \\ (i,j)\neq(1,1)}}^{N} \left(\int_{\eta_{j-1}}^{\eta_j} \int_{\xi_{i-1}}^{\xi_i} |\boldsymbol{\xi}|^{\gamma-(2+\alpha)}\, d\xi\, d\eta \right) \cdot \left(\int_{\eta_{j-1}}^{\eta_j} \int_{\xi_{i-1}}^{\xi_i} |\boldsymbol{\xi}|^{\alpha/2-\gamma-1}\, d\xi\, d\eta. \right)$$

By further applying the Chebyshev integral inequality in 2D as in Lemma 4.1.4, we get

$$|II_1| \leq Ch^2 \sum_{j=1}^{N} \sum_{\substack{i=1 \\ (i,j)\neq(1,1)}}^{N} \int_{\eta_{j-1}}^{\eta_j} \int_{\xi_{i-1}}^{\xi_i} |\boldsymbol{\xi}|^{-\alpha/2-3}\, d\xi\, d\eta. \tag{4.24}$$

Rewrite the summation as

$$\begin{aligned} &\sum_{j=1}^{N} \sum_{\substack{i=1 \\ (i,j)\neq(1,1)}}^{N} \int_{\eta_{j-1}}^{\eta_j} \int_{\xi_{i-1}}^{\xi_i} |\boldsymbol{\xi}|^{-\alpha/2-3}\, d\xi\, d\eta \\ &= \int_h^L \int_0^h |\boldsymbol{\xi}|^{-\alpha/2-3}\, d\boldsymbol{\xi} + \int_h^L \int_h^L |\boldsymbol{\xi}|^{-\alpha/2-3}\, d\boldsymbol{\xi} + \int_0^h \int_h^L |\boldsymbol{\xi}|^{-\alpha/2-3}\, d\boldsymbol{\xi}. \end{aligned} \tag{4.25}$$

Combining (4.24) and (4.25) and then applying Lemma 4.1.3, we get

$$|II_1| \leq Ch^2 \left(\int_h^L \int_0^h |\boldsymbol{\xi}|^{-\alpha/2-3}\, d\xi\, d\eta + \int_h^L \int_h^L |\boldsymbol{\xi}|^{-\alpha/2-3}\, d\xi\, d\eta \right) \leq Ch^{1-\alpha/2}.$$

For term II_2, by using Property 4.1.1 (i), we first rewrite it as

$$\begin{aligned} II_2 = \sum_{j=1}^{N} \sum_{\substack{i=1 \\ (i,j)\neq(1,1)}}^{N} \Big\{ &\int_{\xi_{i-1}}^{\xi_i} K_{I_iI_j}^{(0,0)}(\xi,\eta_j) \left(\partial_{1,0}\psi_\gamma(\xi,\eta_j) + \partial_{0,1}\psi_\gamma(\xi_j,\xi) \right) d\xi \\ &- \int_{\xi_{i-1}}^{\xi_i} K_{I_iI_j}^{(0,0)}(\xi,\eta_{j-1}) \left(\partial_{1,0}\psi_\gamma(\xi,\eta_{j-1}) + \partial_{0,1}\psi_\gamma(\xi_{j-1},\xi) \right) d\xi \Big\}. \end{aligned}$$

Then, applying Lemma 4.1.1 (ii), we get

$$\begin{aligned}
|II_2| &\leq Ch \sum_{\substack{j=1 \\ (i,j)\neq(1,1)}}^{N} \sum_{i=1}^{N} \Big(\int_{\xi_{i-1}}^{\xi_i} \Big(\sqrt{\xi^2+\eta_j^2}\Big)^{\gamma-(2+\alpha)} d\xi \Big) \Big(\int_{\xi_{i-1}}^{\xi_i} \Big(\sqrt{\xi^2+\eta_j^2}\Big)^{\alpha/2-\gamma} d\xi \Big) \\
&\leq Ch^{-1} \sum_{\substack{j=1 \\ (i,j)\neq(1,1)}}^{N} \sum_{i=1}^{N} \Big(\int_{\eta_{j-1}}^{\eta_j} \int_{\xi_{i-1}}^{\xi_i} |\boldsymbol{\xi}|^{\gamma-(2+\alpha)} d\xi\, d\eta \Big) \Big(\int_{\eta_{j-1}}^{\eta_j} \int_{\xi_{i-1}}^{\xi_i} |\boldsymbol{\xi}|^{\alpha/2-\gamma} d\xi\, d\eta \Big).
\end{aligned}$$

Further by applying the 2D Chebyshev inequality in Lemma 4.1.4, we have

$$|II_2| \leq Ch \sum_{\substack{j=1 \\ (i,j)\neq(1,1)}}^{N} \sum_{i=1}^{N} \int_{\eta_{j-1}}^{\eta_j} \int_{\xi_{i-1}}^{\xi_i} |\boldsymbol{\xi}|^{-\alpha/2-2} d\xi_1\, d\xi_2 \leq Ch^{1-\alpha/2}.$$

Combining the estimation of terms I and II, we show that for any $u \in C^{1,\alpha/2}(\mathbb{R}^2)$ and $\gamma \in (\alpha, 2)$,

$$\|e(\mathbf{x})\| = \|(-\Delta)^{\alpha/2}u(\mathbf{x}) - (-\Delta)_{h,\gamma}^{\alpha/2}u(\mathbf{x})\|_{L_\infty(\Omega)} \leq Ch^{1-\alpha/2}.$$

For $\gamma = 2$, the error function is slightly different from (4.22), which is

$$\begin{aligned}
&e_{\alpha,2}^h(\mathbf{x}) \\
&= -C_{2,\alpha} \Big\{ \int_0^h \int_0^h \Big(\psi_2(\xi,\eta) - \frac{1}{2}\left[\psi_2(h,0) + \psi_2(0,h)\right] \Big) \cdot |\boldsymbol{\xi}|^{-\alpha}\, d\xi\, d\eta \\
&\quad + \frac{1}{4} \sum_{\substack{j=1 \\ (i,j)\neq(1,1)}}^{N} \sum_{i=1}^{N} \int_{\eta_{j-1}}^{\eta_j} \int_{\xi_{i-1}}^{\xi_i} \Big(4\psi_2(\xi,\eta) - \sum_{s=j-1}^{j} \sum_{k=i-1}^{i} \psi_2(\xi_k,\eta_s) \Big) |\boldsymbol{\xi}|^{-\alpha}\, d\xi\, d\eta \Big\} \\
&= -C_{2,\alpha}(\widetilde{I} + \widetilde{II}).
\end{aligned} \tag{4.26}$$

The estimation of this error function can follow the same line as in proving (4.22) by simply taking $\gamma = 2$. Therefore, we proved that for all $\gamma \in (\alpha, 2]$,

$$\|e(\mathbf{x})\| = \|(-\Delta)^{\alpha/2}u(\mathbf{x}) - (-\Delta)_{h,\gamma}^{\alpha/2}u(\mathbf{x})\|_{L_\infty(\Omega)} \leq Ch^{1-\alpha/2}.$$

□

Theorem 4.1.3. *Suppose that $u \in C^{3,\alpha/2}(\mathbb{R}^2)$ has finite support on the domain Ω. Let $(-\Delta)^{\alpha/2}_{2,h}$ be the finite difference approximation of the fractional Laplacian. If the splitting parameter is chosen as $\gamma = 2$, there is*

$$\|(-\Delta)^{\alpha/2}u(\mathbf{x}) - (-\Delta)^{\alpha/2}_{h,\gamma}u(\mathbf{x})\|_{L_\infty(\Omega)} \le Ch^2, \qquad \text{for } \alpha \in (0,2) \tag{4.27}$$

with C a positive constant depending on α.

Proof. We start from the local truncation error in (4.26).

For term $\widetilde{I}$, by Talylor theorem and Lemma 4.1.1 (i), for any $(\xi,\eta) \in [0,h] \times [0,h]$, there is a positive constant C, such that

$$\begin{aligned}&\left|\psi_2(\xi,\eta) - \frac{1}{2}[\psi_2(h,0) + \psi_2(0,h)]\right| \\ &\le Ch \max_{(\xi,\eta)\in[0,h]^2} \{|\partial_{1,0}\psi_2(\xi,0)|, |\partial_{0,1}\psi_2(0,\eta)|\} \\ &\le Ch^{1+\alpha/2}.\end{aligned}$$

Therefore, we have

$$|\widetilde{I}| \le Ch^{1+\alpha/2}\int_0^h\int_0^h |\boldsymbol{\xi}|^{-\alpha}\, d\xi\, d\eta \le Ch^{3-\alpha/2}.$$

For term $\widetilde{II}$, by Lemma 4.1.2 (ii), we obtain

$$\widetilde{II} = \frac{1}{4}\left(II_1 + II_2 + II_3\right),$$

where II_1, II_2, II_3 are defined as

$$II_1 = \sum_{\substack{j=1 \\ (i,j)\neq(1,1)}}^{N}\sum_{i=1}^{N}\int_{\eta_{j-1}}^{\eta_j}\int_{\xi_{i-1}}^{\xi_i} K^{(1,1)}_{I_iI_j}(\xi,\eta)\cdot\partial_{2,2}\psi_2(\xi,\eta)\, d\xi\, d\eta,$$

$$II_2 = \sum_{\substack{j=1 \\ (i,j)\neq(1,1)}}^{N} \sum_{i=1}^{N} \sum_{k=0}^{1} (-1)^k \Big\{ \int_{\xi_{i-1}}^{\xi_i} \Big(K_{I_iI_j}^{(1,k)}(\xi,\eta_j)\partial_{2,k}\psi_2(\xi,\eta_j) - K_{I_iI_j}^{(1,k)}(\xi,\eta_{j-1})\partial_{2,k}\psi_2(\xi,\eta_{j-1}) \Big)\, d\xi + \int_{\eta_{j-1}}^{\eta_j} \Big(K_{I_iI_j}^{(k,1)}(\xi_i,\eta)\partial_{k,2}\psi_2(\xi_i,\eta) - K_{I_iI_j}^{(k,1)}(\xi_{i-1},\eta)\partial_{k,2}\psi_2(\xi_{i-1},\eta) \Big)\, d\eta \Big\}, \quad (4.28)$$

$$II_3 = \sum_{\substack{j=1 \\ (i,j)\neq(1,1)}}^{N} \sum_{i=1}^{N} \sum_{\substack{s=0 \\ (k,s)\neq(0,0)}}^{1} \sum_{k=0}^{1} \Big(K_{I_iI_j}^{(k,s)}(\xi_i,\eta_j)\partial_{k,s}f(\xi_i,\eta_j) - K_{I_iI_j}^{(k,s)}(\xi_i,\eta_{j-1})\partial_{k,s}f(\xi_i,\eta_{j-1}) - K_{I_iI_j}^{(k,s)}(\xi_{i-1},\eta_j)\partial_{k,s}f(\xi_{i-1},\eta_j) + K_{I_iI_j}^{(k,s)}(\xi_{i-1},\eta_{j-1})\partial_{k,s}f(\xi_{i-1},\eta_{j-1}) \Big). \quad (4.29)$$

Next, we will focus on the estimation of term II_j ($j = 1, 2, 3$). To apply Lemma 4.1.1, each term II_j should be firstly rewritten symmetrically.

For term II_1, in order to apply Lemma 4.1.1 (i), we have to first rewrite it symmetrically

$$II_1 = \frac{1}{2} \sum_{\substack{j=1 \\ (i,j)\neq(1,1)}}^{N} \sum_{i=1}^{N} \int_{\eta_{j-1}}^{\eta_j} \int_{\xi_{i-1}}^{\xi_i} K_{I_iI_j}^{(1,1)}(\xi,\eta) \cdot \big(\partial_{2,2}\psi_2(\xi,\eta) + \partial_{2,2}\psi_2(\eta,\xi)\big)\, d\xi\, d\eta. \quad (4.30)$$

From the definition of $K_{I_iI_j}^{(1,1)}(\xi,\eta)$, it is easy to check that

$$|K_{I_iI_j}^{(1,1)}(\xi,\eta)| \le Ch^2 \int_{\eta_{j-1}}^{\eta_j} \int_{\xi_{i-1}}^{\xi_i} |\boldsymbol{\xi}|^{-\alpha}\, d\xi\, d\eta, \quad (4.31)$$

From Lemma 4.1.1 (i) by taking $s = k = 2$, we have

$$|\partial_{2,2}\psi_2(\xi,\eta) + \partial_{2,2}\psi_2(\eta,\xi)| \le C \int_{\eta_{j-1}}^{\eta_j} \int_{\xi_{i-1}}^{\xi_i} |\boldsymbol{\xi}|^{\alpha/2-3}\, d\xi\, d\eta. \quad (4.32)$$

Combining (4.30), (4.31) and (4.32), the term $II_{2,2}$ can be bounded as follows

$$|II_1| \quad \leq Ch^2 \sum_{\substack{j=1 \\ (i,j)\neq(1,1)}}^{N} \sum_{i=1}^{N} \left(\int_{\eta_{j-1}}^{\eta_j} \int_{\xi_{i-1}}^{\xi_i} |\boldsymbol{\xi}|^{-\alpha} \, d\xi \, d\eta \right) \cdot \left(\int_{\eta_{j-1}}^{\eta_j} \int_{\xi_{i-1}}^{\xi_i} |\boldsymbol{\xi}|^{\alpha/2-3} \, d\xi \, d\eta \right).$$

By further applying the 2D extension of the Chebyshev integral inequality as in Lemma 4.1.4, we get

$$|II_1| \leq Ch^4 \sum_{\substack{j=1 \\ (i,j)\neq(1,1)}}^{N} \sum_{i=1}^{N} \int_{\eta_{j-1}}^{\eta_j} \int_{\xi_{i-1}}^{\xi_i} |\boldsymbol{\xi}|^{-\alpha/2-3} \, d\xi \, d\eta. \tag{4.33}$$

Rewrite the summation as

$$\begin{aligned} &\sum_{\substack{j=1 \\ (i,j)\neq(1,1)}}^{N} \sum_{i=1}^{N} \int_{\eta_{j-1}}^{\eta_j} \int_{\xi_{i-1}}^{\xi_i} |\boldsymbol{\xi}|^{-\alpha/2-3} \, d\xi \, d\eta \\ &= \int_h^L \int_0^h |\boldsymbol{\xi}|^{-\alpha/2-3} \, d\boldsymbol{\xi} + \int_h^L \int_h^L |\boldsymbol{\xi}|^{-\alpha/2-3} \, d\boldsymbol{\xi} + \int_0^h \int_h^L |\boldsymbol{\xi}|^{-\alpha/2-3} \, d\boldsymbol{\xi}. \end{aligned} \tag{4.34}$$

Combining (4.33) and (4.34), and then applying Lemma 4.1.3, we get

$$|II_1| \leq Ch^4 \left(\int_h^L \int_0^h |\boldsymbol{\xi}|^{-\alpha/2-3} \, d\boldsymbol{\xi} + \int_h^L \int_h^L |\boldsymbol{\xi}|^{-\alpha/2-3} \, d\boldsymbol{\xi} \right) \leq Ch^{3-\alpha/2}.$$

For term II_2, in order to apply Lemma 4.1.1 (i), we have to first rewrite it symmetrically. By exchanging the position of i and j in the summation of the second integral, we have

$$\begin{aligned} II_2 = \sum_{\substack{j=1 \\ (i,j)\neq(1,1)}}^{N} \sum_{i=1}^{N} \sum_{k=0}^{1} (-1)^k \Big\{ \int_{\xi_{i-1}}^{\xi_i} \Big(& K_{I_i I_j}^{(1,k)}(\xi, \eta_j) \partial_{2,k} \psi_2(\xi, \eta_j) \\ & - K_{I_i I_j}^{(1,k)}(\xi, \eta_{j-1}) \partial_{2,k} \psi_2(\xi, \eta_{j-1}) \Big) \, d\xi \\ + \int_{\eta_{i-1}}^{\eta_i} \Big(K_{I_j I_i}^{(k,1)}(\xi_j, \eta) \partial_{k,2} \psi_2(\xi_j, \eta) & - K_{I_j I_i}^{(k,1)}(\xi_{j-1}, \eta) \partial_{k,2} \psi_2(\xi_{j-1}, \eta) \Big) \, d\eta \Big\} \end{aligned}$$

Notice that $\xi_i = \eta_i$ and $K^{(1,k)}_{I_i I_j}(\xi, \eta) = K^{(k,1)}_{I_j I_i}(\eta, \xi)$ for $k = 0, 1$, we can further rewrite it as

$$\begin{aligned} II_2 = \sum_{\substack{j=1 \\ (i,j)\neq(1,1)}}^{N} \sum_{i=1}^{N} \sum_{k=0}^{1} (-1)^k \bigg\{ &\int_{\xi_{i-1}}^{\xi_i} K^{(1,k)}_{I_i I_j}(\xi, \eta_j) \big(\partial_{2,k}\psi_2(\xi, \eta_j) + \partial_{k,2}\psi_2(\eta_j, \xi)\big)\, d\xi \\ &- \int_{\xi_{i-1}}^{\xi_i} K^{(1,k)}_{I_i I_j}(\xi, \eta_{j-1}) \big(\partial_{2,k}\psi_2(\xi, \eta_{j-1}) + \partial_{k,2}\psi_2(\eta_{j-1}, \xi)\big)\, d\xi \bigg\} \end{aligned}$$

By definition, it is easy to show that for $\xi \in [\xi_{i-1}, \xi_i]$ and $k = 0, 1$,

$$\begin{aligned} \left| K^{(1,k)}_{I_i I_j}(\xi, \eta_{j-1}) \right| &= \bigg| \int_{\eta_j}^{\eta_{j-1}} \int_{\xi_{i-1}}^{\xi} (\xi - \widehat{\xi}) \frac{(\eta_{j-1} - \widehat{\eta})^k}{k!} |\widehat{\boldsymbol{\xi}}|^{-\alpha} d\widehat{\xi}\, d\widehat{\eta} \\ &\quad + \int_{\eta_j}^{\eta_{j-1}} \int_{\xi_i}^{\xi} (\xi - \widehat{\xi}) \frac{(\eta_{j-1} - \widehat{\eta})^k}{k!} |\widehat{\boldsymbol{\xi}}|^{-\alpha} d\widehat{\xi}\, d\widehat{\eta} \bigg| \\ &\leq C h^{1+k} \int_{\eta_{j-1}}^{\eta_j} \int_{\xi_{i-1}}^{\xi_i} |\widehat{\boldsymbol{\xi}}|^{-\alpha} d\widehat{\boldsymbol{\xi}}. \end{aligned}$$

By Lemma 4.1.1 (i) for $k = 0, 1$, we have

$$h^2 \left| \partial_{2,k}\psi_2(\xi, \eta) + \partial_{k,2}\psi_2(\eta, \xi) \right| \leq C \int_{\eta_{j-1}}^{\eta_j} \int_{\xi_{i-1}}^{\xi_i} |\boldsymbol{\xi}|^{\alpha/2-1-k}\, d\boldsymbol{\xi}. \tag{4.35}$$

Then, term II_2 is bounded by

$$\begin{aligned} |II_2| \quad &\leq \sum_{\substack{j=1 \\ (i,j)\neq(1,1)}}^{N} \sum_{j=1}^{N} \sum_{k=0}^{1} C h^k \left(\int_{\eta_{j-1}}^{\eta_j} \int_{\xi_{i-1}}^{\xi_i} |\boldsymbol{\xi}|^{-\alpha}\, d\boldsymbol{\xi} \right) \left(\int_{\eta_{j-1}}^{\eta_j} \int_{\xi_{i-1}}^{\xi_i} |\boldsymbol{\xi}|^{\alpha/2-1-k}\, d\boldsymbol{\xi} \right) \\ &\leq C \sum_{k=0}^{1} h^{k+2} \sum_{\substack{j=1 \\ (i,j)\neq(1,1)}}^{N} \sum_{j=1}^{N} \int_{\eta_{j-1}}^{\eta_j} \int_{\xi_{i-1}}^{\xi_i} |\boldsymbol{\xi}|^{-\alpha/2-1-k}\, d\boldsymbol{\xi}. \end{aligned} \tag{4.36}$$

Following the same line as the estimation of the summation in term II_1, we get

$$\begin{aligned} & h^{k+2}\sum_{\substack{j=1\\(i,j)\neq(1,1)}}^{N}\sum_{j=1}^{N}\int_{\eta_{j-1}}^{\eta_j}\int_{\xi_{i-1}}^{\xi_i}|\boldsymbol{\xi}|^{-\alpha/2-1-k}\,d\boldsymbol{\xi} \\ \leq\ & Ch^{k+2}\left(\int_h^L\int_0^h|\boldsymbol{\xi}|^{-(\alpha/2+1+k)}\,d\boldsymbol{\xi}+\int_h^L\int_h^L|\boldsymbol{\xi}|^{-(\alpha/2+1+k)}\,d\boldsymbol{\xi}\right). \end{aligned} \tag{4.37}$$

By Lemma 4.1.3, since $\alpha/2+1+k\in(1,2)$ for $k=0$ and $\alpha/2+1+k\in(2,3)$ for $k=1$, we have

$$\int_h^L\int_0^h|\boldsymbol{\xi}|^{-(\alpha/2+1+k)}\,d\boldsymbol{\xi}\leq Ch^{1-\alpha/2-k}\quad\text{for}\quad k=0,1 \tag{4.38}$$

and

$$\int_h^L\int_h^L|\boldsymbol{\xi}|^{-(\alpha/2+1+k)}\,d\boldsymbol{\xi}\leq\begin{cases}C & \text{if}\quad k=0\\ Ch^{-\alpha/2} & \text{if}\quad k=1.\end{cases} \tag{4.39}$$

Finally, combining (4.36)–(4.39), term II_2 is bounded by

$$|II_2|\leq C\left(h^2+h^3\cdot h^{-\alpha/2}\right)\leq Ch^2. \tag{4.40}$$

For term II_3, first by letting $\widetilde{j}=j-1$ and $\widetilde{i}=i-1$, and noticing that $\xi_i=\eta_i$, we have

$$\begin{aligned} II_3 = \sum_{\substack{s=0\\(k,s)\neq(0,0)}}^{1}\sum_{k=0}^{1}\Bigg\{ & \sum_{\substack{j=1\\(i,j)\neq(1,1)}}^{N}\sum_{i=1}^{N}K_{I_iI_j}^{(k,s)}(\xi_i,\xi_j)\partial_{k,s}f(\xi_i,\xi_j)-\sum_{\substack{j=0\\(i,j)\neq(1,0)}}^{N-1}\sum_{i=1}^{N}K_{I_iI_{j+1}}^{(k,s)}(\xi_i,\xi_j)\partial_{k,s}f(\xi_i,\xi_j) \\ & -\sum_{\substack{j=1\\(i,j)\neq(0,1)}}^{N}\sum_{i=0}^{N-1}K_{I_{i+1}I_j}^{(s,k)}(\xi_i,\xi_j)\partial_{s,k}f(\xi_i,\xi_j)+\sum_{\substack{i=0\\(i,j)\neq(0,0)}}^{N-1}\sum_{j=0}^{N-1}K_{I_{i+1}I_{j+1}}^{(s,k)}(\xi_i,\xi_j)\partial_{s,k}f(\xi_i,\xi_j)\Bigg\}. \end{aligned} \tag{4.41}$$

We further rewrite it by

$$
\begin{aligned}
II_3^{k,s} = & \sum_{\substack{j=1 \\ (i,j)\neq(1,1)}}^{N-1} \sum_{i=1}^{N-1} \left(K_{I_iI_j}^{(k,s)} - K_{I_iI_{j+1}}^{(k,s)} - K_{I_{i+1}I_j}^{(k,s)} + K_{I_{i+1}I_{j+1}}^{(k,s)} \right) (\xi_i, \xi_j) \cdot \partial_{k,s} f(\xi_i, \xi_j) \\
& + \sum_{i=1}^{N-1} \left(K_{I_iI_N}^{(k,s)}(\xi_i, \xi_N) - K_{I_{i+1}I_N}^{(k,s)}(\xi_i, \xi_N) \right) \partial_{k,s} f(\xi_i, \xi_N) \\
& + \sum_{j=1}^{N-1} \left(K_{I_NI_j}^{(k,s)}(\xi_N, \xi_j) - K_{I_NI_{j+1}}^{(k,s)}(\xi_N, \xi_j) \right) \partial_{k,s} f(\xi_N, \xi_j) \\
& + \sum_{i=2}^{N-1} \left(K_{I_{i+1}I_1}^{(k,s)}(\xi_i, \xi_0) - K_{I_iI_1}^{(k,s)}(\xi_i, \xi_0) \right) \partial_{k,s} f(\xi_i, \xi_0) \\
& + \sum_{j=2}^{N-1} \left(K_{I_1I_{j+1}}^{(k,s)}(\xi_0, \xi_j) - K_{I_1I_j}^{(k,s)}(\xi_0, \xi_j) \right) \partial_{k,s} f(\xi_0, \xi_j) \\
& + K_{I_NI_N}^{(k,s)}(\xi_N, \xi_N) \partial_{k,s} f(\xi_N, \xi_N) + K_{I_NI_1}^{(k,s)}(\xi_N, \xi_0) \partial_{k,s} f(\xi_N, \xi_0) \\
& + K_{I_1I_N}^{(k,s)}(\xi_0, \xi_N) \partial_{k,s} f(\xi_0, \xi_N) + K_{I_2I_1}^{(k,s)}(\xi_1, \xi_0) \partial_{k,s} f(\xi_1, \xi_0) \\
& + K_{I_1I_2}^{(k,s)}(\xi_0, \xi_1) \partial_{k,s} f(\xi_0, \xi_1) + K_{I_2I_2}^{(k,s)}(\xi_1, \xi_1) \partial_{k,s} f(\xi_1, \xi_1) \\
& - K_{I_1I_2}^{(k,s)}(\xi_1, \xi_1) \partial_{k,s} f(\xi_1, \xi_1) - K_{I_2I_1}^{(k,s)}(\xi_1, \xi_1) \partial_{k,s} f(\xi_1, \xi_1). \\
= & \, II_{3,1}^{(k,s)} + II_{3,2}^{(k,s)} + II_{3,3}^{(k,s)}. \qquad (4.42)
\end{aligned}
$$

To avoid introducing too many notations, we still keep using $II_{3,i}^{(k,s)}$ $(i = 1, 2, 3)$, but they represent the sum of the double summation, single summation and no summation terms in (4.42), respectively. Next we will focus on the estimations of the summations

$\sum_{\substack{s=0 \\ (k,s)\neq(0,0)}}^{1}\sum_{k=0}^{1} II_{3,i}^{(k,s)}$ $(i = 1, 2, 3)$. First, by exchanging the positions of k, s and i, j, there is

$$\begin{aligned}
&\sum_{\substack{k=0 \\ (k,s)\neq(0,0)}}^{1}\sum_{s=0}^{1} II_{3,1}^{(k,s)} \\
={}& \sum_{\substack{k=0 \\ (k,s)\neq(0,0)}}^{1}\sum_{s=0}^{1}\sum_{\substack{j=1 \\ (i,j)\neq(1,1)}}^{N-1}\sum_{i=1}^{N-1} \left(K_{I_iI_j}^{(k,s)} - K_{I_iI_{j+1}}^{(k,s)} - K_{I_{i+1}I_j}^{(k,s)} + K_{I_{i+1}I_{j+1}}^{(k,s)}\right)(\xi_i,\xi_j)\partial_{k,s}f(\xi_i,\xi_j) \\
={}& \sum_{\substack{k=0 \\ (k,s)\neq(0,0)}}^{1}\sum_{s=0}^{1}\sum_{\substack{j=1 \\ (i,j)\neq(1,1)}}^{N-1}\sum_{i=1}^{N-1} \left(K_{I_jI_i}^{(s,k)} - K_{I_jI_{i+1}}^{(s,k)} - K_{I_{j+1}I_i}^{(s,k)} + K_{I_{j+1}I_{i+1}}^{(s,k)}\right)(\xi_j,\xi_i)\partial_{s,k}f(\xi_j,\xi_i).
\end{aligned} \tag{4.43}$$

By Property 4.1.1 (i), it is clear that

$$\begin{aligned}
&\left(K_{I_iI_j}^{(k,s)} - K_{I_iI_{j+1}}^{(k,s)} - K_{I_{i+1}I_j}^{(k,s)} + K_{I_{i+1}I_{j+1}}^{(k,s)}\right)(\xi_i,\xi_j) \\
={}& \left(K_{I_jI_i}^{(s,k)} - K_{I_jI_{i+1}}^{(s,k)} - K_{I_{j+1}I_i}^{(s,k)} + K_{I_{j+1}I_{i+1}}^{(s,k)}\right)(\xi_j,\xi_i).
\end{aligned} \tag{4.44}$$

Combining (4.44) and (4.45), we can rewrite the summation symmetrically as

$$\begin{aligned}
&\sum_{\substack{k=0 \\ (k,s)\neq(0,0)}}^{1}\sum_{s=0}^{1} II_{3,1}^{(k,s)} \\
={}& \frac{1}{2}\sum_{\substack{k=0 \\ (k,s)\neq(0,0)}}^{1}\sum_{s=0}^{1}\sum_{\substack{j=1 \\ (i,j)\neq(1,1)}}^{N-1}\sum_{i=1}^{N-1} \left(K_{I_iI_j}^{(k,s)} - K_{I_iI_{j+1}}^{(k,s)} - K_{I_{i+1}I_j}^{(k,s)} + K_{I_{i+1}I_{j+1}}^{(k,s)}\right)(\xi_j,\xi_i) \\
&\cdot\left(\partial_{k,s}f(\xi_i,\xi_j) + \partial_{s,k}f(\xi_j,\xi_i)\right).
\end{aligned} \tag{4.45}$$

By using Property 4.1.1 (ii) with $w(\boldsymbol{\xi}) = |\boldsymbol{\xi}|^{-\alpha}$, we get

$$\left|\left(K_{I_iI_j}^{(k,s)} - K_{I_iI_{j+1}}^{(k,s)} - K_{I_{i+1}I_j}^{(k,s)} + K_{I_{i+1}I_{j+1}}^{(k,s)}\right)(\xi_j,\xi_i)\right| \leq Ch^{3+(k+s)}|\boldsymbol{\xi}_{i-1,j-1}|^{-\alpha-1}. \tag{4.46}$$

Further, by triangle inequality and Lemma 4.1.1 (i), we have

$$\begin{aligned}
&\sum_{\substack{k=0 \\ (k,s)\neq(0,0)}}^{1}\sum_{s=0}^{1} II_{3,1}^{(k,s)} \\
&\leq \frac{1}{2}\sum_{\substack{k=0 \\ (k,s)\neq(0,0)}}^{1}\sum_{s=0}^{1}\sum_{\substack{j=1 \\ (i,j)\neq(1,1)}}^{N-1}\sum_{i=1}^{N-1}\left|\left(K_{I_iI_j}^{(k,s)} - K_{I_iI_{j+1}}^{(k,s)} - K_{I_{i+1}I_j}^{(k,s)} + K_{I_{i+1}I_{j+1}}^{(k,s)}\right)(\xi_j,\xi_i)\right| \\
&\qquad\qquad\qquad\qquad\cdot\left|\partial_{k,s}f(\xi_i,\xi_j) + \partial_{s,k}f(\xi_j,\xi_i)\right| \\
&\leq Ch^{-1+(k+s)}\sum_{\substack{k=0 \\ (k,s)\neq(0,0)}}^{1}\sum_{s=0}^{1}\sum_{\substack{j=1 \\ (i,j)\neq(1,1)}}^{N-1}\sum_{i=1}^{N-1}\int_{\xi_{i-1}}^{\xi_i}\int_{\xi_{j-1}}^{\xi_j}|\boldsymbol{\xi}|^{-\alpha-1}d\boldsymbol{\xi}\cdot\int_{\xi_{i-1}}^{\xi_i}\int_{\xi_{j-1}}^{\xi_j}|\boldsymbol{\xi}|^{\alpha/2+1-(k+s)}d\boldsymbol{\xi}.
\end{aligned} \tag{4.47}$$

Finally, by Lemma 4.1.4, we have

$$\begin{aligned}
&\sum_{\substack{k=0 \\ (k,s)\neq(0,0)}}^{1}\sum_{s=0}^{1} II_{3,1}^{(k,s)} \\
&\leq Ch^{1+(k+s)}\sum_{\substack{k=0 \\ (k,s)\neq(0,0)}}^{1}\sum_{s=0}^{1}\sum_{\substack{j=1 \\ (i,j)\neq(1,1)}}^{N-1}\sum_{i=1}^{N-1}\int_{\xi_{i-1}}^{\xi_i}\int_{\xi_{j-1}}^{\xi_j}|\boldsymbol{\xi}|^{-\alpha/2-(k+s)}d\boldsymbol{\xi} \\
&\leq Ch^{1+(k+s)}\sum_{\substack{k=0 \\ (k,s)\neq(0,0)}}^{1}\sum_{s=0}^{1}\left(\int_0^h\int_h^L|\boldsymbol{\xi}|^{-\alpha/2-(k+s)}d\boldsymbol{\xi} + \int_h^L\int_h^L|\boldsymbol{\xi}|^{-\alpha/2-(k+s)}d\boldsymbol{\xi}\right) \\
&\leq Ch^2.
\end{aligned} \tag{4.48}$$

Next, we focus on term $II_{3,2}^{(k,s)}$, i.e.

$$\begin{aligned} II_{3,2}^{(k,s)} &= \sum_{i=1}^{N-1}\left(K_{I_iI_N}^{(k,s)}-K_{I_{i+1}I_N}^{(k,s)}\right)(\xi_i,\xi_N)\partial_{k,s}f(\xi_i,\xi_N)\\ &\quad+\sum_{j=1}^{N-1}\left(K_{I_NI_j}^{(k,s)}-K_{I_NI_{j+1}}^{(k,s)}\right)(\xi_N,\xi_j)\partial_{k,s}f(\xi_N,\xi_j)\\ &\quad+\sum_{i=2}^{N-1}\left(K_{I_{i+1}I_1}^{(k,s)}-K_{I_iI_1}^{(k,s)}\right)(\xi_i,\xi_0)\partial_{k,s}f(\xi_i,\xi_0)\\ &\quad+\sum_{j=2}^{N-1}\left(K_{I_1I_{j+1}}^{(k,s)}-K_{I_1I_j}^{(k,s)}\right)(\xi_0,\xi_j)\partial_{k,s}f(\xi_0,\xi_j). \end{aligned} \tag{4.49}$$

Following the same line as the estimation of term $II_{3,1}^{(k,s)}$ by exchanging k, s and using Property 4.1.1 (i), we get

$$\begin{aligned} &\sum_{\substack{k=0\\(k,s)\neq(0,0)}}^{1}\sum_{s=0}^{1} II_{3,2}^{(k,s)}\\ &=\sum_{\substack{k=0\\(k,s)\neq(0,0)}}^{1}\sum_{s=0}^{1}\Big\{\sum_{i=1}^{N-1}\left(K_{I_iI_N}^{(k,s)}-K_{I_{i+1}I_N}^{(k,s)}\right)(\xi_i,\xi_N)\left(\partial_{k,s}f(\xi_i,\xi_N)+\partial_{s,k}f(\xi_N,\xi_i)\right)\\ &\qquad+\sum_{i=2}^{N-1}\left(K_{I_{i+1}I_1}^{(k,s)}-K_{I_iI_1}^{(k,s)}\right)(\xi_i,\xi_0)\left(\partial_{k,s}f(\xi_i,\xi_0)+\partial_{s,k}f(\xi_0,\xi_i)\right)\Big\} \end{aligned}$$

Finally, following the same line as the estimation of term $II_{3,1}^{k,s}$, we have

$$\begin{aligned} &\Big|\sum_{\substack{k=0\\(k,s)\neq(0,0)}}^{1}\sum_{s=0}^{1} II_{3,2}^{(k,s)}\Big|\\ &\leq Ch^{1+(k+s)}\sum_{\substack{k=0\\(k,s)\neq(0,0)}}^{1}\sum_{s=0}^{1}\Big\{\sum_{i=1}^{N-1}\int_{\xi_{N-1}}^{\xi_N}\int_{\xi_{i-1}}^{\xi_i}|\boldsymbol{\xi}|^{-\alpha/2-(k+s)}d\boldsymbol{\xi}+\sum_{i=2}^{N-1}\int_{\xi_0}^{\xi_1}\int_{\xi_{i-1}}^{\xi_i}|\boldsymbol{\xi}|^{-\alpha/2-(k+s)}d\boldsymbol{\xi}\Big\}\\ &\leq Ch^{1+(k+s)}\sum_{\substack{k=0\\(k,s)\neq(0,0)}}^{1}\sum_{s=0}^{1}\left(\int_{L-h}^{L}\int_{0}^{L}|\boldsymbol{\xi}|^{-\alpha/2-(k+s)}d\boldsymbol{\xi}+\int_0^h\int_h^L|\boldsymbol{\xi}|^{-\alpha/2-(k+s)}d\boldsymbol{\xi}\right)\\ &\leq Ch^{3-\alpha/2}. \end{aligned} \tag{4.50}$$

For term $II_{3,3}^{(k,s)}$, we have

$$\begin{aligned} II_{3,2}^{(k,s)} &= K_{I_N I_N}^{(k,s)}(\xi_N,\xi_N)\partial_{k,s}f(\xi_N,\xi_N) + K_{I_N I_1}^{(k,s)}(\xi_N,\xi_0)\partial_{k,s}f(\xi_N,\xi_0) \\ &\quad + K_{I_1 I_N}^{(k,s)}(\xi_0,\xi_N)\partial_{k,s}f(\xi_0,\xi_N) + K_{I_2 I_1}^{(k,s)}(\xi_1,\xi_0)\partial_{k,s}f(\xi_1,\xi_0) \\ &\quad + K_{I_1 I_2}^{(k,s)}(\xi_0,\xi_1)\partial_{k,s}f(\xi_0,\xi_1) + K_{I_2 I_2}^{(k,s)}(\xi_1,\xi_1)\partial_{k,s}f(\xi_1,\xi_1) \\ &\quad - K_{I_1 I_2}^{(k,s)}(\xi_1,\xi_1)\partial_{k,s}f(\xi_1,\xi_1) - K_{I_2 I_1}^{(k,s)}(\xi_1,\xi_1)\partial_{k,s}f(\xi_1,\xi_1). \end{aligned}$$

Then by Definition 4.1.3 and Lemma 4.1.1 (ii), it follows directly that

$$\Big|\sum_{\substack{k=0 \\ (k,s)\neq(0,0)}}^{1}\sum_{s=0}^{1} II_{3,3}^{(k,s)}\Big| \le Ch^2. \tag{4.51}$$

Finally, combining the estimations of terms $\widetilde{I}$ and $\widetilde{II}$, it shows that for any $u \in C^{3,\alpha/2}(\mathbb{R}^2)$, specially by taking $\gamma = 2$ gives,

$$\|e_{\alpha,\gamma}^{h}(\mathbf{x})\| = \|(-\Delta)_2^{\alpha/2}u(\mathbf{x}) - (-\Delta)_{h,\gamma}^{\alpha/2}u(\mathbf{x})\|_{L_\infty(\Omega)} \le Ch^2.$$

□

4.1.3. Numerical Experiments. Consider the functions of the form

$$u(x,y) = \begin{cases} [(1-x^2)(1-y^2)]^{s+\alpha/2}, & \text{if} \quad (x,y)\in\Omega \\ 0, & \text{otherwise,} \end{cases} \tag{4.52}$$

which is in $C^{s,\alpha/2}(\mathbb{R}^2)$ and has compact support on $\Omega = \{\mathbf{x}\in\mathbb{R}^2 : |x| < 1 \text{ and } |y| < 1\}$. To test the analytical results in Theorem 4.1.2 and 4.1.3, we specifically consider the cases by taking $s = 1$ and $s = 3$. Since the fractional Laplacian of this type of function can not be computed analytically, we will use the numerical solution by taking $\gamma = 2$ and $N = 8192$ as the exact solution for all the following numerical tests.

Example 4.3.1. For $s = 1$, i.e. $u \in C^{1,\alpha/2}(\mathbb{R}^2)$, as shown in Theorem 4.1.2 that for $u \in C^{1,\alpha/2}(\mathbb{R}^2)$, the accuracy of the weighted trapezoidal method in l_∞-norm is $O(h^{1-\alpha/2})$ for small mesh size h, and it is independent of the splitting parameter $\gamma \in (\alpha, 2]$. Figure 4.1 presents the numerical errors by taking $\gamma = 1 + \alpha/2$ and 2.

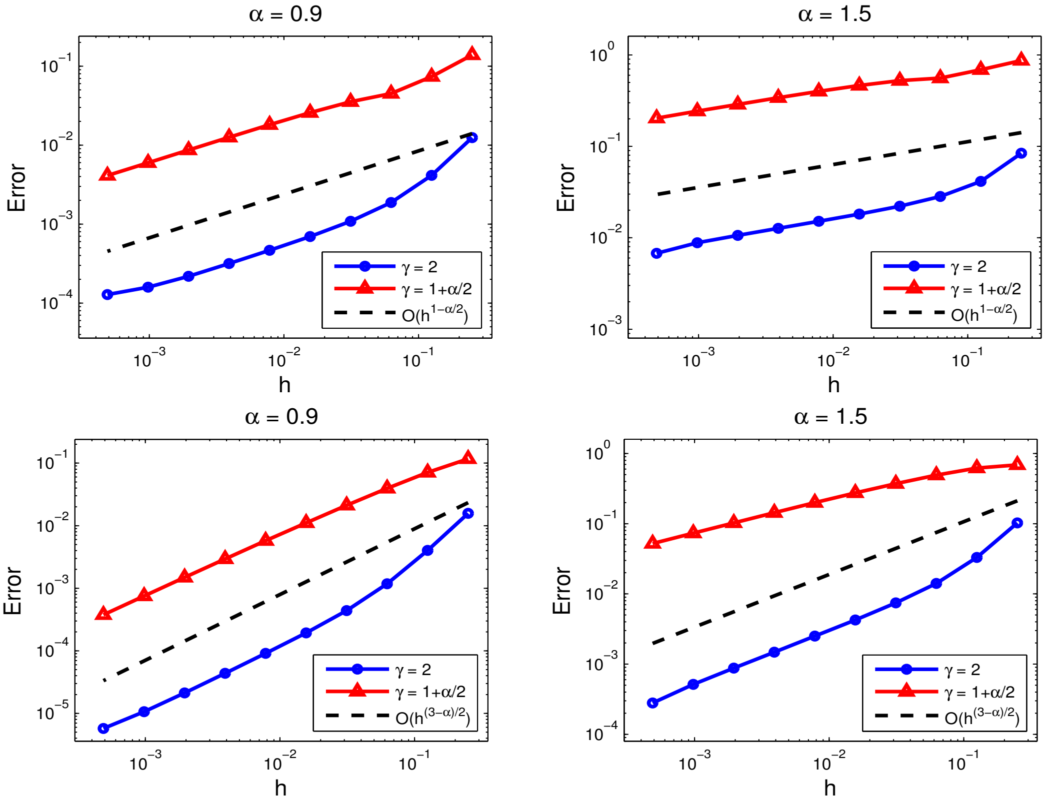

Figure 4.1. Numerical errors of the weighted trapezoidal method for $\gamma = 2$ and $1 + \alpha/2$ for u defined in (3.47) with $s = 1$. The errors are defined in l_∞-norm (top row) or l_2-norm (bottom row).

Additionally, Figure 4.1 (bottom) compares the numerical errors in l_2-norm for different choice of γ. It shows that choosing the parameter $\gamma = 2$ leads to a better convergence rate in l_2-norm.

Example 4.3.2. For $s = 3$, i.e. $u \in C^{3,\alpha/2}(\mathbb{R}^2)$, as shown in Theorem 4.1.3, only by taking $\gamma = 2$, the accuracy of the weighted trapezoidal method in l_∞-norm is $O(h^2)$.

Table 4.1. Numerical errors of the fractional Laplacian for $u \in C^{3,\alpha/2}(\mathbb{R}^2)$.

α \ h	1/16	1/32	1/64	1/128	1/256	1/512	1/1024
0.2	1.062E-4	2.679E-5	6.716E-6	1.679E-6	4.187E-7	1.0344E-7	2.463E-8
	c.r.	1.9852	1.9959	1.9998	2.0039	2.0170	2.0704
1	4.594E-3	1.154E-3	2.892E-4	7.231E-5	1.803E-5	4.457E-6	1.061E-6
	c.r.	1.9928	1.9970	1.9995	2.0035	2.0167	2.0702
1.9	6.695E-2	1.653E-2	4.383E-3	1.176E-3	3.011E-4	7.489E-5	1.780E-5
	c.r.	2.0183	1.9146	1.8983	1.9654	2.0075	2.0726

Table 4.1 presents numerical errors $\|(-\Delta)^{\alpha/2}u - (-\Delta)_h^{\alpha/2}u\|_{l_\infty(\Omega)}$ and convergence rates of the weighted trapezoidal method for various α by taking u in (3.47) with $s = 3$, where the splitting parameters are taken to be $\gamma = 2$. It shows that the convergence rates of the weighted trapezoidal method is $O(h^2)$ for any $\alpha \in (0, 2)$, which confirms our analytical results in Theorem 4.1.3. In addition, we find that for the same mesh size h, the larger the parameter α, the bigger the numerical errors.

4.2. HIGHER DIMENSIONAL CASE

4.2.1. Numerical Scheme. The weighted trapezoidal method can be extended to any d dimension for $d \geq 2$. In the following, we will first use the general d-dimensional notation to derive the weighted trapezoidal method. Then, to show it clear, we will explicitly provide the numerical scheme in 3D. As proved in 1D and 2D cases, for smooth enough functions $u \in C^{3,\alpha/2}(\mathbb{R}^d)$ $(d = 1, 2)$ with $\gamma = 2$, the weighted trapezoidal method has second order accuracy. We conjecture that the same analytical result will hold in any d-dimension $(d \geq 1)$ and will justify it numerically.

Consider the d-dimensional fractional Laplacian in (1.2). By changing of variables, i.e. letting $\xi_i = |x_i - \hat{x}_i|$ $(i = 1, 2, \ldots, d)$ and defining vector $\boldsymbol{\xi} = (\xi_1, \ldots, \xi_d)$, the fractional Laplacian can be further written as

$$(-\Delta)^{\alpha/2} u(\mathbf{x}) = C_{d,\alpha} \int_{(\mathbb{R}^+)^d} \Big(\sum_{\mathbf{v} \in I^{\text{ver}}_{(\mathbf{x},\boldsymbol{\xi})}} u(\mathbf{v}) - 2^d u(\mathbf{x}) \Big) \cdot |\boldsymbol{\xi}|^{-(d+\alpha)} \, d\boldsymbol{\xi}, \tag{4.53}$$

where $(\mathbb{R}^+)^d := \underbrace{(0,\infty) \times (0,\infty) \times \cdots \times (0,\infty)}_{d-\text{th intervals}}$, and we define the d-dimensional cube $I_{(\mathbf{x},\boldsymbol{\xi})}$ which is centered at $\mathbf{x}$ with radius $\xi_1, \ldots, \xi_d$ in each direction. For any d-dimensional cube, we define its vertex set as

$$I^{\text{ver}} := \Big\{ \mathbf{v} \in \mathbb{R}^d \,|\, \mathbf{v} \text{ is the vertex of cube } I \Big\}. \tag{4.54}$$

Following the same line as 2D case, we introduce a function $\psi_\gamma(\mathbf{x}, \boldsymbol{\xi})$ and define it as

$$\psi_\gamma(\mathbf{x}, \boldsymbol{\xi}) := \Big(\sum_{\mathbf{v} \in I^{\text{ver}}_{(\mathbf{x},\boldsymbol{\xi})}} u(\mathbf{v}) - 2^d u(\mathbf{x}) \Big) \cdot |\boldsymbol{\xi}|^{-\gamma}.$$

Consider a d-dimensional cube $\Omega = (a_1, b_1) \times \cdots \times (a_d, b_d)$ and let $L = \max\{b_1 - a_1, \ldots, b_d - a_d\}$. For functions u which is compactly supported on Ω, we can further rewrite the fractional Laplacian by splitting it into two parts,

$$\begin{aligned} (-\Delta)^{\alpha/2} u(\mathbf{x}) \;\; = \;\; & -C_{d,\alpha} \Big(\int_{(0,L)^d} \psi_0(\mathbf{x}, \boldsymbol{\xi}) \cdot |\boldsymbol{\xi}|^{-(d+\alpha)} \, d\boldsymbol{\xi} \\ & + \int_{(\mathbb{R}^+)^d \setminus (0,L)^d} \psi_0(\mathbf{x}, \boldsymbol{\xi}) \cdot |\boldsymbol{\xi}|^{-(d+\alpha)} \, d\boldsymbol{\xi} \Big). \end{aligned} \tag{4.55}$$

The second integral in (4.55) can be found exactly. Precisely, for any $\mathbf{x} \in \Omega$, if $\boldsymbol{\xi} \in (\mathbb{R}^+)^d \backslash (0, L)^d$, then all the vertices $\mathbf{v}$ of the d-dimensional cube $I_{(\mathbf{x},\boldsymbol{\xi})}$ satisfy $\mathbf{v} \in \mathbb{R}^d \backslash \Omega$, and thus $u(\mathbf{v}) = 0$. Hence, we obtain

$$\begin{aligned} &\int_{(\mathbb{R}^+)^d \backslash (0,L)^d} \psi_0(\mathbf{x}, \boldsymbol{\xi}) \cdot |\boldsymbol{\xi}|^{-(d+\alpha)} \, d\boldsymbol{\xi} \\ &\quad = -2^d u(\mathbf{x}) \int_{(\mathbb{R}^+)^d \backslash (0,L)^d} |\boldsymbol{\xi}|^{-(d+\alpha)} \, d\boldsymbol{\xi} = -2^d \, w_L \, u(\mathbf{x}), \end{aligned} \tag{4.56}$$

where the coefficient w_L is defined by

$$w_L = \int_{(\mathbb{R}^+)^d \backslash (0,L)^d} |\boldsymbol{\xi}|^{-(d+\alpha)} \, d\boldsymbol{\xi}.$$

Next, we apply the weighted trapezoidal method to approximate the first integral in (4.55). We adopt the uniform mesh by choosing a positive integer N, and define the mesh size $h = L/N$. Denote grid points $\xi_{1,i} = \cdots = \xi_{d,i} = ih$, for $0 \le i \le N$, evidently $\xi_{1,N} = \cdots = \xi_{d,N} = L$. For brevity, we introduce the notation $\boldsymbol{\xi}_{\mathbf{n}} := (\xi_{1,n_1}, \xi_{2,n_2}, \ldots, \xi_{d,n_d})$, where $\mathbf{n} := (n_1, \ldots, n_d)$ for $0 \le n_i \le N$ $(i = 1, \ldots, d)$.

We formulate the first integral in (4.55) as the weighted integral of ψ_γ, with $|\boldsymbol{\xi}|^{\gamma-(d+\alpha)}$ representing the weight function,

$$\int_{(0,L)^d} \psi_0(\mathbf{x}, \boldsymbol{\xi}) \cdot |\boldsymbol{\xi}|^{-(d+\alpha)} \, d\boldsymbol{\xi} = \sum_{\boldsymbol{\tau} \in \{1,2,\ldots,N\}^d} \int_{I_{\boldsymbol{\tau}}} \psi_\gamma(\mathbf{x}, \boldsymbol{\xi}) \cdot |\boldsymbol{\xi}|^{\gamma-(d+\alpha)} \, d\boldsymbol{\xi}, \tag{4.57}$$

where $\boldsymbol{\tau} := (\tau_1, \ldots, \tau_d)$ is a d-dimensional vector belongs to the set

$$\{1, 2, \ldots, N\}^d := \left\{ \boldsymbol{\tau} \in (\mathbb{N}^+)^d \,\middle|\, 1 \le \tau_i \le N, \; i = 1, \ldots, d \right\},$$

and the d-dimensional interval $I_{\boldsymbol{\tau}}$ is defined by

$$I_{\boldsymbol{\tau}} := [(\tau_1 - 1)h, \tau_1 h] \times \cdots \times [(\tau_d - 1)h, \tau_d h].$$

For $\boldsymbol{\tau} \neq (1, 1, \ldots, 1)$, we apply the weighted trapezoidal method to approximate the integrals in (4.57)

$$\int_{I_\tau} \psi_\gamma(\mathbf{x}, \boldsymbol{\xi}) \cdot |\boldsymbol{\xi}|^{\gamma-(d+\alpha)}\, d\boldsymbol{\xi} \approx \frac{1}{2^d}\left(\sum_{\widehat{\boldsymbol{\xi}} \in I_\tau^{\text{ver}}} \psi_\gamma(\mathbf{x}, \widehat{\boldsymbol{\xi}})\right) \cdot \int_{I_\tau} |\boldsymbol{\xi}|^{\gamma-(d+\alpha)}\, d\boldsymbol{\xi}, \tag{4.58}$$

where $I_{\boldsymbol{\tau}}^{\text{ver}}$ includes all the vertices of $I_{\boldsymbol{\tau}}$.

For $\boldsymbol{\tau} = (1, 1, \ldots, 1)$, there is $I_{\mathbf{1}} = (0, h) \times \cdots \times (0, h)$, directly applying the weighted trapezoidal rule as in (4.58) will lead to

$$\int_{I_1} \psi_\gamma(\mathbf{x}, \boldsymbol{\xi}) \cdot |\boldsymbol{\xi}|^{\gamma-(d+\alpha)}\, d\boldsymbol{\xi} \approx \frac{1}{2^d}\left(\sum_{\widehat{\boldsymbol{\xi}} \in I_{\mathbf{1}}^{\text{ver}}} \psi_\gamma(\mathbf{x}, \widehat{\boldsymbol{\xi}})\right) \cdot \int_{I_1} |\boldsymbol{\xi}|^{\gamma-(d+\alpha)}\, d\boldsymbol{\xi}. \tag{4.59}$$

However, since $\mathbf{0}$ is one of the vertex of $I_{\mathbf{1}}$, it arises a problem when evaluating $\psi_\gamma(\mathbf{x}, \mathbf{0})$, which is singular at $\mathbf{0}$. For this reason, we consider $\psi_\gamma(\mathbf{x}, \mathbf{0})$ as a limit $\lim_{\boldsymbol{\xi} \to \mathbf{0}} \psi_\gamma(\mathbf{x}, \boldsymbol{\xi})$. Next, we focus on the approximation of this limit.

- For $\gamma \in (\alpha, 2)$, the limit equals zero, thus the integral $I_{\mathbf{1}}$ is approximated by

$$\int_{I_1} \psi_\gamma(\mathbf{x}, \boldsymbol{\xi}) \cdot |\boldsymbol{\xi}|^{\gamma-(d+\alpha)}\, d\boldsymbol{\xi} \approx \frac{1}{2^d} \sum_{\widehat{\boldsymbol{\xi}} \in I_{\mathbf{1}}^{\text{ver}} \backslash \{\mathbf{0}\}} \psi_\gamma(\mathbf{x}, \widehat{\boldsymbol{\xi}}) \int_{I_1} |\boldsymbol{\xi}|^{\gamma-(d+\alpha)}\, d\boldsymbol{\xi}. \tag{4.60}$$

- For $\gamma = 2$, we approximate the limit by

$$\lim_{\boldsymbol{\xi} \to \mathbf{0}} \psi_2(\mathbf{x}, \boldsymbol{\xi}) = \left(\frac{2^d}{d} - 1\right) \sum_{i=1}^{d} \psi_2(\mathbf{x}, h\mathbf{e}_i) - \sum_{\substack{\widehat{\boldsymbol{\xi}} \in I_{\mathbf{1}}^{\text{ver}} \backslash \{\mathbf{0}\} \\ \widehat{\boldsymbol{\xi}} \neq h\mathbf{e}_1, \ldots, h\mathbf{e}_d}} \psi_2(\mathbf{x}, \widehat{\boldsymbol{\xi}}),$$

and it follows that the integral $I_{\mathbf{1}}$ can be approximated by

$$\begin{aligned}
&\int_{I_{\mathbf{1}}} \psi_2(\mathbf{x}, \boldsymbol{\xi}) \cdot |\boldsymbol{\xi}|^{2-(d+\alpha)}\, d\boldsymbol{\xi} \approx \frac{1}{2^d}\bigg\{ \left(\frac{2^d}{d} - 1\right) \sum_{i=1}^{d} \psi_2(\mathbf{x}, h\mathbf{e}_i) \\
&- \sum_{\substack{\widehat{\boldsymbol{\xi}} \in I_{\mathbf{1}}^{\text{ver}} \setminus \{\mathbf{0}\} \\ \widehat{\boldsymbol{\xi}} \neq h\mathbf{e}_1, \ldots, h\mathbf{e}_d}} \psi_2(\mathbf{x}, \widehat{\boldsymbol{\xi}}) + \sum_{\widehat{\boldsymbol{\xi}} \in I_{\mathbf{1}}^{\text{ver}} \setminus \{\mathbf{0}\}} \psi_\gamma(\mathbf{x}, \widehat{\boldsymbol{\xi}}) \bigg\} \int_{I_{\mathbf{1}}} |\boldsymbol{\xi}|^{2-(d+\alpha)}\, d\boldsymbol{\xi} \\
&= \frac{1}{d} \sum_{i=1}^{d} \psi_2(\mathbf{x}, h\mathbf{e}_i) \int_{I_{\mathbf{1}}} |\boldsymbol{\xi}|^{2-(d+\alpha)}\, d\boldsymbol{\xi} \qquad (4.61)
\end{aligned}$$

Define $I_{(\widehat{\boldsymbol{\xi}}, h)}$ be the d-dimensional cube centered at $\widehat{\boldsymbol{\xi}}$ with radius h in each direction. Therefore, summing $\boldsymbol{\tau}$ over $\{1, 2, \ldots, N\}^d$, and then combining (4.58) with (4.60) or (4.61), we have the following approximations.

For $\gamma \in (1 - \alpha, 2)$,

$$\begin{aligned}
&\sum_{\boldsymbol{\tau} \in \{1,2,\ldots,N\}^d} \int_{I_{\boldsymbol{\tau}}} \psi_\gamma(\mathbf{x}, \boldsymbol{\xi}) \cdot |\boldsymbol{\xi}|^{\gamma-(d+\alpha)}\, d\boldsymbol{\xi} \\
&\approx \frac{1}{2^d}\bigg\{ \sum_{\substack{\boldsymbol{\tau} \in \{1,\ldots,N\}^d \\ \boldsymbol{\tau} \neq (1,\ldots,1)}} \sum_{\widehat{\boldsymbol{\xi}} \in I_{\boldsymbol{\tau}}^{\text{ver}}} \psi_\gamma(\mathbf{x}, \widehat{\boldsymbol{\xi}}) \int_{I_{\boldsymbol{\tau}}} |\boldsymbol{\xi}|^{\gamma-(d+\alpha)}\, d\boldsymbol{\xi} + \sum_{\widehat{\boldsymbol{\xi}} \in I_{\mathbf{1}}^{\text{ver}} \setminus \{\mathbf{0}\}} \psi_\gamma(\mathbf{x}, \widehat{\boldsymbol{\xi}}) \int_{I_{\boldsymbol{\tau}}} |\boldsymbol{\xi}|^{\gamma-(d+\alpha)}\, d\boldsymbol{\xi} \bigg\} \\
&= \frac{1}{2^d} \sum_{\mathbf{n} \in \{0,1,\ldots,N\}^d} \psi_\gamma(\mathbf{x}, \boldsymbol{\xi}_{\mathbf{n}}) \int_{I_{(\xi_{\mathbf{n}}, h)} \cap [0,L]^d} |\boldsymbol{\xi}|^{\gamma-(d+\alpha)}\, d\boldsymbol{\xi}, \qquad (4.62)
\end{aligned}$$

For $\gamma = 2$,

$$\begin{aligned}
&\sum_{\boldsymbol{\tau}\in\{1,2,\dots,N\}^d} \int_{I_{\boldsymbol{\tau}}} \psi_\gamma(\mathbf{x},\boldsymbol{\xi}) \cdot |\boldsymbol{\xi}|^{\gamma-(d+\alpha)}\, d\boldsymbol{\xi} \\
&\approx \frac{1}{2^d} \sum_{\substack{\boldsymbol{\tau}\in\{1,\dots,N\}^d \\ \boldsymbol{\tau}\neq(1,\dots,1)}} \sum_{\widehat{\boldsymbol{\xi}}\in I_{\boldsymbol{\tau}}^{\mathrm{ver}}} \psi_\gamma(\mathbf{x},\widehat{\boldsymbol{\xi}}) \int_{I_{\boldsymbol{\tau}}} |\boldsymbol{\xi}|^{\gamma-(d+\alpha)}\, d\boldsymbol{\xi} + \frac{1}{d}\sum_{i=1}^{d} \psi_2(\mathbf{x}, h\mathbf{e}_i) \int_{I_{\mathbf{1}}} |\boldsymbol{\xi}|^{2-(d+\alpha)}\, d\boldsymbol{\xi} \\
&\approx \sum_{i=1}^{d} \psi_\gamma(\mathbf{x}, h\mathbf{e}_i) \left(\frac{1}{2^d} \int_{I_{(h\mathbf{e}_i,h)}\cap(0,L]^d} |\boldsymbol{\xi}|^{\gamma-(d+\alpha)}\, d\boldsymbol{\xi} + \left(\frac{1}{d} - \frac{1}{2^d}\right) \int_{I_{\mathbf{1}}} |\boldsymbol{\xi}|^{\gamma-(d+\alpha)}\, d\boldsymbol{\xi} \right) \\
&\quad + \frac{1}{2^d} \sum_{\widehat{\boldsymbol{\xi}}\in I_{\mathbf{1}}^{\mathrm{ver}}\backslash\{h\mathbf{e}_1,\dots,h\mathbf{e}_d\}} \psi_\gamma(\mathbf{x},\widehat{\boldsymbol{\xi}}) \int_{(I_{(\widehat{\boldsymbol{\xi}},h)}\backslash I_{\mathbf{1}})\cap(0,L]^d} |\boldsymbol{\xi}|^{\gamma-(d+\alpha)}\, d\boldsymbol{\xi} \\
&\quad + \frac{1}{2^d} \sum_{\substack{\mathbf{n}\in\{0,1,\dots,N\}^d, \\ \boldsymbol{\xi}_{\mathbf{n}}\notin I_{\mathbf{1}}}} \psi_\gamma(\mathbf{x},\boldsymbol{\xi}_{\mathbf{n}}) \int_{I_{(\boldsymbol{\xi}_{\mathbf{n}},h)}\cap(0,L]^d} |\boldsymbol{\xi}|^{\gamma-(d+\alpha)}\, d\boldsymbol{\xi}.
\end{aligned} \tag{4.63}$$

In fact, the left-hand side of (4.62) and (4.63) can be viewed as summing over the d-dimensional intervals $I_{\boldsymbol{\tau}}$, while the right-hand side can be viewed as summing over the grid points in $(0, L]^d$.

Combining (4.55)–(4.57) and (4.62) (or (4.63)), the discretization of the d-dimensional fractional Laplacian is

$$(-\Delta)_{h,\gamma}^{\alpha/2} u(\mathbf{x}) = -C_{d,\alpha}\Big(a_{\mathbf{0}}\, u(\mathbf{x}) + \sum_{\substack{\mathbf{n}\in\{0,1,\dots,N\}^d \\ \mathbf{n}\neq\mathbf{0}}} a_{\mathbf{n}} \sum_{\mathbf{v}\in I_{(\mathbf{x},\boldsymbol{\xi}_{\mathbf{n}})}^{\mathrm{ver}}} u\,(\mathbf{v}) \Big),$$

where $\mathbf{v}$ are the vertices of the d-dimensional cube $I_{(\mathbf{x},\boldsymbol{\xi}_{\mathbf{n}})}$, which is centered at $\mathbf{x}$ with radius $\boldsymbol{\xi}_{\mathbf{n}}$. For different γ, $a_{\mathbf{n}}$ is given as follows.

- For $\gamma \in (\alpha, 2)$,

$$a_{\mathbf{n}} = \frac{1}{2^{d-k}} \int_{I_{(\boldsymbol{\xi}_{\mathbf{n}},h)}\cap[0,L]^d} |\boldsymbol{\xi}|^{\gamma-(d+\alpha)}\, d\boldsymbol{\xi}, \quad \text{if } \mathbf{n}\in V_k \ (0 \le k \le d);$$

where

$$V_k = \{\mathbf{n} \in \{0, 1, \dots, N\}^d \mid \text{ if there are } k \text{ entries of } \mathbf{n} \text{ equal } 0\}.$$

- For $\gamma = 2$, we only list the $a_{\mathbf{n}}$'s which are different from $\gamma \in (\alpha, 2)$

$$a_{\mathbf{n}} = \begin{cases} \dfrac{1}{2^{d-k}} \displaystyle\int_{(I_{(\xi_{\mathbf{n}},h)} \backslash I_{\mathbf{1}}) \cap (0,L]^d} |\boldsymbol{\xi}|^{2-(d+\alpha)}\, d\boldsymbol{\xi}, & \text{if } \mathbf{n} \in V_k \ (0 \le k \le d) \\ & \text{and } \boldsymbol{\xi}_{\mathbf{n}} \in I_{\mathbf{1}} \backslash \{h\mathbf{e}_1, \dots, h\mathbf{e}_d\}, \\ \dfrac{2}{2^d} \displaystyle\int_{I_{(\xi_{\mathbf{n}},h)} \cap (0,L]^d} |\boldsymbol{\xi}|^{2-(d+\alpha)}\, d\boldsymbol{\xi} + \left(\dfrac{2}{d} - \dfrac{2}{2^d}\right) \displaystyle\int_{I_{\mathbf{1}}} |\boldsymbol{\xi}|^{2-(d+\alpha)}\, d\boldsymbol{\xi}, & \\ & \text{if } \quad \boldsymbol{\xi}_{\mathbf{n}} = h\mathbf{e}_i \quad \text{for} \quad i = 1, 2, \dots, d. \end{cases}$$

and

$$a_{\mathbf{0}} = -\sum_{k=0}^{d-1} 2^{d-k} \sum_{\mathbf{n} \in V_k \backslash \{\mathbf{0}\}} a_{\mathbf{n}} - 2^d w_L.$$

For easy illustration, we present the 3D matrix-vector form of the fractional Laplacian in the following. The high dimensional cases can follow the same line.

Denote the 3D vector

$$\mathbf{u}_{x,y,z} = (\mathbf{u}_{x,y,1}^T, \mathbf{u}_{x,y,2}^T, \dots, \mathbf{u}_{x,y,N_z-1}^T)^T,$$

where $\mathbf{u}_{x,y,k} = (\mathbf{u}^T_{x,1,k}, \ldots, \mathbf{u}^T_{x,N_y-1,k})^T$ for $k = 1, 2, \ldots, N_z-1$, and $\mathbf{u}_{x,j,k} = (u_{1,j,k}, \ldots, u_{N_x-1,j,k})^T$ for $j = 1, 2, \ldots, N_y - 1$ and $k = 1, 2, \ldots, N_z - 1$. The matrix representation of the 3D fractional Laplacian $(-\Delta)^{\alpha/2}_{h,\gamma} u(x, y, z)$ is $A^{(3)}\mathbf{u}_{x,y,z}$, that

$$\mathrm{A}^{(3)} = \begin{pmatrix} A_{x,y,0} & A_{x,y,1} & \ldots & A_{x,y,N_z-3} & A_{x,y,N_z-2} \\ A_{x,y,1} & A_{x,y,0} & A_{x,y,1} & \cdots & A_{x,y,N_z-3} \\ \vdots & \ddots & \ddots & \ddots & \vdots \\ A_{x,y,N_z-3} & \ldots & A_{x,y,1} & A_{x,y,0} & A_{x,y,1} \\ A_{x,y,N_z 2} & A_{x,y,N_z-3} & \ldots & A_{x,y,1} & A_{x,y,0} \end{pmatrix}_{[(N_x-1)(N_y-1)(N_z-1)]^2},$$

where

$$\mathrm{A}_{x,y,k} = \begin{pmatrix} A_{x,0,k} & A_{x,1,k} & \ldots & A_{x,N_y-3,k} & A_{x,N_y-2,k} \\ A_{x,1,k} & A_{x,0,k} & A_{x,1,k} & \cdots & A_{x,N_y-3,k} \\ \vdots & \ddots & \ddots & \ddots & \vdots \\ A_{x,N_y-3,k} & \ldots & A_{x,1,k} & A_{x,0,k} & A_{x,1,k} \\ A_{x,N_y-2,k} & A_{x,N_2-3,k} & \ldots & A_{x,1,k} & A_{x,0,k} \end{pmatrix}_{[(N_x-1)(N_y-1)]^2},$$

for $k = 0, 1, \ldots, N_z - 2$, and

$$\mathrm{A}_{x,j,k} = \begin{pmatrix} a_{0,j,k} & a_{1,j,k} & \ldots & a_{N_x-3,j,k} & a_{N_x-2,j,k} \\ a_{1,j,k} & a_{0,j,k} & a_{1,j,k} & \cdots & a_{N_x-3,j,k} \\ \vdots & \ddots & \ddots & \ddots & \vdots \\ a_{N_x-3,j,k} & \ldots & a_{1,j,k} & a_{0,j,k} & a_{1,j,k} \\ a_{N_x-2,j,k} & a_{N_x-3,j,k} & \ldots & a_{1,j,k} & a_{0,j,k} \end{pmatrix}_{(N_x-1)^2},$$

for $j = 0, 1, \ldots, N_y - 2$ and $k = 0, 1, \ldots, N_z - 2$. Notice that each $A_{x,j,k}$ is a symmetric Toeplitz matrix, and each $A_{x,y,k}$ is a block-Toeplitz matrix constructed by the matrices $A_{x,j,k}$ for $j = 0, 1, \ldots, N_y - 2$. Similarly, the matrix $A^{(3)}$ is also a block-Toeplitz matrix with each block $A_{x,y,k}$ also be a block-Toepliz matrix. The computation of $\mathrm{A}^{(3)}\mathbf{u}$ can be achieved efficiently by using the fast Fourier transform (FFT), which we will introduce in Section 6.

4.2.2. Numerical Experiments. As suggested in 1D and 2D cases, for $u \in C^{3,\alpha/2}(\mathbb{R}^d)$ ($d = 1, 2$), the weighted trapezoidal method is second order accuracy by taking the splitting parameter $\gamma = 2$. We conjecture the same result also holds in 3D and will numerically justify it by considering the following example.

Example. Consider the functions of the form

$$u(x, y, z) = \begin{cases} [(1 - x^2)(1 - y^2)(1 - z^2)]^{3+\alpha/2}, & \text{if} \quad (x, y, z) \in \Omega \\ 0, & \text{otherwise,} \end{cases} \tag{4.64}$$

which is in $C^{3,\alpha/2}(\mathbb{R}^3)$ and has compact support on $\Omega = \{\mathbf{x} \in \mathbb{R}^3 : |x| < 1\ |y| < 1\ |z| < 1\}$. Since the fractional Laplacian of this type of function can not be computed analytically, we will use the numerical solution by taking $\gamma = 2$ and $N = 256$ as the exact solution.

Table 4.2. Numerical errors of the fractional Laplacian for $u \in C^{3,\alpha/2}(\mathbb{R}^3)$.

h α	1/4	1/8	1/16	1/32	1/64
0.3	1.2160E-2	3.6919E-3	9.6941E-4	2.3505E-4	4.7266E-5
	c.r.	1.7197	1.9292	2.0441	2.3141
1	1.3202E-1	3.9773E-2	1.0791E-2	2.6827E-3	5.4721E-4
	c.r.	1.7309	1.8820	2.0081	2.2935
1.9	1.6007E-0	4.1340E-1	1.0402E-1	2.5075E-2	5.0615E-3
	c.r.	1.9531	1.9907	2.0525	2.3086

Table 4.2 presents numerical errors $\|(-\Delta)^{\alpha/2}u - (-\Delta)^{\alpha/2}_{h,\gamma}u\|_{l_\infty(\Omega)}$ and convergence rates of the weighted trapezoidal method for various α by taking u in (4.64), where the splitting parameter is taken to be $\gamma = 2$. It shows that the weighted trapezoidal method in 3D also has second order accuracy by taking $\gamma = 2$, which justifies our conjecture.

In this Section, we extend the weighted trapezoidal method from one dimension to general d dimension ($d \geq 2$). Different to the 1D case which either $\gamma = 1 + \alpha/2$ or 2 can provide an accuracy of $\mathcal{O}(h^2)$, our analysis in two dimension suggest that $\gamma = 2$ is the only optimal choice to get second order accuracy for $u \in C^{3,\alpha/2}(\mathbb{R}^2)$. Our extensive simulations in 3D also suggests the same result that only by taking $\gamma = 2$ can provide a second order accuracy. Therefore, we conjecture that $\gamma = 2$ is the only choice of the splitting parameter that will provide a second order accuracy for functions in $C^{3,\alpha/2}(\mathbb{R}^d)$ with $d \geq 2$.

5. THE WEIGHTED LINEAR INTERPOLATION METHOD

The interpolation methods are widely applied in numerical approximation. However, directly applying the traditional interpolation method to approximate the fractional Laplacian lead to low accuracy because of the hypersingularity. In this section, we propose a weighted linear interpolation method. For smooth enough functions, it provides second order accuracy. This method is comparable with the weighted trapezoidal method that is proposed in Section 3. The common feature of these two methods is the application of the weighted integral. In addition, the weighted linear interpolation method can be easily extended to higher dimensions.

5.1. ONE-DIMENSIONAL CASE

To simply show the main idea of the weighted linear interpolation method, we will start with the derivation in 1D. Error analysis are presented for functions with different smoothness conditions. Numerical examples will be provided to test the analytical results.

5.1.1. Numerical Scheme. First, following the same lines as the weighted trapezoidal method, we can rewrite the fractional Laplacian as in (3.2). The evaluation of the second integral in (3.2) is the same as the weighted trapezoidal method, which is obtained in (3.3). Here, we introduce a *weighted linear interpolation method* to approximate the first integral in (3.2).

First, we interpolate $\psi_\gamma(x,\xi)$ with respect to $\xi \in [0, L]$ by using the piecewise linear basis function ϕ_i as

$$\psi_\gamma(x,\xi) \approx \mathcal{P}\psi_\gamma(x,\xi) = \sum_{i=0}^{N} \psi_\gamma(x,\xi_i)\phi_i(\xi). \tag{5.1}$$

where

$$\phi_i(\xi) = \begin{cases} \dfrac{\xi - \xi_{i-1}}{\xi_i - \xi_{i-1}}, & \text{if} \quad \xi \in [\xi_{i-1}, \xi_i], \\ \dfrac{\xi_{i+1} - \xi}{\xi_{i+1} - \xi_i}, & \text{if} \quad \xi \in [\xi_i, \xi_{i+1}], \\ 0, & \text{otherwise}. \end{cases} \tag{5.2}$$

Because of the singularity at $\xi = 0$, the value of $\psi_\gamma(x, \xi_0)$ is defined as a limit as $\xi \to 0$, i.e. $\psi_\gamma(x, \xi_0) := \lim_{\xi \to 0} \psi_\gamma(x, \xi)$. The parameter γ is taken in $(\alpha - 1, 2]$ to guarantee the convergence of the method. Assume that u is smooth enough, to find the limit, we separate our discussion in two cases.

Case 1: For $\gamma \in (\alpha - 1, 2)$,

$$\psi_\gamma(x, \xi_0) = \lim_{\xi \to 0} \frac{u(x - \xi) + u(x + \xi) - 2u(x)}{\xi^2} \cdot \xi^{2-\gamma} \approx u''(x) \lim_{\xi \to 0} \xi^{2-\gamma} = 0. \tag{5.3}$$

Case 2: For $\gamma = 2$,

$$\psi_2(x, \xi_0) = \lim_{\xi \to 0} \frac{u(x - \xi) + u(x + \xi) - 2u(x)}{\xi^2} \approx u''(x). \tag{5.4}$$

Notice that the further approximation of $u''(x)$ for $\gamma = 2$ in (5.4) depends on the interpolation basis functions (i.e. whether it is constant, linear, quadratic, and so on) to match up with the accuracy of the approximation of the first integral in (3.2). But here we will only focus on the linear basis functions, which we expect to get a second order accuracy for smooth enough functions u. Therefore, we use the central difference scheme to approximate $u''(x)$, and following (5.4), $\psi_2(x, \xi_0)$ can be further approximated as

$$\psi_2(x, \xi_0) \approx \frac{u(x - h) - 2u(x) + u(x + h)}{h^2} = \psi_2(x, \xi_1). \tag{5.5}$$

Substituting (5.1) into the first integral in (3.2) gives

$$\int_0^L \psi_\gamma(x,\xi)\xi^{-1-\alpha+\gamma}d\xi \approx \sum_{i=0}^{N} \psi_\gamma(x,\xi_i) \int_0^L \phi_i(\xi)\cdot\xi^{-1-\alpha+\gamma}d\xi, \tag{5.6}$$

where $\psi_\gamma(x,\xi_0)$ is approximated by (5.3) if $\gamma \in (\alpha-1,2)$ or by (5.5) if $\gamma = 2$.

Combining (3.2), (3.3) and (5.6), the fractional Laplacian $(-\Delta)^{\alpha/2}$ is approximated by

$$(-\Delta)^{\alpha/2}_{h,\gamma}u(x) = -C_{1,\alpha}\sum_{i=0}^{N}\psi_\gamma(x,\xi_i)\int_0^L \phi_i(\xi)\,\xi^{-1-\alpha+\gamma}d\xi + \frac{2C_{1,\alpha}}{\alpha L^\alpha}u(x), \text{ for } x \in (a,\, b),$$

where the function $\psi_\gamma(x,\xi_i)$ $(i = 1,\ldots,N)$ is defined in (3.5) and $\psi_\gamma(x,\xi_0)$ is approximated by (5.3) (or (5.5)) if $\gamma \in (\alpha-1,2)$ (or $\gamma = 2$).

The fully discretization of the fractional Laplacian has the same expression as the weighted trapezoidal method in (3.9), i.e.

$$(-\Delta)^{\alpha/2}_{h,\gamma}u_i = -C_{1,\alpha}\Big(a_0\,u_i + \Big(\sum_{j=1}^{i-1}a_ju_{i-j} + \sum_{j=1}^{N-1-i}a_ju_{i+j}\Big)\Big), \tag{5.7}$$

for $i = 1,2,\ldots,N-1$, where for $\gamma \in (\alpha-1,2)$,

$$\begin{aligned} a_i &= \frac{1}{\xi_i^\gamma}\int_0^L \phi_i(\xi)\cdot\xi^{-1-\alpha+\gamma}\,d\xi, \quad \text{for} \quad i = 1,\ldots,N,\\ a_0 &= -2\Bigg(\sum_{i=1}^{N}a_i + \frac{1}{\alpha L^\alpha}\Bigg), \end{aligned} \tag{5.8}$$

while for $\gamma = 2$, the calculation of a_i is the same as (5.8), except,

$$a_1 = \frac{1}{\xi_1^\gamma}\int_0^L (\phi_0(\xi)+\phi_1(\xi))\cdot\xi^{-1-\alpha+\gamma}\,d\xi. \tag{5.9}$$

The matrix-vector form is the same as the weighted trapezoidal method in (3.10).

5.1.2. Error Estimates. In this section, we provide error estimates on our weighted linear interpolation method in discretizing the fractional Laplacian.

Theorem 5.1.1 (Accuracy for functions in $C^{1,\alpha/2}(\mathbb{R})$)**.** *Suppose that* $u \in C^{1,\alpha/2}(\mathbb{R})$ *has finite support on an open set* $\Omega \in \mathbb{R}$, *and* $(-\Delta)_{h,\gamma}^{\alpha/2}$ *in (5.7) is the weighted linear interpolation approximation of the fractional Laplacian* $(-\Delta)^{\alpha/2}$. *Then, for any* $\gamma \in (\alpha - 1, 2]$, *there is*

$$\|(-\Delta)^{\alpha/2}u(x) - (-\Delta)_{h,\gamma}^{\alpha/2}u(x)\|_{\infty,\Omega} \le Ch^{1-\alpha/2}, \qquad \textit{for } \ \alpha \in (0,2) \tag{5.10}$$

with C *a positive constant depending on* α *and* γ.

Proof. Define the error function

$$e_{\alpha,\gamma}^h(x) \;=\; (-\Delta)^{\alpha/2}u(x) - (-\Delta)_{h,\gamma}^{\alpha/2}u(x).$$

From (5.6), we obtain

$$\begin{aligned} e_{\alpha,\gamma}^h &= \int_0^h \psi_\gamma(x,\xi)\xi^{\gamma-(1+\alpha)}d\xi - \int_0^h \big(\psi_\gamma(x,\xi_0)\phi_0(\xi) + \psi_\gamma(x,\xi_1)\phi_1(\xi)\big)\,\xi^{\gamma-(1+\alpha)}d\xi \\ &\quad + \sum_{i=2}^{N}\int_{\xi_{i-1}}^{\xi_i} \big(\psi_\gamma(x,\xi) - \psi_\gamma(x,\xi_{i-1})\phi_{i-1}(\xi) - \psi_\gamma(x,\xi_i)\phi_i(\xi)\big)\,\xi^{\gamma-(1+\alpha)}\,d\xi \\ &= I + II. \end{aligned} \tag{5.11}$$

For term I with $\gamma \in (\alpha - 1, 2)$, by the approximation of $\psi_\gamma(\xi_0)$ in (5.3) and triangle inequality, we get

$$\begin{aligned} |I| &= \left|\int_0^h \psi_\gamma(\xi)\,\xi^{\gamma-(1+\alpha)}\,d\xi - \int_0^h \psi_\gamma(\xi_1)\phi_1(\xi)\,\xi^{\gamma-(1+\alpha)}\,d\xi\right| \\ &\le \left|\int_0^h \psi_\gamma(\xi)\,\xi^{\gamma-(1+\alpha)}\,d\xi\right| + h^{-1}\left|\psi_\gamma(\xi_1)\int_0^h \xi^{\gamma-\alpha}\,d\xi\right|. \end{aligned}$$

Then, by applying Lemma 3.2.2 (i), there is a positive constant C such that

$$|I| \leq C\left|\int_0^h \xi^{\alpha/2+1-\gamma}\,\xi^{\gamma-(1+\alpha)}\,d\xi\right| + h^{-1}\left|h^{\alpha/2+1-\gamma}\int_0^h \xi^{\gamma-\alpha}\,d\xi\right| \leq Ch^{1-\alpha/2}.$$

For term I with $\gamma = 2$, by the approximation of $\psi_\gamma(\xi_0)$ in (5.4) and triangle inequality, there is

$$\begin{aligned} |I| &= \left|\int_0^h \psi_2(\xi)\,\xi^{1-\alpha}\,d\xi - \int_0^h \psi_2(\xi_1)\,\xi^{1-\alpha}\,d\xi\right| \\ &\leq \left|\int_0^h \psi_2(\xi)\,\xi^{1-\alpha}\,d\xi\right| + \left|\psi_2(\xi_1)\int_0^h \xi^{1-\alpha}\,d\xi\right|. \end{aligned}$$

Then, by applying Lemma 3.2.2 (i), there is a positive constant C such that

$$|I| \leq C\left|\int_0^h \xi^{\alpha/2-1}\,\xi^{1-\alpha}\,d\xi\right| + \left|h^{-1+\alpha/2}\int_0^h \xi^{1-\alpha}\,d\xi\right| \leq Ch^{1-\alpha/2}.$$

For term II with any $\gamma \in (\alpha-1, 2]$, we first rewrite it as

$$\begin{aligned} II = \sum_{i=2}^{N}\int_{\xi_{i-1}}^{\xi_i} \Big(&\big(\psi_\gamma(x,\xi) - \psi_\gamma(x,\xi_{i-1})\big)\,\phi_{i-1}(\xi) \\ &+ \big(\psi_\gamma(x,\xi) - \psi_\gamma(x,\xi_i)\big)\,\phi_i(\xi)\Big)\,\xi^{\gamma-(1+\alpha)}\,d\xi. \end{aligned}$$

Then by triangle inequality and Talyor theorem, we have

$$\begin{aligned} |II| &\leq \sum_{i=2}^{N}\int_{\xi_{i-1}}^{\xi_i} \Big(\big|\psi_\gamma(x,\xi) - \psi_\gamma(x,\xi_{i-1})\big|\,\phi_{i-1}(\xi) \\ &\qquad + \big|\psi_\gamma(x,\xi) - \psi_\gamma(x,\xi_i)\big|\,\phi_i(\xi)\Big)\,\xi^{\gamma-(1+\alpha)}\,d\xi \\ &\leq Ch\sum_{i=2}^{N}\int_{\xi_{i-1}}^{\xi_i} \Big(\max_{\eta\in[\xi_{i-1},\xi_i]}\big|\psi_\gamma(\eta)\big|\,\phi_{i-1}(\xi) + \max_{\widetilde{\eta}\in[\xi_{i-1},\xi_i]}\big|\psi_\gamma(\widetilde{\eta})\big|\,\phi_i(\xi)\Big)\,\xi^{\gamma-(1+\alpha)}\,d\xi. \end{aligned}$$

Finally, by applying Lemma 3.2.2 (i), we get

$$\begin{aligned} |II| &\le Ch\sum_{i=2}^{N}\int_{\xi_{i-1}}^{\xi_i} \xi^{\alpha/2-\gamma}\left(\phi_{i-1}(\xi)+\phi_i(\xi)\right)\xi^{\gamma-(1+\alpha)}\,d\xi \\ &\le Ch\int_h^L \xi^{-1-\alpha/2}\,d\xi \le Ch^{1-\alpha/2}. \end{aligned}$$

Therefore, we proved that for $\gamma \in (\alpha-1, 2]$, $|e^h_{\alpha,\gamma}| \le Ch^{1-\alpha/2}$. □

Next, we will show that for a smooth enough function u, the accuracy of the weighted linear interpolation method can be improved to $\mathcal{O}(h^2)$ uniformly for any $\alpha \in (0, 2)$.

Theorem 5.1.2 (Convergence rate for $u \in C^{3,\alpha/2}(\mathbb{R})$)**.** *Suppose that $u \in C^{3,\alpha/2}(\mathbb{R})$ has finite support on an open set $\Omega \in \mathbb{R}$, and $(-\Delta)^{\alpha/2}_{h,\gamma}$ defined in (5.7) is a weighted linear interpolation approximation of the fractional Laplacian $(-\Delta)^{\alpha/2}$. If the parameter is chosen as $\gamma = 1$ or 2, there is*

$$\|(-\Delta)^{\alpha/2}u(x) - (-\Delta)^{\alpha/2}_{h,\gamma}u(x)\|_{\infty,\Omega} \le Ch^2, \qquad \textit{for } \alpha \in (0,2) \tag{5.12}$$

with C a positive constant depending on α.

Proof. For brevity, we start with the local truncation error in (5.11).

First, we focus on the case of $\gamma = 2$.

Recall that for $\gamma = 2$, we approximate $\psi_\gamma(x, \xi_0)$ by $\psi_\gamma(x, \xi_1)$ as in (5.5). Then by Taylor theorem and Lemma 3.2.2 (ii), we have

$$\begin{aligned} |I| &= \left|\int_0^h \left(\psi_2(\xi) - \psi_2(\xi_1)\right)\,\xi^{1-\alpha}\,d\xi\right| \\ &\le Ch\max_{\eta\in[0,h]}|\psi_2'(\eta)|\int_0^h \xi^{1-\alpha}d\xi \le Ch^{3-\alpha/2}. \end{aligned}$$

Now, we focus on term II. By the definition of the interpolation operator $\mathcal{P}$, we can first rewrite II and then using the triangle inequality, that

$$\begin{aligned} |II| &= \left| \sum_{j=1}^{N-1} \int_{\xi_j}^{\xi_{j+1}} (\psi_2(x,\xi) - \mathcal{P}\psi_2) \xi^{1-\alpha} d\xi \right| \\ &\leq \sum_{j=1}^{N-1} \left| \int_{\xi_j}^{\xi_{j+1}} (\psi_2(x,\xi) - \mathcal{P}\psi_2) \xi^{1-\alpha} d\xi \right| = \sum_{j=1}^{N-1} II_j. \end{aligned}$$

Next, let's focus on the error estimation for each II_j ($j = 1, 2, \ldots, N-1$). By using the error estimates for the linear interpolation for function $\psi_2(x,\xi)$ for $\xi \in (\xi_j, \xi_{j+1})$, there is

$$II_j = \left| \int_{\xi_j}^{\xi_{j+1}} (\psi_2(x,\xi) - \mathcal{P}\psi_2) \xi^{1-\alpha} d\xi \right| \leq Ch^2 \max_{\eta \in [\xi_j, \xi_{j+1}]} |\psi_2''(x,\eta)| \left(\xi_{j+1}^{2-\alpha} - \xi_j^{2-\alpha} \right).$$

Following similar lines as the estimations in (3.36) and (3.37), by summing over j from 1 to $N-1$, we can prove $|II| \leq Ch^2$, and it follows that $|e_{\alpha,\gamma}^h| \leq Ch^2$.

Next, we focus on the case of $\gamma = 1$.

Different to $\gamma = 2$, in this case, we have $\psi_\gamma(x, \xi_0) = 0$ as in (5.3). Then we have

$$\begin{aligned} |I| &= \left| \int_0^h \psi_1(x,\xi) \xi^{-\alpha} d\xi - \psi_1(x,\xi_0) \int_0^h \xi^{-\alpha} \phi_0(\xi) d\xi - \psi_1(x,\xi_1) \int_0^h \xi^{-\alpha} \phi_1(\xi) d\xi \right| \\ &= \left| \int_0^h (\psi_2(x,\xi) - \psi_2(x,\xi_1)) \, \xi^{1-\alpha} d\xi \right| \leq Ch^{3-\alpha/2}. \end{aligned}$$

Noticing that, although the term I is approximated through different ways for $\gamma = 2$ and 1, but they eventually have the same expression.

The estimation of term II follows the same line as the case of $\gamma = 2$, for brevity, we start from the estimation of each term I_j ($j = 1, 2, \ldots, N-1$). Again, by using the error estimates for the linear interpolation for function $\psi_1(x,\xi)$ for $\xi \in (\xi_j, \xi_{j+1})$, there is

$$II_j = \left| \int_{\xi_j}^{\xi_{j+1}} (\psi_1(x,\xi) - \mathcal{P}\psi_1) \xi^{-\alpha} d\xi \right| \leq Ch^2 \max_{\eta \in [\xi_j, \xi_{j+1}]} |\psi_1''(\eta)| \left(\xi_{j+1}^{1-\alpha} - \xi_j^{1-\alpha} \right).$$

Then, by applying Lemma 3.2.2 (ii) with $m = 2$, for any $\eta \in (\xi_j, \xi_{j+1})$, there is

$$II_j \le Ch^2 \max_{\eta \in [\xi_j, \xi_{j+1}]} \eta^{\alpha/2} \left(\xi_{j+1}^{1-\alpha} - \xi_j^{1-\alpha} \right) \le Ch^3 \xi_j^{-\alpha/2} \tag{5.13}$$

Finally, summing over j from 1 to $N - 1$, we have

$$|II| \le Ch^3 \sum_{j=1}^{N-1} \xi_j^{-\alpha/2} \le Ch^2 \int_0^L \xi^{-\alpha/2} d\xi \le Ch^2. \tag{5.14}$$

Thus, we proved that for $\gamma = 1$ or 2, there is $|e_{\alpha,\gamma}^h| \le Ch^2$. □

Theorem 5.1.2 shows that for $u \in C^{3,\alpha/2}(\mathbb{R})$, if the splitting parameter is chosen as $\gamma = 1$ or 2, our weighted linear interpolation method has a second order accuracy uniformly for any $\alpha \in (0, 2)$. Similar to the weighted trapezoidal method, in 1D case, the weighted linear interpolation method also has two optimal choices of the splitting parameter γ to get the second order accuracy.

5.1.3. Numerical Experiments. In this section, we study the accuracy of the weighted linear interpolation method in discretizing the fractional Laplacian $(-\Delta)^{\alpha/2}$. We will use the function u of the form in (3.47) in the following examples.

Example 4.1.1. Choose $s = 1$ in (3.47), i.e. $u \in C^{1,\alpha/2}(\mathbb{R})$. As shown in Theorem 5.1.1 that in this case, the accuracy of the weighted linear interpolation method in l_∞-norm is of order $O(h^{1-\alpha/2})$ for small mesh size h, and it is independent of the splitting parameter $\gamma \in (\alpha - 1, 2]$. Figure 5.1 presents the numerical errors by taking different γ in l_∞- and l_2-norms. It shows that choosing the parameter $\gamma = 1$ leads to more accurate results than $\gamma = 2$. Also, the convergence rates in l_2-norm are of order $O(h^{(3-\alpha)2/2})$ for both $\gamma = 1$ and 2.

Example 4.1.2. Choose $s = 3$ in (3.47), i.e. $u \in C^{3,\alpha/2}(\mathbb{R})$, as shown in Theorem 5.1.2 that in this case, by taking $\gamma = 1$ or 2, the accuracy of the weighted linear interpolation method in l_∞-norm is of order $O(h^2)$.

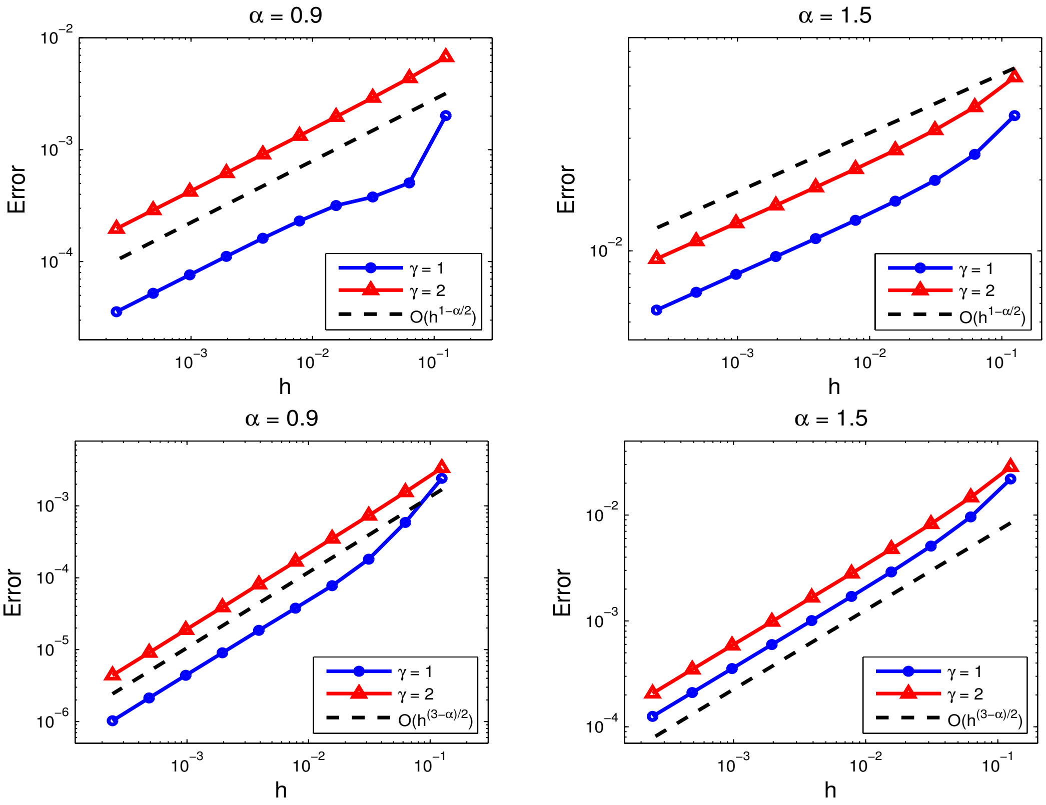

Figure 5.1. Numerical errors of the weighted linear interpolation method for $\gamma = 1$ and 2 for defined in (3.47) with $s = 1$. The errors are defined in l_∞-norm (top row) or l_2-norm (bottom row).

Tables 5.1 and 5.2 present numerical errors $\|(-\Delta)^{\alpha/2}u - (-\Delta)^{\alpha/2}_{h,\gamma}u\|_{l_\infty(\Omega)}$ and convergence rates of the weighted linear interpolation method for various α by taking u in (3.47) with $s = 3$, where the splitting parameters are taken to be $\gamma = 1$ or 2, respectively. The symbol 'c.r.' represents convergence rate.

We find that in both cases, for the same mesh size h, the larger the parameter α, the bigger the numerical errors. For $\gamma = 1$ or 2, both of Table 5.1 and Table 5.2 show that the convergence rates of the weighted linear interpolation method is $O(h^2)$ for any $\alpha \in (0, 2)$, which confirms our analytical result in Theorem 5.1.2. The errors by taking $\gamma = 2$ are always smaller than the errors by taking $\gamma = 1$ for the same mesh size h. Similar to the

Table 5.1. Numerical errors by weighted interpolation method for $u \in C^{3,\alpha/2}(\mathbb{R})$ with $\gamma = 1$.

h α		1/32	1/64	1/128	1/256	1/512	1/1024	1/2048
0.2		6.132E-5	1.532E-5	3.830E-6	9.575E-7	2.394E-7	5.984E-8	1.496E-8
		c.r.	2.0006	2.0002	2.0001	2.0000	2.0000	2.0000
0.6		2.707E-4	6.752E-5	1.686E-5	4.214E-6	1.053E-6	2.633E-7	6.583E-8
		c.r.	2.0034	2.0013	2.0005	2.0002	2.0001	2.0001
1		7.319E-4	1.810E-4	4.502E-5	1.122E-5	2.802E-6	7.001E-7	1.749E-7
		c.r.	2.0155	2.0077	2.0039	2.0019	2.0010	2.0006
1.5		3.151E-3	9.494E-4	2.540E-4	6.475E-5	1.616E-5	4.000E-6	9.872E-7
		c.r.	1.7309	1.9020	1.9722	2.0022	2.0145	2.0186
1.9		1.490E-2	4.418E-3	1.186E-3	3.045E-4	7.659E-5	1.907E-5	4.726E-6
		c.r.	1.7542	1.8975	1.9613	1.9913	2.0057	2.0126

weighted trapezoidal method, specially by taking $\gamma = 2$ for $\alpha = 1$, the errors are smaller than all the other α's, and its accuracy is of order $O(h^{2.5})$, which is higher than the second order accuracy.

Table 5.2. Numerical errors by weighted interpolation method for $u \in C^{3,\alpha/2}(\mathbb{R})$ with $\gamma = 2$.

h α		1/32	1/64	1/128	1/256	1/512	1/1024	1/2048
0.2		3.317E-5	8.361E-6	2.095E-6	5.242E-7	1.31E-7	3.277E-8	8.193E-9
		c.r.	1.9881	1.9966	1.9990	1.9997	1.9999	2.0000
0.6		5.645E-5	1.507E-5	3.860E-6	9.738E-7	2.443E-7	6.115E-8	1.530E-8
		c.r.	1.9052	1.9651	1.9869	1.9950	1.9981	1.9993
1		9.778E-5	2.381E-5	4.821E-6	9.079E-7	1.655E-7	2.970E-8	5.290E-9
		c.r.	2.0378	2.3043	2.4088	2.4559	2.4783	2.4890
1.5		2.057E-3	5.635E-4	1.376E-4	3.207E-5	7.347E-6	1.675E-6	3.824E-7
		c.r.	1.8682	2.0344	2.1006	2.1261	2.1330	2.1308
1.9		1.406E-2	4.112E-3	1.089E-3	2.760E-4	6.850E-5	1.683E-5	4.115E-6
		c.r.	1.7736	1.9167	1.9804	2.0105	2.0251	2.0321

5.2. TWO-DIMENSIONAL CASE

The generalization of the weighted linear interpolation method from one dimension to higher dimensions is straightforward. In this section, we will derive the numerical scheme of the weighted linear interpolation method in two dimension and provide numerical examples to test its accuracy.

5.2.1. Numerical Scheme.

Consider the 2D fractional Laplacian in (4.1). We Start from the fractional Laplacian in (4.4) with the second integral in (4.4) computed exactly as in (4.5).

We will focus on the approximation of the first integral in (4.4) by the weighted linear interpolation method. First, we interpolate $\psi_\gamma(\mathbf{x}, \boldsymbol{\xi})$ with respect to $\boldsymbol{\xi}$ on $[0, L]^2$ as

$$\psi_\gamma(\mathbf{x}, \boldsymbol{\xi}) \approx \sum_{i=0}^{N}\sum_{j=0}^{N} \psi_\gamma(\mathbf{x}, \xi_i, \eta_j)\phi_i(\xi)\phi_j(\eta). \tag{5.15}$$

Because of the singularity at $(\xi, \eta) = (0, 0)$, the value of $\psi_\gamma(\mathbf{x}, \xi_0, \eta_0)$ is defined as $\psi_\gamma(\mathbf{x}, \xi_0, \eta_0) := \lim_{(\xi,\eta)\to(0,0)} \psi_\gamma(\mathbf{x}, \boldsymbol{\xi})$. We separate our discussion in two cases for different splitting parameters γ.

Case 1: For $\gamma \in (\alpha - 1, 2)$, the limit vanishes, i.e.

$$\psi_\gamma(\mathbf{x}, \xi_0, \eta_0) = \lim_{(\xi,\eta)\to(0,0)} \psi_\gamma(\mathbf{x}, \xi, \eta) = 0. \tag{5.16}$$

Case 2: For $\gamma = 2$, the value of $\psi_\gamma(\mathbf{x}, \xi_0, \eta_0)$ is approximated by

$$\psi_2(\mathbf{x}, \xi_0, \eta_0) = \lim_{(\xi,\eta)\to(0,0)} \psi_2(\mathbf{x}, \xi, \eta) \approx \frac{1}{2}\left(\psi_2(\mathbf{x}, 0, h) + \psi_2(\mathbf{x}, h, 0)\right). \tag{5.17}$$

Substituting (5.15) into the first integral in (4.4) gives

$$\int_{(0,L)^2} \psi_0(\mathbf{x},\boldsymbol{\xi}) \cdot |\boldsymbol{\xi}|^{-(2+\alpha)}\, d\boldsymbol{\xi} \approx \sum_{i=0}^{N}\sum_{j=0}^{N} \psi_\gamma(\mathbf{x},\xi_i,\eta_j) \cdot \int_0^L \int_0^L \phi_i(\xi)\phi_j(\eta) \cdot |\boldsymbol{\xi}|^{\gamma-(2+\alpha)}\, d\xi\, d\eta, \tag{5.18}$$

where $\psi_\gamma(\mathbf{x},\xi_0,\eta_0)$ is approximated by (5.16) if $\gamma \in (\alpha-1, 2)$ or by (5.17) if $\gamma = 2$.

Combining (4.4), (4.5) and (5.18), the two-dimensional fractional Laplacian is approximated by

$$(-\Delta)^{\alpha/2}_{h,\gamma} u(\mathbf{x}) = -C_{2,\alpha}\Big(\sum_{i=0}^{N}\sum_{j=0}^{N} \psi_\gamma(\mathbf{x},\xi_i,\eta_j) \int_0^L \int_0^L \phi_i(\xi)\phi_j(\eta) \cdot |\boldsymbol{\xi}|^{\gamma-(2+\alpha)}\, d\xi\, d\eta \\ -4u(\mathbf{x}) \int_{\mathbb{R}^2\setminus(0,L)^2} |\boldsymbol{\xi}|^{-2-\alpha}\, d\boldsymbol{\xi}\Big). \tag{5.19}$$

Finally, the fully discretization of the fractional Laplacian can be written in the same form as the weighted trapezoidal method in (4.14), where for $\gamma \in (\alpha-1, 2)$,

$$a_{ij} = \frac{1}{|\boldsymbol{\xi}_{i,j}|^\gamma} \begin{cases} 2\int_0^L \int_0^L \phi_i(\xi)\phi_j(\eta) \cdot |\boldsymbol{\xi}|^{\gamma-(2+\alpha)}\, d\xi\, d\eta, & \text{if} \quad i = 0,\ j = 1,\dots,N, \\ 2\int_0^L \int_0^L \phi_i(\xi)\phi_j(\eta) \cdot |\boldsymbol{\xi}|^{\gamma-(2+\alpha)}\, d\xi\, d\eta, & \text{if} \quad i = 1,\dots,N,\ j = 0, \\ \int_0^L \int_0^L \phi_i(\xi)\phi_j(\eta) \cdot |\boldsymbol{\xi}|^{\gamma-(2+\alpha)}\, d\xi\, d\eta, & \text{if} \quad i,j = 1,\dots,N, \end{cases}$$

$$a_{00} = -2\left(\sum_{i=1}^{N} a_{i0} + \sum_{j=1}^{N} a_{0j}\right) - 4\sum_{i=1}^{N}\sum_{j=1}^{N} a_{ij} - 4w_L,$$

and for $\gamma = 2$, only a_{01} and a_{10} are different, which are listed as follows,

$$a_{ij} = \frac{1}{|\boldsymbol{\xi}_{i,j}|^\gamma} \begin{cases} \int_0^L \int_0^L (\phi_0(\xi)\phi_0(\eta) + 2\phi_0(\xi)\phi_1(\eta)) \cdot |\boldsymbol{\xi}|^{\gamma-(2+\alpha)}\, d\xi\, d\eta, & \text{if } i = 0,\ j = 1, \\ \int_0^L \int_0^L (\phi_0(\xi)\phi_0(\eta) + 2\phi_1(\xi)\phi_0(\eta)) \cdot |\boldsymbol{\xi}|^{\gamma-(2+\alpha)}\, d\xi\, d\eta, & \text{if } i = 1,\ j = 0. \end{cases}$$

The same as the weighted trapezoidal method, its matrix-vector form is written as $A^{(2)}\mathbf{u}_{x,y}$ with $A^{(2)}$ expressed in (4.15).

5.2.2. Numerical Experiments. In this section, we numerically study the accuracy of the weighted linear interpolation method in discretizing the fractional Laplacian $(-\Delta)^{\alpha/2}$ with functions have finite support.

Consider the functions of the form in (4.52), we specifically consider the cases by taking $s = 1$ and $s = 3$. Since the fractional Laplacian of this type of functions can not be computed analytically, we will use the numerical solution by the weighted trapezoidal method with $\gamma = 2$ and $N_x = N_y = 8192$ to be the exact solution for all the following numerical tests.

Example 5.2.1. For $s = 1$, i.e. $u \in C^{1,\alpha/2}(\mathbb{R}^2)$, as shown in Theorem 5.1.1 that for $u \in C^{1,\alpha/2}(\mathbb{R})$, the accuracy of the weighted linear interpolation method in l_∞-norm is $O(h^{1-\alpha/2})$ for small mesh size h, and it is independent of the splitting parameter $\gamma \in (\alpha - 1, 2]$. Our extensive numerical results suggest that this result is also hold in two dimension. Figure 5.2 presents the numerical errors by taking $\gamma = 1$ and 2 in both l_∞- and l_2-norms.

It shows that choosing the parameter $\gamma = 2$ leads to more accurate results in both l_∞- and l_2-norms. For $\gamma = 2$, the convergence rate in l_2-norm is of order $O(h^{(3-\alpha)/2})$, which is 0.5 order greater than the convergence rate in l_∞-norm. However, for $\gamma = 1$, the convergence rate in l_2-norm is lower than $O(h^{(3-\alpha)/2})$ for larger α, i.e., $\alpha = 1.5$, see Figure 5.2 bottom right.

Example 5.2.2. For $s = 3$, i.e. $u \in C^{3,\alpha/2}(\mathbb{R}^2)$, Theorem 5.1.2 in one dimension shows that either by taking $\gamma = 2$ or 1 can provide the second order accuracy. However, in two dimension, our extensive numerical experiments show that only by taking $\gamma = 2$ can provide the second order accuracy. This result is analogue to the weighted trapezoidal method, that in higher dimensions, the only optimal choice of the splitting parameter is $\gamma = 2$.

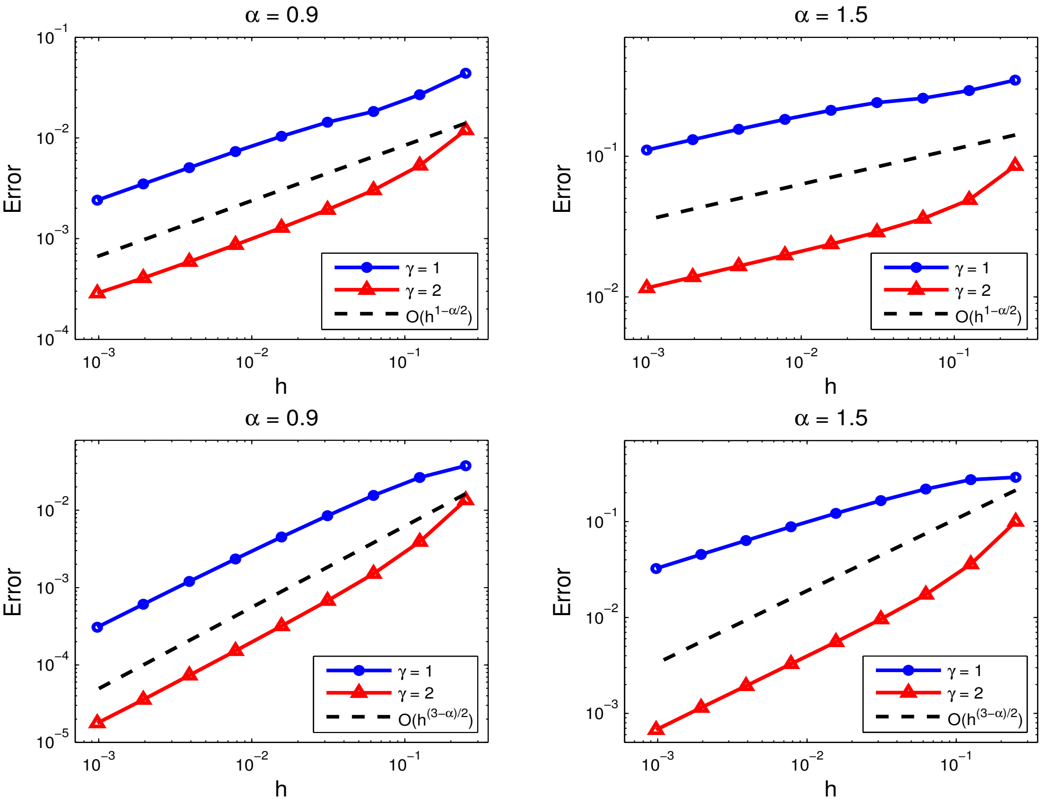

Figure 5.2. Numerical errors of the weighted linear interpolation method for $\gamma = 1$ and 2 with $u \in C^{1,\alpha/2}(\mathbb{R}^2)$ defined in (4.52) with $s = 1$. The errors are defined in l_∞-norm (top row) or l_2-norm (bottom row).

Table 5.3. Numerical errors by weighted linear interpolation method for $u \in C^{3,\alpha/2}(\mathbb{R}^2)$.

α \ h		1/16	1/32	1/64	1/128	1/256	1/512	1/1024
0.2		6.856E-5	1.658E-5	4.105E-6	1.022E-6	2.541E-7	6.228E-8	1.434E-8
	c.r.		2.0476	2.0143	2.0057	2.0081	2.0286	2.1190
1		2.784E-3	6.418E-4	1.536E-4	3.749E-5	9.212E-6	2.237E-6	5.044E-7
	c.r.		2.1168	2.0631	2.0345	2.0248	2.0422	2.1487
1.9		6.361E-2	1.531E-2	4.178E-3	1.110E-3	2.816E-4	6.932E-5	1.626E-5
	c.r.		2.0551	1.8733	1.9120	1.9791	2.0222	2.0922

Table 5.3 presents numerical errors $\|(-\Delta)^{\alpha/2}u - (-\Delta)_{h,\gamma}^{\alpha/2}u\|_{l_\infty(\Omega)}$ and convergence rates of the weighted linear interpolation method for various α by taking u in (4.52) with $s = 3$, where the splitting parameter is taken to be $\gamma = 2$. We find that for the same mesh size h, the larger the parameter α, the bigger the numerical errors. It also shows that the convergence rates of the weighted linear interpolation method is $O(h^2)$ for any $\alpha \in (0, 2)$.

In this section, we proposed a weighted linear interpolation method to discretize the fractional Laplacian. Similar to the weighted trapezoidal method, we treated the hyper-singular integral as a weighted integral of function $\psi_\gamma(\mathbf{x}, \boldsymbol{\xi})$ with a weight function $|\boldsymbol{\xi}|^{\gamma-(2+\alpha)}$. The accuracy of this method is studied analytically and numerically, and it has the same accuracy as the weighted trapezoidal method.

6. COMPARISON OF NUMERICAL METHODS

Because of the nonlocality, so far, numerical methods for discretizing the fractional Laplacian (1.2) still remain scant, with the main numerical challenge stemming from the approximation of the hypersingular integral. In Sections 3–5, we proposed two novel finite difference methods which are both based on the weighted integrals. These two methods provide the same convergence rates for discretizing the fractional Laplacian. In application, the weighted trapezoidal method has lower computational cost than the weighted linear interpolation method especially in higher dimensions. The higher computational cost arises from the computation of more double/triple integrals in 2D/3D. In this section, we will compare our weighted trapezoidal method with a finite difference method proposed in [49], which is the current state of the art for directly discretizing the fractional Laplacian. In addition, we will compare the two finite difference methods with a finite element method for solving the fractional Poisson equation. For brevity, numerical results will only be presented in one dimension and same conclusions can be extended to higher dimensions.

6.1. NUMERICAL METHODS

In this section, we will first revisit the finite difference and finite element methods in the literature for discretizing the fractional Laplacian and solving the fractional Poisson equation.

6.1.1. Interpolation Method. The finite difference method proposed in [49] is the current state-of-the-art method for directly discretizing the fractional Laplacian. In the following context, we refer this method as the *linear interpolation method*. Notice that, the linear interpolation method is similar to our weighted linear interpolation method in Section 5. However, our weighted linear interpolation method has higher order accuracy than the linear interpolation method, which will be justified in our numerical examples. For brevity, we only address the differences between the linear interpolation method and the weighted linear interpolation method in the following. We will also explain the reason which causes the lower accuracy of the linear interpolation method.

Following the same line as the weighted trapezoidal and weighted linear interpolation methods in Sections 3–5, the fractional Laplacian is rewritten as in (3.2). The difference is from the approximation of the first integral. In [49], the first integral in (3.2) is split into two parts, i.e.,

$$\int_0^L \psi_0(x,\xi)\,\xi^{-(1+\alpha)}\,d\xi = \int_0^h \psi_0(x,\xi)\,\xi^{-(1+\alpha)}\,d\xi + \int_h^L \psi_0(x,\xi)\,\xi^{-(1+\alpha)}\,d\xi. \tag{6.1}$$

For the sake of convenience, here we adopt the notation (3.5) in Chapter 3 and define

$$\psi_0(x,\xi) = u(x-\xi) - 2u(x) + u(x+\xi).$$

Then the integral on $[0, h]$ is approximated by

$$\int_0^h \psi_0(x,\xi)\xi^{-(1+\alpha)}d\xi = \int_0^h \psi_2(x,\xi)\xi^{1-\alpha}d\xi \approx \frac{1}{2-\alpha}h^{2-\alpha}\psi_2(x,h),$$

i.e., the same approximation as in (3.11). The second integral is approximated by

$$\int_h^L \psi_0(x,\xi)\,\xi^{-(1+\alpha)}\,d\xi \;\approx\; \sum_{i=1}^{N}\psi_0(x,\xi_i)\int_h^L \frac{\phi_i(\xi)}{\xi^{1+\alpha}}d\xi. \tag{6.2}$$

where ϕ_i is defined in (5.2).

Finally, following the same line as the weighted linear interpolation method, the fully discretization of the fractional Laplacian is

$$(-\Delta)_{h,\gamma}^{\alpha/2}u_i = -C_{1,\alpha}\Big(a_0\,u_i + \Big(\sum_{j=1}^{i-1} a_j u_{i-j} + \sum_{j=1}^{N-1-i} a_j u_{i+j}\Big)\Big),$$

for $i = 1, 2, \ldots, N-1$, where

$$a_i = \begin{cases} \displaystyle\int_h^L \phi_1(\xi)\, \xi^{-(1+\alpha)}\, d\xi + \frac{h^{-\alpha}}{2-\alpha}, & \text{for} \quad i = 1, \\ \displaystyle\int_h^L \phi_i(\xi)\, \xi^{-(1+\alpha)}\, d\xi, & \text{for} \quad i = 2, \ldots, N, \end{cases}$$

$$a_0 = -2\left(\sum_{i=1}^{N} a_i + \frac{1}{\alpha L^\alpha}\right).$$

For smooth enough functions $u \in C^{3,\alpha/2}(\mathbb{R})$, our weighted linear interpolation method has second order accuracy. However, as is shown in [49, Lemma 3] that for $u \in C^4(\mathbb{R})$, the accuracy of the linear interpolation method is $\mathcal{O}(h^{2-\alpha})$ for $\alpha \in (0, 2)$. Compare to our weighted linear interpolation method, the main reason that causes the lower accuracy of the linear interpolation method is that the second integral in (6.1) is not rewritten as a weighted integral with optimal choice of γ (i.e. $\gamma = 1$ or 2). Instead, the splitting parameter is chosen as $\gamma = 0$ in (6.2) to approximate the integral on $[h, L]$, which can be partially viewed as one of the non-optimal cases of the weighted linear interpolation. As proved in Theorem 5.1.2, the weighted linear interpolation method has the second order of accuracy only when $\gamma = 1$ or 2 is chosen.

6.1.2. Finite Element Method. We introduce a finite element method to solve the fractional Poisson equation with extended homogeneous boundary condition [2, 72, 75]:

$$(-\Delta)^{\alpha/2} u(x) = f(x), \qquad \text{for } x \in \Omega, \tag{6.3}$$

$$u(x) = 0, \qquad \text{for } x \in \Omega^c, \tag{6.4}$$

where f is a function on Ω and $\Omega^c = \mathbb{R}\backslash\Omega$ represents the complement of Ω. The extended Dirichlet condition is readily incorporated in the definition (1.2) of the fractional Laplacian, by simply replacing $u(y)$ with 0 in the integral when $y \notin \Omega$.

The nature functional space for the fractional Poisson equation (6.3)-(6.4) is

$$H_\Omega^{\alpha/2}(\mathbb{R}) = \left\{ v \in H^{\alpha/2}(\mathbb{R}) : v = 0 \text{ in } \mathbb{R}\backslash\Omega \right\}, \tag{6.5}$$

where the space $H^{\alpha/2}(\mathbb{R})$ is denoted as

$$H^{\alpha/2}(\mathbb{R}) = \{v \in l_2(\mathbb{R}) : |v|_{H^{\alpha/2}(\mathbb{R})} < \infty\},$$

with $|\cdot|_{H^{\alpha/2}(\mathbb{R})}$ being the Aronszajn–Slobodeckij seminorm [2], defined as

$$|v|_{H^{\alpha/2}(\mathbb{R})} = \left(\iint_{\mathbb{R}^2} \frac{(v(x) - v(y))^2}{|x-y|^{1+\alpha}} dxdy \right)^{1/2}.$$

The space $(H_\Omega^{\alpha/2}(\mathbb{R}), \|\cdot\|_{H^{\alpha/2}(\mathbb{R})})$ is a Hilbert space, equipped with the norm

$$\|v\|_{H^{\alpha/2}(\mathbb{R})} = \|v\|_{l_2(\mathbb{R})} + |v|_{H^{\alpha/2}(\mathbb{R})}.$$

Then, the weak formulation of (6.3)-(6.4) is to find $u \in H_\Omega^{\alpha/2}(\mathbb{R})$ such that

$$\frac{C_{1,\alpha}}{2} \int_{\mathbb{R}} \int_{\mathbb{R}} \frac{u(y) - u(x)}{|y-x|^{1+\alpha}} \left(v(y) - v(x) \right) \, dy \, dx = \int_\Omega f(x) v(x) \, dx, \quad \forall v \in H_\Omega^{\alpha/2}(\mathbb{R}). \tag{6.6}$$

The existence and uniqueness of the solution to (6.6) has been proven in [85, Theorem 6.3.4]. Let $A(\cdot,\cdot) : H_\Omega^{\alpha/2}(\mathbb{R}) \times H_\Omega^{\alpha/2}(\mathbb{R}) \longrightarrow \mathbb{R}$ and $F(\cdot) : H_\Omega^{\alpha/2}(\mathbb{R}) \longrightarrow \mathbb{R}$ respectively be the bilinear form and functional associated with the weak formulation (6.6),

$$A(u,v) := \frac{C_{1,\alpha}}{2} \int_{\mathbb{R}} \int_{\mathbb{R}} \frac{u(y) - u(x)}{|y-x|^{1+\alpha}} \left(v(y) - v(x) \right) \, dy \, dx \quad \text{and} \quad F(v) := \int_\Omega f(x) v(x) \, dx,$$

then the problem (6.6) is equivalent to find $u \in H_\Omega^{\alpha/2}(\mathbb{R})$ such that

$$A(u,v) = F(v), \quad \forall v \in H_\Omega^{\alpha/2}(\mathbb{R}). \tag{6.7}$$

For an integer $N > 0$, take the mesh size $h = \frac{b-a}{h}$, consider the uniform partition $x_i = a + ih$ for $i = 0, 1, \ldots, N$. Choose the finite element space $H^{\alpha/2}_{\Omega,h}(\mathbb{R}) = \text{span}\{\phi_1, \ldots, \phi_N\} \subset H^{\alpha/2}_{\Omega}(\mathbb{R})$, where the basis functions ϕ_i $(i = 1, 2, \ldots, N)$ are the standard "hat" functions. The corresponding Galerkin approximation of problem (6.7) is to find $u_h \in H^{\alpha/2}_{\Omega,h}(\mathbb{R})$, such that

$$A(u_h, v_h) = F(v_h), \quad \forall v_h \in H^{\alpha/2}_{\Omega,h}(\mathbb{R}), \tag{6.8}$$

Computationally, we express the approximate solution u_h as a linear combination of the basis functions ϕ_j, written as $u_h(x) = \sum_{j=1}^{N-1} U_j \phi_j(x)$, where u_j is an approximation to $u(x_j)$. Choose the test function $v_h = \phi_i(x)$. Substitute u_h and v_h into (5.7), we obtain

$$\sum_{j=1}^{N-1} A(\phi_j, \phi_i) U_j = F(\phi_i), \quad \text{for} \quad i = 1, 2, \ldots, N-1. \tag{6.9}$$

Let $U = (u_1, u_2, \ldots, u_{N-1})^T$, and $F = (F(\phi_1), F(\phi_2), \ldots, F(\phi_{N-1}))^T$. Then (6.9) can be simply written as $AU = F$, where $A = \{A(\phi_j, \phi_i)\}_{i,j=1}^{N-1}$ is the stiffness matrix for the finite element approximation.

The integral $F(\phi_i)$ in (6.9) can be either integrated exactly or numerically approximated by the Gauss quadrature rules (i.e. a four-point Gauss quadrature is applied in [25]). In contrast, the double integral

$$A_{ij} := A(\phi_j, \phi_i) = \frac{C_{1,\alpha}}{2} \int_{\mathbb{R}} \int_{\mathbb{R}} \frac{\phi_j(y) - \phi_j(x)}{|y - x|^{1+\alpha}} \left(\phi_i(y) - \phi_i(x)\right) \, dy \, dx \tag{6.10}$$

must be treated carefully, because of the singularity in the integrand. The traditional Gauss quadrature method fails to provide accurate approximation to (6.10). In fact, the integral in (5.9) can be found analytically. If the function ϕ_i is chosen as in (5.2), then we get for

$\alpha \in (0,2)\backslash\{1\}$, the coefficient matrix $A = (A_{ij}^{(\alpha)})$, where

$$A_{ij}^{(\alpha)} = \frac{C_{1,\alpha} h^{1-\alpha}}{\alpha(1-\alpha)(2-\alpha)(3-\alpha)} \begin{cases} 2^{4-\alpha} - 8, & j = i, \\ 3^{3-\alpha} - 2^{5-\alpha} + 7, & |j-i| = 1, \\ \sum_{k=0}^{4} (-1)^k \binom{4}{k} (|i-j| + 2 - k)^{3-\alpha}, & |j-i| > 1, \end{cases} \tag{6.11}$$

and for $\alpha = 1$, the coefficient matrix $A = (A_{ij}^{(1)})$,

$$A_{ij}^{(1)} = \frac{C_{1,\alpha}}{2} \begin{cases} 8 \ln 2, & j = i, \\ 9 \ln 3 - 16 \ln 2, & |j-i| = 1, \\ 16 \ln 4 - 36 \ln 3 + 24 \ln 2, & |j-i| = 2, \\ \sum_{k=0}^{4} (-1)^k \binom{4}{k} (|i-j| + 2 - k)^{3-\alpha} \ln(|i-j| + 2 - k), & |j-i| > 2. \end{cases} \tag{6.12}$$

where $\binom{m}{n}$ denotes the binomial coefficient. It is clear that as $\alpha \to 1$, we have $A_{ij}^{(\alpha)} \to A_{ij}^{(1)}$. and the matrix A is symmetric and Toeplitz for all $\alpha \in (0,2)$.

Even though the entries of matrix A can be calculated exactly, the implementation of the finite element scheme is not straightforward. The problem arises from the computations of the summations in (6.11) and (6.12), when $|i-j|$ is large (i.e. $|i-j| = 8192$) and α is small (i.e. $\alpha = 0.1$). In such situation, the machine errors pollute the true value of $A_{ij}^{(\alpha)}$, and thus affect the accuracy of the method.

To resolve this issue, we rewrite the summation in the last line of (6.11) into an infinite sum by applying the binomial theorem which cancels all the higher power terms $|i-j|^{3-\alpha}$. For example, for $\alpha \neq 1$ and $|j-i| > 1$, the summation can be rewritten as

$$\sum_{k=0}^{4} (-1)^k \binom{4}{k} (|i-j| + 2 - k)^{3-\alpha} = 2 \sum_{n=2}^{\infty} \binom{3-\alpha}{2n} |i-j|^{(3-\alpha)-2n} \cdot (2^{2n} - 4). \tag{6.13}$$

The expressions on the left- and right-hand sides of (6.13) are equivalent, but their computer implementation lead to different results, and their difference is significant when α is small and $|i - j|$ is large. To illustrate it, we take $\alpha = 0.1$ and $|i - j| = 8192$, the direct implementation of the left-hand side gives 1.2207×10^{-4}, but the true value is around -2.45847×10^{-5}, and the relative error of direct implementation is around 5.9653.

The right hand side of (6.13) has infinite summation terms. In practice, we truncate it to a finite sum by taking the number of the summation terms large enough, and thus the error from the truncation is neglected.

6.2. NUMERICAL COMPARISONS

In this section, we will compare the performance of the weighted trapezoidal method, linear interpolation method and the finite element method. The first two examples compare the accuracy of the two finite difference methods in approximating the fractional Laplacian, the last two examples compare the accuracy of the three numerical methods for solving the fractional Poisson equation with extended homogeneous Dirichlet boundary condition.

6.2.1. Discretization of the Fractional Laplacian. In this section, we will compare our weighted trapezoidal method with the linear interpolation method proposed in [49], which is the current state of the art for directly discretizing the fractional Laplacian.

Example 1. We will compare the accuracy of the two finite difference schemes acting on a bump function

$$u(x) = \begin{cases} e^{-1/(1-x^2)}, & \text{if} \quad x \in (-1, 1), \\ 0, & \text{otherwise}. \end{cases} \tag{6.14}$$

which is compactly supported on $[-1, 1]$ and is in $C^\infty(\mathbb{R})$. Since the fractional Laplacian of $u(x)$ can not be computed analytically, in the following comparison, we will use the numerical solution with a very small mesh size $h = 2^{-13}$ to be the exact solution.

The top two rows of Figure 6.1 show the fractional Laplacian of the bump function by using the weighted trapezoidal method. The bottom row presents the numerical errors in l_∞-norm and l_2-norm of the weighted trapezoidal method [33] and the interpolation method [49], where an order line of 2 is also presented for easy comparison. The accuracy of

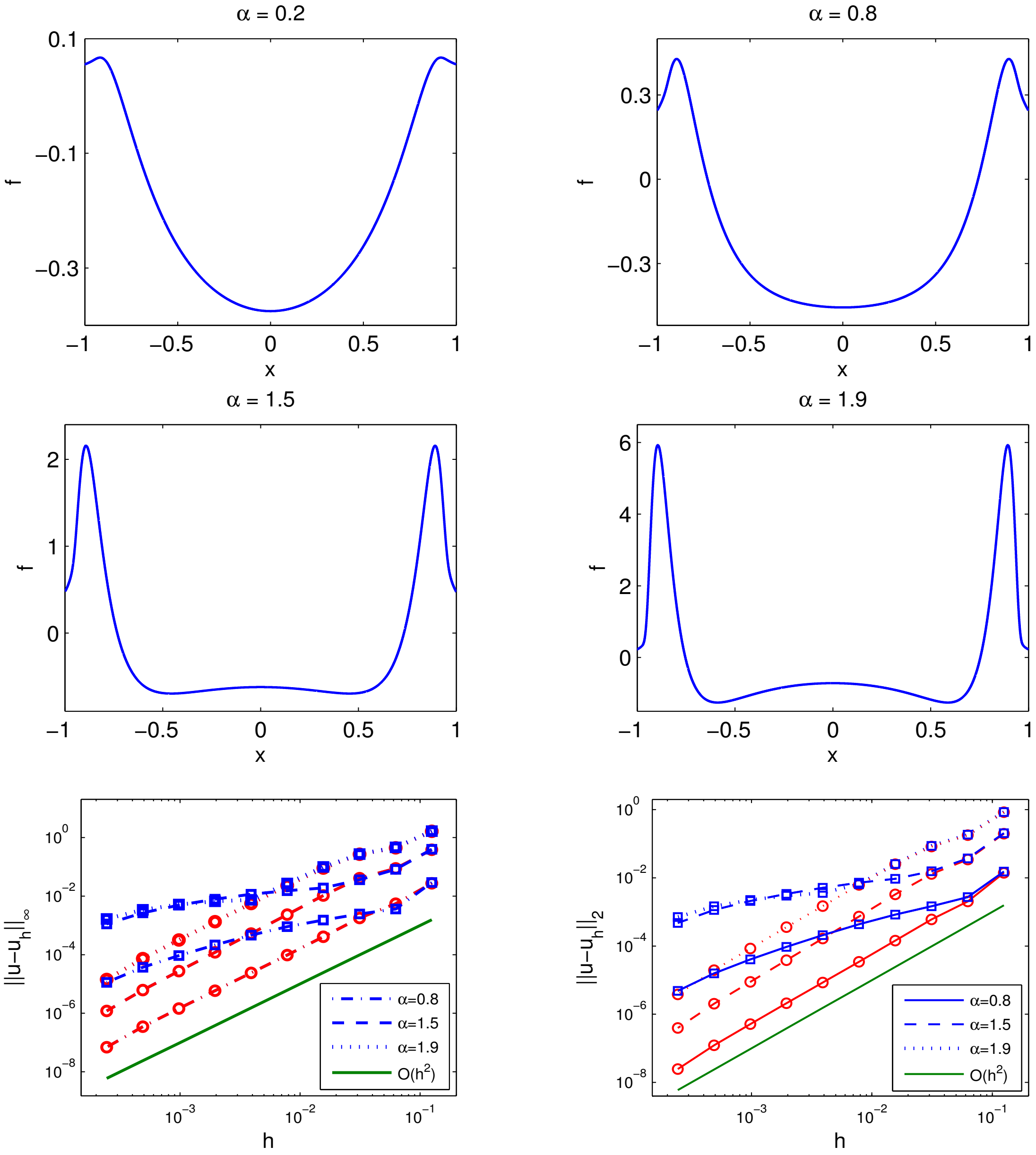

Figure 6.1. Bump function and numerical errors. Top two rows: The fractional Laplacian of the bump function by using weighted trapezoidal method for $\alpha = 0.2, 0.8, 1.5, 1.9$. Bottow row: Numerical errors in computing $(-\Delta)^{\alpha/2}u(x)$ by the weighted trapezoidal method [33] ('○') and the linear interpolation method in [49] ('□') in l_∞-norm (left) and l_2-norm (right).

the weighted trapezoidal method is $O(h^2)$, which is much better than the accuracy of the linear interpolation method of order $O(h^{2-\alpha})$. The numerical results justify the analytical results for the accuracy of these two methods. Although the smoothness of the solution in this example has been increased to $u \in C^\infty(\mathbb{R})$, the accuracy of the linear interpolation method is still $O(h^{2-\alpha})$ and the weighted trapezoidal method is of order $O(h^2)$. In other words, increase the smoothness of the function won't help to increase the accuracy of both methods. Moreover, the accuracy of the linear interpolation method depends on α, which decreases to $O(1)$ as $\alpha \to 2^-$. Although the accuracy can be improved to $O(h^{3-\alpha})$ by using a quadratic interpolation, the accuracy for $\alpha \in (1, 2)$ is still less that the second order, and significantly complicates the simulations. It also shows that for each $\alpha \in (0, 2)$, when a small mesh size h is used, the errors of the weighted trapezoidal method are much smaller than those from the interpolation method. For both of these two methods, the errors are smaller for smaller α.

Example 2. We consider a function u of the form:

$$u(x) = \begin{cases} -(1-x^2)^s, & \text{for } x \in \Omega = (-1, 1), \\ 0, & \text{otherwise}, \end{cases} \qquad x \in \mathbb{R}, \tag{6.15}$$

for $s \in \mathbb{N}$. It is easy to verify that $u(x) \in C^{s-\epsilon}(\mathbb{R})$ for any $\epsilon \in (0, s)$, and it is compactly supported on $(-1, 1)$. The fractional Laplacian of $u(x)$ can be computed analytically [35]:

$$(-\Delta)^{\alpha/2}u(x) = \frac{-2^\alpha \Gamma(\frac{\alpha+1}{2})\Gamma(s+1)}{\sqrt{\pi}\Gamma(-\frac{\alpha}{2}+s+1)} \cdot {}_2F_1\left(\frac{\alpha+1}{2}, -s+\frac{\alpha}{2}; \frac{1}{2}; |x|^2\right), \tag{6.16}$$

where ${}_2F_1$ denotes the Gauss hypergeometric function. In this example, we will test the accuracy of our method for $s = 2, 3, 4$.

The first column of Figure 6.2 compares the numerical errors $\|(-\Delta)^{\alpha/2}u - (-\Delta)_h^{\alpha/2}u\|_{l_2(\Omega)}$ by the two finite difference methods for $\alpha = 0.6, 1.3, 1.9$. We can get similar conclusions as in Example 1 that the weighted trapezoidal method always has higher order accuracy and smaller errors than the linear interpolation method in all the cases for $\alpha = 0.6, 1.5, 1.9$ in a given example for $s = 2, 3$, or 4. And both of these two methods have smaller errors for smaller α. In addition, as we improving the smoothness of the function u, the accuracy of the weighted trapezoidal method is increasing. However, the accuracy of the linear interpolation has no significant increment as the weighted trapezoidal method, and it can not exceed $O(h^{2-\alpha})$.

The second column compares the convergence rates of the weighted trapezoidal method and the linear interpolation method in l_∞-norm, where u is defined in (6.15) with $s = 2, 3, 4$ from top to bottom. In all of the cases for $s = 2, 3, 4$, the weighted trapezoidal method has higher order accuracy than the linear interpolation method. As the function u becoming smoother (increasing s from 2 to 4), the accuracy of the weighted trapezoidal method becoming higher for a fixed α in a given norm. However, the accuracy of the linear interpolation method has no such significant improvement and the order $O(h^{2-\alpha})$ is the highest accuracy it can reach.

6.2.2. Solution of the Fractional Poisson Equation. We will compare the accuracy of the three numerical methods in solving the fractional Poisson equation with homogeneous Dirichlet boundary condition (6.3)-(6.4). In our numerical simulations, we evaluate $F(\phi_i)$ exactly. Functions with different smoothness conditions will be considered.

Example 3. We will compare the accuracy of the three numerical methods in solving the following fractional Poisson equation,

$$\begin{cases} (-\Delta)^{\alpha/2} u = 1, & \text{in } \Omega, \\ u = 0, & \text{in } \mathbb{R} \backslash \Omega. \end{cases} \tag{6.17}$$

This particular example (6.17) has been studied and applied in various areas. For example, it can be used to estimate the first eigenvalues of the fractional Laplacian [35]. Also, its solution $u(x) \in C^{0,\alpha/2}(\mathbb{R})$ can be understood from particle point of view, which represents the probability density of the first exit time of the symmetric $\alpha-$stable Lévy process from

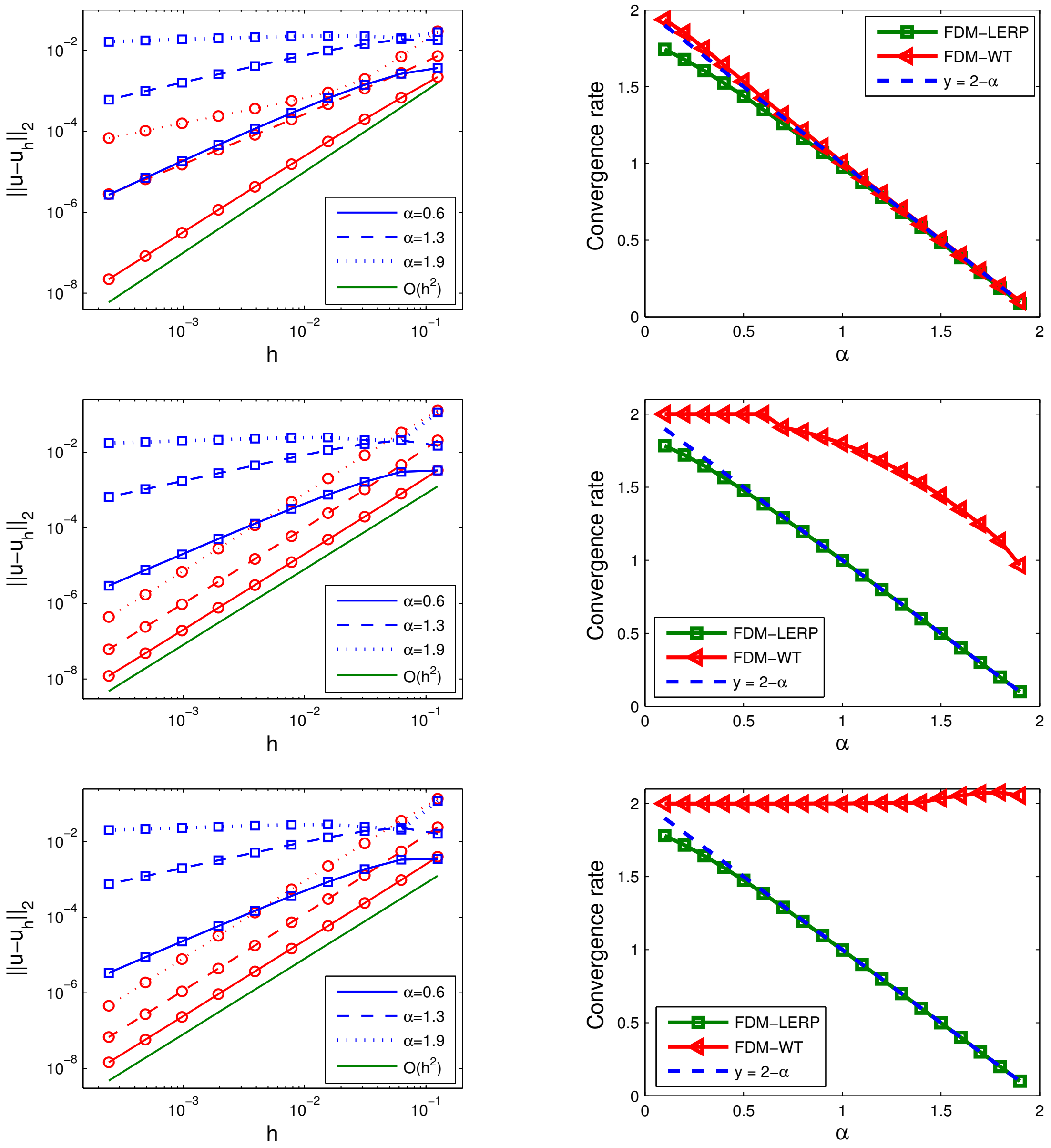

Figure 6.2. Comparison of numerical errors and rates. The first column: Numerical errors in computing $(-\Delta)^{\alpha/2}u(x)$ by the weighted trapezoidal method [33] (‘○’) and the linear interpolation method in [49] (‘□’) in l_2-norm. The second column: Convergence rates of the weighted trapezoidal method and the linear interpolation method in l_∞-norm. The function $u(x)$ is defined in (6.15) with $s = 2, 3, 4$ from top to bottom.

domain $[-1, 1]$ [49]. The analytical solution of (6.17) can be found exactly by taking $s = \alpha/2$ in (6.16), which is

$$u(x) = (1 - x^2)^{\alpha/2}/\Gamma(\alpha + 1), \qquad \text{for} \quad x \in (-1, 1).$$

Figure 6.3 shows the errors in l_2-norm of the finite element method, weighted trapezoidal method and linear interpolation method for $\alpha = 0.6, 1, 1.5, 1.9$.

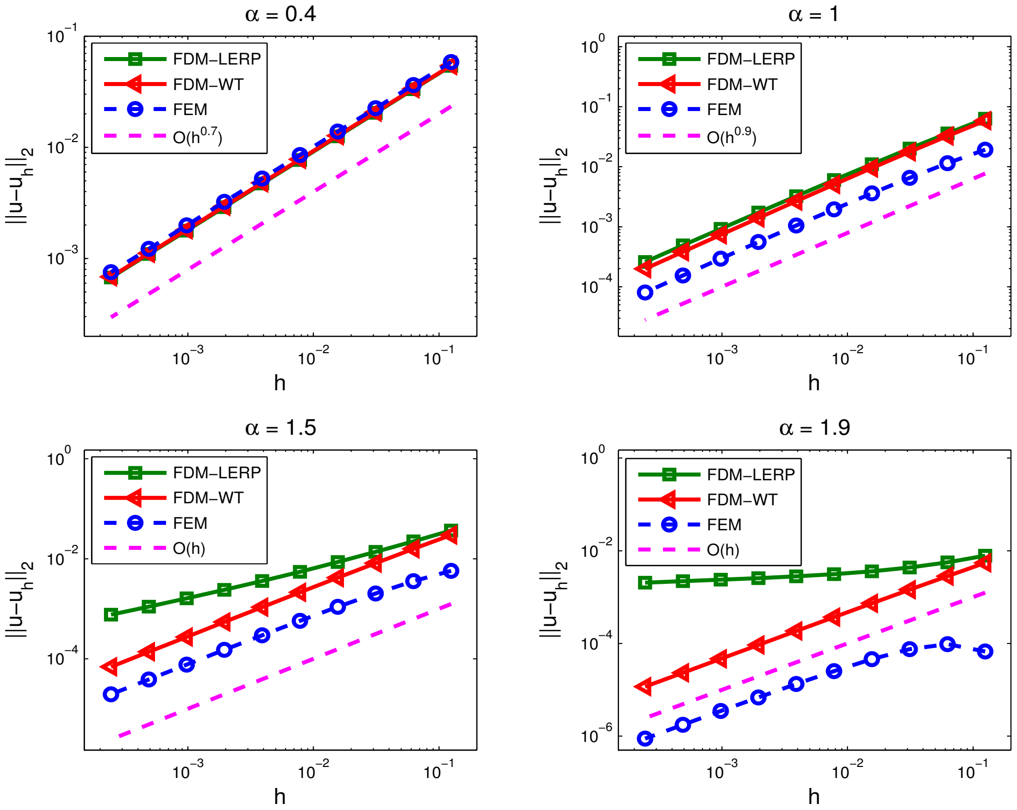

Figure 6.3. Numerical errors in solving the fractional Poisson equation (6.17) by finite element method, weighted trapezoidal method, and linear interpolation method.

In all these cases, the accuracy of the finite element method and the weighted trapezoidal method are almost the same and better than the linear interpolation method. The accuracy of all these three methods are decreasing as α increasing. Compare among the three methods, the errors of the finite element method are smaller than the other methods for larger α, i.e. $0.5 \leq \alpha < 2$, but are larger for smaller α.

To see the accuracy more clear for each method, we define the convergence rate of a given method as $O(h^{g(\alpha)})$, where the power of h is a function with respect to α. Figure 6.4 describes the relation between the accuracy and the fractional power α for each numerical method. The left panel of Figure 6.4 shows the values of $g(\alpha)$ versus the fractional power α for the numerical errors in l_∞-norm. All these three numerical methods are convergent, because all the values of $g(\alpha)$ are positive. The accuracy of the finite element and the weighted trapezoidal method are of order $O(h^{\alpha/2})$ for any $\alpha \in (0, 2)$. The linear interpolation method has accuracy $O(h^{\alpha/2})$ for $0 < \alpha \leq 1.3$, however, for larger α, i.e. $1.4 \leq \alpha < 2$, the accuracy is decreasing, and the order is around $O(h^{1.1(2-\alpha)})$ which approaches to $O(1)$ as $\alpha \to 2^-$.

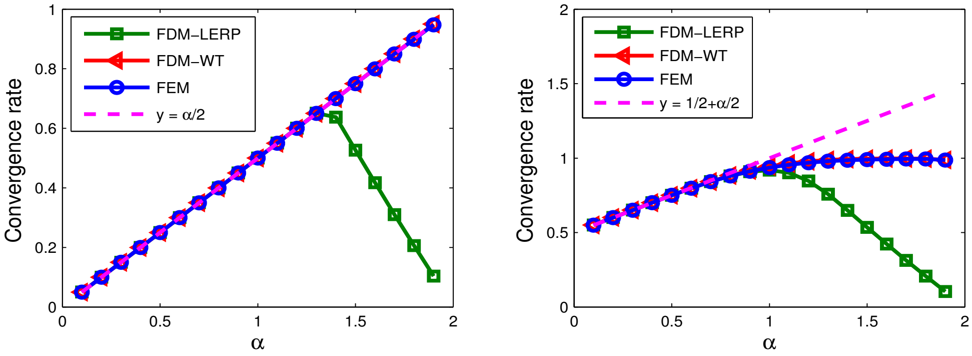

Figure 6.4. Relations between the convergence rates for solving the fractional Poisson equation and the fractional power α in l_∞-norm (left) and in l_2-norm (right).

The right panel of Figure 6.4 shows the values of $g(\alpha)$ versus the fractional power α for the numerical errors in l_2-norm. In the cases of small α, i.e. $\alpha \in (0, 0.8]$, all these three numerical methods have the accuracy of order $O(h^{(\alpha+1)/2})$. However, for $\alpha > 0.8$, the accuracy of the weighted trapezoidal method and the finite element method increase slower, and stop increasing at the rate of order $O(h)$ for $\alpha \in (1, 2)$. The accuracy of the linear interpolation method starts decreasing at $\alpha = 1$, and based on our extensive numerical experiments, in the cases for $\alpha \in [1.3, 2)$, we conjecture that the linear interpolation method has the accuracy of order $O(h^{1.1(2-\alpha)})$. In addition, the accuracy of the finite element method and the weighted trapezoidal method are the same in all the cases for $\alpha \in (0, 2)$ in l_∞-norm and l_2-norm and are better than the linear interpolation method for larger α. Furthermore, as mentioned in [49], because of the singularity of the solution at the boundaries, both of the quadratic and the linear interpolation provide the same convergence rate in l_∞-norm. In other words, increasing the order of the interpolation weight functions won't increase the accuracy.

In sum, the numerical experiment shows that for $u(x) \in C^{0,\alpha/2}(\mathbb{R})$, the weighted trapezoidal method is more preferable, since it has higher accuracy than the linear interpolation method and is easier to implement than the finite element method.

Example 4. We compare the accuracy of the three numerical methods in solving the fractional Poisson equation (6.3)-(6.4) of the following form

$$\begin{cases} (-\Delta)^{\alpha/2} u(x) = f(x), & \text{for} \quad x \in (-1, 1), \\ u(x) = 0, & \text{for} \quad x \in \mathbb{R} \backslash (-1, 1). \end{cases} \tag{6.18}$$

with

$$f(x) = C \cdot {}_2F_1\left(\frac{\alpha+1}{2}, -3; \frac{1}{2}; |x|^2\right), \qquad \text{where} \quad C = \frac{2^\alpha \Gamma(\frac{\alpha+1}{2}) \Gamma(4 + \frac{\alpha}{2})}{\sqrt{\pi}\Gamma(4)}.$$

The solution can be found analytically as

$$u(x) = -(1 - x^2)^{3+\alpha/2}, \qquad \text{for} \quad x \in (-1, 1),$$

which is in $C^{3,\alpha/2}(\mathbb{R})$. Based on Theorem 3.2.4 and the convergence theorem in [34], the weighted trapezoidal method is shown of second order accuracy in both discretizing the fractional Laplacian and solving the fractional Poisson equation under the smoothness condition that $u \in C^{3,\alpha/2}(\mathbb{R})$. The following figures numerically compare the accuracy of the three numerical methods.

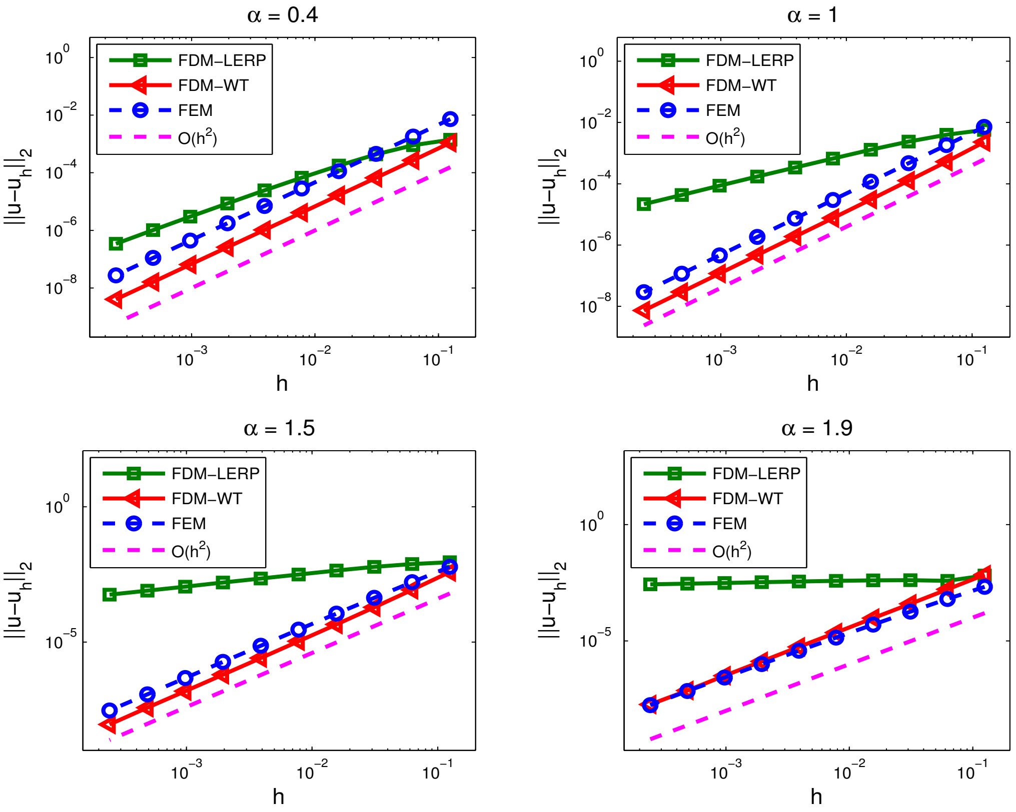

Figure 6.5. Numerical errors in solving the fractional Poisson problem (6.18) by finite element method, weighted trapezoidal method, and linear interpolation method for $\alpha = 0.4, 1, 1.5, 1.9$.

Figure 6.5 presents the numerical errors of the finite element method, weighted trapezoidal method and linear interpolation method in l_2-norm, where an order line of 2 is also presented for easy comparison. For all $\alpha \in (0, 2)$, the weighted trapezoidal method is precisely of second order accuracy. The finite element method has second order accuracy for all $\alpha \in (0, 1)$, but it has accuracy slightly less than second order for some cases of $\alpha \in (1, 2)$. Moreover, in most of the cases (i.e. $\alpha = 0.4, 1, 1.5$), the errors of the finite element method are greater than the errors of the weighted trapezoidal method for a given mesh size. The linear interpolation method has the lowest accuracy among these three numerical methods. and its accuracy decreases as α increases, especially as $\alpha \to 2$, i.e. in the case of $\alpha = 1.9$, the accuracy decreases to $O(1)$.

To find the relation between the accuracy of the three numerical methods and the fractional power α, we define the accuracy to be $O(h^{g(\alpha)})$ as we did in Example 3. Figure 6.6 shows the function $g(\alpha)$ versus the fractional power α. Both of the weighted trapezoidal method and the finite element method have second order accuracy for all $\alpha \in (0, 2)$ in both l_∞-norm and l_2-norm. The linear interpolation method has lower accuracy, and we make the following conjecture that it has accuracy of order $O(h^{2-\alpha})$ in both of l_∞-norm and l_2-norm for larger α, i.e. $0.6 < \alpha < 2$.

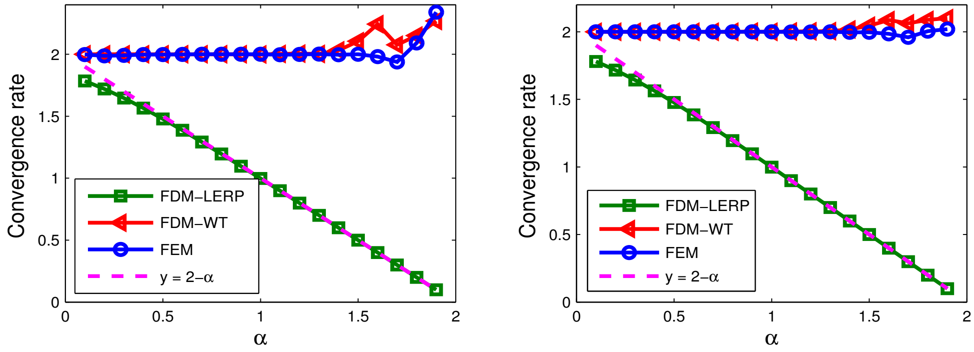

Figure 6.6. Relations between the convergence rates for solving the fractional Poisson equation and the fractional power α in l_∞-norm (left) and in l_2-norm (right).

As a conclusion, for function $u(x) \in C^{3,\alpha/2}(\mathbb{R})$, the finite element method and the weighted trapezoidal method are much more accurate than the linear interpolation method, especially for large α. As mentioned in [49], applying the quadratic interpolation may increase the accuracy to $O(h^{3-\alpha})$ for smooth enough functions (i.e. $u(x) \in C^4(\mathbb{R})$). However, using a quadratic interpolation significantly complicates the simulations, and the accuracy for $\alpha \in (1, 2)$ is still less than second order. Moreover, with almost the same accuracy, the weighted trapezoidal method is easier to implement than the finite element method.

In summary, the weighted trapezoidal method is the most effective method among the three numerical methods in both of discretizing the fractional Laplacian and solving the fractional Poisson equation with homogeneous Dirichlet boundary condition in terms of its accuracy and computational complexity. By choosing the splitting parameter optimally, we are able to overcome the α-dependence of the accuracy estimate for $u \in C^{3,\alpha/2}(\mathbb{R})$ (a less severe smoothness assumption than that used in [49]), achieving an accuracy of $O(h^2)$ *for any* $\alpha \in (0, 2)$. Moreover, while generally giving rise to a full matrix, as is usually the case for discretization of nonlocal operators, the discretized fractional Laplacian is a symmetric Toeplitz matrix, whose structure can be exploited through the use of fast algorithms [15, 81, 84] which we will introduce in the next section.

7. THE FAST IMPLEMENTATION

The nonlocal nature of the fractional Laplacian $(-\Delta)^{\alpha/2}$ raises questions about computational efficiency, especially in high dimensions. Usually, the matrix representation of the fractional Laplacian A is a dense matrix, and it is costly to directly compute the matrix-vector product $A\mathbf{u}$. In this section, we propose an efficient method to compute the matrix-vector product $A\mathbf{u}$. It is based on the properties of the Toeplitz and circulant matrices and the fast Fourier transformation (FFT) [15, 81, 84]. The main merits of our algorithm include that it requires less computational cost and memory, and thus it is more efficient in solving higher dimensional problems. Moreover, our method can be easily implemented in computer codes.

7.1. ONE-DIMENSIONAL CASE

Denote the column vector $\mathbf{u}_x = (u_1, u_2, \ldots, u_{N_x-1})^T$. Next, we will focus on the fast algorithm to the matrix-vector product $\mathrm{A}^{(1)}\mathbf{u}_x$, where $\mathrm{A}^{(1)}$ is the matrix define in (3.10). Notice that the matrix $\mathrm{A}^{(1)}$ is Toeplitz, which can be embedded into a double sized circulant matrix $\mathrm{C}^{(1)}$ as

$$\mathrm{C}^{(1)}_{(2N_x-2)\times(2N_x-2)} = \begin{pmatrix} A^{(1)} & T^{(1)} \\ T^{(1)} & A^{(1)} \end{pmatrix}_{(2N_x-2)\times(2N_x-2)}, \tag{7.1}$$

where the matrix $T^{(1)}$ is also a Toeplitz matrix defined by

$$\mathrm{T}^{(1)}_{(N_x-1)\times(N_x-1)} = \begin{pmatrix} 0 & a_{N_x-2} & \cdots & a_2 & a_1 \\ a_{N_x-2} & 0 & a_{N_x-2} & \dots & a_2 \\ \vdots & \ddots & \ddots & \ddots & \vdots \\ a_2 & \dots & a_{N_x-2} & 0 & a_{N_x-2} \\ a_1 & a_2 & \dots & a_{N_x-2} & 0 \end{pmatrix}_{(N_x-1)\times(N_x-1)} . \tag{7.2}$$

The circulant matrix $C^{(1)}$ can be decomposed as

$$C^{(1)} = F^{-1}\mathrm{diag}(F \cdot \mathbf{c})F, \tag{7.3}$$

where F is an $2(N_x - 1) \times 2(N_x - 1)$ discrete Fourier transform matrix, denoted as

$$F(j,k) = \frac{1}{\sqrt{2(N_x-1)}} \exp\left(\frac{2\pi ijk}{2(N_x-1)}\right), \qquad 0 \le j,k \le 2(N_x - 1), \tag{7.4}$$

and $\mathbf{c} = (a_0, a_1, \dots, a_{N_x-2}, 0, a_{N_x-2}, \dots, a_1)^T$, which is the first column of the circulant matrix $C^{(1)}$. By introducing a vector

$$\mathbf{v}_x = \begin{pmatrix} \mathbf{u}_x \\ 0 \end{pmatrix}_{2(N_x-1)\times 1} , \tag{7.5}$$

The matrix-vector product A$\mathbf{u}_x$ is extended to a double sized matrix-vector product $C\mathbf{v}_x$, and can be decomposed as

$$C^{(1)}\mathbf{v}_x = F^{-1}\mathrm{diag}(F \cdot \mathbf{c})F\mathbf{v}_x. \tag{7.6}$$

In application, matrix operations F and F^{-1} can be realized by the fast Fourier transform and inverse fast Fourier transform respectively, and thus the computational cost is $O(2(N_x - 1)\log(2(N_x - 1)))$. The first $(N_x - 1)$ elements of $C^{(1)}\mathbf{v}_x$ gives the matrix-vector product $\mathrm{A}^{(1)}\mathbf{u}_x$.

7.2. TWO-DIMENSIONAL CASE

Denote the column vector $\mathbf{u}_{x,y}$ as

$$\mathbf{u}_{x,y} = (\mathbf{u}_{x,1}^T, \mathbf{u}_{x,2}^T, \ldots, \mathbf{u}_{x,N_y-1}^T)^T,$$

where $\mathbf{u}_{x,j} = (u_{1,j}, u_{2,j}, \ldots, u_{N_x-1,j})^T$ for $j = 1, 2, \ldots, N_y - 1$. Next, we will focus on the fast algorithm for the matrix-vector product $\mathrm{A}^{(2)}\mathbf{u}_{x,y}$.

Notice that the matrix $\mathrm{A}_{x,j}$ $(j = 0, \ldots, N_y - 2)$ is Toeplitz, which can be embedded into a double sized circulant matrix $C_{x,j}$ as

$$\mathrm{C}_{x,j} = \begin{pmatrix} \mathrm{A}_{x,j} & \mathrm{T}_{x,j} \\ \mathrm{T}_{x,j} & \mathrm{A}_{x,j} \end{pmatrix}_{(2N_x-2)\times(2N_x-2)}, \tag{7.7}$$

where the matrix $\mathrm{T}_{x,j}$ is also a Toeplitz matrix defined by

$$\mathrm{T}_{x,j} := \begin{pmatrix} 0 & a_{N_x-2,j} & \ldots & a_{2j} & a_{1j} \\ a_{N_x-2,j} & 0 & a_{N_x-2,j} & \cdots & a_{2j} \\ \vdots & \ddots & \ddots & \ddots & \vdots \\ a_{2j} & \ldots & a_{N_x-2,j} & 0 & a_{N_x-2,j} \\ a_{1j} & a_{2j} & \ldots & a_{N_x-2,j} & 0 \end{pmatrix}_{(N_x-1)\times(N_x-1)},$$

The original matrix $\mathrm{A}^{(2)}$ is now extended to a matrix with each block be a circulant matrix, i.e.

$$\widetilde{\mathrm{C}}^{(2)} = \begin{pmatrix} C_{x,0} & C_{x,1} & \dots & C_{x,N_y-3} & C_{x,N_y-2} \\ C_{x,1} & C_{x,0} & C_{x,1} & \cdots & C_{x,N_y-3} \\ \vdots & \ddots & \ddots & \ddots & \vdots \\ C_{x,N_y-3} & \dots & C_{x,1} & C_{x,0} & C_{x,1} \\ C_{x,N_y-2} & C_{x,N_y-3} & \dots & C_{x,1} & C_{x,0} \end{pmatrix}_{[(2N_x-2)\times(N_y-1)]^2}.$$

Notice that the matrix $\widetilde{\mathrm{C}}^{(2)}$ is a block-Toeplitz matrix, which can be embedded into a double sized block-circulant matrix $\mathrm{C}^{(2)}$ as

$$\mathrm{C}^{(2)} = \begin{pmatrix} \widetilde{\mathrm{C}}^{(2)} & \widetilde{\mathrm{T}}^{(2)} \\ \widetilde{\mathrm{T}}^{(2)} & \widetilde{\mathrm{C}}^{(2)} \end{pmatrix}_{[(2N_x-2)\times(2N_y-2)]^2}.$$

where

$$\widetilde{\mathrm{T}}^{(2)} = \begin{pmatrix} 0 & C_{x,N_y-2} & \dots & C_{x,2} & C_{x,1} \\ C_{x,N_y-2} & 0 & C_{x,N_y-2} & \cdots & C_{x,2} \\ \vdots & \ddots & \ddots & \ddots & \vdots \\ C_{x,2} & \dots & C_{x,N_y-2} & 0 & C_{x,N_y-2} \\ C_{x,1} & C_{x,2} & \dots & C_{x,N_y-2} & 0 \end{pmatrix}_{[(2N_x-2)\times(N_y-1)]^2}.$$

Now, we focus on the fast implementation of the matrix-vector product $\mathrm{C}^{(2)}\mathbf{u}_{x,y}$. We notice that the matrix $\mathrm{C}^{(2)}$ is a block circulant matrix with circulant blocks (BCCB). The fast algorithm is available in the literature [24, Theorem 5.8.1] for computing this type of matrix. The circulant matrix $\mathrm{C}^{(2)}$ can be decomposed as

$$\mathrm{C}^{(2)} = (F_{2N_y-2} \otimes F_{2N_x-2})^{-1}\mathrm{diag}(\hat{\mathbf{c}})(F_{2N_x-2} \otimes F_{2N_x-2}),$$

where $F_{2N_y-2} \otimes F_{2N_x-2}$ represent the 2D discrete Fourier transform matrix, and $\hat{\mathbf{c}}$ is denoted by

$$\hat{\mathbf{c}} = (F_{2N_y-2} \otimes F_{2N_x-2})\mathbf{c}.$$

with $\mathbf{c}$ be the first column of $\mathrm{C}^{(2)}$.

By introducing double sized vectors

$$\mathbf{v}_{x,j} = \begin{pmatrix} \mathbf{u}_{x,j} \\ 0 \end{pmatrix}_{(2N_x-2)\times 1}, \quad \text{for} \quad j = 1, 2, \ldots, N_y - 1,$$

we define a vector

$$\widetilde{\mathbf{v}}_{x,y} = (\mathbf{v}_{x,1}^T, \mathbf{v}_{x,2}^T, \ldots, \mathbf{v}_{x,N_y-1}^T)^T,$$

and then further introduce a double sized vector

$$\mathbf{v}_{x,y} = \begin{pmatrix} \widetilde{\mathbf{v}}_{x,y} \\ 0 \end{pmatrix}_{[(2N_x-2)\times(2N_y-2)]\times 1}.$$

The matrix-vector product $\mathrm{A}^{(2)}\mathbf{u}_{x,y}$ is extended to a quadruple sized matrix-vector product $\mathrm{C}^{(2)}\mathbf{v}_{x,y}$, and can be decomposed as

$$\mathrm{C}^{(2)}\mathbf{v}_{x,y} = (F_{2N_y-2} \otimes F_{2N_x-2})^{-1} \left[\mathrm{diag}((F_{2N_y-2} \otimes F_{2N_x-2}) \cdot \mathbf{c})\right] (F_{2N_y-2} \otimes F_{2N_x-2})\mathbf{v}_{x,y}.$$

In application, the matrices $F_{2N_y-2} \otimes F_{2N_x-2}$ and $(F_{2N_y-2} \otimes F_{2N_x-2})^{-1}$ can be realized as the 2D Fourier transform and inverse Fourier transform respectively, we thus can apply the fast Fourier transform (FFT) to reduce the computation to only $O((2N_x - 2) \times (2N_y -$

2) $\log((2N_x - 2) \times (2N_y - 2)))$ operations. Finally, the first $(2N_x - 2) \times (N_y - 1)$ elements of $\mathrm{C}^{(2)}\mathbf{v}_{x,y}$ provide the matrix-vector product $\widetilde{\mathrm{C}}^{(2)}\widetilde{\mathbf{v}}_{x,y}$. And then extracting the first, third, $\ldots$, $(N_y - 1)$-th $(N_x - 1)$ elements of $\widetilde{\mathrm{C}}^{(2)}\widetilde{\mathbf{v}}_{x,y}$, we get the matrix-vector product $\mathrm{A}^{(2)}\mathbf{u}_{x,y}$.

7.3. THREE-DIMENSIONAL CASE

The fast implementation in 3D case can be done in the similar way as in 2D case. Denote the $(N_x - 1)(N_y - 1)(N_z - 1)$-by-1 column vector $\mathbf{u}_{x,y,z}$,

$$\mathbf{u}_{x,y,z} = (\mathbf{u}^T_{x,y,1}, \mathbf{u}^T_{x,y,2}, \ldots, \mathbf{u}^T_{x,y,N_3-1})^T. \tag{7.8}$$

where $\mathbf{u}_{x,y,k}$ for $k = 1, 2, \ldots, N_z - 1$ are defined by

$$\mathbf{u}_{x,y,k} = (\mathbf{u}^T_{x,1,k}, \mathbf{u}^T_{x,2,k}, \ldots, \mathbf{u}^T_{x,N_y-1,k})^T, \tag{7.9}$$

and the vector $\mathbf{u}_{x,j,k} = (u_{1,j,k}, u_{2,j,k}, \ldots, u_{N_x-1,j,k})^T$ for $j = 1, 2, \ldots, N_y-1$, $k = 1, 2, \ldots, N_z-1$. Next, we will focus on the fast algorithm for the matrix-vector product $\mathrm{A}^{(3)}\mathbf{u}_{x,y,z}$.

Notice that the matrix $\mathrm{A}_{x,j,k}$ $(j = 0, \ldots, N_y-2,\ k = 0, \ldots, N_z-2)$ is Toeplitz, which can be embedded into a double sized circulant matrix $C_{x,j,k}$ as

$$\mathrm{C}_{x,j,k} = \begin{pmatrix} \mathrm{A}_{x,j,k} & \mathrm{T}_{x,j,k} \\ \mathrm{T}_{x,j,k} & \mathrm{A}_{x,j,k} \end{pmatrix}_{(2N_x-2)\times(2N_x-2)}, \tag{7.10}$$

where the matrix $\mathrm{T}_{x,j,k}$ is also a Toeplitz matrix defined by

$$\mathrm{T}_{x,j,k} := \begin{pmatrix} 0 & a_{N_x-2,j,k} & \ldots & a_{2jk} & a_{1jk} \\ a_{N_x-2,jk} & 0 & a_{N_x-2,jk} & \cdots & a_{2jk} \\ \vdots & \ddots & \ddots & \ddots & \vdots \\ a_{2jk} & \ldots & a_{N_x-2,jk} & 0 & a_{N_x-2,jk} \\ a_{1jk} & a_{2jk} & \ldots & a_{N_x-2,jk} & 0 \end{pmatrix}_{(N_x-1)\times(N_x-1)},$$

The matrix $\mathrm{A}_{x,y,k}$ then can be extended to a matrix with each block be a circulant matrix, i.e.

$$\widetilde{\mathrm{C}}_{x,y,k} = \begin{pmatrix} C_{x,0,k} & C_{x,1,k} & \ldots & C_{x,N_y-3,k} & C_{x,N_y-2,k} \\ C_{x,1,k} & C_{x,0,k} & C_{x,1,k} & \cdots & C_{x,N_y-3,k} \\ \vdots & \ddots & \ddots & \ddots & \vdots \\ C_{x,N_y-3,k} & \ldots & C_{x,1,k} & C_{x,0,k} & C_{x,1,k} \\ C_{x,N_y-2,k} & C_{x,N_y-3,k} & \ldots & C_{x,1,k} & C_{x,0,k} \end{pmatrix}_{[(2N_x-2)\times(N_y-1)]^2}.$$

Notice that for a given $k = 0, 1, \ldots, N_z - 2$, the matrix $\widetilde{\mathrm{C}}_{x,y,k}$ is a block-Toeplitz matrix, which can be embedded into a double sized block-circulant matrix $\mathrm{C}_{x,y,k}$ as

$$\mathrm{C}_{x,y,k} = \begin{pmatrix} \widetilde{\mathrm{C}}_{x,y,k} & \widetilde{\mathrm{T}}_{x,y,k} \\ \widetilde{\mathrm{T}}_{x,y,k} & \widetilde{\mathrm{C}}_{x,y,k} \end{pmatrix}_{[(2N_x-2)\times(2N_y-2)]^2}.$$

where

$$\widetilde{\mathrm{T}}_{x,y,k} = \begin{pmatrix} 0 & C_{x,N_y-2,k} & \cdots & C_{x,2,k} & C_{x,1,k} \\ C_{x,N_y-2,k} & 0 & C_{x,N_y-2,k} & \cdots & C_{x,2,k} \\ \vdots & \ddots & \ddots & \ddots & \vdots \\ C_{x,2,k} & \cdots & C_{x,N_y-2,k} & 0 & C_{x,N_y-2,k} \\ C_{x,1,k} & C_{x,2,k} & \cdots & C_{x,N_y-2,k} & 0 \end{pmatrix}_{[(2N_x-2)\times(N_y-1)]^2} .$$

The original matrix $\mathrm{A}^{(3)}$ is extended to a matrix with each block be a circulant matrix, i.e.

$$\widetilde{\mathrm{C}}_{x,y,z} = \begin{pmatrix} C_{x,y,0} & C_{x,y,1} & \cdots & C_{x,y,N_z-3} & C_{x,y,N_z-2} \\ C_{x,y,1} & C_{x,y,0} & C_{x,y,1} & \cdots & C_{x,y,N_z-3} \\ \vdots & \ddots & \ddots & \ddots & \vdots \\ C_{x,y,N_z-3} & \cdots & C_{x,y,1} & C_{x,y,0} & C_{x,y,1} \\ C_{x,y,N_z-2} & C_{x,y,N_z-3} & \cdots & C_{x,y,1} & C_{x,y,0} \end{pmatrix}_{[(2N_x-2)\times(N_y-1)]^2} .$$

Notice that the matrix $\widetilde{\mathrm{C}}_{x,y,z}$ is a block-Toeplitz matrix, which can be embedded into a double sized block-circulant matrix $\mathrm{C}_{x,y,z}$ as

$$\mathrm{C}_{x,y,z} = \begin{pmatrix} \widetilde{\mathrm{C}}_{x,y,z} & \widetilde{\mathrm{T}}_{x,y,z} \\ \widetilde{\mathrm{T}}_{x,y,z} & \widetilde{\mathrm{C}}_{x,y,z} \end{pmatrix}_{[(2N_x-2)\times(2N_y-2)\times(2N_z-2)]^2} .$$

where

$$\widetilde{\mathrm{T}}_{x,y,z} = \begin{pmatrix} 0 & C_{x,y,N_z-2} & \cdots & C_{x,y,2} & C_{x,y,1} \\ C_{x,y,N_z-2} & 0 & C_{x,y,N_z-2} & \cdots & C_{x,y,2} \\ \vdots & \ddots & \ddots & \ddots & \vdots \\ C_{x,y,2} & \cdots & C_{x,y,N_z-2} & 0 & C_{x,y,N_z-2} \\ C_{x,y,1} & C_{x,y,2} & \cdots & C_{x,y,N_z-2} & 0 \end{pmatrix}_{[(2N_x-2)\times(N_y-1)]^2} .$$

Now, we focus on the fast implementation of the matrix-vector product $\mathrm{C}_{x,y,z}\mathbf{u}_{x,y,z}$. The circulant matrix $\mathrm{C}_{x,y,z}$ can be decomposed as

$$\mathrm{C}_{x,y,z} = (F_{2N_z-2} \otimes F_{2N_y-2} \otimes F_{2N_x-2})^{-1}\mathrm{diag}(\hat{\mathbf{c}})(F_{2N_z-2} \otimes F_{2N_y-2} \otimes F_{2N_x-2}),$$

where $F_{2N_z-2} \otimes F_{2N_y-2} \otimes F_{2N_x-2}$ represent the 3D discrete Fourier transform matrix, and $\hat{\mathbf{c}}$ is denoted by

$$\hat{\mathbf{c}} = (F_{2N_z-2} \otimes F_{2N_y-2} \otimes F_{2N_x-2})\mathbf{c}.$$

with $\mathbf{c}$ be the first column of $\mathrm{C}_{x,y,z}$.

By introducing double sized vectors

$$\mathbf{v}_{x,j,k} = \begin{pmatrix} \mathbf{u}_{x,j,k} \\ 0 \end{pmatrix}_{(2N_x-2)\times 1}, \quad \text{for} \quad j = 1, 2, \ldots, N_y - 1, \quad k = 1, 2, \ldots, N_z - 1,$$

we first define a vector

$$\widetilde{\mathbf{v}}_{x,y,k} = (\mathbf{v}^T_{x,1,k}, \mathbf{v}^T_{x,2,k}, \ldots, \mathbf{v}^T_{x,N_y-1,k})^T,$$

and then further introduce a double sized vector

$$\mathbf{v}_{x,y,k} = \begin{pmatrix} \widetilde{\mathbf{v}}_{x,y,k} \\ 0 \end{pmatrix}_{[(2N_x-2)\times(2N_y-2)]\times 1},$$

we then define another vector

$$\widetilde{\mathbf{v}}_{x,y,z} = (\mathbf{v}^T_{x,y,1}, \mathbf{v}^T_{x,y,2}, \ldots, \mathbf{v}^T_{x,y,N_y-1})^T,$$

and at the end we introduce a double sized vector

$$\mathbf{v}_{x,y,z} = \begin{pmatrix} \widetilde{\mathbf{v}}_{x,y,z} \\ 0 \end{pmatrix}_{[(2N_x-2)\times(2N_y-2)\times(2N_z-2)]\times 1},$$

The matrix-vector product $\mathrm{A}_{x,y,z}\mathbf{u}_{x,y,z}$ is extended to a octuple sized matrix-vector product $\mathrm{C}_{x,y,z}\mathbf{v}_{x,y,z}$, and can be decomposed as

$$\mathrm{C}_{x,y,z}\mathbf{v}_{x,y,z} = (F_{2N_z-2} \otimes F_{2N_y-2} \otimes F_{2N_x-2})^{-1} \left[\mathrm{diag}(\hat{\mathbf{c}})\right] (F_{2N_z-2} \otimes F_{2N_y-2} \otimes F_{2N_x-2})\mathbf{v}_{x,y,z}.$$

In application, the matrices $F_{2N_z-2} \otimes F_{2N_y-2} \otimes F_{2N_x-2}$ and $(F_{2N_z-2} \otimes F_{2N_y-2} \otimes F_{2N_x-2})^{-1}$ can be realized as the 3D Fourier transform and inverse Fourier transform respectively, we thus can apply the fast Fourier transform (FFT) to reduce the computation to only $O((2N_x-2)(2N_y-2)(2N_z-2)\log((2N_x-2)(2N_y-2)(2N_z-2)))$ operations.

The matrix representation of the fractional Laplacian A is a full dense matrix which leads to large computational cost if compute the matrix-vector product $A\mathbf{u}$ directly. In this section, we propose a fast algorithm to compute the matrix-vector product $A\mathbf{u}$. In one dimension, the fractional Laplacian $A^{(1)}$ discretized by the weighted trapezoidal or weighted linear interpolation method is a symmetric Toeplitz matrix. It is known that any Toeplitz matrix can be embedded into a double sized circulant matrix which can be diagonalized by a discrete Fourier transform. Therefore, it allows us to use the fast Fourier transform (FFT) which reduces the computational cost to $O((2N_x - 2)\log((2N_x - 2)))$. Moreover, this fast algorithm can be directly extended to higher dimensions.

8. THE FRACTIONAL SCHRÖDINGER EQUATION IN AN INFINITE POTENTIAL WELL

The fractional Schrödinger equation, a fundamental model of fractional quantum mechanics, was first introduced by Laskin as the path integral of the Lévy trajectories [63, 64]. It is a nonlocal integro-differential equation that is expected to reveal some novel phenomena of the quantum mechanics. Recently, the fractional Schrödinger equation in an infinite potential well has attracted massive attention from both physicists and mathematicians, and numerous studies have been devoted to finding its eigenvalues and eigenfunctions; see [8, 27, 47, 48, 50, 59, 63, 66] and references therein. However, one continuing debate in the literature is whether the fractional linear Schrödinger equation in an infinite potential well has the same eigenfunctions as those of its standard (non-fractional) counterpart [8, 27, 47, 50, 66]. The main goal of this section is to numerically study the ground and first excited states of the fractional Schrödinger equation in an infinite potential well so as to advance the understanding of this problem.

We consider the one-dimensional (1D) fractional Schrödinger equation of the following form [8, 47, 48, 50, 53, 63, 66]:

$$i\partial_t\psi(x,t) = (-\Delta)^{\alpha/2}\psi + V(x)\psi + \beta|\psi|^2\psi, \qquad x \in \mathbb{R}, \quad t > 0, \tag{8.1}$$

where $\psi(x,t)$ is a complex-valued wave function, and $i = \sqrt{-1}$ is the imaginary unit. The constant $\beta \in \mathbb{R}$ describes the strength of local (or short-range) interactions between particles (positive for repulsive interactions and negative for attractive interactions), and $V(x)$ represents an external trapping potential. In this section, we are interested in the case that $\beta \geq 0$ and $V(x)$ is an infinite potential well (also known as a box potential), i.e.,

$$V(x) = \begin{cases} 0, & \text{if } |x| < L, \\ \infty, & \text{otherwise}, \end{cases} \qquad x \in \mathbb{R}, \tag{8.2}$$

with the constant $L > 0$. The fractional Laplacian $(-\Delta)^{\alpha/2}$ is defined in (1.2) through the hyper-singular integral.

The fractional Schrödinger equation (8.1) has two conserved quantities: the L_2 *norm, or mass of the wave function*, which we will take to be normalized,

$$\|\psi(\cdot,t)\|^2 := \int_{\mathbb{R}} |\psi(x,t)|^2 dx = \int_{\mathbb{R}} |\psi(x,0)|^2 dx = \|\psi(\cdot,0)\|^2 = 1, \qquad t \geq 0, \tag{8.3}$$

and *the total energy*

$$E(\psi(\cdot,t)) := \int_{\mathbb{R}} \left(\psi^*(-\Delta)^{\alpha/2}\psi + V(x)|\psi|^2 + \frac{\beta}{2}|\psi|^4\right) dx = E(\psi(\cdot,0)),\ t \geq 0, \tag{8.4}$$

where f^* represents the complex conjugate of a function f.

8.1. STATIONARY STATES

To find the stationary states of (8.1), we write the wave function in the form:

$$\psi(x,t) = e^{-i\mu t}\phi(x), \qquad x \in \mathbb{R}, \quad t \geq 0, \tag{8.5}$$

where $\mu \in \mathbb{R}$. Substituting the ansatz (8.5) into (8.1) and taking the normalized mass conservation (8.3) into account, we obtain the following time-independent fractional Schrödinger equation:

$$\mu\phi(x) = (-\Delta)^{\alpha/2}\phi + V(x)\phi + \beta|\phi|^2\phi, \qquad x \in \mathbb{R} \tag{8.6}$$

with the constraint

$$\|\phi\|^2 = \int_{\mathbb{R}} |\phi(x)|^2 dx = 1. \tag{8.7}$$

This is a constrained nonlocal nonlinear eigenvalue problem, and the eigenvalue μ (also called *chemical potential*) can be calculated from its corresponding eigenfunction $\phi(x)$ via:

$$\mu = \mu(\phi) := \int_{\mathbb{R}} \left(\phi^*(-\Delta)^{\alpha/2}\phi + V(x)|\phi|^2 + \beta|\phi|^4\right) dx = E(\phi) + \frac{\beta}{2}\int_{\mathbb{R}} |\phi|^4 dx. \tag{8.8}$$

In fact, the eigenfunctions of (8.6)–(8.7) are equivalent to the critical points of the energy $E(\phi)$ over the set $\mathcal{T} = \{\phi(x) \mid \|\phi\|^2 = 1 \text{ and } E(\phi) < \infty\}$.

Let $\Omega = (-L, L)$ denote the interval where the potential $V(x) \equiv 0$. For $x \in \Omega^c$, the potential $V(x) = \infty$; consequently, the wave function $\phi(x) \equiv 0$, since the mass $\|\phi\|^2 = 1$ and the energy $E(\phi) < \infty$ [63, 64]. Hence, solving for the eigenfunctions of the fractional Schrödinger equation in an infinite potential well reduces to finding $\phi(x)$ for $x \in \Omega$, under the condition $\phi(x) \equiv 0$ for $x \in \Omega^c$. The corresponding eigenvalue can be calculated by

$$\mu = \mu(\phi) := \int_{\mathbb{R}} \left(\phi^*(-\Delta)^{\alpha/2}\phi + \beta|\phi|^4\right) dx. \tag{8.9}$$

8.1.1. Standard Schrödinger Equation.

For the convenience of readers, we briefly review the eigenvalues and eigenfunctions of the standard Schrödinger equation in this section. First, we present their exact solutions in the linear ($\beta = 0$) cases. In the nonlinear cases with $\beta \gg 1$, we obtain the leading-order approximations to the eigenvalues and eigenfunctions. These analytical results can be used to compare with those of the fractional Schrödinger equation so as to understand the differences between the standard and fractional Schrödinger equations.

Replacing $(-\Delta)^{\alpha/2}$ in (8.6) with the standard Laplacian $-\Delta$, we obtain the standard time-independent Schrödinger equation. Its eigenfunction $\phi(x)$ for $x \in \Omega$ can be found by solving the following problem [7, 42, 50]:

$$\mu\phi(x) = -\Delta\phi(x) + \beta|\phi(x)|^2\phi(x), \qquad x \in \Omega, \tag{8.10}$$

along with the homogeneous Dirichlet boundary conditions

$$\phi(L) = \phi(-L) = 0, \tag{8.11}$$

and the constraint of normalization

$$\|\phi\|^2 = \int_{-L}^{L} |\phi(x)|^2 dx = 1. \tag{8.12}$$

Note that the two-point homogeneous Dirichlet boundary conditions are applied to (8.10), as the standard Laplacian Δ is a local operator. That is, the eigenvalues and eigenfunctions of the standard Schrödinger equation can be solved in a piecewise approach – finding the solutions inside of the infinite potential well and then using their continuity at $x = \pm L$ to match up with those outside the potential well.

In the linear (i.e., $\beta = 0$) cases, the eigenvalues and eigenfunctions of (8.10)–(8.12) can be found exactly. For $x \in \Omega$, the s-th eigenfunction has the form [7, 42, 63]:

$$\phi_s(x) = \sqrt{\frac{1}{L}} \sin\left[\frac{(s+1)\pi}{2}\Big(1 + \frac{x}{L}\Big)\right], \quad x \in \Omega, \qquad s \in \mathbb{N} \cup \{0\}, \tag{8.13}$$

and the corresponding eigenvalue is

$$\mu_s := \mu(\phi_s) = \left[\frac{(s+1)\pi}{2L}\right]^2, \qquad s \in \mathbb{N} \cup \{0\}, \tag{8.14}$$

where the ground states and the first excited states correspond to $s = 0$ and $s = 1$, respectively.

In the nonlinear ($\beta \neq 0$) cases, the constrained eigenvalue problem (8.10)–(8.12) cannot be exactly solved. However, the results in (8.13)–(8.14) provide a good approximation to the eigenfunctions and eigenvalues in the weakly interacting regimes with $\beta \sim o(1)$. In the strongly repulsive interacting cases (i.e., $\beta \gg 1$), we can find the leading-order approximation (also called *Thomas–Fermi approximation*) to the s-th ($s \in \mathbb{N}^0$) eigenfunction [7, 93]:

$$\begin{aligned}\phi_s(x) \approx \phi_s^a(x) = \sqrt{\frac{\mu_s^a}{\beta}}\Bigg\{ \sum_{r=0}^{\lfloor (s+1)/2 \rfloor} \tanh\left[\frac{\sqrt{2\mu_s^a}L}{2}\left(\left(1+\frac{x}{L}\right) - \frac{4r}{s+1}\right)\right] \\ + \sum_{r=0}^{\lfloor s/2 \rfloor} \tanh\left[\frac{\sqrt{2\mu_s^a}L}{2}\left(\frac{4r+2}{s+1} - \left(1+\frac{x}{L}\right)\right)\right] - c_s \tanh\left(\frac{\sqrt{2\mu_s^a}L}{2}\right)\Bigg\}, \qquad (8.15)\end{aligned}$$

for $x \in \Omega$, where $\lfloor r \rfloor$ defines the floor function of a real number r, and the constant

$$c_s = \begin{cases} 1, & \text{if } s \text{ is even,} \\ 0, & \text{if } s \text{ is odd.} \end{cases}$$

Correspondingly, the leading-order approximation to the s-th eigenvalue is

$$\mu_s \approx \mu_s^a = \frac{1}{L^2}\left[\frac{L}{2}\beta + (s+2)\sqrt{\beta L + (s+2)^2} + (s+2)^2\right], \qquad s \in \mathbb{N} \cup \{0\}. \quad (8.16)$$

The approximations in (8.15) show that when $\beta \gg 1$, all the stationary states of the standard nonlinear Schrödinger equation have boundary layers. In addition to boundary layers, for $s \geq 1$, the excited states also have inner layers, and the number of inner layers in the s-th excited state is equal to s.

8.1.2. Fractional Schrödinger Equation. In contrast to the standard Schrödinger equation, the stationary states of the fractional Schrödinger equation have not been well understood yet. Unlike the standard Laplacian, the fractional Laplacian is a nonlocal operator describing long-range interactions. For example, the function $(-\Delta)^{\alpha/2}\phi(x)$ depends on the wave function $\phi(y)$ not only for $y \in \Omega$, but also for $y \notin \Omega$, albeit $\phi(y) \equiv 0$ when $y \notin \Omega$. As a result, we consider the following eigenvalue problem in the fractional cases:

$$\mu\phi(x) = (-\Delta)^{\alpha/2}\phi(x) + \beta|\phi(x)|^2\phi(x), \qquad x \in \Omega, \quad \alpha \in (0, 2), \tag{8.17}$$

with the *nonlocal boundary condition* [28, 83]

$$\phi(x) = 0, \qquad x \in \mathbb{R}\backslash\Omega, \tag{8.18}$$

and the normalization constraint

$$\|\phi\|^2 = \int_{-L}^{L} |\phi(x)|^2 \, dx = 1. \tag{8.19}$$

Here, we take the nonlocal character of the fractional Laplacian into account and apply the nonlocal boundary condition (8.18) to the time-independent fractional Schrödinger equation (8.17).

Due to the nonlocality, it is very challenging to solve (8.17)–(8.19) analytically, and thus the analytical solutions to its eigenvalues and eigenfunctions still remain an open question. For the eigenvalues, so far only some estimates and asymptotic approximations are reported in the literature for the linear ($\beta = 0$) cases [3, 17, 35, 59]. For the convenience of readers, we will review the main results in the following remarks:

Remark 8.1.1. (Lower and upper bounds of eigenvalues) *Various lower and upper bound estimates are reported for the eigenvalue μ_s of the fractional linear ($\beta = 0$) Schrödinger equation in an interval of length l [3, 17, 35, 58, 59]. In [17, p.9], the lower and upper bounds of the eigenvalue μ_s are given by*

$$\frac{1}{2}\left[\frac{(s+1)\pi}{l}\right]^{\alpha} \le \mu_s \le \left[\frac{(s+1)\pi}{l}\right]^{\alpha}, \qquad s \in \mathbb{N} \cup \{0\}, \quad \alpha \in (0, 2], \tag{8.20}$$

where $\alpha = 2$ corresponds to the standard Schrödinger equation. When $s = 0$ (corresponding to the ground states), different estimates can be found in [3, 35], i.e.,

$$\frac{(\alpha+1)(\alpha+2)(6-\alpha)}{(12+14\alpha)}\,p(\alpha) \;\le\; \mu_0 \;\le\; \frac{B(\frac{1}{2}, 1+\frac{\alpha}{2})}{B(\frac{1}{2}, 1+\alpha)}\,p(\alpha), \tag{8.21}$$

with

$$p(\alpha) = \frac{2^\alpha\,\Gamma(1+\frac{\alpha}{2})\,\Gamma(\frac{1+\alpha}{2})}{\Gamma(\frac{1}{2})}, \tag{8.22}$$

for any $\alpha \in (0,2)$, where $B(a,b)$ defines the Beta function of a and b. Note that the lower and upper bounds in (8.21) are, respectively, from [35] and [3].

It is easy to verify that when $s = 0$, the estimates in (8.21) are much sharper than those in (8.20) for most of α (except those close to 2), but the estimate in (8.20) is valid for any $s \in \mathbb{N} \cup \{0\}$. To the best of our knowledge, the lower and upper bounds in (8.21) are the best analytical estimates for the eigenvalue μ_0 in the literature. More numerical estimates on lower and upper bounds can be found in [58, 59] and references therein.

Remark 8.1.2. (Asymptotic approximations of eigenvalues) *When $\beta = 0$, the asymptotic approximation of the s-th eigenvalue of the fractional linear Schrödinger equation in an interval $(-1, 1)$ is given by [59, Theorem 1]:*

$$\mu_s = \left[\frac{(s+1)\pi}{2} - \frac{(2-\alpha)\pi}{8}\right]^\alpha + O\left(\frac{2-\alpha}{(s+1)\sqrt{\alpha}}\right), \qquad \alpha \in (0,2], \qquad s \ge (C/\alpha)^{\frac{3}{2\alpha}}$$

with C a positive constant. When $\alpha = 2$, it gives the exact eigenvalue $\mu_s = [(s+1)\pi/2]^2$ (for $s \in \mathbb{N} \cup \{0\}$) of the standard linear Schrödinger equation in an infinite potential well.

In section 8.3, we will compare these estimated results with our numerical solutions (see Tables 8.1–8.2) and provide more discussions. Even though the estimates of eigenvalues have been discussed extensively in [3, 17, 35, 58, 59], the results on the eigenfunctions are still limited. In [16, 38, 74], the existence and uniqueness of the ground states are discussed for the general fractional Schrödinger equations. In [66], Luchko conjectured that the eigenfunctions of the fractional Schrödinger equation cannot be written in terms of elementary functions. In [96], Zoia et al. studied the eigenfunctions by solving eigenvectors of the matrix representing the fractional Laplacian. Recently, Żaba and Garbaczewski studied in [90] the eigenfunctions of the fractional Schrödinger equation in a finite potential well when $\alpha = 1$, and they found that the eigenfunctions in a finite potential well converge to those in an infinite potential well, as the depth of the potential well goes to infinity. More discussions on the properties of eigenfunctions can be found in [4, 35, 48, 59, 66] and references therein. Surprisingly, no study has been carried out by directly solving the fractional Schrödinger equation with an infinite potential well, and furthermore no results can be found in the literature on the stationary states of the fractional nonlinear ($\beta \neq 0$) Schrödinger equation in an infinite potential well.

8.2. FRACTIONAL GRADIENT FLOW AND ITS DISCRETIZATION

In this section, we propose a numerical method for computing the ground and first excited states of the fractional Schrödinger equation in an infinite potential well. First, we apply an imaginary time (i.e., $\tau = it$) in (8.1) and introduce a normalized fractional gradient flow. Then, we discretize it by using the weighted trapezoidal method in space and the semi-implicit Euler method in time. Our method can be used to find the ground and first excited states of both linear and nonlinear fractional Schrödinger equation in an infinite potential well.

Denote $\tau = it$ as an imaginary time, and let $\phi(x,\tau) = \psi(x,t)$. Then the normalized fractional gradient flow is given by:

$$\begin{aligned}
&\frac{\partial \phi(x,\tau)}{\partial \tau} = -(-\Delta)^{\alpha/2}\phi - \beta|\phi|^2\phi + \mu(\tau)\phi, \qquad x \in \Omega, \qquad \tau > 0,\\
&\phi(x,\tau) = 0, \qquad x \in \mathbb{R}\backslash\Omega, \qquad \tau \ge 0,\\
&\int_\Omega |\phi(x,\tau)|^2 dx = 1, \qquad \tau \ge 0
\end{aligned} \tag{8.23}$$

along with the initial condition

$$\phi(x,0) = \varphi(x), \qquad x \in \Omega, \qquad \text{with} \quad \|\varphi\| = 1. \tag{8.24}$$

Here, $\mu(\tau)$ is computed from (8.9).

The gradient flow (8.23)–(8.24) is the fractional counterpart of the normalized gradient flow which has many applications, such as finding stationary states of Bose–Einstein condensates [6, 19, 92], and studying optimal eigenvalue partition problems [11, 29]. To efficiently solve the normalized gradient flow, an operator splitting (or projection) method is often used in the literature [5, 6, 29, 92], and the resulting scheme is often referred to as a gradient flow with discrete normalization. Denote $\Delta\tau > 0$ as time step, and define time sequence $\tau_n = n\Delta\tau$ for $n = 0, 1, \ldots$. Then from $\tau = \tau_n$ to $\tau = \tau_{n+1}$, we solve the following fractional gradient flow with discrete normalization (FGFDN):

$$\begin{aligned}
&\frac{\partial \phi(x,\tau)}{\partial \tau} = -(-\Delta)^{\alpha/2}\phi - \beta|\phi|^2\phi, \qquad x \in \Omega, \qquad \tau_n < \tau < \tau_{n+1},\\
&\phi(x,\tau) = 0, \qquad x \in \mathbb{R}\backslash\Omega, \quad \tau_n \le \tau \le \tau_{n+1},\\
&\phi(x,\tau_{n+1}) = \frac{\phi(x,\tau_{n+1}^-)}{\|\phi(\cdot,\tau_{n+1}^-)\|}, \qquad x \in \Omega,
\end{aligned} \tag{8.25}$$

where $\phi(x,\tau_{n+1}^-)$ is the solution obtained from (8.25) at $\tau = \tau_{n+1}$, and the norm $\|\cdot\| = \|\cdot\|_{L^2(\Omega)}$. The FGFDN in (8.25) can be also viewed as first applying the steepest decent method to the energy functional (8.4) and then projecting the solution to satisfy the normalization constraint (8.3). For more discussions on the gradient flow with discrete normalization, see [5, 6, 29] and references therein. To discretize the fractional Laplacian, we apply the weighted trapezoidal method introduced in Section 3.

Let $\Phi(\tau) = \big(\phi_1(\tau), \phi_2(\tau), \ldots, \phi_{J-1}(\tau)\big)^T$ denote the solution vector at time τ. Then the semi-discretization of the fractional gradient flow in (8.25) is given by

$$\frac{d\Phi(\tau)}{d\tau} = A\Phi(\tau) + F(\Phi, \Phi), \qquad \tau \in (\tau_n, \tau_{n+1}), \tag{8.26}$$

where the matrix A is the discretization of the fractional Laplacian, defined in (3.10) with $\gamma = 1 + \alpha/2$. The vector function $F(\Phi, \Phi') = \Big(f(\phi_1, \phi'_1), f(\phi_2, \phi'_2), \ldots, f(\phi_{J-1}, \phi'_{J-1})\Big)^T$ with $f(\phi_j, \phi'_j) = -\beta|\phi_j|^2\phi'_j$.

The semi-discretization of the fractional gradient flow in (8.26) is a system of nonlinear ordinary differential equations (ODEs). Its temporal discretization can be realized by standard numerical methods for initial value problems. Here, we will use the semi-implicit Euler method, and more discussion on other methods can be found in [5, 6, 29]. Denote Φ^n as the numerical approximation of the solution vector $\Phi(\tau_n)$. Then, we discretize (8.26) as:

$$\frac{\Phi^{(1)} - \Phi^n}{\Delta\tau} = A\Phi^{(1)} + F(\Phi^n, \Phi^{(1)}), \qquad n = 0, 1, \ldots, \tag{8.27}$$

and the projection in (8.25) is discretized as

$$\Phi^{n+1} = \frac{\Phi^{(1)}}{\|\Phi^{(1)}\|}, \qquad \text{with} \quad \|\Phi^{(1)}\| = \Big(h\sum_{j=1}^{J-1} |\phi_j^{(1)}|^2\Big)^{1/2}. \tag{8.28}$$

When $n = 0$, the initial condition at $\tau = 0$ is discretized by

$$\phi_j^0 = \varphi(x_j), \qquad 1 \le j \le J - 1. \tag{8.29}$$

The scheme (8.27)–(8.29) can be used to compute for both the ground states and the first excited states of the fractional Schrödinger equation in an infinite potential well. In our simulations, the ground and first excited states are obtained by requiring that

$$\frac{\|\Phi^{n+1} - \Phi^{n}\|_\infty}{\Delta\tau} < \varepsilon \tag{8.30}$$

for a small tolerance $\varepsilon > 0$. We remark that in order to obtain a good approximation to the stationary states, a small time step is needed in the simulations.

8.3. FRACTIONAL LINEAR SCHRÖDINGER EQUATION.

In this section, we will numerically study the ground and first excited states of the fractional linear ($\beta = 0$) Schrödinger equation in an infinite potential well. In Sections 8.3.1–8.3.2, the ground and first excited states of the fractional linear Schrödinger equation in an infinite potential well are studied by numerically solving the fractional gradient flow in (8.25) with $\beta = 0$. In our simulations, we choose $L = 1$, equivalently, $\Omega = (-1, 1)$. The mesh size is $h = 1/4096$, and the time step is $\Delta\tau = 0.005$. The initial condition is chosen as

$$\varphi(x) = \sin\left[\frac{(s+1)\pi}{2}(1+x)\right], \qquad x \in \Omega, \qquad s = 0 \text{ or } 1, \tag{8.31}$$

where we choose $s = 0$ for computing the ground states, respectively, $s = 1$ for the first excited states. We choose the tolerance $\varepsilon = 10^{-5}$ in (8.30). In the following, we will use the subscripts “*g*” and “*1*” to represent the ground states and the first excited states, respectively.

For the s-th ($s \in \mathbb{N} \cup \{0\}$) state, we define its *expected value of position* as

$$\langle x \rangle_s = \int_{\mathbb{R}} x\, |\phi_s(x)|^2 dx = \int_{\Omega} x\, |\phi_s(x)|^2 dx.$$

It is easy to obtain that $\langle x \rangle_s = 0$ if $|\phi_s(x)|$ is symmetric with respect to the potential center $x = 0$. Furthermore, we define the *variance in position* as

$$\mathrm{Var}_s(x) = \int_{\mathbb{R}} (x - \langle x \rangle_s)^2 \, |\phi_s(x)|^2 dx = \int_{\Omega} (x - \langle x \rangle_s)^2 \, |\phi_s(x)|^2 dx,$$

which can be used to study the scattering of particles in the potential well.

8.3.1. Ground States. Figure 8.1 (left) depicts the ground state wave function $\phi_g(x)$ of the fractional linear Schrödinger equation in an infinite potential well for $\alpha = 0.2, 0.7, 1.1, 1.5$, and 1.9; Figure 8.1 (right) shows the expected value of position and its variance of the ground state solutions for $\alpha \in (0, 2]$, where $\alpha = 2$ corresponds to the standard Schrödinger equation. From Figure 8.1, we find that the wave function of the ground state is symmetric with respect to the center of the potential well $x = 0$, i.e., $\phi_g(x) = \phi_g(-x)$ for $x \in (-1, 1)$. The wave function $|\phi_g(x)|$ monotonically increases for $x \in (-1, 0)$ and monotonically decreases for $x \in (0, 1)$, and it reaches the maximum value at $x = 0$. Furthermore, the ground state of the fractional Schrödinger equation in an infinite potential well depends significantly on the parameter α. If α is small, the nonlocal interactions from the fractional Laplacian are strong, resulting in a flatter shape of the wave function. While

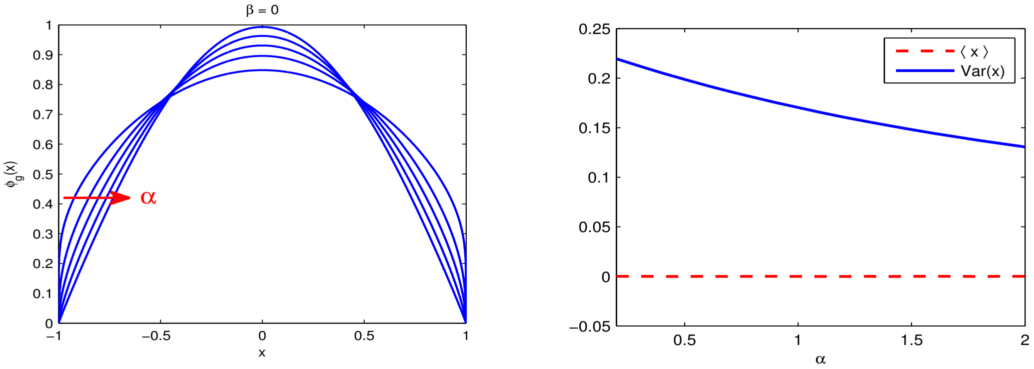

Figure 8.1. Ground states and expected value of position. Left: Ground state solutions for $\alpha = 0.2, 0.7, 1.1, 1.5$, and 1.9, where the arrow indicates the change of $\phi_g(x)$ for progressively increasing α. Right: The expected value of position and its variance of the ground state solutions.

if $\alpha \to 2$, the wave function of the ground state converges to $\phi_g(x) = \sin[\pi(1+x)/2]$ – the ground state solution of the standard Schrödinger equation. Our solutions are consistent with the observations in [4, 48, 59, 66].

Figure 8.1 (right) shows that the expected value of the position $\langle x \rangle_g \equiv 0$, independent of the parameter α. However, the variance in position highly depends on the parameter α. The smaller the parameter α, the larger the variance in position. When $\alpha \to 0$, the nonlocal interactions represented by the fractional Laplacian become stronger, resulting in a larger scattering of particles. Hence, the decrease in the parameter α leads to an increase in variance in position. While $\alpha \to 2$, the variance in position converges to that of the standard Schrödinger equation. We remark that for the standard linear Schrödinger equation, the expected value of position and its variance of the s-th stationary state can be exactly computed as:

$$\langle x \rangle_s = 0 \qquad \text{and} \qquad \mathrm{Var}_s(x) = \frac{L^2}{3}\left(1 - \frac{6}{\pi^2(s+1)^2}\right), \qquad s \in \mathbb{N} \cup \{0\}, \tag{8.32}$$

that is, for any stationary states, the average position is always at $x = 0$ – the center of the infinite potential well. The variance in position increases as s increases, and as $s \to \infty$, the variance $\mathrm{Var}_s(x) \to L^2/3$.

Furthermore, we compare our results with those reported in the literature [90, 96]. In [96], Zoia et al. study the ground state by computing the first eigenvector of the matrix representing the fractional Laplacian. While in [90], Żaba et al. study the stationary states of the fractional linear Schrödinger equation in a finite potential well of the following form:

$$\widetilde{V}(x) = \begin{cases} 0, & x \in \Omega, \\ V_0, & x \in \mathbb{R}\backslash\Omega, \end{cases} \qquad x \in \mathbb{R}, \tag{8.33}$$

where $V_0 > 0$ is a constant. They find that the ground states in a finite potential well

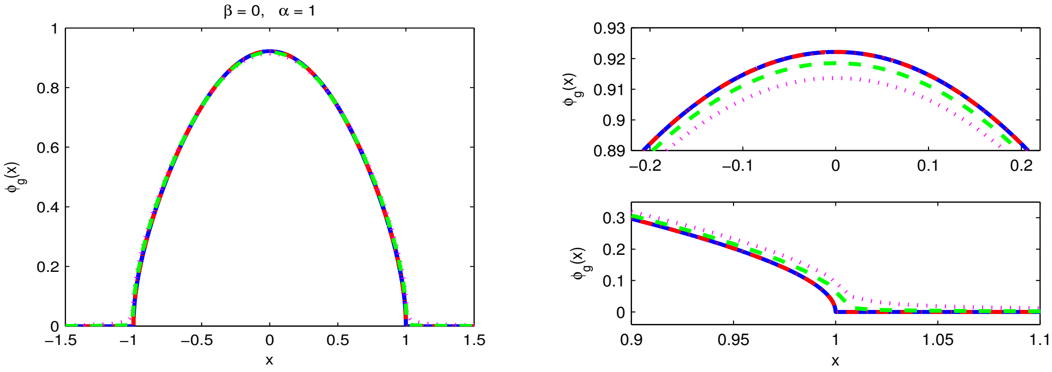

Figure 8.2. Comparison of the ground state solutions obtained from our method (solid line), Zoia's method in [96] (dashdot line), and Żaba's method in [90] with $V_0 = 100$ (dotted line) and $V_0 = 500$ (dashed line). The right panel is an enlarged display of the left panel around the maximum and boundary of the ground state solution.

converge to those in an infinite potential well, as $V_0 \to \infty$, where only the case $\alpha = 1$ is considered. In Figure 8.2, we compare the ground state solutions obtained by our method, Zoia's method in [96], and Żaba's method in [90], where $\alpha = 1$. It shows that the ground

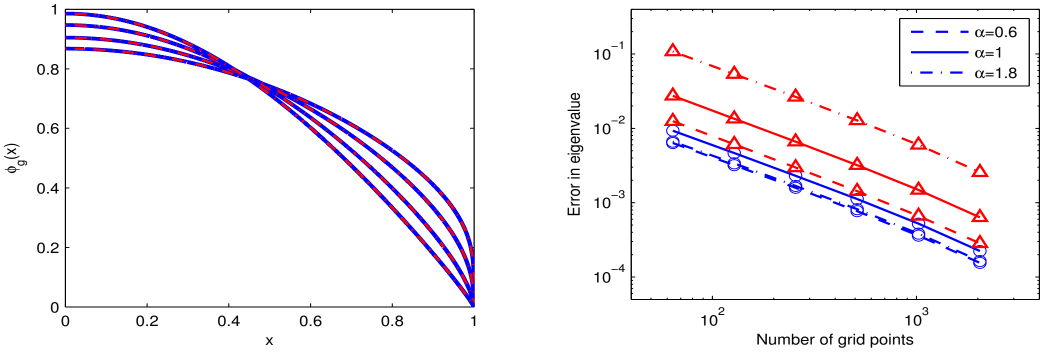

Figure 8.3. Comparison of the ground state solutions and errors of eigenvalues. Left: Further comparison of the ground state solutions computed by our method (solid line) and Zoia's method in [96] (dashdot line) for $\alpha = 0.3, 0.6, 1.3$, and 1.8, where the solutions for only $0 \leq x \leq 1$ are displayed for brevity. Right: Errors of the eigenvalues versus the number of grid points which are computed by our method ('$\circ$') and Zoia's method in [96] ('$\triangle$').

state solution obtained by our method is the same as that by Zoia's method. The ground state solution by Żaba's method approaches our solutions, as the depth of the potential well V_0 increases. In Figure 8.3, we further compare our method with Zoia's method by comparing the eigenfunctions for any $\alpha \in (0, 2)$ and the convergence of eigenvalues as the number of grid points increases. Figure 8.3 (left) and our extensive simulations show that for any $\alpha \in (0, 2)$, the ground state solutions obtained by our method are the same as those by Zoia's method. However, our numerical method has better accuracy in eigenvalues, especially when α is large (see Figure 8.3 right). Moreover, our method can be used to compute the ground and first excited states of the fractional Schrödinger equation not only in the linear ($\beta = 0$) cases but also in the nonlinear ($\beta \neq 0$) cases.

In Table 8.1, we compare our simulated eigenvalues μ_g^h with the approximate results in [59, 96] and the lower and upper bound estimates in [3, 17, 35]. Columns 2–6 represent the best analytical lower bounds from [35], asymptotical approximations in [59], numerical approximations by Zoia's method in [96], our numerical results, the best analytical upper bounds from [3] (indicated by '†') and [17] (indicated by '‡'), respectively. Note that in Tables 8.1–8.2, we only compare with the analytical lower and upper bound estimates reported in [3, 17, 35]. For more discussions on numerical bounds, we refer readers to [58, 59]. Table 8.1 shows that as $\alpha \to 2$, the eigenvalue μ_g converges to $\pi^2/4$ – the eigenvalue of the ground states of standard linear Schrödinger equation in an infinite potential well. Our numerical results are consistent with the lower and upper bound estimates obtained in [3, 17, 35]. Furthermore, our results suggest that the lower bound estimates reported in [35] are much sharper than those in [3, 17]. When α is small, the differences between the eigenvalues obtained by Zoia's and our methods are insignificant. However, the difference becomes larger as α increases, since the eigenvalues by Zoia's method have larger errors when α increases (also see Figure 8.3 right).

8.3.2. The First Excited States. Figure 8.4 (left) depicts the first excited state wave function $\phi_1(x)$ of the fractional linear Schrödinger equation in an infinite potential well for $\alpha = 0.2, 0.7, 1.1, 1.5$, and 1.9, and Figure 8.4 (right) shows the expected value of

Table 8.1. The eigenvalue μ_g of the ground states of the fractional linear ($\beta = 0$) Schrödinger equation in an infinite potential well.

α	Lower bounds	Results in [59]	Results in [96]	Our results	Upper bounds
0.01	0.9960	0.9976	0.996633	0.996636	$0.9974^{\dagger}$
0.1	0.9676	0.9809	0.97258	0.97261	$0.9786^{\dagger}$
0.2	0.9499	0.9712	0.9574	0.9575	$0.9675^{\dagger}$
0.3	0.9442	0.9699	0.9527	0.9528	$0.9655^{\dagger}$
0.5	0.9620	0.9908	0.9701	0.9702	$0.9862^{\dagger}$
0.6	0.9839	1.0126	0.9911	0.9913	$1.0084^{\dagger}$
0.8	1.0521	1.0789	1.0573	1.0576	$1.0763^{\dagger}$
1	1.1538	1.1781	1.1576	1.1578	$1.1781^{\dagger}$
1.1	1.2183	1.2415	1.2218	1.2222	$1.2432^{\dagger}$
1.3	1.3781	1.4007	1.3832	1.3837	$1.4064^{\dagger}$
1.5	1.5861	1.6114	1.5970	1.5976	$1.6223^{\dagger}$
1.8	2.0140	2.0555	2.0479	2.0488	$2.0777^{\dagger}$
1.9	2.1952	2.2477	2.2430	2.2441	$2.2747^{\dagger}$
1.99	2.3784	2.4441	2.4425	2.4437	$2.4563^{\ddagger}$

position and its variance of $\phi_1(x)$ for $\alpha \in (0, 2]$, where $\alpha = 2$ corresponds to the standard Schrödinger equation. It shows that the wave function $\phi_1(x)$ varies for different values of α, and as $\alpha \to 2$, it converges to $\phi_1(x) = \sin(\pi(1 + x))$ – the first excited state solution of the standard linear Schrödinger equation in an infinite potential well. In addition, the

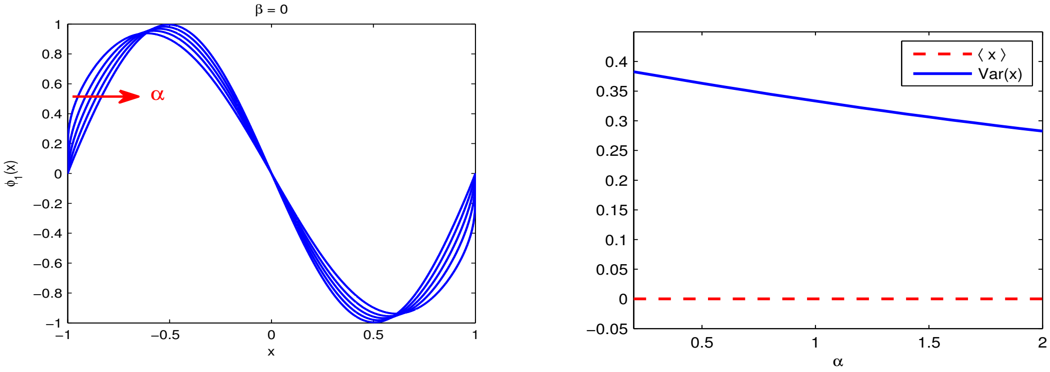

Figure 8.4. The first excited state solutions and expected value of position. Left: The first excited state solutions for $\alpha = 0.2, 0.7, 1.1, 1.5$, and 1.9, where the arrow indicates the change of $\phi_1(x)$ for progressively increasing α. Right: The expected value of position and its variance of the first excited state solutions.

wave function $\phi_1(x)$ of the first excited states is antisymmetric with respect to the center of the infinite potential well $x = 0$, i.e., $\phi_1(x) = -\phi_1(-x)$ for $x \in (-1, 1)$ and $\phi(0) = 0$. For the standard linear Schrödinger equation, $\phi_1(x)$ is also symmetric on each subinterval $(-1, 0)$ and $(0, 1)$, but in the fractional cases the wave function loses the symmetry in each subinterval.

In addition, we find from Figure 8.4 (right) that for any $\alpha \in (0, 2)$, the expected value $\langle x\rangle_1 \equiv 0$, due to the antisymmetry of the wave function $\phi_1(x)$ with respect to $x = 0$, while the variance in position changes for different α. The smaller the parameter α, the stronger the scattering of particles, and thus the larger the variance in position, which is similar to our observations in Figure 8.1 for ground states. However, we find that for a fixed α, the variance $\mathrm{Var}_1(x) > \mathrm{Var}_g(x)$. In fact, the energy of the first excited states is higher than that of the ground states, and consequently the scattering of particles in the first excited states is stronger, which leads to a larger variance in position of the first excited states.

To further study the symmetry of $\phi_1(x)$, we denote $\rho_1(x) = |\phi_1(x)|^2$ as the position density of the first excited states. The fact that $\phi_1(x)$ is antisymmetric about the center of the potential well implies that the position density $\rho_1(x)$ is symmetric with respect to $x = 0$. Furthermore, there exist two points $x_c \in (0, 1)$ and $-x_c \in (-1, 0)$ at which the density function $\rho_1(x)$ reaches its maximum values, i.e., $\rho_1(x_c) = \rho_1(-x_c) = \max_{x\in[-1,1]}\{\rho_1(x)\}$.

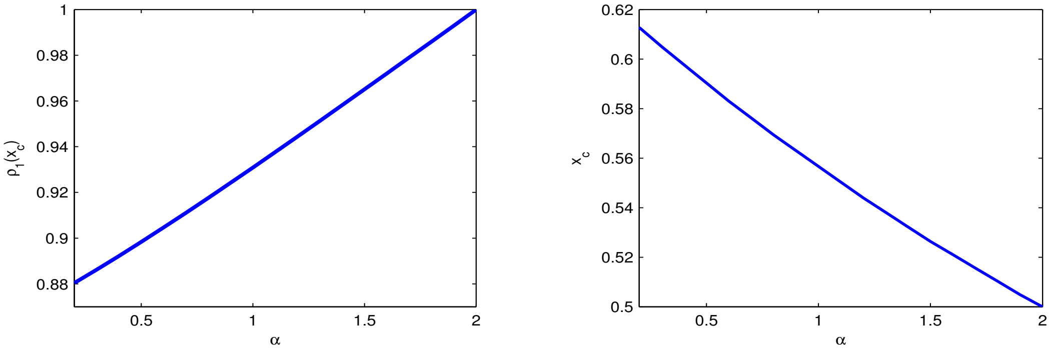

Figure 8.5. The maximum value of the position density and the position. Left: The maximum value of the position density $\rho_1(x_c)$ versus the parameter α. Right: The position x_c versus the parameter α.

The point x_c varies for different parameter α. Figure 8.5 shows the values of x_c and $\rho_1(x_c)$ for various α. We see that the larger the parameter α, the smaller the value of x_c, but the larger the density function $\rho_1(x_c)$. The maximum value $\rho_1(x_c)$ increases almost linearly as the parameter α. In particular, the point $x_c = \frac{1}{2}$ and the maximum density function $\rho_1(\pm\frac{1}{2}) = 1$ for the standard linear Schrödinger equation.

In Figure 8.6, we compare our first excited state solution with that obtained by Zoia's method in [96], and the approximate solution using a finite potential well in [90], where $\alpha = 1$. It shows that the first excited state wave functions obtained by our method and Zoia's method are the same. While the wave function in a finite potential well gives a good approximation to that in an infinite potential well, when the potential well is deep enough (i.e., V_0 is sufficiently large). In Figure 8.7, we further compare our method with Zoia's method in simulating the first excited states. Similar to the observations in Figure 8.3, the first excited state wave functions obtained by our method are the same as those by Zoia's method, but our method converges much faster, especially when α is large (see Figure 8.7 right). For example, when $\alpha = 1.8$, the eigenvalue that computed by our method with 128

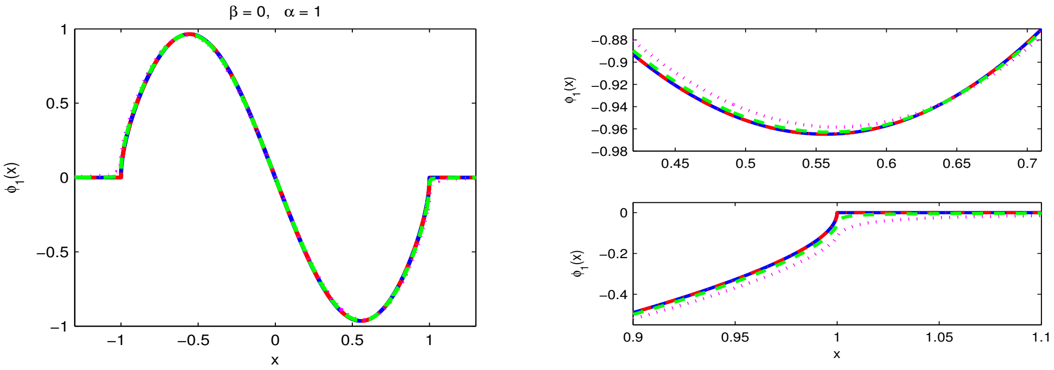

Figure 8.6. Comparison of the first excited state solutions from our method (solid line), Zoia's method in [96] (dashdot line), and Żaba's method in [90] with $V_0 = 100$ (dotted line) and $V_0 = 500$ (dashed line). The right panel is an enlarged display of the left panel around the maximum and boundary of the first excited state solution.

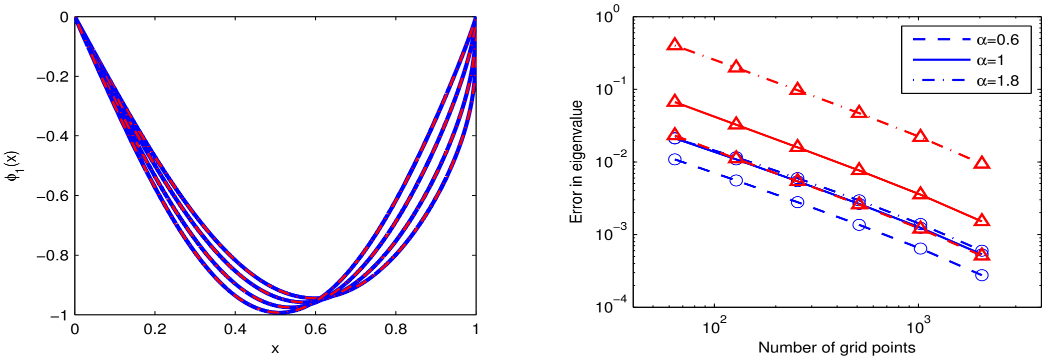

Figure 8.7. Comparison of the first excited state solutions and the errors of the eigenvalues. Left: Further comparison of the first excited state solutions computed by our method (solid line) and Zoia's method in [96] (dashdot line), for $\alpha = 0.3, 0.6, 1.3$, and 1.8, where the solutions for only $0 \leq x \leq 1$ are displayed for brevity. Right: Errors of the eigenvalues versus the number of grid points which are computed by our method ('$\circ$') and Zoia's method in [96] ('$\triangle$').

grid points has almost the same error as that obtained by Zoia's method with 2048 grid points, which implies that our method can achieve a better approximation with less number of grid points.

In Table 8.2, we compare our simulated eigenvalues μ_1^h with the approximate results in [59, 96] and the lower and upper bound estimates in [17]. Columns 2–6 display the best analytical lower bounds from [17], asymptotical approximations in [59], numerical approximations by Zoia's method in [96], our numerical results, the best analytical upper bounds from [17], respectively. It shows that the eigenvalue of the first excited states increases as α increases, and as $\alpha \to 2$, it converges to $\mu_1 = \pi^2$ – the eigenvalue of the first excited states of the standard linear Schrödinger equation in an infinite potential well. Our numerical results μ_1^h are consistent with the estimates obtained in [17] as well as the approximations in [59, 96]. Furthermore, our results suggest that the asymptotic results in [59] are more accurate for the first excited states than for the ground states, as the asymptotic approximation has the error $O\left((2-\alpha)/(s+1)\sqrt{\alpha}\right)$.

Table 8.2. The eigenvalue μ_1 of the first excited states of the fractional linear ($\beta = 0$) Schrödinger equation in an infinite potential well.

α	Lower bounds	Results in [59]	Results in [96]	Our results	Upper bounds
0.01	0.5058	1.0086	1.008717	1.008719	1.0115
0.1	0.5606	1.0913	1.09218	1.09221	1.1213
0.2	0.6286	1.1948	1.1965	1.1966	1.2573
0.3	0.7049	1.3122	1.3147	1.3148	1.4098
0.5	0.8862	1.5977	1.6014	1.6016	1.7725
0.6	0.9937	1.7708	1.7750	1.7753	1.9874
0.8	1.2494	2.1941	2.1991	2.1995	2.4987
1	$\pi/2$	2.7489	2.7543	2.7549	π
1.1	1.7613	3.0892	3.0946	3.0954	3.5226
1.3	2.2144	3.9319	3.9367	3.9380	4.4289
1.5	2.7842	5.0545	5.0581	5.0600	5.5683
1.8	3.9250	7.5003	7.5000	7.5033	7.8500
1.9	4.4010	8.5942	8.5919	8.5959	8.8021
1.99	4.8786	9.7330	9.7285	9.7332	9.7573

8.4. FRACTIONAL NONLINEAR SCHRÖDINGER EQUATION

There have been many discussions on the stationary states of the fractional linear Schrödinger equation in an infinite potential well based on different representations of the fractional Laplacian $(-\Delta)^{\alpha/2}$. However, to the best of our knowledge, no study has been reported in the nonlinear ($\beta \neq 0$) cases yet. In this section, we numerically study the ground and first excited states of the fractional Schrödinger equation with repulsive nonlinear interactions (i.e., $\beta > 0$) and attempt to understand the effects of local (or short-range) interactions and the competition of the local and nonlocal interactions. In our simulations, we choose $L = 1$, the mesh size $h = 1/4096$, the time step $\Delta\tau = 0.001$, and the convergence tolerance $\varepsilon = 10^{-5}$ in (8.30). The initial condition is chosen as defined in (8.31).

8.4.1. Ground States. Figure 8.8 a)-c) displays the ground state wave function $\phi_g(x)$ of the fractional nonlinear Schrödinger equation in an infinite potential well for various α and β. It shows that the wave function of the ground states $\phi_g(x)$ is always symmetric with respect to the center of the infinite potential well $x = 0$. As $\alpha \to 2$, the wave function converges to the ground state solution of the standard Schrödinger equation with the same nonlinear parameter β. In contrast to the linear cases, the local repulsive interactions may lead to boundary layers in the ground states. Here, we divide our discussions into two interaction regimes: the weak interactions when $\beta \sim o(1)$ and the strong interactions when $\beta \gg 1$. For $\beta \sim o(1)$, the effects of local repulsive interactions are significant only

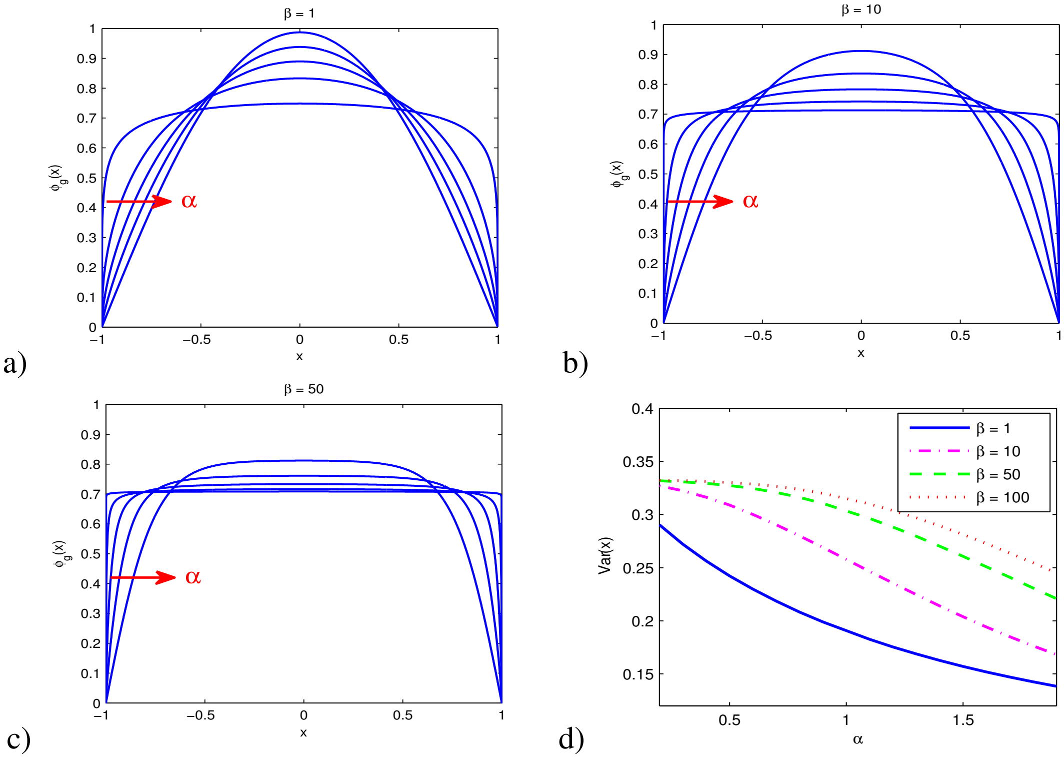

Figure 8.8. Ground state wave functions of the fractional nonlinear Schrödinger equation and the variance in position. a)-c): Ground state wave functions of the fractional nonlinear Schrödinger equation for $\alpha = 0.2, 0.7, 1.1, 1.5$, and 1.99, where the arrow indicates the change in the wave function for progressively increasing α. d): The variance in position of the ground state solutions.

when α is small, resulting in two boundary layers at $x = \pm 1$ (see the case of $\alpha = 0.2$ and $\beta = 1$ in Figure 8.8). While in the strongly interacting cases (e.g. $\beta = 50$), the local interactions become significant for any $\alpha \in (0, 2)$. Due to the normalization condition, the wave function $\phi_g(x)$ inside the potential well tends to approach the value $\sqrt{2}/2$. However, since the wave function $\phi_g(x) \equiv 0$ at $x = \pm 1$, two layers emerge at the boundaries of the potential well.

In Figure 8.8 d), we present the variance in position of $\phi_g(x)$ for $\alpha \in (0, 2)$ and $\beta = 1, 10, 50$, and 100. Since the wave function $\phi_g(x)$ is symmetric with respect to $x = 0$, the expected value of position $\langle x \rangle_g \equiv 0$, independent of the parameters α and β. Here, we omit showing it for brevity. Figure 8.8 d) shows that the variance in position monotonically increases as α decreases or β increases, implying that strong local or nonlocal interactions yield a large scattering of particles in the potential well. Comparing Figure 8.8 d) to Figure 8.1 (right), we find that even weak local interactions (e.g., $\beta = 1$) can significantly change the variance in position, especially when α is small. Moreover, Figure 8.8 d) suggests that when β is small (e.g., $\beta = 1$), the nonlocal interactions from the fractional Laplacian are dominant, and the variance decreases concave up as α increases, similar to the cases of $\beta = 0$. When β is large, the local repulsive interactions become significant, and the decrease of the variance becomes concave down as α increases. In addition, due to the constraint $\|\phi_g\|^2 = 1$, the variance of position converges to $1/3$ as $\alpha \to 0$ or $\beta \to \infty$.

The ground state solutions in Figure 8.8 show that the width of boundary layers depends on both the parameters α and β. To further study their relation, we define w as the width of the boundary layers. In our simulations, it is computed by $w = 1 - |\bar{x}|$, where $\bar{x}$ satisfies

$$\left| \frac{\partial \phi_g(x)}{\partial x} \Big|_{x=\bar{x}} \right| = \eta, \qquad \text{with } \eta \sim O(1) \text{ a constant.}$$

Here, we choose $\eta = \sqrt{2}/2$. In Figure 8.9, we present the log-log plots of the width of boundary layers w versus β for different α. It shows that when β is large, $\log(w)$ linearly decreases as $\log(\beta)$ increases, which implies that

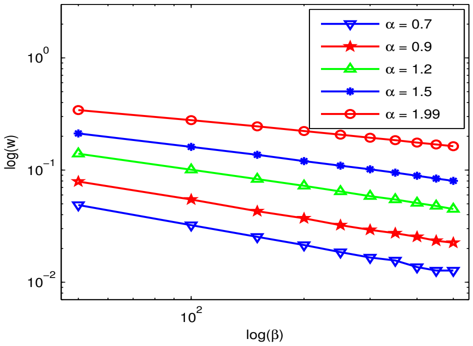

Figure 8.9. Log-log plots of the width of boundary layers versus β in the ground states of the fractional nonlinear Schrödinger equation in an infinite potential well.

$$w = O(\beta^{-q}) \tag{8.34}$$

with $q > 0$ a constant depending on α. In particular, the width of the boundary layers $w \sim O\left(\beta^{-1/2}\right)$ in the ground states of the standard Schrödinger equation [7].

In [90], the ground state solutions in a finite potential well are studied when $\beta = 0$ and $\alpha = 1$, and it shows that the ground state solutions in a finite potential well provide good approximations to those in an infinite potential well when the potential well is deep enough. Similarly, here we consider a finite potential of the form in (8.33) and compare the ground state solutions in finite and infinite potential wells when $\beta \neq 0$ and $\alpha \in (0, 2)$. Figure 8.10 depicts the ground states for different depth of the potential well V_0, where $\beta = 10$. It shows that the ground state solution in a deep (i.e., large V_0) finite potential well gives a good approximation to that in an infinite potential well. Furthermore, when α increases, a deeper finite potential well is needed to obtain a better approximation.

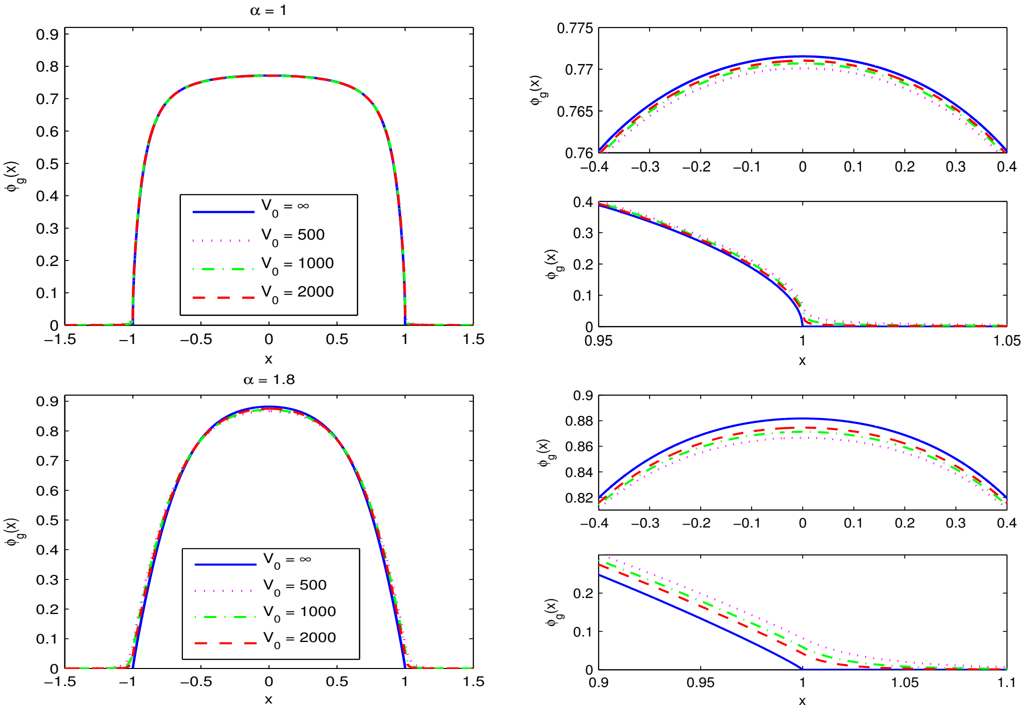

Figure 8.10. Comparison of the ground states of the fractional nonlinear Schrödinger equation in a finite potential well with depth V_0 and those in an infinite potential well, where $\beta = 10$. The right panel is an enlarged display of the left panel around the maximum and boundary of the ground state solution.

Table 8.3. The simulated eigenvalue μ_g^h and the kinetic energy $\mu_{g,\text{kin}}^h$ of the ground states of the fractional nonlinear Schrödinger equation in an infinite potential well.

α	$\beta = 1$		$\beta = 5$		$\beta = 10$		$\beta = 50$	
	$\mu_{g,\text{kin}}^h$	μ_g^h	$\mu_{g,\text{kin}}^h$	μ_g^h	$\mu_{g,\text{kin}}^h$	μ_g^h	$\mu_{g,\text{kin}}^h$	μ_g^h
0.3	0.9627	1.4864	0.9843	3.5062	0.9930	6.0233	1.0099	26.498
0.5	0.9808	1.5295	1.0220	3.5915	1.0483	6.1236	1.1055	26.612
0.7	1.0304	1.6056	1.0870	3.7341	1.1345	6.3053	1.2743	26.869
0.9	1.1124	1.7143	1.1793	3.9272	1.2475	6.5622	1.5009	27.309
1	1.1664	1.7817	1.2368	4.0419	1.3145	6.7174	1.6318	27.603
1.1	1.2302	1.8586	1.3028	4.1691	1.3894	6.8901	1.7734	27.948
1.3	1.3904	2.0449	1.4646	4.4625	1.5661	7.2890	2.0882	28.791
1.5	1.6031	2.2827	1.6748	4.8137	1.7869	7.7632	2.4488	29.839
1.7	1.8823	2.5860	1.9483	5.2335	2.0653	8.3209	2.8637	31.098
1.9	2.2475	2.9743	2.3054	5.7380	2.4211	8.9754	3.3460	32.582

Denote the kinetic energy $\mu_{s,\text{kin}}$ of the s-th stationary state as

$$\mu_{s,\text{kin}} = \int_{\mathbb{R}} \phi_s^* (-\Delta)^{\alpha/2} \phi_s \, dx, \qquad s \in \mathbb{N} \cup \{0\}.$$

Especially when $\beta = 0$, we have the eigenvalue $\mu_s \equiv \mu_{s,\text{kin}}$ for any α. In Table 8.3, we present the simulated eigenvalue μ_g^h and the kinetic energy $\mu_{g,\text{kin}}^h$ corresponding to the ground states of the fractional nonlinear Schrödinger equation in an infinite potential well. It shows that both the eigenvalue μ_g and the kinetic energy $\mu_{g,\text{kin}}$ increase as the parameter α or β becomes larger. However, when β increases, the kinetic energy becomes insignificant compared to the eigenvalue, especially when α is small. This implies that one could ignore the kinetic energy when β is large and α is small. Furthermore, we find that if $\beta \gg 1$, the eigenvalue $\mu_g \sim O(\beta/2)$.

8.4.2. The First Excited States. Figure 8.11 a)-c) shows the first excited state solution $\phi_1(x)$ of the fractional nonlinear Schrödinger equation in an infinite potential well. The wave function $\phi_1(x)$ is antisymmetric with respect to the center of the potential well $x = 0$, independent of the parameters α and β. As $\alpha \to 2$, the wave function converges to the first excited state solution of the standard Schrödinger equation with the same nonlinear parameter β. The effect of local interactions becomes more significant when α is small, resulting in sharp boundary layers at $x = \pm 1$ as well as one inner layer at $x = 0$. The width of the boundary and inner layers decreases as α decreases or β increases. Numerical simulations show that our method converges fast in computing both the ground and first excited states.

In addition, Figure 8.11 d) displays the variance of $\phi_1(x)$ for $\alpha \in (0, 2)$ and $\beta = 1$, 10, 50, and 100. Note that the expected value of position $\langle x \rangle_1 \equiv 0$, independent of the parameters α and β. The properties of the variance in position can be divided into two cases: when $\alpha < 1$, the larger the parameter β, the smaller the variance, and as $\beta \to \infty$, the

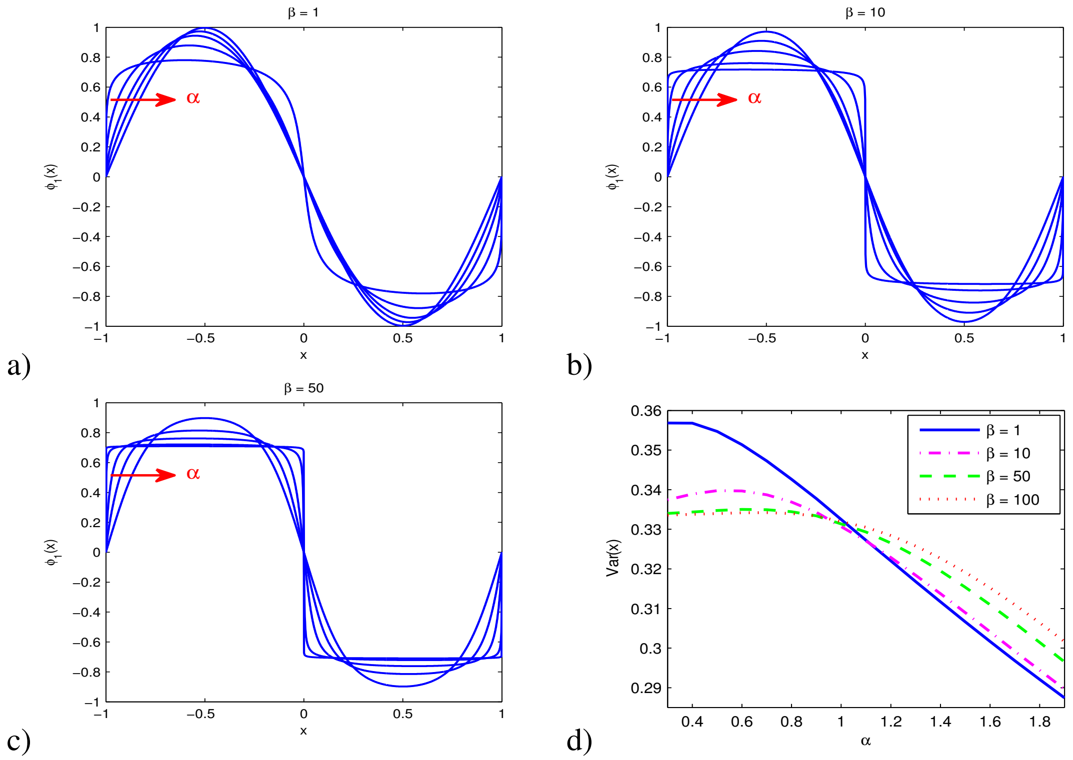

Figure 8.11. The first excited state wave functions of the fractional nonlinear Schrödinger equation and the variance in position. a)-c): The first excited state wave functions of the fractional nonlinear Schrödinger equation for $\alpha = 0.2, 0.7, 1.1, 1.5$, and 1.99, where the arrow indicates the change in the wave function for progressively increasing α. d): The variance in position of the first excited state solutions.

variance converges to $1/3$. While $\alpha > 1$, the larger the parameter β, the bigger the variance, implying that in this case the scattering of particles is mainly caused by the local repulsive interactions.

Similarly, we also compare in Figure 8.12 the first excited state solutions in an infinite potential well with those in a finite potential well with different depth V_0, where $\beta = 10$. As the depth $V_0 \to \infty$, the first excited states in a finite potential well approaches those in an infinite potential well, which is consistent with the observations in [90] for the linear cases.

In Table 8.4, we present our numerical results of the eigenvalue μ_1^h and the kinetic energy $\mu_{1,\text{kin}}^h$ of the first excited states for various α and β. It shows that both the eigenvalue

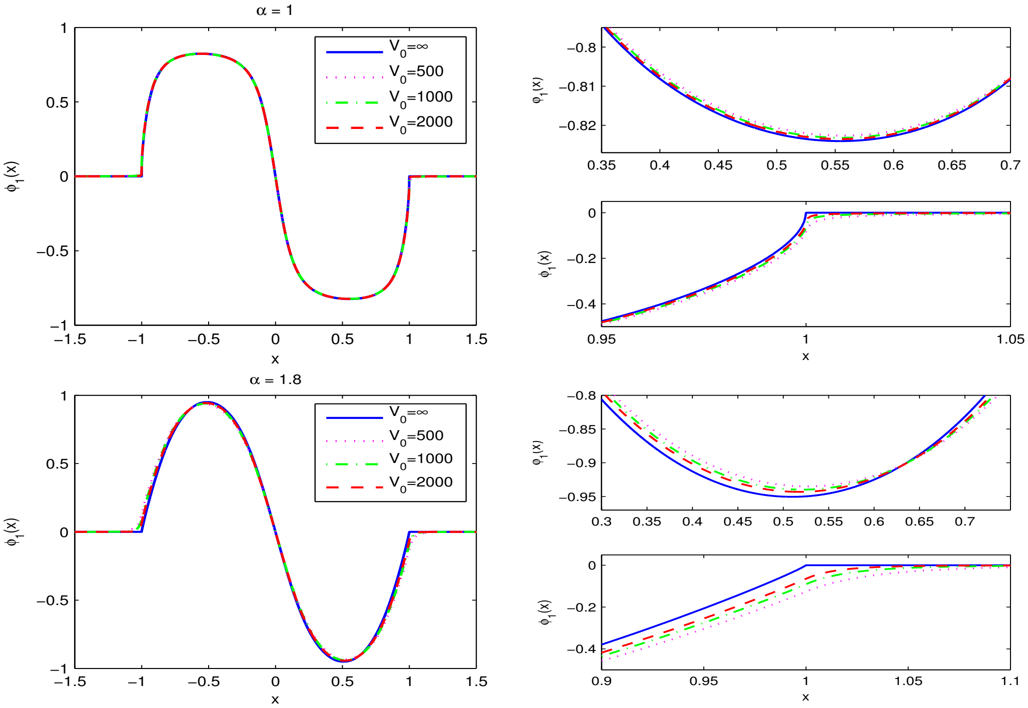

Figure 8.12. Comparison of the first excited states of the fractional nonlinear Schrödinger equation in a finite potential well with depth V_0 and those in an infinite potential well, where $\beta = 10$. The right panel is an enlarged display of the left panel around the maximum and boundary of the first excited state solution.

Table 8.4. The simulated eigenvalue μ_1^h and the kinetic energy $\mu_{1,\text{kin}}^h$ of the first excited states of the fractional nonlinear Schrödinger equation in an infinite potential well.

α	$\beta = 1$		$\beta = 5$		$\beta = 10$		$\beta = 50$	
	$\mu_{1,\text{kin}}^h$	μ_1^h	$\mu_{1,\text{kin}}^h$	μ_1^h	$\mu_{1,\text{kin}}^h$	μ_1^h	$\mu_{1,\text{kin}}^h$	μ_1^h
0.3	1.3349	1.8998	1.3931	3.9589	1.4218	6.4828	1.4683	26.959
0.5	1.6179	2.2252	1.7023	4.3923	1.7670	6.9702	1.9441	27.513
0.7	1.9853	2.6258	2.0777	4.9209	2.1759	7.5983	2.5376	27.389
0.9	2.4669	3.1332	2.5546	5.5599	2.6714	8.3680	3.2328	29.626
1	2.7621	3.4392	2.8444	5.9300	2.9657	8.8115	3.6219	30.383
1.1	3.1014	3.7882	3.1769	6.3407	3.2994	9.2992	4.0438	31.233
1.3	3.9422	4.6457	4.0022	7.3118	4.1179	10.429	5.0093	33.223
1.5	5.0630	5.7807	5.1077	8.5449	5.2071	11.819	6.1905	35.630
1.7	6.5666	7.2967	6.5982	10.144	6.6768	13.561	7.6797	38.507
1.9	8.5970	9.3385	8.6185	12.255	8.6766	15.797	9.6183	41.942

and kinetic energy increase as the parameter α or β becomes larger. Comparing Tables 8.4 and 8.3, we find that for fixed parameters α and β, the kinetic energy $\mu_{1,\text{kin}}$ of the first excited states is much larger than $\mu_{g,\text{kin}}$ of the ground states, which mainly caused by the emergence of the inner layer in the first excited states. Similar to the cases of the ground states, the kinetic energy is significant compared to the eigenvalue only when the local interactions are weak (i.e., β is small).

In this section, we numerically studied the ground and first excited states of the one-dimensional fractional Schrödinger equation in an infinite potential well. We proposed a normalized fractional gradient flow and discretize it by the weighted trapezoidal method in space and the semi-implicit Euler method in time. Our numerical results suggested that the eigenfunctions of the fractional Schrödinger equation are different from those of its standard counterpart. The nonlocal interactions are strong when α is small, leading to a large scattering of particles in an infinite potential well. In addition, our simulated eigenvalues are consistent not only with the approximation results in [59, 96] but also with the best lower and upper bounds in [3, 17, 35].

9. PLANE WAVE DYNAMICS OF THE FRACTIONAL SCHRÖDINGER EQUATION

The plane wave solutions play an important role in understanding the NLS equation, and especially the phenomena associated to their stability are of great interest. In the standard ($\alpha = 2$) NLS, the stability of the plane wave solutions has been well studied, in contrast, because of the nonlocality, the study on the plane wave solution of the fractional NLS still remain limited. In this section, we aim to understand the stability and dynamics of the plane wave solutions under the nonlocal effects of the fractional Laplacian and to compare the properties of different numerical methods in simulating the plane waves of the fractional NLS.

We consider the following fractional nonlinear Schrödinger (NLS) equation:

$$i\frac{\partial u(x,t)}{\partial t} = (-\Delta)^{\alpha/2}u(x,t) + \gamma|u(x,t)|^2u(x,t), \quad t > 0, \tag{9.1}$$

$$u(x,0) = \psi(x), \tag{9.2}$$

where $u(x,t)$ is a complex-valued wave function of $x \in \mathbb{R}$ and $t \geq 0$. The fractional Laplacian $(-\Delta)^{\alpha/2}$ is defined via the pseudo-differential operator in (1.1).

The fractional NLS (9.1) has some similar properties to the standard NLS. It has two important conserved quantities: the *mass* of the wave function:

$$N(t) = \|u(\cdot,t)\|^2 := \int_{\mathbb{R}} |u(x,t)|^2 dx \equiv N(0), \tag{9.3}$$

and the *total energy* (or *Hamiltonian*):

$$\begin{aligned} E(t) &= \int_{\mathbb{R}} \left[\mathrm{Re}\Big(u^*(x,t)(-\Delta)^{\alpha/2}u(x,t)\Big) + \frac{\gamma}{2}|u(x,t)|^4\right] dx \\ &\equiv E(0), \end{aligned} \tag{9.4}$$

where $\mathrm{Re}(\phi)$ and ϕ^*, respectively, represent the real part and the complex conjugate of a function ϕ. The fractional NLS is *time reversible*, that is, (9.1) remains invariant if one replaces the time t by $-t$ and takes its conjugate. These properties are usually used as benchmarks to develop and examine numerical methods for the fractional NLS.

In addition, the fractional NLS (9.1) admits the plane wave solution of the form:

$$u(x,t) = a\exp\big(i(\lambda_k\, x - \omega t)\big), \tag{9.5}$$

provides that the *dispersion relation*

$$\omega = |\lambda_k|^\alpha + \gamma|a|^2, \tag{9.6}$$

is satisfied. Here, 'a' is the amplitude of the plane wave solution, $\lambda_k \in \mathbb{R}$ is the wave numbers, and ω is the time frequency.

9.1. LINEAR STABILITY ANALYSIS

Due to the nonlocality, the stability and dynamics of the plane wave solutions in the fractional NLS are significantly different from those in the standard NLS [33]. Consider a finite domain of size L, and thus the wave number is chosen as $\lambda_k = 2k\pi/L$ with $k \in \mathbb{Z}$. Due to the nonlinearity of (9.1), the plane wave solution is stable only under certain conditions. Here, we will focus on the linear stability analysis of the plane wave solution (9.5). Consider a perturbed solution of the form

$$\widetilde{u}(x,t) = u(x,t)(1 + \varepsilon(x,t)), \tag{9.7}$$

where $u(x,t)$ is the plane wave solution in (9.5), and $\varepsilon(x,t)$ is a small perturbation function satisfying $|\varepsilon| \ll 1$. We assume that ε is periodic on an interval $[-\frac{1}{2}L,\ \frac{1}{2}L]$, and it can be expanded in Fourier series as

$$\varepsilon(x,t) = \sum_{l\in\mathbb{Z}} \widehat{\varepsilon}_l(t)\exp(i\mu_l x)$$

with $\mu_l = 2l\pi/L$ for $l \in \mathbb{Z}$. In what follows, we set $\mathrm{Re}(\widehat{\varepsilon}_0(0)) = 0$ without loss of generality. Indeed, having $\mathrm{Re}(\widehat{\varepsilon}_0(0)) \neq 0$ simply rescales the amplitude a of the unperturbed wave (9.5) in the order $\mathcal{O}(\varepsilon)$.

Substituting (9.7) into the fractional NLS (9.1) and taking the leading order terms of ε, we obtain

$$\varepsilon_t = i\Big(|\lambda_k|^\alpha\varepsilon - \sum_{l\in\mathbb{Z}} \widehat{\varepsilon}_l(t)|\lambda_k+\mu_l|^\alpha \exp(i\mu_l x) - \gamma|a|^2(\varepsilon^* + \varepsilon)\Big), \tag{9.8}$$

where ε^* denotes the complex conjugate of ε. Taking the Fourier transform of (9.8) and its complex conjugate, we get the following system of ODEs:

$$\frac{d}{dt}\begin{pmatrix} \widehat{\varepsilon}_l \\ \widehat{\varepsilon}^*_{-l} \end{pmatrix} = G_l \begin{pmatrix} \widehat{\varepsilon}_l \\ \widehat{\varepsilon}^*_{-l} \end{pmatrix},$$

for $l \in \mathbb{Z}\backslash\{0\}$, where

$$G_l = i\begin{pmatrix} |\lambda_k|^\alpha - \gamma|a|^2 - |\lambda_k+\mu_l|^\alpha & -\gamma|a|^2 \\ \gamma|a|^2 & -|\lambda_k|^\alpha + \gamma|a|^2 + |\lambda_k - \mu_l|^\alpha \end{pmatrix}.$$

The eigenvalues of matrix G_l are computed as:

$$\Lambda_l = -\frac{i}{2}(|\lambda_k+\mu_l|^\alpha - |\lambda_k-\mu_l|^\alpha) \pm \frac{1}{2}\sqrt{\Delta_l}, \tag{9.9}$$

where

$$\begin{aligned}\Delta_l = &-\Big[(|\lambda_k + \mu_l|^\alpha + |\lambda_k - \mu_l|^\alpha) - 2|\lambda_k|^\alpha\Big] \\ &\cdot\Big[(|\lambda_k + \mu_l|^\alpha + |\lambda_k - \mu_l|^\alpha) - 2(|\lambda_k|^\alpha - 2\gamma|a|^2)\Big].\end{aligned}$$

The modes $(\widehat{\varepsilon}_l, \widehat{\varepsilon}_l^*)^T$ exponentially grow if at least one of the eigenvalues Λ_l in (9.9) has positive real part, which occurs for

$$\Delta_l > 0. \tag{9.10}$$

If $\Delta_l > 0$ for at least one $l \in \mathbb{Z}$, then the plane wave solution (9.5) is unstable. This instability condition depends not only on the parameters λ_k and a from the plane wave solution, but also on α and γ from the fractional NLS (9.1).

Below we will focus on how the instability condition (9.10) depends on the exponent α in the fractional NLS (9.1) and the wave number λ_k in the initial condition. For the standard NLS ($\alpha = 2$), it is known that the plane wave is stable in the defocusing ($\gamma > 0$) case and unstable in the focusing ($\gamma < 0$) case. Moreover, stability of the plane wave in the standard NLS is independent of its wave number λ_k. For the fractional NLS ($0 < \alpha < 2$), both these well-established facts no longer hold: the plane wave may be unstable in the defocusing case (for $\alpha \in (0, 1)$), and its (in)stability is affected by λ_k, γ and a. These situations are delineated in Theorems 9.1.1 and 9.1.2 below.

Theorem 9.1.1 (Stability for $\alpha \in [1, 2]$)**.**

(a) For $\gamma > 0$ *(defocusing), a plane wave with* any λ_k *is always stable.*

(b) For $\gamma < 0$ *(focusing), the plane wave solution is linearly unstable if there exists at least one* $l \in \mathbb{Z}$ *such that*

$$2|\lambda_k|^\alpha < |\lambda_k + \mu_l|^\alpha + |\lambda_k - \mu_l|^\alpha < 2|\lambda_k|^\alpha - 4\gamma|a|^2. \tag{9.11}$$

Proof. Let us introduce a notation:

$$\delta_l = \delta(\mu_l) = |\lambda_k + \mu_l|^\alpha + |\lambda_k - \mu_l|^\alpha - 2|\lambda_k|^\alpha;$$

then the analytical instability condition (9.10) takes the form

$$\Delta_l = -\delta_l(\delta_l + 4\gamma|a|^2) > 0. \tag{9.12}$$

For $1 \leq \alpha \leq 2$, the function $f(x) = |x|^\alpha$ is convex. By the Jensen's inequality [57], we obtain:

$$\begin{aligned} |\lambda_k|^\alpha &= \left|\frac{1}{2}(\lambda_k + \mu_l) + \frac{1}{2}(\lambda_k - \mu_l)\right|^\alpha \\ &\leq \frac{1}{2}|\lambda_k + \mu_l|^\alpha + \frac{1}{2}|\lambda_k - \mu_l|^\alpha; \qquad \alpha \in [1,\, 2], \end{aligned} \tag{9.13}$$

which implies that $\delta_l \geq 0$, for any μ_l.

(a). For $\gamma > 0$, we get $\Delta_l = -\delta_l(\delta_l + 4\gamma|a|^2) < 0$ for any μ_l, and thus the plane wave solution is always stable in this case.

(b). For $\gamma < 0$, $\Delta_l > 0$ is equivalent to $0 < \delta_l < -4\gamma|a|^2$, which leads the result. □

The instability condition for $\alpha \in (0, 1)$ is more complicated than $\alpha \in [1, 2]$. Let $\widetilde{\mu}_0$ be the largest root of $\delta(\mu_l) = 0$. We then have the following Theorem for $\alpha \in (0, 1)$.

Theorem 9.1.2 (Stability for $\alpha \in (0, 1)$)**.**

(a) For $\gamma > 0$ (defocusing), the plane wave solution is linearly unstable if there exists at least one $l \in \mathbb{Z}$ such that

$$|\mu_l| < \widetilde{\mu}_0 \qquad \text{and} \qquad \delta(\mu_l) > -4\gamma|a|^2. \tag{9.14}$$

This condition can be further expressed more explicitly, *(a1) If* $-4\gamma|a|^2 < (2^\alpha - 2)|\lambda_k|^\alpha$*, then the second condition* $\delta(\mu_l) > -4\gamma|a|^2$ *is satisfied automatically, thus the plane wave solution is linearly unstable if there exists at least one* $l \in \mathbb{Z}$ *such that* $|\mu_l| < \widetilde{\mu}_0$*, see Figure 9.1 on the left.*

(a2) If $-4\gamma|a|^2 > (2^\alpha - 2)|\lambda_k|^\alpha$*, then we can prove* $\delta(\mu_l) = -4\gamma|a|^2$ *has four distinct roots* $\mu_l = \pm\widetilde{\mu}_i$ *(*$i = 1$ *or* 2*) satisfy* $-\widetilde{\mu}_2 < -\widetilde{\mu}_1 < 0 < \widetilde{\mu}_1 < \widetilde{\mu}_2 < \widetilde{\mu}_0$*, thus the plane wave solution is linearly unstable if there exists at least one* $l \in \mathbb{Z}$ *such that* $|\mu_l| < \widetilde{\mu}_1$ *or* $\widetilde{\mu}_2 < |\mu_l| < \widetilde{\mu}_0$*, see Figure 9.1 on the right.*

(b) For $\gamma < 0$ *(focusing), the plane wave solution is linearly unstable if there exists at least one* $l \in \mathbb{Z}$ *such that*

$$|\mu_l| > \widetilde{\mu}_0 \qquad \text{and} \qquad \delta(\mu_l) < -4\gamma|a|^2.$$

Precisely, the equation $\delta(\mu_l) = -4\gamma|a|^2$ *has two distinct real roots* $\mu_l = \pm\widetilde{\mu}_3$ *satisfy* $-\widetilde{\mu}_3 < 0 < \widetilde{\mu}_0 < \widetilde{\mu}_3$*, thus the plane wave solution is linearly unstable if there exists at least one* $l \in \mathbb{Z}$ *such that* $\tilde{\mu}_0 < |\mu_l| < \tilde{\mu}_3$*, see Figure 9.2.*

Proof. First of all, the instability condition (9.12) is equivalent to the following two cases:

$$\delta(\mu_l) + 4\gamma|a|^2 > 0 \quad \text{and} \quad \delta(\mu_l) < 0; \quad \text{or}$$
$$\delta(\mu_l) + 4\gamma|a|^2 < 0 \quad \text{and} \quad \delta(\mu_l) > 0.$$

In case (a) for $\gamma > 0$, assuming that

$$\delta(\mu_l) + 4\gamma|a|^2 < 0 \Rightarrow \delta(\mu_l) < -4\gamma|a|^2 < 0$$

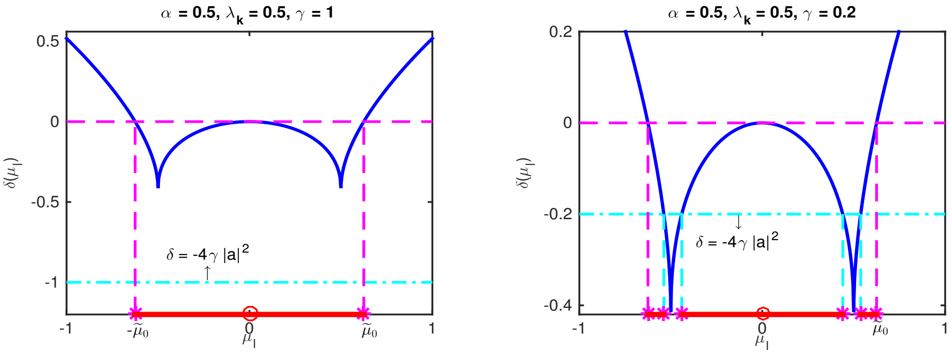

Figure 9.1. Illustration of Theorem 9.1.2 (a). Analytical stability for $\alpha \in (0, 1)$ and $a = 0.5$ for $\gamma > 0$. The intervals colored in red correspond to the instability conditions in Theorem 9.1.2 (a). Left: corresponds to the case (a1); Right: corresponds to the case (a2).

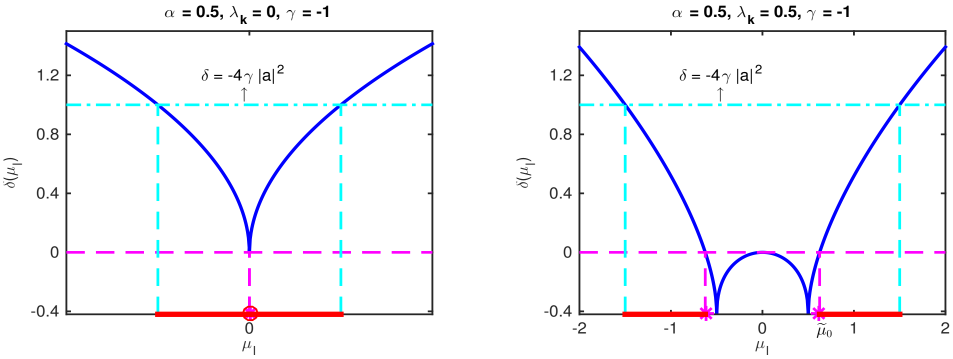

Figure 9.2. Illustration of Theorem 9.1.2 (b). Analytical stability for $\alpha \in (0, 1)$ and $a = 0.5$ for $\gamma < 0$. The intervals colored in red correspond to the instability conditions in Theorem 9.1.2 (b). Left: corresponds to the case by taking $\lambda_k = 0$; Right: corresponds to the case by taking $\lambda_k \neq 0$.

conflicting to $\delta(\mu_l) > 0$, which implies that the instability condition (9.12) can not be satisfied by case 2. That is the instability condition (9.12) is equivalent to

$$\delta(\mu_l) + 4\gamma|a|^2 > 0 \quad \text{and} \quad \delta(\mu_l) < 0.$$

To get the instability condition in (9.14), it is left to show

$$\delta(\mu_l) < 0 \quad \Leftrightarrow \quad |\mu_l| < \widetilde{\mu}_0. \tag{9.15}$$

The function $\delta(\mu_l)$ is presented in the left plot of Figure 9.1. Analytically, it is easy to show that $\delta(\mu_l)$ is increasing on $(|\lambda_k|, \infty)$ and decreasing on $(0, |\lambda_k|)$. In addition, since

$$\delta(|\lambda_k|) = (2^\alpha - 2)|\lambda_k|^\alpha < 0 \quad \text{and} \quad \delta(2|\lambda_k|) = (3^\alpha - 1)|\lambda_k|^\alpha > 0,$$

by Intermediate theorem, there exists one solution $\widetilde{\mu}_0 \in (|\lambda_k|, 2|\lambda_k|)$ such that $\delta(\widetilde{\mu}_l) = 0$, and this root is unique because $\delta(\mu_l)$ is increasing on $(|\lambda_k|, \infty)$. By the symmetric property of function $\delta(\mu_l)$, it is easy to prove the $\delta(\mu_l)$ is increasing on $(-\infty, -|\lambda_k|)$ and decreasing on $(-|\lambda_k|, 0)$. In addition, there exists a unique solution $-\widetilde{\mu}_0 \in (-2|\lambda_k|, -|\lambda_k|)$ such that $\delta(-\widetilde{\mu}_l) = 0$. Therefore, we prove the equivalence of the two statements in (9.16) and thus proved case (a). Next, we will further prove the statements (a1) and (a2).

Since $\pm|\lambda_k|$ are the global minimum of function $\delta(\mu_l)$, we consider $\delta(\pm|\lambda_k|) = (2^\alpha - 2)|\lambda_k|^\alpha$ be the critical line, and separate our discussion into two cases:

(a1). if $-4\gamma|a|^2 < (2^\alpha - 2)|\lambda_k|^\alpha$, the plot of $\delta(\mu_l)$ is presented on the left of Figure 9.1;

(a2). if $-4\gamma|a|^2 > (2^\alpha - 2)|\lambda_k|^\alpha$, the plot of $\delta(\mu_l)$ is presented on the right of Figure 9.1.

Therefore, the statements (a1) and (a2) directly followed by the illustration from Figure 9.1.

In case (b) for $\gamma < 0$, since that

$$\delta(\mu_l) + 4\gamma|a|^2 > 0 \Rightarrow \delta(\mu_l) > -4\gamma|a|^2 > 0$$

conflicts to $\delta(\mu_l) < 0$, which implies that the instability condition (9.10) is equivalent to

$$\delta(\mu_l) + 4\gamma|a|^2 < 0 \quad \text{and} \quad \delta(\mu_l) > 0.$$

Following the same line as the proof of case (a), we have

$$\delta(\mu_l) > 0 \quad \Leftrightarrow \quad |\mu_l| > \widetilde{\mu}_0. \tag{9.16}$$

The function $\delta(\mu_l)$ is displayed in Figure 9.2 for $\lambda_k = 0$ on the left and $\lambda \neq 0$ on the right. Let $\pm\widetilde{\mu}_3$ be the two roots of equation $\delta(\mu_l) = -4\gamma|a|^2$, since for $\gamma < 0$, it always has $-4\gamma|a|^2 > 0$, which follows that

$$-\widetilde{\mu}_3 < -\widetilde{\mu}_0 < 0 < \widetilde{\mu}_0 < \widetilde{\mu}_3.$$

Therefore, we proved case (b). □

Remark 9.1.1. *As a special case, for $\lambda_k = 0$, the instability condition (9.35) reduces to*

$$0 < |\mu_l|^\alpha < -2\gamma|a|^2, \tag{9.17}$$

for all $\alpha \in (0, 2]$, and the case $\alpha = 2$ is consistent with the condition obtained in the literature on the standard NLS; see [12, 37, 86] and references therein.

Remark 9.1.1 shows that the stability of the plane wave solution in the standard (i.e., $\alpha = 2$) NLS is independent of the wave number λ_k, and thus λ_k is ignored in the analysis [12, 22, 37, 86]. However, in the fractional NLS, the wave number λ_k of the plane wave solution plays an important role in its stability, which is one main difference between the fractional and standard NLS.

Figures 9.3 and 9.4 illustrate the behavior of $\mathrm{Re}(\Lambda_l) = \frac{1}{2}\sqrt{\Delta_l}$ versus μ_l for $\gamma > 0$ and $\gamma < 0$, respectively; we only show the location of unstable modes, where $\mathrm{Re}(\Lambda_l) > 0$. In the defocusing ($\gamma > 0$) case, no instability occurs if the frequency $\lambda_k = 0$, for any $\alpha \in (0, 2]$. If the wave number $\lambda_k \neq 0$, Figure 9.3 shows that all modes are stable for $1 \leq \alpha \leq 2$, and thus the plane wave solution is always stable in this case, which is consistent to the analysis in Theorem 9.1.1 (a). In contrast if $0 < \alpha < 1$, unstable modes appear in low-μ_l region, and the number of unstable modes depends on λ_k, γ and a. The results in Figure 9.3 also justify Theorem 9.1.2. In fact, the left plot of Figure 9.3 illustrates Theorem 9.1.2 (a1) and the right of Figure 9.3 illustrates Theorem 9.1.2 (a2). For a fixed α, the unstable modes in Figure 9.3 (left/right) correspond to the unstable region that is colored in red of Figure 9.1 (left/right). As shown in Theorem 9.1.2 (a2), if $-4\gamma|a|^2 > (2^\alpha - 2)|\lambda_k|^\alpha$, there is a "stable-gap" at low-μ_l area., and the width of the gap is $|\widetilde{\mu}_2 - \widetilde{\mu}_1|$.

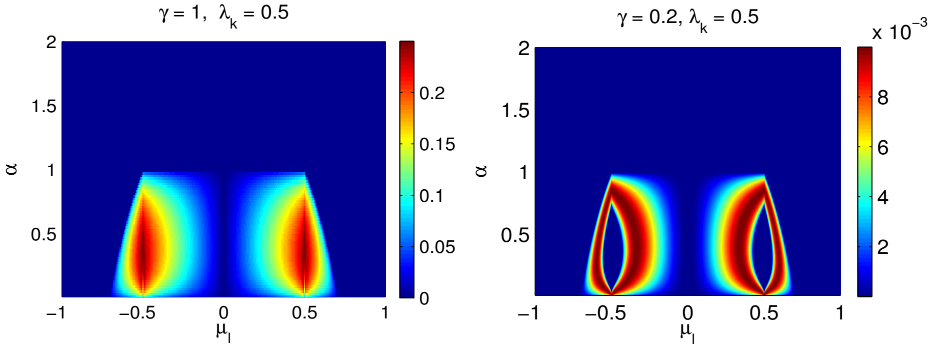

Figure 9.3. Contour plots of $\mathrm{Re}(\Lambda_l)$ for the plane wave solution (9.5) with $a = \frac{1}{2}$. Note that when $\alpha < 1$, $\mathrm{Re}(\Lambda_l) > 0$ for $|\mu_l| \ll 1$, although its value is small.

In the focusing ($\gamma < 0$) case, Figure 9.4 shows that the unstable modes could occur for any $0 < \alpha \leq 2$. When $1 < \alpha \leq 2$, unstable modes always exist in the low-μ_l region, and the size of unstable band depends on $|\gamma||a|^2$. By contrast, if $0 < \alpha \leq 1$, the unstable modes are sensitive to λ_k. For $\lambda_k = 0$, instability start from low-μ_l modes and could spread to high-μ_l region if α is small. For $\lambda_k \neq 0$, unstable modes start from relatively high-μ_l

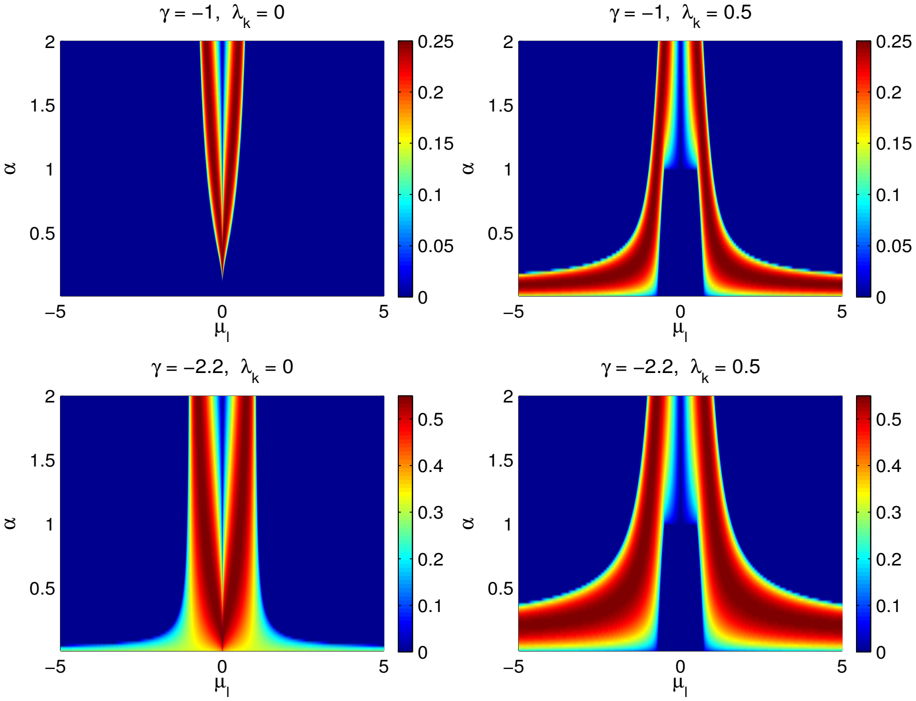

Figure 9.4. Contour plots of $\mathrm{Re}(\Lambda_l)$ for $\gamma < 0$. Same as in Figure 9.6, but for $\gamma < 0$. Note that γ in the first and second rows are different. Note that when $\alpha > 1$, $\mathrm{Re}(\Lambda_l) > 0$ for $|\mu_l| \ll 1$, although its value is small.

region, and there is a “stable-gap" at the low-μ_l area, the width of the gap is $\widetilde{\mu}_0$ which is suggested in Theorem 9.1.2 (b) (see also Figure 9.2 on the right). As a special case, the width of the gap is $|\lambda_k|$, if $\alpha = 1$.

Figs. 9.3 and 9.4 show that the instability behaviors of the plane wave solutions for $\alpha > 1$ and $\alpha < 1$ are significantly different. Namely, the stability of low-μ_l modes changes at $\alpha = 1$. To further understand it, we present $\mathrm{Re}(\Lambda_l)$ versus μ_l for $\alpha = 0.9, 1$ and 1.1 in Figure 9.5. It shows that when $\gamma > 0$ and $\alpha \geq 1$, $\mathrm{Re}(\Lambda_l) \leq 0$ for any $l \in \mathbb{Z}$, implying all modes are stable and thus the plane wave solution are stable in this case. While $\gamma < 0$ and $\lambda_k \neq 0$, the unstable modes starts from $\mu_{\pm 1}$ for $\alpha = 1.1$, but they appear only at relatively high frequency region for $\alpha = 0.9$ or 1.

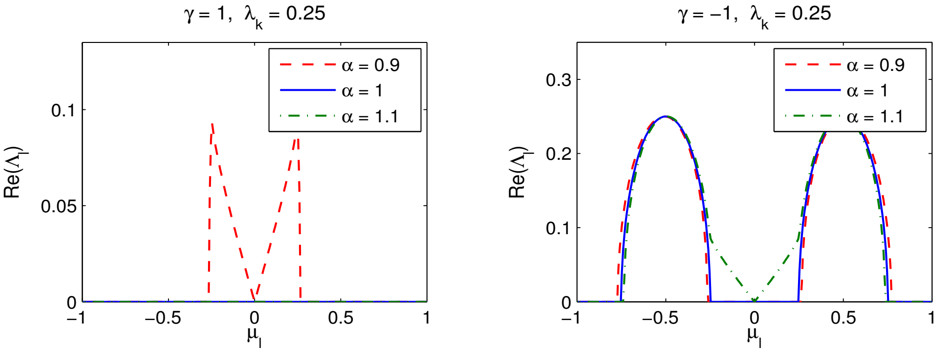

Figure 9.5. Comparison of unstable modes for $\alpha = 0.9, 1$ and 1.1.

9.2. NUMERICAL METHODS

To further understand the nonlinear stage of the plane wave dynamics of the fNLS, only linear stability analysis is not enough. Therefore, numerical simulations play an important role in the study of the fractional NLS. However, in contrast to the standard NLS, only a few numerical methods are available in the literature for solving the fractional NLS. In this section, we aim to develop and compare the numerical methods for solving the fractional NLS, which preserve one or more analytical properties of the fractional NLS, including mass conservation, energy conservation, time reversible, and dispersion relation.

First, we truncate (9.1)–(9.2) into a finite computational domain $[-L/2, L/2]$ with periodic boundary conditions and consider the following problem:

$$i\partial_t u(x,t) = (-\Delta)^{\alpha/2}u(x,t) + \gamma|u(x,t)|^2 u(x,t), \qquad t > 0, \tag{9.18}$$

$$u(x,0) = \psi(x), \tag{9.19}$$

for $x \in [-L/2, L/2]$. Usually, we choose L to be sufficiently large, unless plane wave solutions are studied. We will leave the discussion of other boundary conditions for our future work.

Let $\tau > 0$ denote a time step, and define the time sequence $t_n = n\tau$ for $n \geq 0$. Define the mesh size $h = L/J$, with J a positive even integer. Denote the spatial grid points $x_j = -L/2 + jh$ for $0 \leq j \leq J$. Let u_j^n be the numerical approximation of the solution $u(x_j, t_n)$. Then, we denote the solution vector at time $t = t_n$ as $U^n = (u_0^n,\ u_1^n,\ \ldots,\ u_J^n)^T$. Due to the definition of $(-\Delta)^{\alpha/2}$ in (1.1), it is natural to use the Fourier spectral method for spatial discretization. Hence, we assume the anzatz:

$$u(x,t) = \sum_{l=-J/2}^{J/2-1} \widehat{u}_l(t) \exp(i\mu_l x), \tag{9.20}$$

where

$$\mu_l = \frac{2\pi l}{L}, \qquad \text{for } -\frac{J}{2} \leq l \leq \frac{J}{2} - 1.$$

In the following, we will focus on the temporal discretization and the properties of the resulting numerical methods.

9.2.1. Split-step Fourier Spectral Method. The split-step method, also known as the time-splitting method, is one of the most popular numerical methods for solving the standard NLS equation (also known as the Gross–Pitaevskii equation in the literature of Bose–Einstein condensation). It is an explicit method and thus avoids solving nonlinear systems at each time step. The main idea of this method is outlined below. From time $t = t_n$ to $t = t_{n+1}$, the fractional NLS (9.18) is solved in two steps:

$$iu_t(x,t) = \gamma|u(x,t)|^2 u(x,t), \tag{9.21}$$

$$iu_t(x,t) = (-\Delta)^{\alpha/2} u(x,t). \tag{9.22}$$

On one hand, multiplying $u^*(x,t)$ at both sides of (9.21) and subtracting from its conjugate, we obtain that $|u(x,t)| = |u(x,t_n)|$ for any $t \in [t_n, t_{n+1}]$. Therefore, (9.21) reduces to

$$iu_t(x,t) = \gamma |u(x,t_n)|^2 u(x,t).$$

Integrating it in time yields the solution to (9.21):

$$u(x,t) = u(x,t_n) \exp\Big(- i\gamma |u(x,t_n)|^2 (t-t_n)\Big), \qquad t \in [t_n, t_{n+1}]. \tag{9.23}$$

On the other hand, substituting (9.20) into (9.22), we obtain that

$$i\widehat{u}_l'(t) = |\mu_l|^\alpha \, \widehat{u}_l(t), \qquad -\frac{J}{2} \le l \le \frac{J}{2} - 1.$$

Integrating it in time gives

$$\widehat{u}_l(t) = \widehat{u}_l(t_n) \exp\big(- i|\mu_l|^\alpha (t-t_n)\big), \tag{9.24}$$

for $t \in [t_n, t_{n+1}]$ and $-\frac{J}{2} \le l \le \frac{J}{2} - 1$. Combining (9.58) and (9.20) gives the numerical approximation to the solution of (9.22).

Let u_j^n denote the numerical approximation of $u(x_j, t_n)$. Then the first-order Strang split-step Fourier spectral method for the fractional NLS can be summarized as follows:

$$u_j^{n+1,-} = u_j^n \, \exp(-i\gamma\tau |u_j^n|^2), \tag{9.25}$$

$$u_j^{n+1} = \sum_{l=-J/2}^{J/2-1} \widehat{u}_l^{n+1,-} \exp(-i|\mu_l|^\alpha \tau) \, \exp(i\mu_l x_j), \quad 0 \le j \le J-1, \ \ n = 0, 1, \ldots \tag{9.26}$$

The numerical scheme in (9.25)–(9.26) has spectral accuracy in space and first-order accuracy in time, and the time accuracy can be easily improved by adapting higher order split-step methods [82]. Combine the steps (9.21) and (9.22) by the second order Strang splitting method, resulting in the second-order split-step Fourier spectral (SSFS) method for the fractional NLS (9.18)–(9.19) as follows:

$$\begin{aligned}
u_j^{n,1} &= u_j^n \exp(-i\gamma\tau|u_j^n|^2/2),\\
u_j^{n,2} &= \sum_{l=-J/2}^{J/2-1} \widehat{u}_l^{n,1} \exp\big(-i|\mu_l|^\alpha\tau\big)\exp\big(i\mu_l x_j\big), && (9.27)\\
u_j^{n+1} &= u_j^{n,2} \exp(-i\gamma\tau|u_j^{n,2}|^2/2), \quad 0 \le j \le J-1, \;\; n = 0, 1, \ldots. && (9.28)
\end{aligned}$$

The initial condition (9.19) is discretized as:

$$u_j^0 = \psi(x_j), \qquad 0 \le j \le J. \tag{9.29}$$

The SSFS method in (9.27)–(9.29) has the spectral order spatial accuracy and the second-order temporal accuracy, which can be efficiently implemented by the fast Fourier transform (FFT).

It is easy to verify that the SSFS method (9.27)–(9.29) is time reversible, i.e., the method remains unchanged if $\tau \leftrightarrow -\tau$ and $n \leftrightarrow n+1$. Moreover, the SSFS method has the properties in the following lemmas

Lemma 9.2.1 (SSFS: Mass conservation)**.** *Suppose that U^n is the numerical solution of the fractional NLS at time t_n, obtained from the SSFS method in (9.27)–(9.29). Then, we have the discrete mass:*

$$N^n = h\sum_{j=0}^{J-1} |u_j^n|^2 = h\sum_{j=0}^{J-1} |u_j^0|^2 \equiv N^0, \qquad n \ge 0, \tag{9.30}$$

i.e., it is conserved at any time t_n.

Proof. From (9.27), we obtain that

$$\begin{aligned}\sum_{j=0}^{J-1}|u_j^{n,2}|^2 &= \sum_{j=0}^{J-1}\Big|\sum_{l=-J/2}^{J/2-1}\widehat{u}_l^{n,1}\exp\left(-i|\mu_l|^{\alpha}\tau\right)\exp\left(i\mu_l x_j\right)\Big|^2\\ &= \sum_{l=-J/2}^{J/2-1}\sum_{s=-J/2}^{J/2-1}\widehat{u}_l^{n,1}(\widehat{u}_s^{n,1})^*\exp\left(-i\tau(|\mu_l|^{\alpha}-|\mu_s|^{\alpha})\right)\sum_{j=0}^{J-1}\exp\left(i(\mu_l-\mu_s)x_j\right)\\ &= J\sum_{l=-J/2}^{J/2-1}|\widehat{u}_l^{n,1}|^2. \end{aligned} \tag{9.31}$$

Then, using the discrete Parseval's relation

$$\sum_{l=-J/2}^{J/2-1}|\widehat{u}_l^{n,1}|^2 = \frac{h}{2L}\sum_{j=0}^{J-1}|u_j^{n,1}|^2 = \frac{1}{J}\sum_{j=0}^{J-1}|u_j^{n,1}|^2,$$

we obtain from (9.27) and (9.31) that

$$N^{n+1} = h\sum_{j=0}^{J-1}|u_j^{n+1}|^2 = h\sum_{j=0}^{J-1}|u_j^{n,2}|^2 = h\sum_{j=0}^{J-1}|u_j^{n,1}|^2 = h\sum_{j=0}^{J-1}|u_j^{n}|^2 = N^n,$$

which implies the mass conservation in (9.30), as $n \geq 0$ is arbitrary. □

Lemma 9.2.2 (SSFS: Dispersion relation)**.** *The SSFS method (9.27)–(9.29) preserves the dispersion relation* $\omega = |\lambda_k|^{\alpha} + \gamma|a|^2$ *of the plane wave solution in the fractional NLS.*

Proof. Assume that at time $t = t_n$ (for any $n \geq 0$), the solution u_j^n has the form:

$$u_j^n = a\exp\left(i(\lambda_k x_j - \omega t_n)\right), \quad \text{with } \lambda_k = 2\pi k/L, \quad \text{for } k \in \mathbb{Z}. \tag{9.32}$$

Note that $\lambda_k = \mu_k$. On one hand, from (9.32) and the solution $u_j^{n,1}$ in (9.27), we get that

$$\widehat{u}_l^{n,1} = \begin{cases} 0, & \text{if} \quad l \neq k,\\ a\exp(-i\omega t_n)\exp(-i\gamma\tau|a|^2/2), & \text{if} \quad l = k,\end{cases}$$

for $-J/2 \leq l \leq J/2-1$. Plugging it into the second step of (9.27) gives that

$$u_j^{n,2} = u_j^n \exp(-i\gamma\tau|a|^2/2)\exp(-i|\mu_k|^\alpha\tau).$$

Substituting the above solution $u_j^{n,2}$ into the last step of (9.27), we get

$$u_j^{n+1} = u_j^n \exp\big[-i\tau(|\mu_k|^\alpha + \gamma|a|^2)\big]. \tag{9.33}$$

On the other hand, setting $n = n+1$ in (9.32), we get

$$u_j^{n+1} = a\exp\big(i(\lambda_k x_j - \omega t_{n+1})\big) = u_j^n \exp(-i\omega\tau). \tag{9.34}$$

Comparing (9.33) and (9.34), we obtain

$$\omega = |\lambda_k|^\alpha + \gamma|a|^2,$$

i.e., the numerical solution from the SSFS method satisfies the dispersion relation of the plane wave solution. □

Lemma 9.2.2 implies that the SSFS method can exactly solve the plane wave solution of the NLS, if there is no numerical error, which makes it an ideal method to study the long-time behavior of the plane wave dynamics. However, the SSFS method, as an explicit method, is conditionally stable in simulating the plane wave solution, and sufficient conditions are need to be derived to avoid its numerical instability, which will be carried out in Section 9.3

9.2.2. Crank–Nicolson Fourier Spectral Method. In this section, we study the Crank–Nicolson Fourier spectral method for solving the fractional NLS. First, let's define the pseudo-differential operator

$$\delta_x^\alpha U^n\big|_j = \sum_{l=-J/2}^{J/2-1} |\mu_l|^\alpha \, \widehat{u}_l^n \exp\left(i\mu_l x_j\right), \tag{9.35}$$

which can be viewed as a numerical approximation of $(-\Delta)^{\alpha/2}u(x,t)$ at point $x = x_j$ and time $t = t_n$.

Then, the Crank–Nicolson Fourier spectral (CNFS) method for the fractional NLS (9.18) reads:

$$i\,\frac{u_j^{n+1} - u_j^n}{\tau} = \frac{1}{2}\left(\delta_x^\alpha U^{n+1}\big|_j + \delta_x^\alpha U^n\big|_j\right) + \frac{\gamma}{2}F(|u_j^{n+1}|^2, |u_j^n|^2)(u_j^{n+1} + u_j^n), \tag{9.36}$$

for $0 \le j \le J$ and $n \ge 0$, where the function F is defined as

$$F(\phi_1, \phi_2) = \int_0^1 (\theta\phi_1 + (1-\theta)\phi_2)\,d\theta.$$

It is easy to compute that

$$F(\phi_1, \phi_2) = \frac{1}{2}\left(\phi_1 + \phi_2\right).$$

At $n = 0$, the initial condition (9.19) is discretized as:

$$u_j^0 = \psi(x_j), \qquad 0 \le j \le J. \tag{9.37}$$

The CNFS method (9.36)–(9.37) is an implicit scheme, which requires solving a nonlinear system at each time step. Hence, the computational cost of the CNFS method is higher than that of the SSFS method. However, the CNFS method conserves not only the mass but also the energy of the fractional NLS. In addition, the CNFS method is time reversible.

Lemma 9.2.3 (CNFS: Mass conservation)**.** *Suppose that U^n is the numerical solution of the fractional NLS at time t_n, obtained from the CNFS method in (9.36)–(9.37). Then, we have the discrete mass*

$$N^n = h\sum_{j=0}^{J-1}|u_j^n|^2 = h\sum_{j=0}^{J-1}|u_j^0|^2 \equiv N^0, \qquad n \geq 0. \tag{9.38}$$

Proof. Multiplying $(u_j^{n+1}+u_j^n)^*$ to (9.36) and summing it up for $0 \leq j \leq J-1$, we obtain

$$\begin{aligned} i\frac{1}{\tau}\sum_{j=0}^{J-1}&(u_j^{n+1}-u_j^n)(u_j^{n+1}+u_j^n)^* \\ &= \frac{1}{2}\sum_{j=0}^{J-1}(u_j^{n+1}+u_j^n)^*\sum_{l=-J/2}^{J/2-1}|\mu_l|^\alpha(\widehat{u}_l^n+\widehat{u}_l^{n+1})\exp(i\mu_l x_j) \\ &+\frac{\gamma}{2}\sum_{j=0}^{J-1}F(|u_j^{n+1}|^2,|u_j^n|^2)|u_j^{n+1}+u_j^n|^2. \end{aligned} \tag{9.39}$$

Note that

$$\begin{aligned} \sum_{j=0}^{J-1}(u_j^{n+1}+u_j^n)^*&\sum_{l=-J/2}^{J/2-1}|\mu_l|^\alpha(\widehat{u}_l^n+\widehat{u}_l^{n+1})\exp(i\mu_l x_j) \\ &= J\sum_{l=-J/2}^{J/2-1}|\mu_l|^\alpha|\widehat{u}_l^n+\widehat{u}_l^{n+1}|^2. \end{aligned} \tag{9.40}$$

Then taking the imaginary part of (9.39) and noticing that $\tau > 0$, we get

$$\sum_{j=0}^{J-1}|u_j^{n+1}|^2 = \sum_{j=0}^{J-1}|u_j^n|^2,$$

which implies that $N^{n+1} = N^n$, and thus (9.38) as $n \geq 0$ is arbitrary. □

Lemma 9.2.4 (CNFS: Energy conservation)**.** *Suppose that U^n is the numerical solution of the fractional NLS at time t_n, obtained from the CNFS method in (9.36)–(9.37). Then, we have the discrete energy*

$$E^n = h\sum_{j=0}^{J-1}\Big[\sum_{l=-J/2}^{J/2-1}|\mu_l|^\alpha|\widehat{u}_l^n|^2 + \frac{\gamma}{2}|u_j^n|^4\Big] \equiv E^0, \qquad n \geq 0. \tag{9.41}$$

Proof. We assume that $|u_j^{n+1}| \neq |u_j^n|$. Multiplying $(u_j^{n+1} - u_j^n)^*$ to (9.36) and summing it up for $0 \leq j \leq J-1$, we get

$$\begin{aligned} i\frac{1}{\tau}\sum_{j=0}^{J-1}|u_j^{n+1} - u_j^n|^2 = \frac{1}{2}\sum_{j=0}^{J-1}(u_j^{n+1} - u_j^n)^*\sum_{l=-J/2}^{J/2-1}|\mu_l|^\alpha(\widehat{u}_l^n + \widehat{u}_l^{n+1})\exp(i\mu_l x_j) \\ +\frac{\gamma}{4}\sum_{j=0}^{J-1}\frac{|u_j^{n+1}|^4 - |u_j^n|^4}{|u_j^{n+1}|^2 - |u_j^n|^2}(u_j^{n+1} + u_j^n)(u_j^{n+1} - u_j^n)^*. \end{aligned} \tag{9.42}$$

Note that

$$\begin{aligned} &\sum_{j=0}^{J-1}(u_j^{n+1} - u_j^n)^*\sum_{l=-J/2}^{J/2-1}|\mu_l|^\alpha(\widehat{u}_l^n + \widehat{u}_l^{n+1})\exp(i\mu_l x_j) \\ &\qquad = \sum_{j=0}^{J-1}\sum_{l=-J/2}^{J/2-1}|\mu_l|^\alpha\big[(|\widehat{u}_l^{n+1}|^2 - |\widehat{u}_l^n|^2) + 2i\mathrm{Im}((\widehat{u}_l^{n+1})^*\widehat{u}_l^n)\big]. \end{aligned}$$

Taking the real part of (9.42) yields

$$\frac{1}{2}\sum_{j=0}^{J-1}\sum_{l=-J/2}^{J/2-1}|\mu_l|^\alpha(|\widehat{u}_l^{n+1}|^2 - |\widehat{u}_l^n|^2) + \frac{\gamma}{4}\sum_{j=0}^{J-1}\big[|u_j^{n+1}|^4 - |u_j^n|^4\big] = 0.$$

Hence, we get

$$\sum_{j=0}^{J-1}\Big[\sum_{l=-J/2}^{J/2-1}|\mu_l|^\alpha|\widehat{u}_l^{n+1}|^2 + \frac{\gamma}{2}|u_j^{n+1}|^4\Big] = \sum_{j=0}^{J-1}\Big[\sum_{l=-J/2}^{J/2-1}|\mu_l|^\alpha|\widehat{u}_l^n|^2 + \frac{\gamma}{2}|u_j^n|^4\Big],$$

for any $n \geq 0$, which implies $E^{n+1} = E^n$ and thus the energy conservation in (9.41). □

Assume that at time $t = t_n$ (for any $n \geq 0$), the solution u_j^n has the form in (9.32). Then, the time frequency ω obtained from the CNFS method (9.36)–(9.37) satisfies the relation:

$$\tan \frac{\omega\tau}{2} = \frac{\tau}{2}(|\lambda_k|^\alpha + \gamma|a|^2). \tag{9.43}$$

If $\omega\tau \ll 1$, the Taylor expansion of (9.43) yields

$$\omega = (|\lambda_k|^\alpha + \gamma|a|^2) + O(\omega^3\tau^2). \tag{9.44}$$

Remark 9.2.1 (CNFS: dispersion relation)**.** *The CNFS method (9.36)–(9.37) does not preserve the exact dispersion relation of the plane wave solution, but it gives a good approximation to the dispersion relation if $\omega^3\tau^2$ is small.*

9.2.3. Relaxation Fourier Spectral Method. In [9], a relaxation method was first introduced for the standard NLS, in which the nonlinear part of the NLS is solved in two steps. It shows that the relaxation method is more efficient than the Crank–Nicolson method, if the finite difference or finite element methods are used for spatial discretization [9]. However, if the Fourier spectral method is use for spatial discretization, the relaxation method has the same computational costs as the Crank–Nicolson method.

First, we write the fractional NLS (9.18) as a system of two equations:

$$\begin{aligned} i\partial_t u(x,t) &= (-\Delta)^{\alpha/2}u(x,t) + \gamma\varphi(x,t)u(x,t), \\ \varphi(x,t) &= |u(x,t)|^2. \end{aligned}$$

Then, the relaxation Fourier spectral (ReFS) method for (9.18) is given by:

$$i\frac{1}{\tau}(u_j^{n+1}-u_j^n)=\frac{1}{2}\left(\delta_x^\alpha U^{n+1}|_j+\delta_x^\alpha U^n|_j\right)+\frac{\gamma}{2}(u_j^{n+1}+u_j^n)\varphi_j^{n+\frac{1}{2}}, \tag{9.45}$$

$$\frac{1}{2}(\varphi_j^{n+\frac{1}{2}}+\varphi_j^{n-\frac{1}{2}})=|u_j^n|^2, \qquad 0\le j\le J, \qquad n\ge 0, \tag{9.46}$$

where the operator δ_x^α is defined in (9.35). At $n=0$, the initial condition is discretized as

$$u_j^0=\psi(x_j), \qquad \varphi_j^{-\frac{1}{2}}=|u_j^0|^2=|\psi(x_j)|^2, \qquad 0\le j\le J. \tag{9.47}$$

The ReFS method (9.45)–(9.47) is implicit, and thus at each time step numerical iterations are needed to solve the nonlinear system. It is easy to show that the ReFS method is time reversible. In addition, the ReFS method has the following properties:

Lemma 9.2.5 (ReFS: Mass conservation)**.** *Suppose that U^n is the numerical solution of the fractional NLS at time t_n, obtained from the ReFS method in (9.45)–(9.47). Then, we have the discrete mass*

$$N^n=h\sum_{j=0}^{J-1}|u_j^n|^2=h\sum_{j=0}^{J-1}|u_j^0|^2\equiv N^0, \qquad n\ge 0. \tag{9.48}$$

Proof. Multiplying $(u_j^{n+1}+u_j^n)^*$ to (9.45) and summing it up for $0\le j\le J-1$, we obtain

$$\begin{aligned}&i\frac{1}{\tau}\sum_{j=0}^{J-1}(u_j^{n+1}-u_j^n)(u_j^{n+1}+u_j^n)^*\\
&=\frac{1}{2}\sum_{j=0}^{J-1}(u_j^{n+1}+u_j^n)^*\sum_{l=-J/2}^{J/2-1}|\mu_l|^\alpha(\widehat{u}_l^{n+1}+\widehat{u}_l^n)\exp(i\mu_l x_j)+\frac{\gamma}{2}\sum_{j=0}^{J-1}|u_j^{n+1}+u_j^n|^2\varphi_j^{n+\frac{1}{2}}.\end{aligned}$$

Taking its imaginary part and noticing that (9.40) and the function φ is real, we obtain

$$\sum_{j=0}^{J-1}|u_j^{n+1}|^2=\sum_{j=0}^{J-1}|u_j^n|^2,$$

which implies that $N^{n+1} = N^n$ and thus (9.38) as $n \geq 0$ is arbitrary. $\square$

Lemma 9.2.6 (ReFS: Energy conservation)**.** *Suppose that U^n is the numerical solution of the fractional NLS at time t_n, obtained from the ReFS method in (9.45)–(9.47). Then, we have the discrete energy*

$$E^n = h\sum_{j=0}^{J-1}\Big[\sum_{l=-J/2}^{J/2-1}|\mu_l|^\alpha|\widehat{u}_l^n|^2 + \gamma|u_j^n|^2\varphi_j^{n-\frac{1}{2}} - \frac{\gamma}{2}(\varphi_j^{n-\frac{1}{2}})^2\Big] \equiv E^0, \tag{9.49}$$

for any $n \geq 0$.

Proof. On one hand, multiplying $(u_j^{n+1}-u_j^n)^*$ to (9.36) and summing it up for $0 \leq j \leq J-1$, we get

$$\begin{aligned} i\frac{1}{\tau}\sum_{j=0}^{J-1}|u_j^{n+1}-u_j^n|^2 = \frac{1}{2}\sum_{j=0}^{J-1}(u_j^{n+1}-u_j^n)^*\sum_{l=-J/2}^{J/2-1}|\mu_l|^\alpha(\widehat{u}_l^n+\widehat{u}_l^{n+1})\exp(i\mu_l x_j) \\ +\frac{\gamma}{2}\sum_{j=0}^{J-1}\varphi_j^{n+\frac{1}{2}}(u_j^{n+1}+u_j^n)(u_j^{n+1}-u_j^n)^*. \end{aligned}$$

Taking its real part yields

$$\frac{1}{2}\sum_{j=0}^{J-1}\sum_{l=-J/2}^{J/2-1}|\mu_l|^\alpha(|\widehat{u}_l^{n+1}|^\alpha - |\widehat{u}_l^n|^\alpha) + \frac{\gamma}{2}\sum_{j=0}^{J-1}\varphi_j^{n+\frac{1}{2}}(|u_j^{n+1}|^2 - |u_j^n|^2) = 0.$$

On the other hand, multiplying $(\varphi_j^{n+\frac{1}{2}} - \varphi_j^{n-\frac{1}{2}})$ to (9.46) and summing it from 0 to n, we obtain

$$\begin{aligned} \frac{1}{2}\Big((\varphi_j^{n+\frac{1}{2}})^2 - (\varphi_j^{-\frac{1}{2}})^2\Big) = \sum_{m=0}^{n}|u_j^m|^2\Big(\varphi_j^{m+\frac{1}{2}} - \varphi_j^{m-\frac{1}{2}}\Big) \\ = \sum_{m=0}^{n}(|u_j^m|^2 - |u_j^{m+1}|^2)\varphi_j^{n+\frac{1}{2}} - |u_j^0|^2\varphi_j^{-\frac{1}{2}} + |u_j^{n+1}|^2\varphi_j^{n+\frac{1}{2}}. \end{aligned}$$

Combining the above two equations leads to

$$\begin{aligned}&\sum_{j=0}^{J-1}\Big[\sum_{l=-J/2}^{J/2-1}|\mu_l|^\alpha|\widehat{u}_l^{n+1}|^2+\gamma|u_j^{n+1}|^2\varphi_j^{n+\frac{1}{2}}-\frac{\gamma}{2}(\varphi_j^{n+\frac{1}{2}})^2\Big]\\ =&\sum_{j=0}^{J-1}\Big[\sum_{l=-J/2}^{J/2-1}|\mu_l|^\alpha|\widehat{u}_l^{0}|^2+\gamma|u_j^{0}|^2\varphi_j^{-\frac{1}{2}}-\frac{\gamma}{2}(\varphi_j^{-\frac{1}{2}})^2\Big],\end{aligned}$$

for any $n \geq 0$, which implying the energy conservation in (9.49). ☐

Assume that at time $t = t_n$ (for any $n \geq 0$), the solution u_j^n has the form in (9.32). Then, we find that the time frequency ω obtained from the ReFS method (9.45)–(9.47) satisfies (9.43) and (9.44).

Remark 9.2.2 (ReFS: dispersion relation)**.** *The ReFS method (9.45)–(9.37) does not preserve the exact dispersion relation of the plane wave solution, but it gives a good approximation to the dispersion relation if $\omega^3\tau^2$ is small.*

9.2.4. Comparison in Simulating Plane Waves. In this section, we will compare the performance of the three Fourier spectral methods – the SSFS, CNFS and ReFS methods in simulating the plane wave dynamics of the fractional NLS.

Example 1 We study the plane wave solutions of the 1D fractional NLS (9.1) on a finite domain $[-\pi, \pi]$. The parameters are chosen as $\gamma = 2$, and the initial condition is taken as

$$u(x, 0) = \exp(i4x), \qquad x \in [-\pi, \pi], \tag{9.50}$$

i.e., the amplitude $a = 1$ and the wave number $\lambda_k = 4$. It is easy to verify that the exact solution of (9.1) with (9.50) is

$$u(x, t) = \exp\big(i(4x - \omega t)\big), \qquad \text{with} \quad \omega = |\lambda_k|^\alpha + \gamma|a|^2 = 4^\alpha + 2. \tag{9.51}$$

In our simulations, we choose the mesh size $h = \pi/32$ and the time step $\tau = 0.02$.

Table 9.1 presents the values of mass $N(t)$ of the SSFS, CNFS and ReFS methods at different time t in solving the 1D fractional NLS (9.18) with $\alpha = 1.5$ and $\gamma = 2$, where the initial condition is (9.50); Table 9.2 displays the corresponding energy $E(t)$. It shows that all of these three methods preserve the mass of the fractional NLS, which is consistent with our analytical results in Section 9.2.

Table 9.1. Mass $N(t)$ by different methods.

Time	SSFS	CNFS	ReFS
t = 0	6.3813600776042669	6.3813600776042669	6.3813600776042669
t = 2	6.3813600776043637	6.3813600776041390	6.3813600776043593
t = 4	6.3813600776044765	6.3813600776040227	6.3813600776044428
t = 6	6.3813600776046160	6.3813600776038797	6.3813600776045032
t = 8	6.3813600776046577	6.3813600776037678	6.3813600776045503
t = 10	6.3813600776047359	6.3813600776036479	6.3813600776046275

Table 9.2. Energy $E(t)$ by different methods.

Time	SSFS	CNFS	ReFS
t = 0	57.432240698438406	57.432240698438406	57.432240698438406
t = 2	57.432240698439358	57.432240698437134	57.432240698439315
t = 4	57.432240698440559	57.432240698436004	57.432240698440161
t = 6	57.432240698441866	57.432240698434526	57.432240698440765
t = 8	57.432240698442264	57.432240698433425	57.432240698441248
t = 10	57.432240698443110	57.432240698432238	57.432240698442030

Table 9.2 shows that both the CNFS and ReFS methods have the energy conservation, which verifies our analysis in Lemmas 9.2.4 and 9.2.6. In addition, the SSFS preserves the energy well in solving the plane wave solution, although it is not analytically proved.

As discussed in Lemma 9.2.2, the SSFS method preserves the dispersion relation of the plane wave solutions, if the numerical errors are insignificant. In contrast, the CNFS and ReFS methods have a good approximation to the dispersion relation only when $\omega\tau \ll 1$ and the numerical errors are neglectable. To illustrate this difference, we present in Figure

9.6 the time evolution of $\mathrm{Re}(u(0,t))$ and $\mathrm{Im}(u(0,t))$ computed from the SSFS and CNFS methods, for $\alpha = 1$ or 2. Note that the results from the ReFS and CNFS methods are almost

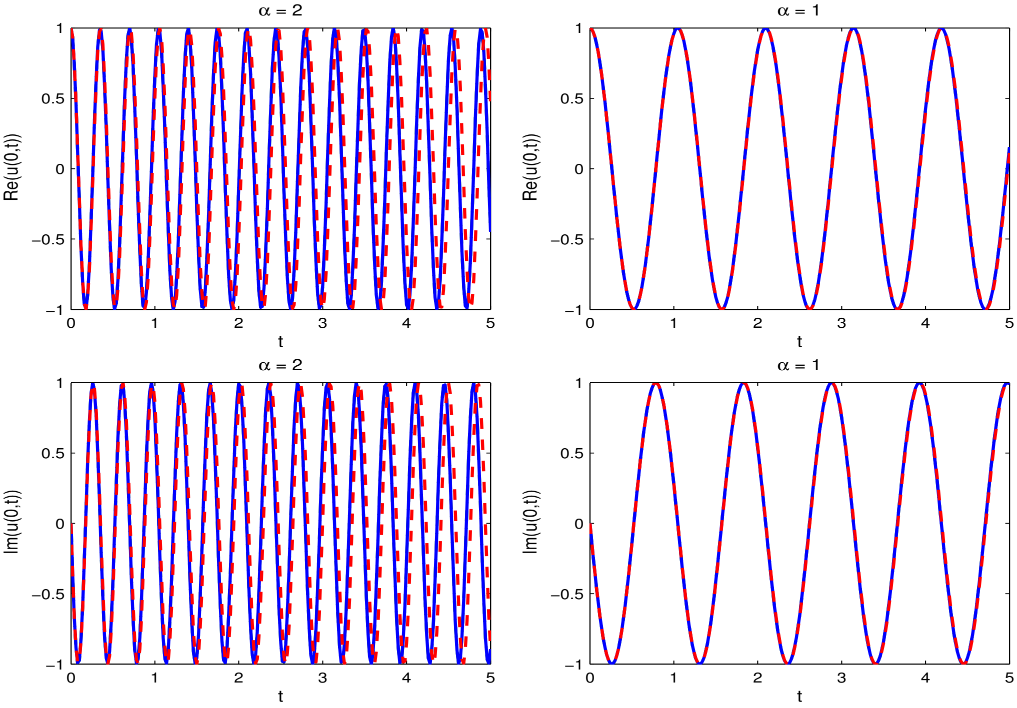

Figure 9.6. Time evolution of $\mathrm{Re}(u(0,t))$ and $\mathrm{Im}(u(0,t))$ from the exact solution (9.52) (dashed dot line), the SSFS method (solid line) and the CNFS method (dashed line). Note that the graphs of the exact solution and the numerical solution from the SSFS method are identical.

the same; thus for a better illustration, we omit the results of the ReFS method from Figure 9.6. In fact, the exact solution of $\mathrm{Re}(u(0,t))$ and $\mathrm{Im}(u(0,t))$ can be obtained by substituting $x = 0$ in (9.51):

$$\mathrm{Re}(u_{\text{exact}}(0,t)) = \cos(\omega t), \qquad \mathrm{Im}(u_{\text{exact}}(0,t)) = -\sin(\omega t), \tag{9.52}$$

i.e., they are periodic functions with period $2\pi/\omega$. Figure 9.6 shows that the graphs of the exact solution and the numerical solution from the SSFS method are the same, independent of the power α, which implies that the SSFS method preserves the exact time frequency of the plane wave solution. However, the solution from the CNFS method is more accurate when the power α is small or the time t is short. For example, when $\alpha = 2$, the numerical solution from the CNFS method has almost the same time frequency as the exact solution in a short time, but their difference becomes significant over time. While $\alpha = 1$, the results from the CNFS method are consistent with the exact solution for a longer time. To understand this, we find that when $\alpha = 2$, the frequency $\omega = 18$, and $\omega = 6$ if $\alpha = 1$. For the same time step τ, the value of $\omega\tau$ is smaller when $\alpha = 1$, and thus the CNFS method has a better approximation to the dispersion relation (reflected by the time frequency) in this case.

In addition, we present the numerical errors in $\text{Re}(u(0,t))$ and $\text{Im}(u(0,t))$ of the SSFS an CNFS methods in Figure 9.7. It shows that for both the SSFS and CNFS methods, the smaller the fractional power α, the smaller the numerical errors, but the numerical errors increase over time. For the same power α, the numerical errors from the CNFS method are much larger than those from the SSFS method, which is mainly because the CNFS method

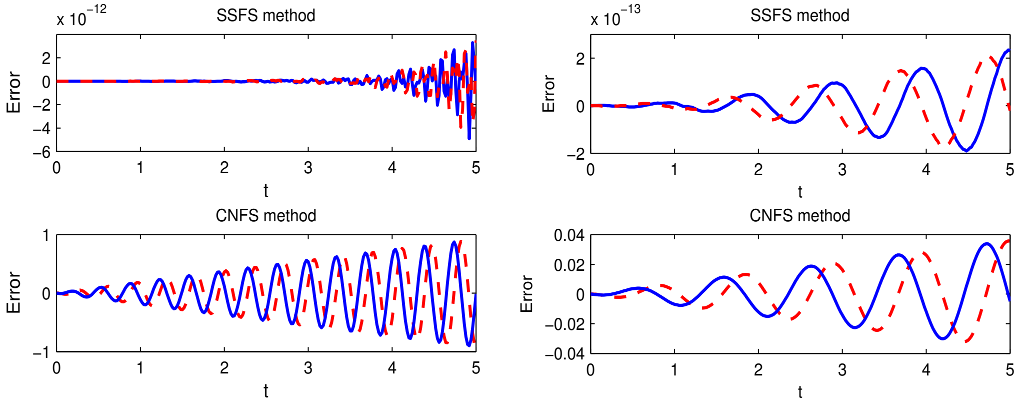

Figure 9.7. Numerical errors in $\text{Re}(u(0,t))$ (solid line) and $\text{Im}(u(0,t))$ (dashed line) of the SSFS and CNFS methods, where $\alpha = 2$ (left) or $\alpha = 1$ (right).

does not satisfy the analytical dispersion relation. Our extensive simulations show that the numerical errors of the CNFS and ReFS methods can be significantly reduced by decreasing the time step τ.

Example 2 We further compare the performance of the SSFS, CNFS and ReFS methods in simulating the plane wave solutions. Here, we consider the fractional NLS (9.1) on a finite domain $[-5\pi, 5\pi]$ with $\alpha = 1.1$ and $\gamma = -1$. The initial condition is chosen as the plane wave solution with a small perturbation [33], i.e.,

$$u(x,0) = \frac{1}{4}[1 + \delta_0 \cos(x/5)], \qquad -5\pi \le x \le 5\pi, \tag{9.53}$$

with $|\delta_0| \ll 1$. In our simulations, we choose $\delta_0 = 10^{-5}$. The mesh size is chosen as $h = 5\pi/512$. It shows that the SSFS method might introduce numerical instability in simulating the plane wave solution of the NLS, and one sufficient condition to ensure its stability is that the mesh size and time step satisfies $\tau < h^\alpha/\pi^{\alpha-1}$ for $\alpha \in (0, 2]$; see [33] for more discussions. In contrast, the CNFS and ReFS methods allow much larger time step τ in the simulations.

To illustrate this, we choose the time step $\tau = 0.00909$, larger than the threshold of the SSFS method, and simulate the plane wave dynamics by the SSFS, CNFS and ReFS methods. Figure 9.8 presents the time evolution of the density $|u(x,t)|$ computed from the SSFS (left), CNFS (middle) and ReFS (right) methods. It shows that many humps appear in the solution of the SSFS method because of its numerical instability. However, due to the mass conservation of the SSFS method, this instability does not grow unboundedly, and the plane wave solution recurs periodically. In contrast, the plane wave solution from the CNFS and ReFS methods remain stable (see Figure 9.8 middle and right panels).

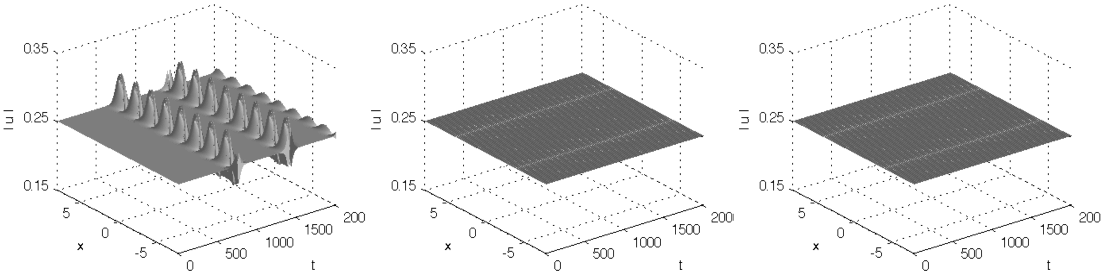

Figure 9.8. Illustration of the instability of SSFS. Time evolution of $|u|$ of (9.1) with the initial condition (9.53) computed by the SSFS (left), CNSF (middle), and ReFS (right) methods, where $\alpha = 1.1$ and $\gamma = -1$ in the 1D fractional NLS (9.1) and $h = 5\pi/512$ and $\tau = 0.00909$. It shows that the SSFS method is numerically unstable.

In summary, the SSFS method is more accurate than the other two methods in simulating plane wave dynamics of the fractional NLS, since it preserves the dispersion relation. However, as an explicit numerical method, it is more unstable, and its numerical instability should be avoided in simulating of the plane wave dynamics.

9.3. NUMERICAL INSTABILITY OF SSFS

In numerical studies of plane wave dynamics, it is desirable for a numerical method to preserve the dispersion relation in (9.6). Among all the three methods, only SSFS method preserve the dispersion relation, and thus is more accurate in the simulation. However, since the SSFS is an explicit method, which is conditionally stable. Time step must be taken small enough to avoid the artificial instability from the SSFS method. In this section, we study the numerical instability of the SSFS method in solving the plane wave solution (9.5). At time $t = t_n$, we consider a perturbed plane wave solution:

$$u_j^n = \widetilde{u}_j^n(1 + \varepsilon_j^n), \qquad \text{with} \quad \widetilde{u}_j^n = ae^{i(\lambda_k x_j - \omega t_n)}, \tag{9.54}$$

where ε_j^n, with $|\varepsilon_j^n| \ll 1$, is a small periodic perturbation on $[-L/2, L/2]$ and can be expanded as:

$$\varepsilon_j^n := \sum_{l=-J/2}^{J/2-1} \widehat{\varepsilon}_l^n e^{i\mu_l x_j}, \qquad 0 \le j \le J-1,$$

where $\widehat{\varepsilon}_l^n$ is the Fourier coefficient of ε_j^n, defined by

$$\widehat{\varepsilon}_l^n := \frac{1}{J}\sum_{j=0}^{J-1} \varepsilon_j^n e^{-i\mu_l x_j}, \qquad -J/2 \le l \le J/2-1.$$

Since ε_j^n is periodic, there is

$$\widehat{\varepsilon}_{l+kJ}^n = \frac{1}{J}\sum_{j=0}^{J-1} \varepsilon_j^n e^{-i\mu_{l+kJ} x_j} = \frac{1}{J}\sum_{j=0}^{J-1} \varepsilon_j^n e^{-i\mu_l x_j} e^{-i\mu_{kJ} x_j} = \widehat{\varepsilon}_l^n, \quad \text{for} \quad k \in \mathbb{Z}, \tag{9.55}$$

where in the last equality, we use the fact that $e^{-i\mu_{kJ}x_j} = 1$ since $\mu_{kJ} x_j = 2\pi jk$ is an integer multiple of 2π. In the following numerical instability analysis, the parameter l is always defined on $[-J/2, J/2-1]$ and the subscript of $\widehat{\varepsilon}_l^n$ is also restricted on $[-J/2, J/2-1]$. For those $\widetilde{l} \in \mathbb{Z}\backslash[-J/2, J/2-1]$, by the periodicity of $\widehat{\varepsilon}_{\widetilde{l}}^n$ as shown in (9.55), we can always find an integer k, such that

$$\widehat{\varepsilon}_{\widetilde{l}}^n = \widehat{\varepsilon}_{\widetilde{l}+kJ}^n, \quad \text{where} \quad \widetilde{l} + kJ \in [-J/2, J/2-1].$$

On one hand, setting $n = n+1$ in (9.54) and taking the discrete Fourier transform of $U^{n+1} := (u_0^{n+1}, u_1^{n+1}, \ldots, u_{J-1}^{n+1})$ yields

$$\widehat{u}_l^{n+1} = a\, e^{-i\,\omega t_{n+1}} \begin{cases} 1 + \widehat{\varepsilon}_0^{n+1}, & l = k, \\ \widehat{\varepsilon}_{l-k}^{n+1}, & l \ne k, \end{cases} \qquad -\frac{J}{2} \le l \le \frac{J}{2} - 1. \tag{9.56}$$

Here we notice that $l - k \in [-J/2 - k, J/2 - 1 - k]$, and thus there are some values of $l - k$ outside of the range $[-J/2, J/2 - 1$. For those $l - k \in [-J/2 - k, -J/2 - 1]$, i.e. $l \in [-J/2, -J/2 - 1 + k]$, by periodicity (9.55), we have $\widehat{\varepsilon}^{n+1}_{l-k} = \widehat{\varepsilon}^{n+1}_{l-k+J}$.

Thus, we rewrite (9.56) by

$$\widehat{u}^{n+1}_l = a\, e^{-i\,\omega t_{n+1}} \begin{cases} 1 + \widehat{\varepsilon}^{n+1}_0, & l = k, \\ \widehat{\varepsilon}^{n+1}_{l-k+J}, & l \in [-\frac{J}{2}, -\frac{J}{2} + k - 1], \\ \widehat{\varepsilon}^{n+1}_{l-k}, & l \in [-\frac{J}{2} + k, \frac{J}{2} - 1] \backslash \{k\}, \end{cases} \tag{9.57}$$

On the other hand, we can obtain u^{n+1}_l from the SSFS scheme in (9.27)–(9.29). To this end, we substitute u^n_j in (9.54) into (9.25) and take the leading order terms of ε^n_j to obtain

$$u^{n+1,-}_j = \widetilde{u}^n_j e^{-i\gamma|a|^2\tau}(1 + \varepsilon^n_j - i\gamma|a|^2\tau(\varepsilon^n_j + (\varepsilon^n_j)^*)) \qquad 0 \le j \le J - 1$$

with $\widetilde{u}^n_j$ defined in (9.54). Then, taking the discrete Fourier transform of $U^{n+1,-}$ yields

$$\widehat{u}^{n+1,-}_l = a\, e^{-i(\omega t_n + \gamma|a|^2\tau)} \begin{cases} 1 + \widehat{\varepsilon}^n_0 - i\gamma|a|^2\tau(\widehat{\varepsilon}^n_0 + (\widehat{\varepsilon}^n_0)^*), & l = k, \\ \widehat{\varepsilon}^n_{l-k} - i\gamma|a|^2\tau(\widehat{\varepsilon}^n_{l-k} + (\widehat{\varepsilon}^n_{k-l})^*), & l \neq k. \end{cases} \tag{9.58}$$

It arises a same issue as in (9.56) that there are some subscripts of $\widehat{\varepsilon}^n_l$ fall out side of $[-J/2, J/2 - 1]$. For this reason, we rewrite (9.58) by

$$\widehat{u}^{n+1,-}_l = a\, e^{-i(\omega t_n + \gamma|a|^2\tau)} \\ \cdot \begin{cases} 1 + \widehat{\varepsilon}^n_0 - i\gamma|a|^2\tau(\widehat{\varepsilon}^n_0 + (\widehat{\varepsilon}^n_0)^*), & l = k, \\ \widehat{\varepsilon}^n_{l-k+J} - i\gamma|a|^2\tau(\widehat{\varepsilon}^n_{l-k+J} + (\widehat{\varepsilon}^n_{k-l-J})^*), & l \in [-\frac{J}{2}, -\frac{J}{2} + k - 1], \\ \widehat{\varepsilon}^n_{l-k} - i\gamma|a|^2\tau(\widehat{\varepsilon}^n_{l-k} + (\widehat{\varepsilon}^n_{k-l-J})^*), & l = -\frac{J}{2} + k, \\ \widehat{\varepsilon}^n_{l-k} - i\gamma|a|^2\tau(\widehat{\varepsilon}^n_{l-k} + (\widehat{\varepsilon}^n_{k-l})^*), & l \in [-\frac{J}{2} + k + 1, \frac{J}{2} - 1] \backslash \{k\}. \end{cases} \tag{9.59}$$

Substituting (9.59) into (9.26) and then take the discrete Fourier transform, we get

$$\begin{aligned}\widehat{u}_l^{n+1} &= a\, e^{-i(\omega t_n+\gamma|a|^2\tau+|\mu_l|^\alpha\tau)} \\ &\cdot \begin{cases} 1+\widehat{\varepsilon}_0^n - i\gamma|a|^2\tau(\widehat{\varepsilon}_0^n+(\widehat{\varepsilon}_0^n)^*), & l=k, \\ \widehat{\varepsilon}_{l-k+J}^n - i\gamma|a|^2\tau(\widehat{\varepsilon}_{l-k+J}^n+(\widehat{\varepsilon}_{k-l-J}^n)^*), & l\in[-\frac{J}{2},-\frac{J}{2}+k-1], \\ \widehat{\varepsilon}_{l-k}^n - i\gamma|a|^2\tau(\widehat{\varepsilon}_{l-k}^n+(\widehat{\varepsilon}_{k-l-J}^n)^*), & l=-\frac{J}{2}+k, \\ \widehat{\varepsilon}_{l-k}^n - i\gamma|a|^2\tau(\widehat{\varepsilon}_{l-k}^n+(\widehat{\varepsilon}_{k-l}^n)^*), & l\in[-\frac{J}{2}+k+1,\frac{J}{2}-1]\backslash\{k\}. \end{cases}\end{aligned} \tag{9.60}$$

Comparing (9.60) with (9.57) and their complex conjugates, we obtain the following equations for $-\frac{J}{2}+1 \le l \le \frac{J}{2}-1$ and $l \neq 0$,

$$\begin{pmatrix} \widehat{\varepsilon}_l^{n+1} \\ (\widehat{\varepsilon}_{-l}^{n+1})^* \end{pmatrix} = A_l \begin{pmatrix} \widehat{\varepsilon}_l^{n} \\ (\widehat{\varepsilon}_{-l}^{n})^* \end{pmatrix},$$

where for $-\frac{J}{2}+1 \le l \le -\frac{J}{2}+k$,

$$A_l = \begin{pmatrix} (1-i\gamma|a|^2\tau)e^{-i(|\mu_{k+l}|^\alpha-|\lambda_k|^\alpha)\tau} & -i\gamma|a|^2\tau e^{-i(|\mu_{k+l}|^\alpha-|\lambda_k|^\alpha)\tau} \\ i\gamma|a|^2\tau e^{i(|\mu_{k-l-J}|^\alpha-|\lambda_k|^\alpha)\tau} & (1+i\gamma|a|^2\tau)e^{i(|\mu_{k-l-J}|^\alpha-|\mu_k|^\alpha)\tau}, \end{pmatrix}.$$

for $-\frac{J}{2}+k+1 \le l \le \frac{J}{2}-k-1$ and $l \neq 0$,

$$A_l = \begin{pmatrix} (1-i\gamma|a|^2\tau)e^{-i(|\mu_{k+l}|^\alpha-|\lambda_k|^\alpha)\tau} & -i\gamma|a|^2\tau e^{-i(|\mu_{k+l}|^\alpha-|\lambda_k|^\alpha)\tau} \\ i\gamma|a|^2\tau e^{i(|\mu_{k-l}|^\alpha-|\lambda_k|^\alpha)\tau} & (1+i\gamma|a|^2\tau)e^{i(|\mu_{k-l}|^\alpha-|\mu_k|^\alpha)\tau}, \end{pmatrix}.$$

for $\frac{J}{2}-k \le l \le \frac{J}{2}-1$,

$$A_l = \begin{pmatrix} (1-i\gamma|a|^2\tau)e^{-i(|\mu_{k+l-J}|^\alpha-|\lambda_k|^\alpha)\tau} & -i\gamma|a|^2\tau e^{-i(|\mu_{k+l-J}|^\alpha-|\lambda_k|^\alpha)\tau} \\ i\gamma|a|^2\tau e^{i(|\mu_{k-l}|^\alpha-|\lambda_k|^\alpha)\tau} & (1+i\gamma|a|^2\tau)e^{i(|\mu_{k-l}|^\alpha-|\mu_k|^\alpha)\tau}. \end{pmatrix}.$$

While for $l = -\frac{J}{2}$, since $-l = \frac{J}{2} \notin [-\frac{J}{2}, \frac{J}{2} - 1]$, it has a different representation,

$$\begin{pmatrix} \widehat{\varepsilon}^{n+1}_{-J/2} \\ (\widehat{\varepsilon}^{n+1}_{-J/2})^* \end{pmatrix} = A_{-J/2} \begin{pmatrix} \widehat{\varepsilon}^{n}_{-J/2} \\ (\widehat{\varepsilon}^{n}_{-J/2})^* \end{pmatrix},$$

where

$$A_{-J/2} = \begin{pmatrix} (1 - i\gamma|a|^2\tau)e^{-i(|\mu_{k-J/2}|^\alpha - |\lambda_k|^\alpha)\tau} & -i\gamma|a|^2\tau e^{-i(|\mu_{k-J/2}|^\alpha - |\lambda_k|^\alpha)\tau} \\ i\gamma|a|^2\tau e^{i(|\mu_{k-J/2}|^\alpha - |\lambda_k|^\alpha)\tau} & (1 + i\gamma|a|^2\tau)e^{i(|\mu_{k-J/2}|^\alpha - |\mu_k|^\alpha)\tau}, \end{pmatrix}.$$

The eigenvalues of matrix A_l are computed as:

$$\Lambda_{l,\pm} = \left(\cos\theta_l - \gamma|a|^2\tau\sin\theta_l\right) \pm \sqrt{(\cos\theta_l - \gamma|a|^2\tau\sin\theta_l)^2 - 1} \tag{9.61}$$

with

$$\theta_l = \begin{cases} \dfrac{\tau}{2}(|\mu_{k-J/2}|^\alpha + |\mu_{k-J/2}|^\alpha - 2|\lambda_k|^\alpha), & \text{if} \quad l = -\frac{J}{2}, \\ \dfrac{\tau}{2}(|\mu_{k+l}|^\alpha + |\mu_{k-l-J}|^\alpha - 2|\lambda_k|^\alpha), & \text{if} \quad -\frac{J}{2} + 1 \le l \le -\frac{J}{2} + k, \\ \dfrac{\tau}{2}(|\mu_{k+l}|^\alpha + |\mu_{k-l}|^\alpha - 2|\lambda_k|^\alpha), & \text{if} \quad 0 < |l| \le \frac{J}{2} - k - 1, \\ \dfrac{\tau}{2}(|\mu_{k+l-J}|^\alpha + |\mu_{k-l}|^\alpha - 2|\lambda_k|^\alpha), & \text{if} \quad \frac{J}{2} - k \le l \le \frac{J}{2} - 1. \end{cases} \tag{9.62}$$

The modes $(\widehat{\varepsilon}^{n+1}_l, (\widehat{\varepsilon}^{n+1}_{-l})^*)^T$ exponentially grow if the eigenvalue $|\Lambda_{l,+}| > 1$ or $|\Lambda_{l,-}| > 1$. Thus, we obtain the instability condition in the following lemma:

Lemma 9.3.1 (Instability condition)**.** *The unstable modes of the split-step Fourier spectral (SSFS) method in solving the plane wave solutions are those satisfying the following condition:*

$$\left|\cos\theta_l - \gamma|a|^2\tau\sin\theta_l\right| > 1, \qquad -\frac{J}{2} \le l \le \frac{J}{2} - 1 \tag{9.63}$$

with θ_l defined in (9.62). This condition includes both the analytically unstable modes satisfying (9.10) and numerically unstable modes introduced by the SSFS method.

In fact, when time step τ is small, a Taylor expansion of $(\cos\theta_l - \gamma|a|^2\tau\sin\theta_l) > 1$ for $0 < |l| \leq \frac{J}{2} - k - 1$ yields

$$[|\mu_{k+l}|^\alpha + |\mu_{k-l}|^\alpha - 2|\lambda_k|^\alpha]\,[|\mu_{k+l}|^\alpha + |\mu_{k-l}|^\alpha - 2(|\lambda_k|^\alpha - 2\gamma|a|^2)] + O(\tau^2) < 0,$$

which corresponds to the analytical instability condition obtained in (9.10). Similarly, a Taylor expansion of $(\cos\theta_l - \gamma|a|^2\tau\sin\theta_l) < -1$ gives that

$$[|\mu_{k-l}|^\alpha + |\mu_{l+k}|^\alpha - 2|\lambda_k|^\alpha]\,[|\mu_{k-l}|^\alpha + |\mu_{l+k}|^\alpha - 2(|\lambda_k|^\alpha - 2\gamma|a|^2)] + O(\tau^2) < \frac{16}{\tau^2}.$$

These are the unstable modes numerically introduced by the SSFS method, and thus we want to avoid them in simulations.

Remark 9.3.1. *For the standard NLS with $\alpha = 2$, the instability condition in (9.63) reduces to*

$$|\cos\left(\mu_l^2\tau\right) - \gamma|a|^2\tau\sin\left(\mu_l^2\tau\right)| > 1, \qquad -\frac{J}{2} \leq l \leq \frac{J}{2} - 1,$$

which is consistent with the conclusion obtained in the literature [12, 86].

It shows that in the standard NLS, although the analytical instability of the plane wave solution is independent of the wave number λ_k, the numerical instability of the SSFS method depends on λ_k. Following the similar arguments in [86], we can obtain from (9.63) the sufficient conditions of the time step τ and mesh size h to avoid numerical instability of the SSFS method in solving the plane wave solution of NLS.

Remark 9.3.2. *In the focusing NLS with* $\gamma < 0$*, one sufficient condition to ensure the SSFS method stable in solving the plane wave solution (9.5) with* $\lambda_k = 0$ *is:*

$$\tau \leq \frac{h^\alpha}{\pi^{\alpha-1}}, \qquad \textit{for} \ \ \alpha \in (0, 2]. \tag{9.64}$$

It is easy to verify that when $\alpha = 2$*, (9.64) reduces to the sufficient condition obtained in the literature [86].*

The detailed derivation of Remark 9.3.2 can be found in Appendix A. Remark 9.3.2 shows that for the same mesh size, the larger the fractional power α, the smaller the threshold of the time step.

Remark 9.3.3. *In the defocusing NLS with* $\gamma > 0$*, one sufficient condition to ensure the SSFS method stable in solving the plane wave solution (9.5) with* $\lambda_k = 0$ *is:*

$$\tau \leq \frac{(2\phi + \pi)h^\alpha}{\pi^\alpha}, \qquad \textit{for} \ \ \alpha \in (0, 2], \tag{9.65}$$

where $\phi \in (-\pi/2, 0)$*, and it satisfies*

$$\cos\phi = \frac{1}{\sqrt{1 + \gamma^2|a|^4\tau^2}}, \qquad \sin\phi = \frac{-\gamma|a|^2\tau}{\sqrt{1 + \gamma^2|a|^4\tau^2}}.$$

The derivation of Remark 9.3.3 can be found in Appendix B. The sufficient condition in (9.65) is implicit. When the mesh size h and time step τ are small, a Taylor expansion of (9.65) leads to an explicit condition:

$$\tau \leq \frac{\pi h^\alpha}{\pi^\alpha + 2\gamma|a|^2h^\alpha} + O(h^\alpha\tau^3), \qquad \text{for} \ \ \alpha \in (0, 2]. \tag{9.66}$$

The sufficient conditions in Remarks 9.3.2 and 9.3.3 provide us some guide for choosing the time step and mesh size in simulating the plane wave solution of the NLS equation.

We remark that our analysis in this section can be generalized to the higher order split-step method. Our conclusions on numerical stability in Lemma 9.3 and Remarks 9.3.1–9.3.3 are also valid for high-order split-step Fourier spectral method. In particular, we numerically verify that the threshold in (9.64) and (9.66) is the same for the higher order split-step method, but the growth rate of numerical instability is different.

9.4. NUMERICAL STUDY ON PLANE WAVE DYNAMICS

We study the dynamics of the unstable plane wave solution by simulating the fractional NLS (9.1) with the first-order split-step Fourier spectral (SSFS) method. To understand the nonlocal effects of the fractional Laplacian, the plane wave dynamics in the fractional NLS are compared to those in the standard NLS. In this section, the time step τ is chosen to be small enough to avoid numerical instability of the SSFS method. The initial condition is chosen as a perturbed plane wave solution of the following form:

$$u(x,0) = a\, e^{i\lambda_k x}\Big(1 + \varepsilon_0 \cos\frac{2\pi x}{L}\Big), \qquad -\frac{L}{2} \le x \le \frac{L}{2}, \tag{9.67}$$

where a and ε_0 are constants, and $|\varepsilon_0| \ll 1$. Our simulations show that different perturbation in the initial condition may slightly affect the dynamics of the plane wave solution, but it does not affect our conclusions on comparing the fractional and standard NLS. In the following, we choose $\varepsilon_0 = 10^{-5}$ and $a = \frac{1}{2}$ in (9.67), and the domain size $L = 5\pi$.

9.4.1. Focusing NLS. We study the dynamics of the plane wave solution when $\gamma < 0$ in (9.1), and the frequency $\lambda_k = 0$ and $\lambda_k \neq 0$ are considered in Examples 9.4.1 and 9.4.2, respectively.

Example 9.4.1 We choose $\lambda_k = 0$ in the initial state (9.67) and the nonlinear coefficient $\gamma = -1$ in the NLS (9.1). The analysis in Remark 9.3.2 shows that for any $\alpha \in [0.76, 2]$, there exists one pair unstable modes at $l = \pm 1$, and thus the plane wave solutions are unstable in this case. Figure 9.9 presents the time evolution of $|u(x,t)|$ for

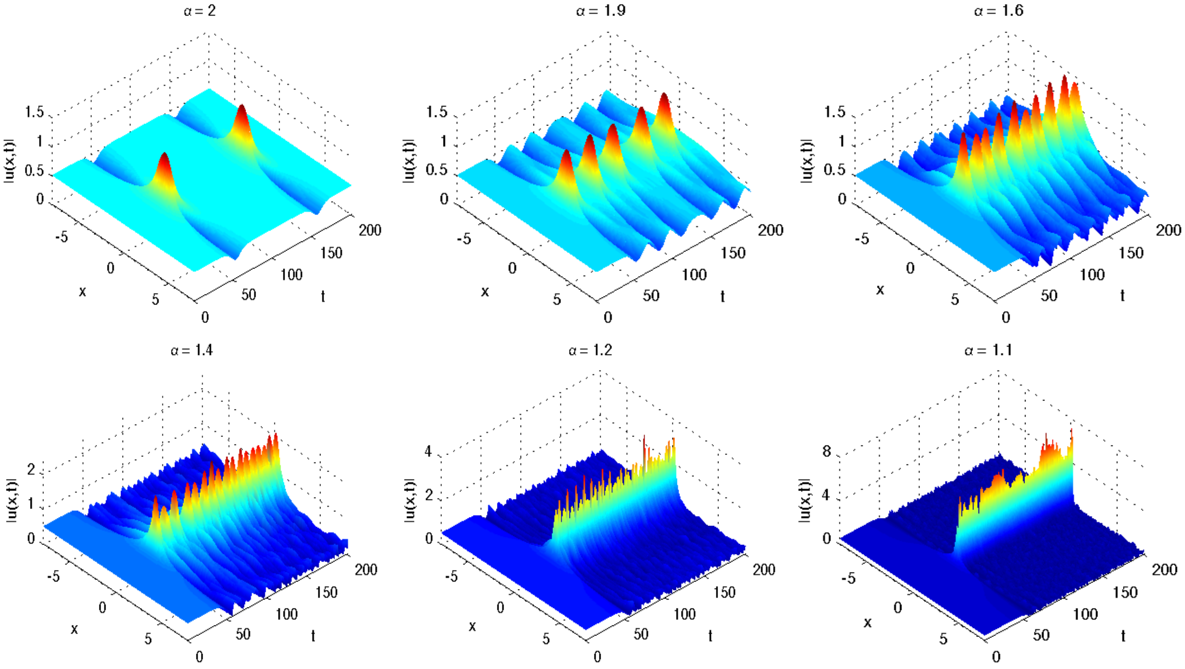

Figure 9.9. Dynamics of the unstable plane wave solution in the 1D focusing NLS with $\gamma = -1$ and $\lambda_k = 0$ in the initial state (9.67). The recurrence of plane wave solution is observed in the standard NLS and the fractional NLS with large fractional power α.

different α. It shows that the solution remains a plane wave for a short time, and then around $t = 50$ one hump appears due to the instability. In the standard NLS with $\alpha = 2$, the well-known recurrence of the plane wave solution is observed, whereby the solution is repeated periodically during the evolution (see Figure 9.9 top left).

In the fractional case $\alpha < 2$, the dynamics of plane wave solution crucially depends on the fractional power α, and its behaviors can be divided into two regimes: $1 < \alpha < 2$ and $0 < \alpha \leq 1$. When α is close to 2, the dynamics is similar to that in the standard NLS. One single hump periodically emerges during the dynamics, and the smaller the fractional power α, the shorter the period. The recurrence of the plane wave solution is observed when α close enough to 2 (e.g., $\alpha = 1.98$ from our extensive simulations). As α decreases, the dynamics loses its periodicity in time, and the recurrence of the plane wave solution ceases (see Figure 9.9 for $\alpha = 1.6$ or 1.3). Moreover, as α approaches 1 from above, the solution tends to collapse shortly after the hump appears (see Figure 9.9 for $\alpha = 1.1$). Figure 9.10

further shows the time evolution of the solution around the time when the peak emerges for the first time. When $\alpha = 1.9$, the peak reaches its maximum around $t = 52$ and then

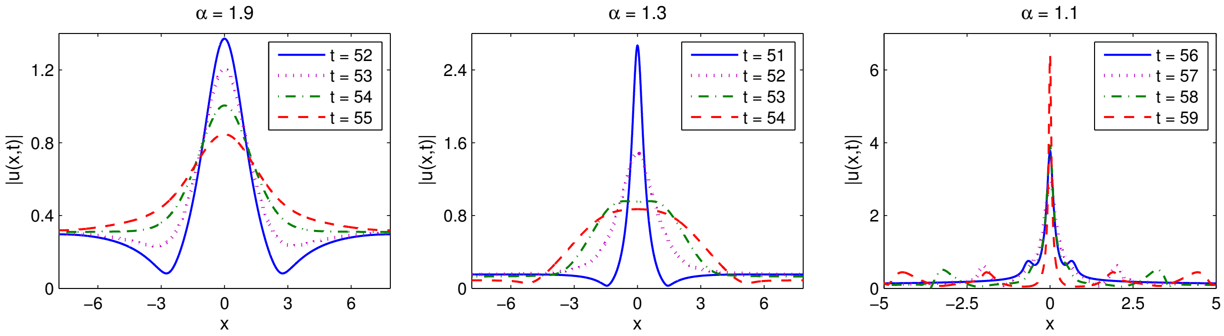

Figure 9.10. Time evolution of the wave function around the peak first appears with $\gamma = -1$ in the fractional NLS (9.1) and $\lambda_k = 0$ in the initial state (9.67).

it quickly dissolves. As α decreases, the hump becomes more concentrated around $x = 0$, which is also taller because of the normalization constraint (see Figure 9.10 middle). While α is close to 1, the solution tends to collapse along with decoherence, which is mainly caused by the nonlocal effects from the fractional Laplacian [54].

For $\alpha \leq 1$, our extensive simulations show that the plane wave solution collapse after the instability develops. The more analytically unstable modes exist in the computational domain, the earlier the collapse occurs.

Figure 9.11 displays the time evolution of the spectrum of the solution $u(x,t)$, with its density dynamics shown in Figure 9.9. Since the spectrum $|\mathcal{F}[u(x,t)]|$ is symmetric with respect to $\mu = 0$, we only present the results for $\mu > 0$ to get a better illustration. Also, our computational spectrum domain is much larger than that displayed in Figure 9.11. In the standard NLS with $\alpha = 2$, the spectrum expands as the unstable modes grow, and correspondingly a bump appears in the density $|u(x,t)|$ (see Figure 9.9 for $\alpha = 2$). This process is repeated periodically. In the fractional case with α close to 2, the dynamics of the spectrum is similar to that in the standard cases. The smaller the fractional power α,

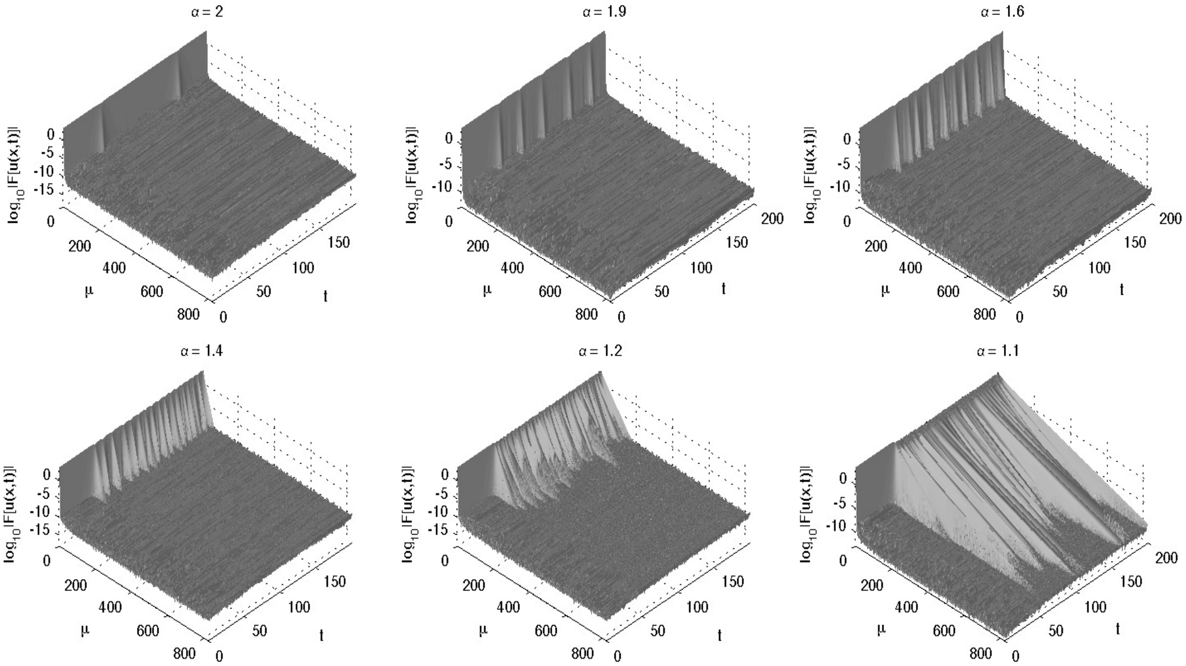

Figure 9.11. Time evolution of $\log_{10}|\mathcal{F}(u(x,t))|$ in the 1D focusing NLS with $\gamma = -1$ and $\lambda_k = 0$ in the initial condition (9.67). The spectrum broadens as the fractional power decreases.

the more frequently the spectrum expands. However, when α is close to 1, the spectrum expands quickly, after the analytical instability is triggered, to a large frequency domain (see Figure 9.11 for $\alpha = 1.1$).

The dynamics of the spectrum in Figure 9.11 clearly demonstrates the nonlocal effects of the fractional Laplacian. Due to the long-range interactions from the fractional Laplacian, the analytical instability at low-μ_l quickly “leaks" to the high wave number region. The smaller the fractional power, the stronger the long-range interactions, the stronger the “leakage" of the instability.

Example 9.4.2 We choose $\lambda_k = 4\pi/L$ in the initial state (9.67) and study the dynamics of unstable plane wave solution. The nonlinear coefficient of the NLS in (9.1) is taken as $\gamma = -1$. Compared to Example 8.3.1, the perturbed plane wave in this case would move with the group velocity:

$$v_g = \frac{\partial \omega}{\partial \lambda_k} = \alpha \frac{|\lambda_k|^\alpha}{\lambda_k}, \qquad \lambda_k \neq 0, \tag{9.68}$$

where ω is the dispersion relation in (9.6).

Figure 9.12 shows the time evolution of $|u(x,t)|$ for different α. In the standard

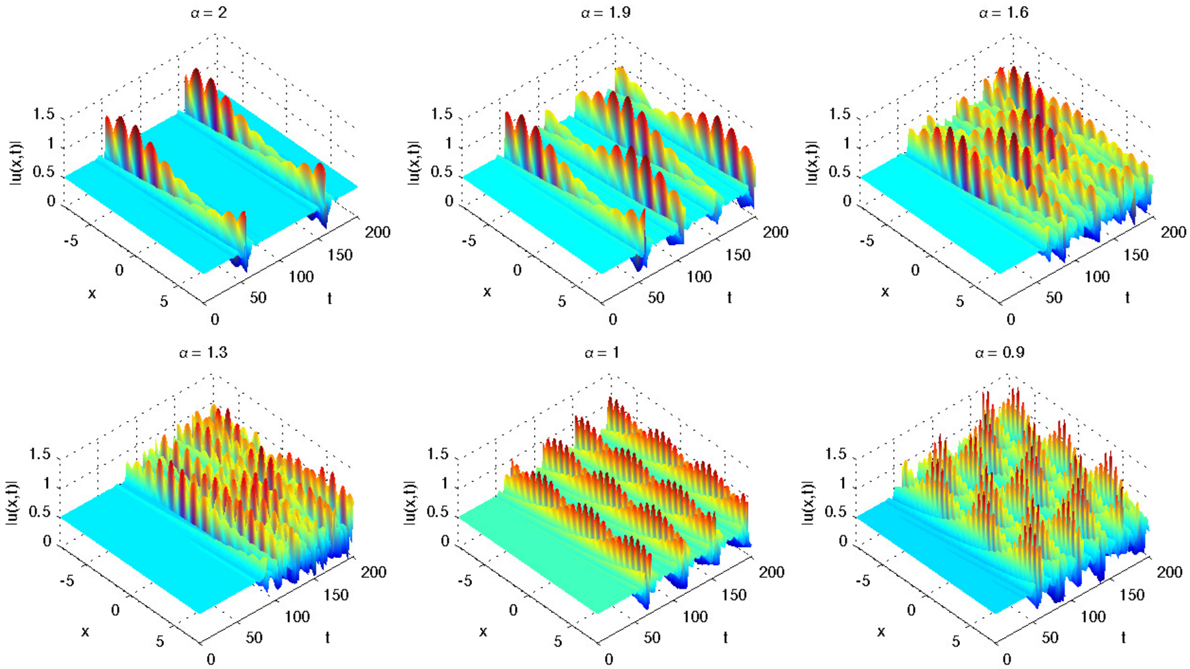

Figure 9.12. Dynamics of the unstable plane wave solution in the 1D focusing NLS with $\gamma = -1$ and $\lambda_k = 4\pi/L$ in the initial state (9.67). The recurrence of the plane wave solution is observed in both standard and fractional NLS.

NLS with $\alpha = 2$, the recurrence of plane wave solution is observed. When the instability develops, one hump appears in the density plot, and it moves along the x-axis. The dynamics when $\alpha = 1.9$ is similar, but the recurrence of the hump becomes more frequent. When $\alpha = 1.6$ or 1.3, there are two unstable pairs at $l = \pm 1$ and ± 2, and thus there may be one or two humps appearing during the dynamics, depending on whether the first or second mode becomes dominant. For $\alpha = 1$ or 0.9, there is only one unstable pair at $l = \pm 3$, and correspondingly three humps in the density.

Note that in contrast to the results in Example 9.4.1, no wave collapse is observed when $\alpha \leq 1$. Figure 9.13 shows the dynamics of the solution around the time when the peak first appears, for $\alpha = 1.9, 1.3$ and 1. It shows that the velocity decreases as the fractional power α increases, consistent with our prediction from (9.68).

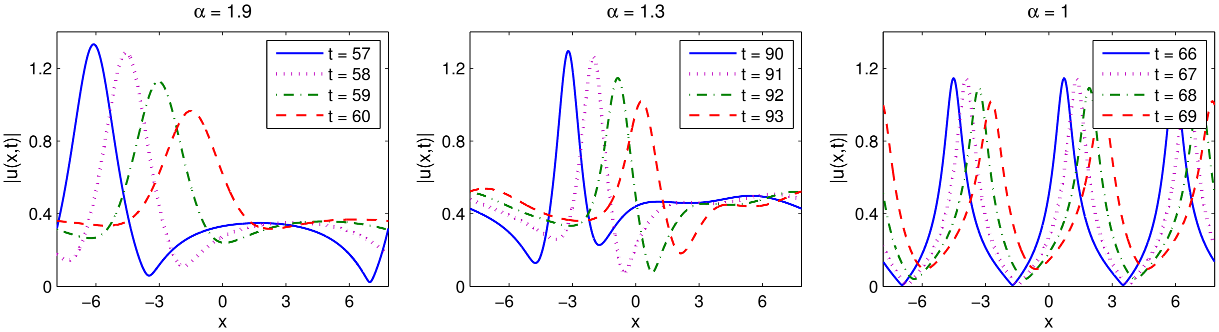

Figure 9.13. Time evolution of the wave function around the time when the peak first appears with $\gamma = -1$ in the fractional NLS (9.1) and $\lambda_k = 4\pi/L$ on the initial state (9.67).

Figure 9.14 shows the time evolution of the spectrum corresponding to the density dynamics in Figure 9.12. Compared to the case with $\lambda_k = 0$, the "leakage" of instability to high-μ_l is greatly reduced when $\lambda_k \neq 0$. In particular, the spectrum is contained in a narrow band when $\alpha = 1$, which is significantly different from the dynamics when $\lambda_k = 0$. For $\alpha < 1$, the spectrum broadens still quickly after the instability develops, but still remains much narrower than in the $\lambda_k = 0$ cases.

9.4.2. Defocusing NLS. In the defocusing cases with $\gamma > 0$, our numerical simulations shows that the plane wave solution is always stable if $\lambda_k = 0$ or $1 \leq \alpha \leq 2$, which is consistent with the analysis in Section 9.1. Therefore, in Example 9.4.3, we will only focus on the case with $\lambda_k \neq 0$ and $0 < \alpha < 1$.

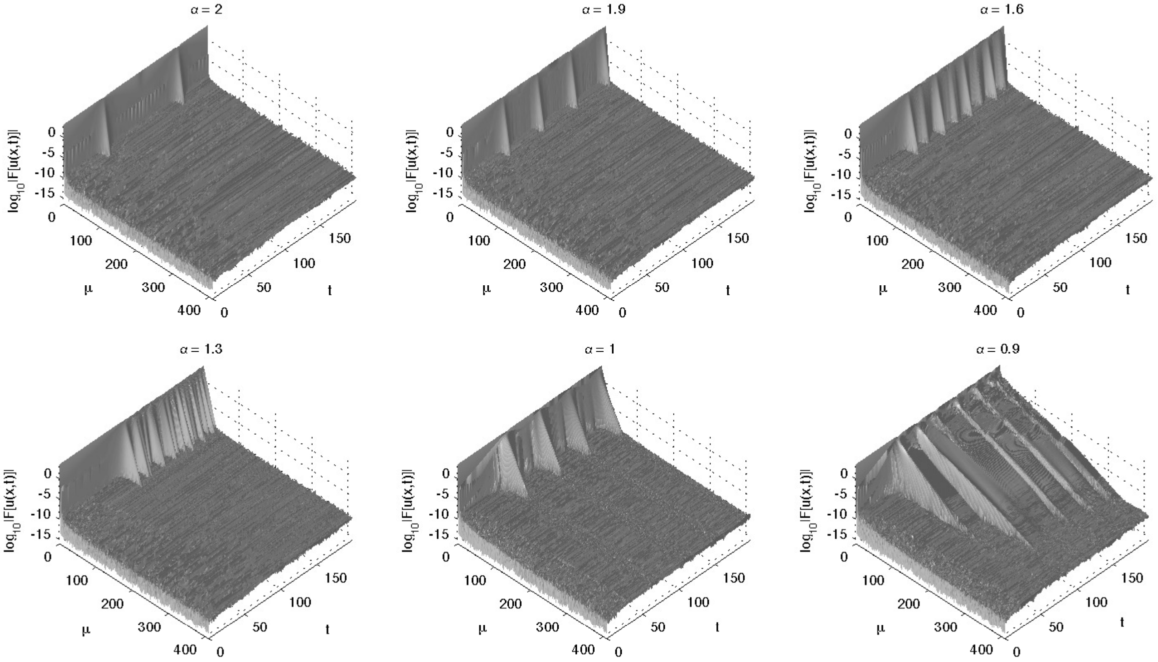

Figure 9.14. Time evolution of $\log_{10} |\mathcal{F}(u(x,t))|$ in the 1D focusing NLS with $\gamma = -1$ and $\lambda_k = 4\pi/L$ in the initial state (9.67).

Example 9.4.3 Let $\lambda_k = 4\pi/L$ in the initial state (9.67) and $\gamma = 1$. Figure 9.15 presents the time evolution of the wave function and its spectrum for $\alpha = 0.9$ and 0.7. For both these values of α, there exist two unstable pairs: at $l = \pm 1$ and ± 2, and thus the plane wave solution is unstable. Since $\lambda_k \neq 0$, the wave moves along the x-axis from left to right (see Figure 9.15 middle). During the dynamics, the recurrence of the plane wave solution is not observed. Figure 9.15 (right) shows that the spectrum broadens after instability develops, and it is much wider for $\alpha = 0.9$ than for $\alpha = 0.7$. This phenomenon is different from that observed in the focusing cases where it appears that the smaller the fractional power α, the wider the spectrum (see Figure 9.14). Moreover, comparing the spectra in Figures 9.14 and 9.15 for $\alpha = 0.9$, one see that the spectrum in the focusing NLS is much wider than that in the defocusing case.

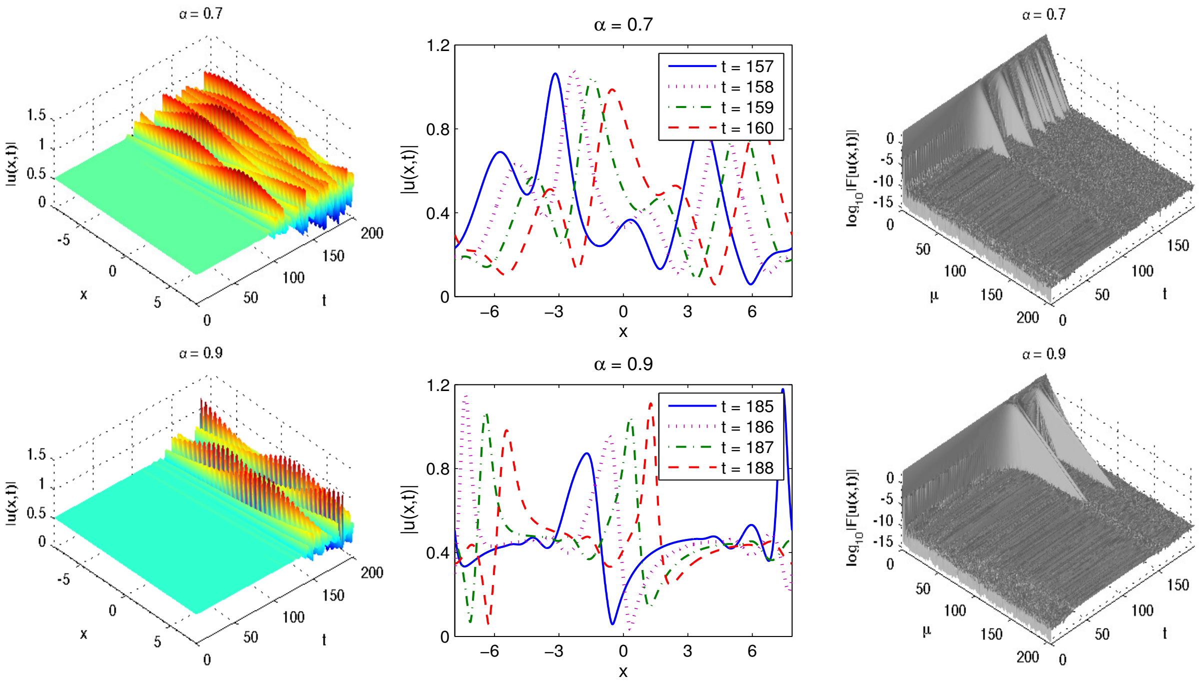

Figure 9.15. Dynamics of the unstable plane wave solution in the 1D defocusing NLS with $\gamma = 1$ and $\lambda_k = 4\pi/L$ in the initial condition (9.67).

In summary, Examples 9.4.1–9.4.3 and our extensive simulations show that the dynamics of a perturbed plane wave solution are significantly different in the standard and fractional NLS. As instability occurs, the dynamics in the fractional NLS tends to be more chaotic than that in the standard case, which makes the recurrence of the plane wave solution less likely. As α decreases from 2, the spectrum of the solution becomes wider. The instability analysis of the plane wave solution in Section 9.1 are consistent with our simulations performed in this section. However, the linear stability analysis fails to predict the broadening of the spectrum, but which is common in the dynamics with long-range interactions [55, 91]. We note that as $\alpha \to 1$, the spectrum of the solution becomes very broad (more so far the focusing case), which suggests that a wave collapse occurs at or close to $\alpha = 1$. Simulations in the regime $\alpha \approx 1$ are, therefore, very time-consuming. More numerical and analytical studies are demanded to understand the dynamics of fractional NLS.

10. CONCLUSION

The main purpose of this dissertation is to provide novel and accurate numerical methods for the fractional Laplacian with applications on solving the fractional Schrödinger equation. In this section, we summarize the main results in this dissertation.

We proposed two novel and accurate finite difference methods – the weighted trapezoidal method and the weighted linear interpolation method to discretize the fractional Laplacian. The novelty of our methods is the use of the weighted integral, which reveals the nonlocal natural of the fractional Laplacian. A splitting parameter γ is introduced so that the fractional Laplacian is rewritten as a weighted integral of function $\psi_\gamma(\mathbf{x}, \boldsymbol{\xi})$ with weight $|\boldsymbol{\xi}|^{\gamma-(d+\alpha)}$. Notably, the choice of the splitting parameter γ plays the most important role in the accuracy of our methods. The universal optimal choice for any d dimension ($d \geq 1$) is $\gamma = 2$, which provides the most accurate results compare to the other choices, i.e., $\gamma \neq 2$, in both methods. Additionally, there is one more optimal choice of the splitting parameter in one dimension for each method. For the weighted trapezoidal method, taking $\gamma = 1 + \alpha/2$ provides the same accuracy as $\gamma = 2$; for the weighted linear interpolation method, besides $\gamma = 2$, the parameter $\gamma = 1$ is another optimal choice that can provide the most accurate results. Moreover, the weighted trapezoidal method closely resembling the central difference scheme for the standard Laplacian $-\Delta$, which is indeed a fractional generalization of the central difference scheme with the 2nd order accuracy for smooth enough functions. In implementation, the computation of the matrix-vector product A**u** is achieved efficiently by using the fast Fourier transform (FFT).

In addition, we prove the accuracy of both numerical methods analytically. The analysis of the weighted trapezoidal method is not as standard as the weighted linear interpolation method. The most important technique that is used in the error analysis of the former method is the weighted Montgomery's identity. The standard Montgomery's identity plays important role in the context of the integral approximation. Recently, the Montgomery's identity is generalized to a weighted version for any order differentiable functions with two variables, however, in contrast to its standard counterpart, it has not yet been applied to the error analysis of the weighted integral approximations. The error analysis of the weighted trapezoidal method not only fills this gap but also suggests a broad application of the weighted Montgomery's identity to the field of the weighted integral approximations.

As the first application of the fractional Laplacian, we numerically solve the ground and the first excited states of the fractional Schrödinger equation in an infinite potential well by a normalized fractional gradient flow combine with the weighted trapezoidal method in space and the semi-implicit Euler method in time. Our numerical results suggest that the eigenfunctions of the fractional Schrödinger equation are different from those of the standard Schrödinger equations. The nonlocal interactions are stronger when the fractional power α is smaller, which leads to a larger scattering of particles in an infinite potential well. In addition, our solutions are consistent not only with the approximation results in [59, 96] but also with the best lower and upper bounds in [3, 17, 35].

As the second application of the fractional Laplacian, we investigate the stability and dynamics of the plane wave solutions of the fractional nonlinear Schrödinger equation from both analytical and numerical perspectives. We presented the linear stability analysis to study the stability of the plane wave solution. Our analysis shows that the stability of the plane wave solution in the fractional NLS is more complicated than its standard counterpart. To further understand the nonlinear stage of the plane wave dynamics, we proposed and compared three numerical methods, i.e., the split-step Fourier spectral (SSFS) method, the Crank–Nicolson Fourier spectral (CNFS), and the relaxation Fourier spectral (ReFS) method, for solving the fractional NLS. The SSFS is more accurate in simulating the plane wave dynamics since it preserves the dispersion relation of the plane wave solutions. We further applied the SSFS method to study the dynamics of the plane wave solution of the fractional NLS, where the time step is taken small enough to avoid the numerical instability from the SSFS method. Our numerical results suggest new phenomena that are different from the standard NLS, such as the well-known recurrence of the plane wave solution does not always occurs in the fractional cases, and the leakage of the low-frequency instability to high frequency is observed. The fractional power α reflects the nonlocality of the system, the smaller the fractional power, the stronger the long-range interactions, the stronger the leakage of instability. In addition, due to the expansion of the spectrum, numerical simulations for the fractional NLS, especially with focusing interactions, could be challenging. More numerical and analytical studies are demanded to understand the dynamics of fractional NLS.

APPENDIX A

DERIVATION OF REMARK 9.3.2

Let's define ϕ, such that

$$\cos(\phi) = \frac{1}{\sqrt{1+\gamma^2|a|^4\tau^2}}, \qquad \sin(\phi) = \frac{-\gamma|a|^2\tau}{\sqrt{1+\gamma^2|a|^4\tau^2}}.$$

Then, the instability condition in (9.63) is equivalent to

$$|\cos(\theta_l - \phi)| > \cos\phi,$$

i.e., there exists an integer p, such that

$$|\theta_l - \phi - p\pi| < |\phi|. \tag{A.1}$$

When $\gamma < 0$, we have $\sin\phi > 0$ and $\cos\phi > 0$. Without loss of generality, we choose $\phi \in (0, \frac{\pi}{2})$. Then, (A.1) can be written as:

$$p\pi < \theta_l < 2\phi + p\pi. \tag{A.2}$$

Now let's first consider the case with $\lambda_k = 0$, for which (9.62) gives that $\theta_l = \tau|\mu_l|^\alpha > 0$. Now we will focus on $p \in \mathbb{Z}^+ \cup \{0\}$ in (A.2) since if $p \leq -1$, $2\phi + p\pi < 0$ but $\theta_l > 0$.

If $p = 0$, (A.2) becomes

$$0 < \tau|\mu_l|^\alpha < 2\arctan(-\gamma|a|^2\tau), \tag{A.3}$$

as $\phi = \arctan(-\gamma|a|^2\tau)$. Furthermore, the Taylor expansion shows that

$$\arctan(-\gamma|a|^2\tau) = -\gamma|a|^2\tau + O(\tau^3), \qquad \text{if} \quad |\gamma||a|^2\tau \ll 1.$$

Substituting it into (A.3) leads to

$$0 < |\mu_l|^\alpha < -2\gamma|a|^2 + O(\tau^2),$$

which corresponds to the analytical instability condition in (9.17).

Note that our goal is to avoid the numerical instability, i.e., finding the condition for mesh size h and time step τ such that (A.2) is not satisfied.

Now we will focus on $p \in \mathbb{Z}^+$ in (A.2). To avoid the numerical instability, we can let $\max_l \theta_l \leq \pi$, i.e.,

$$\tau \max_{-J/2 \leq l \leq J/2-1} |\mu_l|^\alpha \leq \pi. \tag{A.4}$$

From the definition of μ_l and mesh size h, we obtain $\max_l |\mu_l|^\alpha = (J\pi/L)^\alpha = (\pi/h)^\alpha$. Substituting it into (A.4) yields the sufficient condition (9.64) in Remark 9.3.1 for avoiding the numerical instability of the SSFS method.

APPENDIX B

DERIVATION OF REMARK 9.3.3

When $\gamma > 0$, we choose $\phi \in (-\frac{\pi}{2}, 0)$ without loss of generality, and then (A.1) becomes

$$2\phi + p\pi < \theta_l < p\pi. \tag{B.1}$$

Now we first consider the case with $\lambda_k = 0$. If $p \leq 0$, (B.1) leads to $\theta_l < 0$, which is a conflict with $\theta_l = \tau|\mu_l|^\alpha > 0$. Hence, we focus on (B.1) with $p \in \mathbb{Z}^+$. To avoid numerical instability, we let $\max_l \theta_l < 2\phi + \pi$, i.e.,

$$\tau \max_{-J/2 \leq l \leq J/2-1} |\mu_l|^\alpha < 2\phi + \pi, \tag{B.2}$$

since $-\pi/2 < \phi < 0$. Substituting $\max_l |\mu_l|^\alpha = (J\pi/L)^\alpha = (\pi/h)^\alpha$ into (B.2) gives the sufficient condition (9.65) in Remark 9.3.3.

REFERENCES

[1] N. Abatangelo and L. Dupaigne. Nonhomogeneous boundary conditions for the spectral fractional Laplacian. *Ann I H Poincare C*, 34(2):439–467, 2017.

[2] G. Acosta and J. P. Borthagaray. A fractional Laplace equation: regularity of solutions and finite element approximations. *SIAM J. Numer. Anal.*, 55:472–495, 2017.

[3] R. Bañuelos and T. Kulczycki. The Cauchy process and the Steklov problem. *J. Funct. Anal.*, 211:355–423, 2004.

[4] R. Bañuelos, T. Kulczycki, and P. J. Méndez-Hernández. On the shape of the ground state eigenfunction for stable processes. *Potential Anal.*, 24:205–221, 2006.

[5] W. Bao and Y. Cai. Mathematical theory and numerical methods for Bose–Einstein condensation. *Kinet. Relat. Mod.*, 6:1–135, 2013.

[6] W. Bao and Q. Du. Computing the ground state solution of Bose–Einstein condensates by a normalized gradient flow. *SIAM J. Sci. Comput.*, 25:1674–1697, 2004.

[7] W. Bao, F. Y. Lim, and Y. Zhang. Energy and chemical potential asymptotics for the ground state of Bose–Einstein condensates in the semiclassical regime. *Bull. Inst. Math. Acad. Sin. (N.S.)*, 2:495–532, 2007.

[8] S. S. Bayin. On the consistency of the solutions of the space fractional Schrödinger equation. *J. Math. Phys.*, 53:042105, 9, 2012.

[9] C. Besse. A relaxation scheme for the nonlinear Schrödinger equation. *SIAM J. Numer. Anal.*, 42:934–952, 2004.

[10] K. Bogdan, K. Burdzy, and Z.-Q. Chen. Censored stable processes. *Probab. Theory Related Fields*, 127:89–152, 2003.

[11] L. A. Cafferelli and F. Lin. An optimal partition problem for eigenvalues. *J. Sci. Comput.*, 31:5–18, 2007.

[12] B. Cano and A. González-Pachón. Plane waves numerical stability of some explicit exponential methods for cubic Schrödinger equation. *J. Comput. Math.*, 34:385–406, 2016.

[13] B. A. Carreras, V. E. Lynch, and G. M. Zaslavsky. Anomalous diffusion and exit time distribution of particle tracers in plasma turbulence model. *Phys. Plasmas*, 8:5096–5103, 2001.

[14] P. Cerone, S. S. Dragomir, and J. Roumeliotis. Some Ostrowski type inequalities for n-time differentiable mappings and applications. *Demonstratio Math.*, 32:697–712, 1999.

[15] S. Chandrasekaran, M. Gu, X. Sun, J. Xia, and J. Zhu. A superfast algorithm for Toeplitz systems of linear equations. *SIAM J. Matrix Anal. A.*, 29:1247–1266, 2007.

[16] X. Chang. Ground state solutions of asymptotically linear fractional Schrödinger equations. *J. Math. Phys.*, 54:061504, 2013.

[17] Z. Chen and R. Song. Two-sided eigenvalue estimates for subordinate processes in domains. *J. Funct. Anal.*, 226:90–113, 2005.

[18] Z.-Q. Chen, P. Kim, and R. Song. Heat kernel estimates for the Dirichlet fractional Laplacian. *J. Eur. Math. Soc.*, 12:1307–1329, 2010.

[19] M. L. Chiofalo, S. Succi, and M. P. Tosi. Ground state of trapped interacting Bose–Einstein condensates by an explicit imaginary-time algorithm. *Phys. Rev. E.*, 62:7438–7444, 2000.

[20] R. Cont and E. Voltchkova. A finite difference scheme for option pricing in jump diffusion and exponential Lévy models. *SIAM J. Numer. Anal.*, 43:1596–1626, 2005.

[21] N. Cusimano, A. Bueno-Orovio, I. Turner, and K. Burrage. On the order of the fractional Laplacian in determining the spatio-temporal evolution of a space-fractional model of cardiac electrophysiology. *PLOS ONE*, 10:1–16, 2015.

[22] M. Dahlby and B. Owren. Plane wave stability of some conservative schemes for the cubic Schrödinger equation. *M2AN Math. Model. Numer. Anal.*, 43:677–687, 2009.

[23] G. Dahlquist and Å. Björck. *Numerical methods in scientific computing. Vol. I.* Society for Industrial and Applied Mathematics (SIAM), Philadelphia, PA, 2008.

[24] P. J. Davis. *Circulant matrices*. John Wiley & Sons, New York-Chichester-Brisbane, 1979.

[25] M. D'Elia and M. Gunzburger. The fractional Laplacian operator on bounded domains as a special case of the nonlocal diffusion operator. *Comput. Math. Appl.*, 66:1245–1260, 2013.

[26] E. Di Nezza, G. Palatucci, and E. Valdinoci. Hitchhiker's guide to the fractional Sobolev spaces. *Bull. Sci. Math.*, 136:521–573, 2012.

[27] J. Dong. Lévy path integral approach to the solution of the fractional Schrödinger equation with infinite square well. *arXiv: 1301.3009v1*, preprint, 2013.

[28] Q. Du, M. Gunzburger, R. B. Lehoucq, and K. Zhou. Analysis and approximation of nonlocal diffusion problems with volume constraints. 54:667–696, 2012.

[29] Q. Du and F. Lin. Numerical approximations of a norm-perserving gradient flow and applications to an optimal partition problem, nonlinearity. 22:67–83, 2009.

[30] S. Duo, L. Ju, and Y. Zhang. A fast algorithm for solving the space-time fractional diffusion equation. *Comput. Math. Appl.*, to appear, 2017.

[31] S. Duo, H.-W. van Wyk, and Y. Zhang. A novel and accurate weighted trapezoidal finite difference method for the fractional laplacian. preprint, 2017.

[32] S. Duo, H. Wang, and Y. Zhang. A comparative study on nonlocal diffusion operators related to the fractional Laplacian. preprint, 2017.

[33] S. Duo and Y. Zhang. Computing the ground and first excited states of the fractional Schrödinger equation in an infinite potential well. *Commun. Comput. Phys.*, 18:321–350, 2015.

[34] S. Duo and Y. Zhang. Mass-conservative fourier spectral methods for solving the fractional nonlinear schrödinger equation. *Comput. Math. Appl.*, 71:2257–2271, 2016.

[35] B. Dyda. Fractional calculus for power functions and eigenvalues of the fractional Laplacian. *Fract. Calc. Appl. Anal.*, 15:536–555, 2012.

[36] A. Erdélyi, W. Magnus, F. Oberhettinger, and F. G. Tricomi. *Higher transcendental functions. Vol. I.* Robert E. Krieger Publishing Co., Inc., Melbourne, Fla., 1981.

[37] E. Faou, L. Gauckler, and C. Lubich. Plane wave stability of the split-step Fourier method for the nonlinear Schrödinger equation. *Forum Math. Sigma*, 2:e5, 45, 2014.

[38] B. Feng. Ground states for the fractional Schrödinger equation. *Electron J. Differ. Eq.*, pages 1–11, 2013.

[39] R. L. Frank. Eigenvalue bounds for the fractional Laplacian: A review. *arXiv:1603.09736*, 2016.

[40] T. Gao, J. Duan, X. Li, and R. Song. Mean exit time and escape probability for dynamical systems driven by Lévy noises. *SIAM J. Sci. Comput.*, 36:A887–A906, 2014.

[41] I. S. Gradshteyn and I. M. Ryzhik. *Table of integrals, series, and products*. Elsevier/Academic Press, Amsterdam, eighth edition, 2015.

[42] W. Greiner. *Quantum Mechanics: An Introduction*. Springer Verlag Gmbh, 2001.

[43] Q. Guan. Integration by parts formula for regional fractional Laplacian. *Comm. Math. Phys.*, 266:289–329, 2006.

[44] Q. Guan and M. Gunzburger. Analysis and approximation of a nonlocal obstacle problem. *J. Comput. Appl. Math.*, 313:102–118, 2017.

[45] Q. Guan and Z. Ma. Boundary problems for fractional Laplacians. *Stoch. Dyn.*, 5:385–424, 2005.

[46] Q.-Y. Guan and Z.-M. Ma. Reflected symmetric α-stable processes and regional fractional Laplacian. *Probab. Theory Rel.*, 134:649–694, 2006.

[47] E. Hawkins and J. M. Schwarz. Comment on "On the consistency of solutions of the space fractional Schrödinger equation" [J. Math. Phys. 53, 042105 (2012)]. *J. Math. Phys.*, 54:014101, 5, 2013.

[48] R. Herrmann. The fractional Schrödinger equation and the infinite potential well – Numerical results using the Riesz derivative. *Gam. Ori. Chron. Phys.*, 1:1–12, 2013.

[49] Y. Huang and A. Oberman. Numerical methods for the fractional Laplacian: a finite difference-quadrature approach. *SIAM J. Numer. Anal.*, 52:3056–3084, 2014.

[50] M. Jeng, S.-L.-Y. Xu, E. Hawkins, and J. M. Schwarz. On the nonlocality of the fractional Schrödinger equation. *J. Math. Phys.*, 51:062102, 2010.

[51] K. Kaleta. Spectral gap lower bound for the one-dimensional fractional Schrödinger operator in the interval. *Studia Math.*, 209:267–287, 2012.

[52] A. R. Khan, J. Pečarić, and M. Praljak. Weighted Montgomery's identities for higher order differentiable functions of two variables. *J. Numer. Anal. Approx. Theory*, 42:49–71, 2013.

[53] K. Kirkpatrick, E. Lenzmann, and G. Staffilani. On the continuum limit for discrete NLS with long-range lattice interactions. *Comm. Math. Phys.*, 317:563–591, 2013.

[54] K. Kirkpatrick and Y. Zhang. Fractional Schrödinger dynamics and decoherence. *Phys. D*, 332:41–54, 2016.

[55] N. Korabel and G. M. Zaslavsky. Transition to chaos in discrete nonlinear Schrödinger equation with long-range interaction. *Phys. A*, 378:223–237, 2007.

[56] S. Kovač, J. Pečarić, and A. Perušić. Estimations of the difference between two weighted integral means and application of the Steffensen's inequality. *An. Univ. Craiova Ser. Mat. Inform.*, pages 128–140, 2016.

[57] M. Kuczma. *An Introduction to the Theory of Functional Equations and Inequalities*. Birkhäuser Verlag, Basel, second edition, 2009.

[58] T. Kulczycki, M. Kwaśnicki, J. Małecki, and A. Stos. Spectral properties of the Cauchy process on half-line and interval. *Proc. Lond. Math. Soc. (3)*, 101:589–622, 2010.

[59] M. Kwaśnicki. Eigenvalues of the fractional Laplace operator in the interval. *J. Funct. Anal.*, 262:2379–2402, 2012.

[60] M. Kwaśnicki. Ten equivalent definitions of the fractional Laplace operator. *Fract. Calc. Appl. Anal.*, 20:7–51, 2017.

[61] T. I. Lakoba. Instability of the split-step method for a signal with nonzero central frequency. *JOSA B*, 30:3260–3271, 2013.

[62] N. S. Landkof. *Foundations of modern potential theory*. Springer-Verlag, New York-Heidelberg, 1972.

[63] N. Laskin. Fractional quantum mechanics and Lévy path integrals. *Phys. Lett. A*, 268:298–305, 2000.

[64] Nick Laskin. Fractals and quantum mechanics. *Chaos*, 10:780–790, 2000.

[65] S. Longhi. Fractional Schrödinger equation in optics. *Optics Lett.*, 40:1117–1120, 2015.

[66] Y. Luchko. Fractional Schrödinger equation for a particle moving in a potential well. *J. Math. Phys.*, 54:012111, 10, 2013.

[67] R. Metzler and J. Klafter. The random walk's guide to anomalous diffusion: a fractional dynamics approach. *Phys. Rep.*, 339:77, 2000.

[68] C. Mou and Y. Yi. Interior regularity for regional fractional Laplacian. *Comm. Math. Phys.*, 340:233–251, 2015.

[69] R. Musina and A. I. Nazarov. On fractional Laplacians. *Comm. Part. Diff. Eq.*, 39:1780–1790, 2014.

[70] P. K. Newton and J. B. Keller. Stability of periodic plane waves. *SIAM J. Appl. Math.*, 47:959–964, 1987.

[71] M. K. Ng. Band preconditioners for block-Toeplitz–Toeplitz-block systems. *Linear Algebra Appl.*, 259:307–327, 1997.

[72] X. Ros-Oton and J. Serra. The Dirichlet problem for the fractional Laplacian: regularity up to the boundary. *J. Math. Pures Appl. (9)*, 101:275–302, 2014.

[73] Stefan G. Samko, Anatoly A. Kilbas, and Oleg I. Marichev. *Fractional integrals and derivatives*. Gordon and Breach Science Publishers, Yverdon, 1993.

[74] S. Secchi. Ground state solutions for nonlinear fractional Schrödinger equations in $\mathbb{R}^N$. *J. Math. Phys.*, 54:031501, 2013.

[75] R. Servadei and E. Valdinoci. Weak and viscosity solutions of the fractional Laplace equation. *Publ. Mat.*, 58:133–154, 2014.

[76] M. F. Shlesinger, B. J. West, and J. Klafter. Lévy dynamics of enhanced diffusion: application to turbulence. *Phys. Rev. Lett.*, 58:1100–1103, 1987.

[77] S. A. Silling. Reformulation of elasticity theory for discontinuities and long-range forces. *J. Mech. Phys. Solids*, 48:175–209, 2000.

[78] R. Song and Z. Vondraček. Potential theory of subordinate killed Brownian motion in a domain. *Probab. Theory Related Fields*, 125:578–592, 2003.

[79] R. Song and Z. Vondraček. On the relationship between subordinate killed and killed subordinate processes. *Electron. Commun. Probab.*, 13:325–336, 2008.

[80] E. M. Stein. *Singular integrals and differentiability properties of functions*. Princeton Mathematical Series, No. 30. Princeton University Press, Princeton, N.J., 1970.

[81] M. Stewart. A superfast Toeplitz solver with improved numerical stability. *SIAM J. Matrix Anal. A.*, 25:669–693, 2003.

[82] G. Strang. On the construction and comparison of difference schemes. *SIAM J. Numer. Anal.*, 5:506–517, 1968.

[83] X. Tian and Q. Du. Analysis and comparison of different approximations to nonlocal diffusion and linear peridynamic equations. *SIAM J. Numer. Anal.*, 51:3458–3482, 2013.

[84] H. Wang, K. Wang, and T. Sircar. A direct $O(N \log^2 N)$ finite difference method for fractional diffusion equations. *J. Comput. Phys.*, 229:8095–8104, 2010.

[85] M. Webb. Analysis and approximation of a fractional differential equation. Master's Thesis, Oxford, 2012.

[86] J. A. C. Weideman and B. M. Herbst. Split-step methods for the solution of the nonlinear Schrödinger equation. *SIAM J. Numer. Anal.*, 23:485–507, 1986.

[87] S. Y. Yolcu and T. Yolcu. Estimates for the sums of eigenvalues of the fractional Laplacian on a bounded domain. *Commun. Contemp. Math.*, 15:1250048, 15, 2013.

[88] S. Y. Yolcu and T. Yolcu. Refined eigenvalue bounds on the Dirichlet fractional Laplacian. *journal of Math. Phys.*, 56, 2015.

[89] H. C. Yuen and W. E. Ferguson. Relationship between Benjamin–Feir instability and recurrence in the nonlinear Schrödinger equation. *Phys. Fluids*, 21:1275–1278, 1978.

[90] M. Żaba and P. Garbaczewski. Solving fractional Schrödinger-type spectral problems: Cauchy oscillator and Cauchy well. *J. Math. Phys.*, 55:092103, 20, 2014.

[91] G. M. Zaslavsky, M. Edelman, and V. E. Tarasov. Dynamics of the chain of forced oscillators with long-range interaction: from synchronization to chaos. *Chaos*, 17:043124, 10, 2007.

[92] R. Zeng and Y. Zhang. Efficiently computing vortex lattices in fast rotating Bose–Einstein condensates. *Comput. Phys. Commun.*, 180:854–860, 2009.

[93] Y. Zhang. *Mathematical analysis and numerical simulation for Bose–Einstein condensation*. PhD thesis, National University of Singapore, 2006.

[94] Y. Zhang, X. Liu, M. R. Belić, W. Zhong, Y. Zhang, and M. Xiao. Propagation dynamics of a light beam in a fractional Schrödinger equation. *Phys. Rev. Lett.*, 115:180403, 2015.

[95] Y. Zhang, H. Zhong, M. R. Belić, Y. Zhu, W. Zhong, Y. Zhang, D. N. Christodoulides, and M. Xiao. Back Cover: PT symmetry in a fractional Schrödinger equation. *Laser and Photonics Reviews*, 10:534–534, 2016.

[96] A. Zoia, A. Rosso, and M. Kardar. Fractional Laplacian in bounded domains. *Phys. Rev. E*, 76:021116, 2007.

VITA

Siwei Duo was born in Tianjin, China. She received her Bachelor of Science degree in Mathematics in 2012 from Sichuan University, Sichuan, China. After receiving her bachelor degree she attended Missouri University of Science and Technology (formerly University of Missouri at Rolla) in the program of Computational and Applied Mathematics. She received her Ph.D. degree in Mathematics in July, 2017. In addition to her studies and research, Siwei served as a teaching assistant from 2014 to 2016 at Missouri University of Science and Technology.